

ISTANBUL TECHNICAL UNIVERSITY ★ GRADUATE SCHOOL OF SCIENCE
ENGINEERING AND TECHNOLOGY

**THE GEOLOGY, PETROLOGY AND THERMOCHRONOLOGY OF ILICA-
ŞAMLI (SOLARYA) VOLCANO-PLUTONIC COMPLEX AND ITS
SIGNIFICANCE ON WESTERN ANATOLIAN GEODYNAMICS**



PhD THESIS

Alp ÜNAL

Department of Geological Engineering

Geological Engineering Programme

NOVEMBER 2019

ISTANBUL TECHNICAL UNIVERSITY ★ GRADUATE SCHOOL OF SCIENCE
ENGINEERING AND TECHNOLOGY

**THE GEOLOGY, PETROLOGY AND THERMOCHRONOLOGY OF ILICA-
ŞAMLI (SOLARYA) VOLCANO-PLUTONIC COMPLEX AND ITS
SIGNIFICANCE ON WESTERN ANATOLIAN GEODYNAMICS**

PhD THESIS

**Alp ÜNAL
(505132301)**

Department of Geological Engineering

Geological Engineering Programme

Thesis Advisor: Prof. Dr. Şafak ALTUNKAYNAK

NOVEMBER 2019

ISTANBUL TEKNİK ÜNİVERSİTESİ ★ FEN BİLİMLERİ ENSTİTÜSÜ

**ILICA-ŞAMLI (SOLARYA) VOLKANO-PLÜTONİK KOMPLEKSİNİN
JEOLojİSİ, PETROLOJİSİ, TERMOKRONOLOJİSİ VE KB ANADOLU
JEODİNAMİĞİNDEKİ YERİ**

DOKTORA TEZİ

**Alp ÜNAL
(505132301)**

Jeoloji Mühendisliği Anabilim Dalı

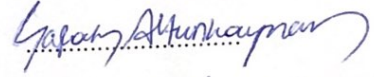
Jeoloji Mühendisliği Programı

Tez Danışmanı: Prof. Dr. Şafak ALTUNKAYNAK

KASIM 2019

Alp Ünal, a Ph.D. student of İTÜ Graduate School of Science Engineering and Technology student ID 505132301, successfully defended the thesis/dissertation entitled "THE GEOLOGY, PETROLOGY AND THERMOCHRONOLOGY OF ILICA-ŞAMLI (SOLARYA) VOLCANO-PLUTONIC COMPLEX AND ITS SIGNIFICANCE ON WESTERN ANATOLIAN GEODYNAMICS", which he prepared after fulfilling the requirements specified in the associated legislations, before the jury whose signatures are below.

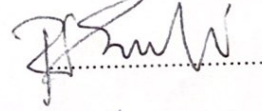
Thesis Advisor : **Prof. Dr. Şafak ALTUNKAYNAK**
İstanbul Technical University



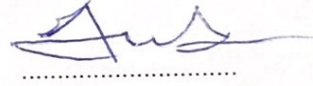
Jury Members : **Prof. Dr. Serdar AKYÜZ**
İstanbul Technical University



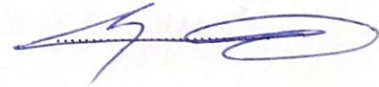
Prof. Dr. Fahri ESENLİ
İstanbul Technical University



Prof. Dr. Ercan ALDANMAZ
Kocaeli University



Prof. Dr. Erdiñç YİĞİTBAŞ
Çanakkale Onsekiz Mart University



Date of Submission : 27 September 2019
Date of Defense : 07 November 2019



To my beloved family,



FOREWORD

First of all, i would like to thank my advisor, Prof. Dr. Şafak ALTUNKAYNAK; this thesis and all my acedemic background would not be possible without her limitless guidance, support and especially encouragement throughout my not only academic but also entire life. I know, from the bottom of my heart, that this simple “thank you” is not enough. I have been and always will be more than proud to be her student...

My special thanks belong to my “family” Işıl Nur GÜRASLAN and Ömer KAMACI, who are not any different from sister and brother which I do not have in my non-academic life. Without their support and patience, this thesis would not be succesful. They will always stay as an important part of my life.

A lot of people have contributed to this thesis that i am grateful to. Especially, I would like to thank to my thesis commettee Prof. Dr. H. Serdar AKYÜZ and Prof. Dr. Ercan ALDANMAZ for their kind and helpful suggestions for my PhD study. I would also like to acknowledge the special contributions of Assoc. Prof. Dr. Gürsel SUNAL, Prof. Dr. İbrahim UYSAL and Asst. Prof. Geoffrey H. HOWARTH who shared all of their scientific experience with me. I would like to thank to all staff of University of Georgia for fruitful and joyful memories during my time at USA. But my special thanks go to Prof. Dr. Paul SCHROEDER, Linda SCHROEDER, Prof. Dr. Mike RODEN and Chris FLEISCHER. They all created wonderful memories that I will not ever forget. I believe that friendship is one of the most important backbones that leads someone to success. I would like to thank to my beloved friends/family who are known as Ules Team for their limitless cheer ups during my PhD study. I have to express my special indebtedness to the co-founder of Ules Team, a wonderful musician Orhan Veli ÖZBAYRAK for not only his support, but for his amazing musics which inspired me all the time. I have to mention here that wonderful actor-geologist Gün AKINCI, geologists Yağmur GERZELİ HAN sand Merve USANMAZ were substantially helpful during the preparation of this thesis, i am grateful for their contributions. Also Yağmur GÜNEŞ, Fırat and Fulya GÜR and Volkan ÖZEN are acknowledged.

A special thanks go to lovely Duygu ÜNLÜ for her endless support during the final and most difficult times of this thesis and my academic life. Lastly, all my family and my beloved parents Sevgi and Arif ÜNAL were inexpressibly supportive not only during this thesis but also my entire life. I would not have survived without them, I love you so much.

“Our true mentor in life is science.” M. Kemal ATATÜRK.

May the science be with me...

August 2019

Alp ÜNAL
(Geologist)



TABLE OF CONTENTS

	<u>Page</u>
TABLE OF CONTENTS.....	xi
LIST OF TABLES	xiii
LIST OF FIGURES	xv
SUMMARY	xix
1. INTRODUCTION.....	1
1.1 Scope Of Thesis	2
1.2 Structure of The Thesis	3
2. NATURE AND GENESIS OF POTASSIC HIGH BA\\SR GRANITOIDS ASSOCIATED WITH SYN-CONVERGENT EXTENSION IN NW TURKEY	5
2.1 Introduction	5
2.2 Geological Setting	7
2.3 Petrography	11
2.4 Geochemistry	13
2.4.1 Analytical methods	14
2.4.1.1 Major, trace elements	14
2.4.1.2 Sr-Nd-Pb-O isotope analyses	14
2.4.2 Results.....	17
2.4.2.1 Major and trace element geochemistry	17
2.4.2.2 The Sr-Nd-Pb and ¹⁸ O isotope geochemistry.....	18
2.5 Discussion	20
2.5.1 Petrological classification	20
2.5.2 Petrogenesis of Solarya plutonic association	28
2.5.2.1 Nature of high Ba–Sr magma.....	28
2.5.2.2 Magma evolution	31
2.5.3 Significance of high Ba-Sr granitoids in western Anatolia Cenozoic geodynamics.....	33
3. THE EMPLACEMENT HISTORY OF GRANITIC INTRUSIONS INTO THE UPPER CRUST: FORCEFUL TO PASSIVE EMPLACEMENT OF EARLY MIOCENE SOLARYA PLUTON (NW TURKEY) AS A CASE STUDY	43
3.1 Introduction	43
3.2 Geological Setting	45
3.2.1 Regional Geology	45
3.2.2 Pluton Interior	46
3.2.3 Wall and Roof Rocks	48
3.2.4 Cover Rocks.....	54
3.3 Analytical Methods	55
3.3.1 Geochronology.....	55
3.3.2 Mineral Chemistry	60
3.4 Results	60
3.4.1 U-Pb Zircon Chronology	60
3.4.2 ⁴⁰ Ar/ ³⁹ Ar Biotite and Feldspar Chronology.....	60

3.4.3 Geothermo-barometry Calculations: Al in hornblende geothermo-barometry	62
3.5 Discussion: Emplacement of the Solarya Pluton.....	64
3.6 Conclusions	72
4. INTERPLAY BETWEEN VOLCANIC AND PLUTONIC SYSTEMS: A CASE STUDY OF THE EARLY MIOCENE SOLARYA VOLCANO-PLUTONIC COMPLEX IN NW ANATOLIA (TURKEY).....	73
4.1 Introduction	73
4.2 Stratigraphy	75
4.3 Petrography.....	79
4.4 Analytical Methods	85
4.4.1 Geochronology.....	85
4.4.2 Geochemistry	86
4.5 Results	89
4.5.1 Geochronology.....	89
4.5.2 Geochemistry	90
4.5.2.1 Major and trace element geochemistry	90
4.5.2.2 Sr-Nd-Pb-O isotopes	98
4.6 Discussion.....	98
4.6.1 Magma source	98
4.6.1.1 Mantle-continental crust interactions.....	101
4.6.2 Evolution of magma.....	103
4.6.3 Connections between regional extension and Volcano-Plutonic Complexes	104
4.7 Conclusions	108
5. CONCLUSIONS.....	109
REFERENCES.....	111
CURRICULUM VITAE	133

LIST OF TABLES

	<u>Page</u>
Table 2. 1: Petrographical features of SPA and HA.	15
Table 2. 2: Representative chemical analyses of Solarya Plutonic Association and Hypabyssal Association	25
Table 2. 3: Taylor (1978) classification of magmatic rocks based on their $\delta^{18}\text{O}_{\text{SMOW}}$	33
Table 3. 1: Zircon U-Pb isotopic data for the SP	58
Table 3. 2: $^{40}\text{Ar}/^{39}\text{Ar}$ biotite and feldspar data for the SP. Bi: Biotite; KF: K-feldspar; Plg: Plagioclase	63
Table 3. 3: Amphibole-plagioclase geothermo-barometry results for the SP	65
Table 4. 1: Petrographical Features of Solarya Volcano-plutonic Complex.....	81
Table 4. 2: Interpretive details for $^{40}\text{Ar}/^{39}\text{Ar}$ results of Solarya Volcano-plutonic Complex	87
Table 4. 3: Major-trace and isotopic compositions of the volcanic association of Solarya Volcano-plutonic Complex.....	92



LIST OF FIGURES

	<u>Page</u>
Figure 2. 1: Tectonic Units of the East Mediterranean Region and simplified geological map of northwestern Anatolia showing the distribution of the Eocene (E1 to E7) and Miocene (1 to 15) post-collisional granitoid plutons along with the main rock units. IAESZ: Izmir-Ankara-Erzincan Suture Zone.	6
Figure 2. 2: Geological map of the study area.	8
Figure 2. 3: Generalized stratigraphic section of the study area (not to scale).	9
Figure 2. 4: Field photographs from the Solarya Plutonic Association a) K-feldspar megacrystalline granodiorite (KFMG) with observable K-feldspar megacrysts and Mafic Microgranular Enclaves (MME) b) Microgranite-granodiorite (MGG) c) Intrusive contact between haplogranite and basement rocks d) Intrusive contact between MGG and hypabyssal association (HA).	10
Figure 2. 5: Micrographs illustrating the main petrographical features of Solarya Plutonic Association (SPA) and hypabyssal association (HA) a) Holocrystalline porphyritic texture of KFMG b) Fine grained microgranular texture of MGG c) Graphic/granophyric textures from haplogranites d) Contact between MME and KFMG e) Holocrystalline microgranular-porphyritic texture of HA f) Holocrystalline microgranular- porphyritic texture of MME (Bio: Biotite, Plg: Plagioclase, Amp: Amphibole, Q: Quartz, K.F.: K-Feldspar, Grp: Graphic/Granophyric texture).	14
Figure 2. 6: a) Total alkali vs. SiO ₂ classification diagram. Alkaline/Sub- alkaline classification of Irvine and Baragar, 1971 is also included to the figure b) Multicationic P–Q classification diagram.	20
Figure 2. 7: AFM diagram of SPA and HA.	21
Figure 2. 8: AFM diagram of SPA and HA.	22
Figure 2. 9: Major elements vs. SiO ₂ Harker variation diagrams for SPA and HA. ...	23
Figure 2. 10: a) Primitive-mantle normalized multi-element patterns for SPA and HA, b) Chondrite-normalized REE patterns SPA and HA. Chondrite normalizing values are from Boynton (1984).	25
Figure 2. 11: a) $\epsilon_{Nd(21)}$ vs. $^{87}Sr/^{86}Sr(21)$ diagram for SPA and HA. Simple bulk-mixing modeling between WAAMM and WACM is also included. b) $\epsilon_{Nd(21)}$ vs. TDM diagram for SPA and HA.	33
Figure 2. 12: a) $\epsilon_{Nd(21)}$ vs. $^{87}Sr/^{86}Sr(21)$ diagram for SPA and HA. Simple bulk-mixing modeling between WAAMM and WACM is also included. b) $\epsilon_{Nd(21)}$ vs. TDM diagram for SPA and HA. Average EMM.	35
Figure 2. 13: $\delta^{18}O$ (smow) variation of SPA (quartz, feldspar) according to Taylor (1978) classification.	36

Figure 2. 14: Plot of $^{87}\text{Sr}/^{86}\text{Sr}$ ($_{21}$) versus SiO_2 (wt%), showing the results of AFC modeling for SPA and HA. EMM.	37
Figure 2. 15: Sr–Rb–Ba plot for (a) Solarya Plutonic Association (b) Eocene and Miocene plutons of western Anatolia	39
Figure 3. 1: Simplified geological map of the NW Anatolia. Black rectangle shows the Solarya Pluton (SP).	44
Figure 3. 2: Geological map of the study area.	46
Figure 3. 3: a) Field photograph of K-feldspar megacrystalline granodiorite (KFMG). b) Micrograph illustrating the porphyritic texture of KFMG (Kf: K-Feldspar; Plg: Plagioclase; Q: Quartz; Hb: Hornblende). c) Field photograph of microgranite-granodiorite (MGG). d) Micrograph illustrating the microgranular texture of KFMG (Kf: K-Feldspar; Q: Quartz).	47
Figure 3. 4: a) N-S cross-section of the study area (X-X'). Figure also illustrates the major faults cutting the SP. b) Steographic projection of three major faults.	49
Figure 3. 5: a) Field photograph of metapelites b) Micrograph of metapelites. The S-1 foliation plane is shown in the figure. c) Field photograph of marbles. d) Micrograph of marbles. e) The contact intrusive between KFMG and wall rocks. f) The contact between haplogranite and roof rocks.	50
Figure 3. 6: a, b) The elongation of wollastonite and diopside in contact schists over a secondary foliation plane (S-2) c, d) Decrease of grain size in marbles outwards the pluton boundary.	51
Figure 3. 7: a, b) Micrographs illustrating the main petrographical features of the contact metamorphic rocks a) Wollastonite (Wo) porphyroblast in hornfels near the contact. b) Cathodoluminescence image of wollastonite (Wo) within the inner zone. c) Co-existence of diopside (Di) and hyperstene (Hp) in the contact metamorphic rocks of the inner zone. d) Tremolite (Tr) and quartz (Q) development in the contact metamorphic rocks towards the outer zone e) Hornblende (Hb), albite (Ab) and diopside (Di) paragenesis in the outer zone f) Garnet (Gr) with calcite (Cal) in the contact metamorphic rocks of the outer zone.	52
Figure 3. 8: a) The structural geology map of the SP and surrounding rocks (wall rocks). b) Steographic projections of the foliation planes of regional metamorphic rocks c) Steographic projections of the foliation planes of regional metamorphic rocks along the contact with the SP.	53
Figure 3. 9: Field photographs of volcanic and sedimentary association a) Dacite b) Sandstone of lower sedimentary association c) and d) upper sedimentary association with granodiorite blocks.	55
Figure 3. 10: a) The $^{206}\text{Pb}/^{238}\text{U}$ vs. $^{207}\text{Pb}/^{235}\text{U}$ concordia diagram for sample AS 211 (KFMG) b) The $^{206}\text{Pb}/^{238}\text{U}$ vs. $^{207}\text{Pb}/^{235}\text{U}$ concordia diagram for sample AS 240 (MGG) c) CL images of dated zircon crystals from AS 211 (KFMG) d) CL images of dated zircon crystals from AS 240 (MGG).	61
Figure 3. 11: a) $^{40}\text{Ar}/^{39}\text{Ar}$ isochron and plateau ages of the SP. The sample name and group are shown on each of the diagrams. Steps in red are used in the isochron age determinations. Steps in grey are used in the plateau age determinations.	62

Figure 3. 12: a) Ring fractures/faults developed due to the emplacement of the SP. Haplogranite and hypabyssal association were emplaced into the ring faults, which are shown by dashed lines. b) W-E cross section along the southern contact of the SP (horizontally not to scale, the cross-section directions are shown in Figure 12a). c) Qz-Ab-Or triangle illustrating the pressure conditions of haplogranites.	67
Figure 3. 13: Schematic cross-sections illustrating the consecutive emplacement stages of the SP. a) The forceful emplacement of the SP b) Fracture development due to the pluton emplacement c) Passive emplacement (cauldron subsidence) stage of the SP d) Block diagram showing the final position of the SP.	70
Figure 3. 14: Schematic diagram of the upwelling magma in cauldron subsidence.	71
Figure 4. 1: Simplified geological map of the NW Anatolia. Black rectangle shows Solarya Volcano-plutonic Complex (SVPC) (1), blue rectangles show Kozak (2), Bayramiç (3), Kestanbol (4) and Alaçamdağ (5) volcano-plutonic complexes. Yellow circles exhibit the major core complexes in NW Anatolia (KM: Kazdağ, MM: Menderes, ÇM: Çataldağ).	74
Figure 4. 2: Geological Map of the area.	75
Figure 4. 3: Generalized stratigraphical column of the study area (not to scale).	76
Figure 4. 4: Field photographs from the SVPC (a) Porphyritic texture of K-feldspar megacrystalline granodiorite developed with K-feldspar megacrysts. Also, mafic microgranular enclave is shown in the figure. (b) Intrusive contact between Hypabyssal Association (HA) and microgranodiorite. (c) Intrusive contact between HA and volcanic association (VA). (d) Contact between HA and VA showing the interfingering relationship. (e) Contact between ash-block flow and ash fall deposits. (f) The interfingering of VA and Lower Sedimentary Association (LSA). Figure also illustrates the pebbles of LSA from different lithologies.	77
Figure 4. 5: The textural properties of the different members of SVPC.	80
Figure 4. 6: Micrographs illustrating the main petrographical features of VA of SVPC (a) Oscillatory zoning (Os) of plagioclase (Plg) in andesite lava, XPL. (b) Sieve texture (Sv) in a single plagioclase crystal (Plg) in dacite lava, XPL. (c, d) Biotite crystal (Bio) in trachyandesite mantled by hornblende (Hb) c:XPL, d:PPL. (e, f) Hornblende crystal (Hb) in trachyandesite mantled by pyroxene (Prx) e:XPL, f:PPL. (g) Corroded plagioclase in dacite lava (XPL) h) Holocrystalline microgranular-porphyritic texture of volcanic enclave (XPL). XPL: Crossed polarised light, PPL: Plane polarised light, scale is 1 mm.	84
Figure 4. 7: $^{36}\text{Ar}/^{40}\text{Ar}$ versus $^{39}\text{Ar}/^{40}\text{Ar}$ ratios and age spectra diagrams for volcanic and hypabyssal associations of SVPC. Figure also shows the isochron ages and the ^{39}Ar release ratio of the samples.	88
Figure 4. 8: a) Total alkali versus SiO_2 classification diagram. (b) SiO_2 versus Zr/TiO_2 classification diagram.	91
Figure 4. 9: (a) K_2O versus SiO_2 diagram of VA using the classification of Peccerillo and Taylor, results of Solarya Plutonic Association (SPA) and HA are also included.	95
Figure 4. 10: Harker variation diagrams VA, presented together with results of SPA and HA. For legend please see Figure 2.9.	96

Figure 4. 11: Primitive-mantle normalized multi- element patterns for SVPC. (b) Chondrite-normalized REE patterns of SVPC.	97
Figure 4. 12: $\epsilon\text{Nd}_{(22)}$ versus $^{87}\text{Sr}/^{86}\text{Sr}_{(22)}$ diagram for SVPC. Simple bulk-mixing modelling is also included to the figure.	99
Figure 4. 13: (a) $\delta^{18}\text{O}_{(\text{SMOW})}$ quartz versus $^{87}\text{Sr}/^{86}\text{Sr}$ diagram for SVPC. (b) $\delta^{18}\text{O}_{(\text{SMOW})}$ whole rock versus $\epsilon\text{Nd}(t)$ diagram for SVPC.	100
Figure 4. 14: (a) $^{207}\text{Pb}/^{204}\text{Pb}$ versus $^{206}\text{Pb}/^{204}\text{Pb}$ diagram for SVPC. EMI: Enriched Mantle I, EMII: Enriched mantle II, DM: Depleted Mantle, HIMU: high U/Pb mantle. (b) The position SVPC samples on $^{208}\text{Pb}/^{204}\text{Pb}$ versus $^{206}\text{Pb}/^{204}\text{Pb}$ diagram.	102
Figure 4. 15: Th/Yb versus Ta/Yb log–log diagram for SVPC. Subduction-enriched mantle (EM) and mantle array are also included.	104
Figure 4. 16: (a) Diagram of $^{87}\text{Sr}/^{86}\text{Sr}_{(22)}$ versus SiO_2 (wt.%), presenting the results of AFC modeling for SVPC. (b) $^{87}\text{Sr}/^{86}\text{Sr}_{(22)}$ versus $1/\text{Sr}$ diagram displaying the AFC and FC trajectories.	106



THE GEOLOGY, PETROLOGY AND THERMOCHRONOLOGY OF ILICA-ŞAMLI (SOLARYA) VOLCANO-PLUTONIC COMPLEX AND ITS SIGNIFICANCE ON WESTERN ANATOLIAN GEODYNAMICS

SUMMARY

Western Anatolia (Turkey), located in the Aegean Extensional Province, is widely known as one of the best regions to examine the nature of post-collisional magmatism and to investigate the link between volcanic and plutonic systems and their emplacement conditions which are crucial to better understand the geodynamic evolution of the region. The Solarya (Ilica-Şamlı) Volcano-plutonic Complex (SVPC) is one of the representatives of this post-collisional magmatic activity and remarkable for its coeval and cogenetic volcanic, hypabyssal and plutonic rocks with high Ba-Sr characteristics. In this study, the field properties, petrography, geochemistry, petrogenesis and thermochronology of SVPC have been investigated to contribute to above issues.

Solarya Plutonic Association consists of three main plutonic members showing different textural properties; the northern part of the plutonic body is formed from K-feldspar megacrystalline granodiorite (KFMG) with distinct porphyritic texture whereas southern part is made up of microgranite-granodiorite (MGG) displaying microgranular texture. Haplogranite, which displays graphic/granophyric textures, is represented by a thin aureole between SP and basement rocks. In addition, mafic microgranular enclaves (MME) and mafic dikes of gabbroic diorite to diorite in composition with distinct microgranular/porphyritic texture are common within the plutonic body. Plutonic rocks pass into hypabyssal association which is represented by granodiorite/quartz-diorite porphyry sheet intrusive rocks. Hypabyssal and volcanic rocks cut one another and fragments of hypabyssal rocks are found in volcanic rocks. Volcanic association is formed from trachyandesite, andesite and dacite lavas with associated pyroclastic rocks. Volcanic rocks commonly interfinger with sedimentary rocks.

The U-Pb zircon dating results of SPA range between 21.8 ± 0.2 Ma to 21.2 ± 0.1 Ma. The $^{40}\text{Ar}/^{39}\text{Ar}$ biotite isochron ages differ from 23.2 ± 0.2 to 21.8 ± 0.1 Ma whereas the K-feldspar and plagioclase separates yield plateau ages of 20.3 ± 0.2 Ma and 21.6 ± 0.4 Ma, respectively. $^{40}\text{Ar}/^{39}\text{Ar}$ radiometric ages of volcanic and hypabyssal associations have $^{40}\text{Ar}/^{39}\text{Ar}$ biotite ages changing from 23.1 ± 0.2 to 21.0 ± 0.2 indicating that they are coeval with SPA.

Plutonic, hypabyssal and volcanic associations of SVPC show similar major-trace and Sr-Nd-Pb-O isotopic compositions indicating a common magma source and similar magma chamber processes. They are medium to high-K calc-alkaline rocks and display enrichment in LILE and depletion in Nb, Ta, P and Ti similar to those of post-collisional magmatic rocks. In addition, SPA presents Ba values between 710

and 1505 ppm and Sr values between 305 and 706 ppm indicating that it is one of the representative examples of high Ba-Sr granitoids. SVPC has initial $^{87}\text{Sr}/^{86}\text{Sr}$ values of 0.70702–0.70862 and $^{143}\text{Nd}/^{144}\text{Nd}$ values vary from 0.51232 to 0.512450. They display ϵNd values of -4.9 and -2.05 . $^{207}\text{Pb}/^{204}\text{Pb}$ and $^{206}\text{Pb}/^{204}\text{Pb}$ isotopic values range between 15.68 and 15.73 and 18.75 to 18.88, respectively. Quartz and whole rock $\delta^{18}\text{O}$ isotopic values vary from 8 to 10.6. The geochemical and isotopic characteristics of SVPC are collectively considered to reflect an enriched mantle (EMII) or sub-continental lithospheric mantle source. Bulk mixing model between ϵNd and $^{87}\text{Sr}/^{86}\text{Sr}$ isotopic data suggests that the crustal contribution to the enriched mantle source is about 25–45%.

Field relations, petrography and geothermo-barometry studies on SVPC combined with $^{40}\text{Ar}/^{39}\text{Ar}$ and U-Pb zircon dating results suggest that different members of the SPA were emplaced into different levels of crust with different mechanisms. The KFMG began its emplacement forcefully in the relatively deeper levels in the crust (av. 1.65 kbar; av. 797°C; 6.1 km depth). After this stage, MGG was passively emplaced into the shallow levels (av. 0.69 kbar; av. 745°C; 2.4 km depth) via cauldron subsidence and in the latter stages the sheet intrusive rocks were emplaced into the ring faults at 1.5 km depth.

Evaluation of all these data together with the geology of the region collectively suggests that Solarya Volcano-plutonic Complex and other coeval volcano-plutonic complexes was developed under syn-convergent extensional regime driven by the convective removal or partial delamination of the continental lithosphere beneath western Anatolia.

ILICA-ŞAMLI (SOLARYA) VOLKANO-PLÜTONİK KOMPLEKSİNİN JEOLJİSİ, PETROLOJİSİ, TERMOKRONOLOJİSİ VE KB ANADOLU JEODİNAMİĞİNDEKİ YERİ

ÖZET

Ege Genişlemeli Bölgesi'nde yer alan Batı Anadolu, çarpışma sonrası magmatizmanın gözlemlenebildiği, volkanik-plütonik sistemler arasındaki ilişkinin ve bu magmaların yerleşim koşullarının incelenebildiği en iyi bölgelerden biridir. Bu özelliklerin araştırılması, bölgenin jeodinamik evriminin anlaşılması açısından önem teşkil etmektedir. Solarya (Ilica-Şamlı) Volkano-plütonik Kompleksi (SVPK) eş yaşlı ve eş kökenli volkanik, hipabisal ve yüksek Ba-Sr karakterine sahip plütonik kayalardan oluşmaktadır ve çarpışma sonrası magmatik aktivitenin temsili ürünlerinden bir tanesidir. Bu çalışmada, yukarıdaki konulara katkı sunmak adına SVPK'nin saha özellikleri, petrografisi, jeokimyası, petrojenezi ve termokronolojisi incelenmiştir.

Solarya (Ilica-Şamlı) Volkano-plütonik Kompleksi, Solarya Plütonik Topluluğu (SPT) ve onunla ilişkili hipabisal ve volkanik kayalardan oluşmaktadır. Solarya Plütonik Topluluğu üç farklı plütonik üyeyi barındırmaktadır; plütonun kuzey kesimi holokristalen porfrik dokusu ile belirgin K-Feldspat megakristalli granodiyoritten (KFMG) oluşmakta, güney kısmında ise holokristalen mikrogranüler doku gösteren mikrogranodiyorit (MGG) yer almaktadır. Üçüncü olarak da grafik/granofirik dokular içeren aplogranit, ana plüton gövdesi ve temel kayaları arasında bir hare şeklinde mostra vermektedir. Plütonik gövde boyunca mikrogranüler/porfrik dokusu ile belirgin gabroik diyorit- diyorit bileşimli mafik mikrogranüler anklavlar (MME) ve mafik dayklar yaygındır. Plütonik kayalar, granodiyorit/kuvars diyorit porfirlerden oluşan hipabisal kayalar ile geçişli konumda bulunmaktadırlar. Volkanik ve hipabisal kayalar ise birbirlerini farklı bölgelerde kesmekte ve hipabisal kayaların parçaları volkanik kayaların içerisinde bulunmaktadır. Volkanik kayalar tabanda andezitik kül yağma ve kül blok akma birimleri ile temsil edilmektedir. Bu birimlerin üzerine andezitik akma breşleri gelmekte ve daha üst seviyelerde andezit lavları egemen olmaktadır. Trakiandezit- bazaltik trakiandezit lavları andezitik volkanik kayaçların hemen üstünde konumlanmaktadırlar. Stratigrafik en üst seviyelerde ise dasitik kül yağma ve kül blok akma birimleri, dasitik akma breşleri ve dasit lavları ile birlikte yer almaktadır. Dasit lavları inceleme alanında hem lav akıntıları hem de domlar ile temsil edilmektedir.

Solarya Plütonik Topluluğu'nun U-Pb zirkon yaşları 21.8 ± 0.2 My ile 21.2 ± 0.1 My arasında değişmektedir. Bunlara uyumlu olarak $^{40}\text{Ar}/^{39}\text{Ar}$ biyotit yaşları 23.2 ± 0.2 My ile 21.8 ± 0.1 My arasında, K-Feldspat ve plajioklas yaşları ise 20.3 ± 0.2 My ile

21.6 ± 0.4 My arasında değişmektedir. Volkanik ve hipabisal kayaların ⁴⁰Ar/³⁹Ar biyotit yaşları benzer sonuçlar vererek 23.1 ± 0.2 My ile 21.0 ± 0.2 My arasında değişmektedir. Bu sonuçlar da plütonik, hipabisal ve volkanik kayaların eş yaşlı olduğunu göstermektedir.

Solarya (Ilıca-Şamlı) Volkano-plütonik Kompleksi'ne ait plütonik, hipabisal ve volkanik kayalar, ortak magma kaynağından geldiklerinin ve benzer magma odası süreçleri geçirdiklerinin bir işaretçisi olarak benzer ana-iz element ve Sr-Nd-Pb-O izotopik özellikler sergilemektedir. SVPK orta- yüksek-K kalk-alkalen seriler ile temsil edilmekte, çarpışma sonrası kayalarına benzer olarak LILE'inde zenginleşme ve Nb, Ta, P ve Ti elementlerinde ise fakirleşme göstermektedir. Buna ek olarak SPT'na ait örneklerin Ba değerlerinin 710 ile 1505 arasında, Sr değerlerinin ise 305 ile 706 arasında değiştiği görülmektedir. Bu değerler de SPT'nun yüksek Ba-Sr'lu granitoidlere bir örnek olduğunu göstermektedir. SVPK'nin ilksel izotopik değerlerine bakıldığında ⁸⁷Sr/⁸⁶Sr değerlerinin 0.70702–0.70862 arasında, ¹⁴³Nd/¹⁴⁴Nd değerlerinin ise 0.51232 ile 0.512450 arasında değiştiği görülmektedir. SVPK –4.9 ile –2.05 εNd arasında değişen değerler sunmaktadır. ²⁰⁷Pb/²⁰⁴Pb and ²⁰⁶Pb/²⁰⁴Pb izotop değerleri sırası ile 15.68 ile 15.73 ve 18.75 ile 18.88 arasında değişmektedir. Kuvars ve tüm kaya δ 18O izotop sonuçları da 8 ile 10.6 arasındadır.

Jeotermobarometre hesaplamaları amfibol ve plajiyoklas mineralleri üzerinde yapılmış mineral kimyası sonuçları kullanılarak hesaplanmıştır. Hesaplanan değerler bir çok farklı araştırmacıyı baz alarak hesaplanmış ve ortalama değerler kullanılmıştır. Bunun sonucunda Solarya Plütonik Topluluğu'na ait üyelerin farklı sıcaklık ve basınç yerleşim koşullarına sahip olduğu görülmektedir. K-Feldspat megakristalli granodiyorit için ortalama yerleşim sıcaklığı 797°C yerleşim basınç değeri ise 1.65 kbar olarak hesaplanmıştır. Yerleşim basınç ve sıcaklık değerleri mikrogranit-granodiyorit için ise ortalama 745°C ve 0.69 kbar olarak ortaya konulmuştur. Aplogranitler üzerinde, içerisindeki mafik mineral eksikliği sebebi ile jeotermobarometre hesaplamaları yapılamamıştır. Ancak kuvars-alkali feldspat-plajiyoklas üçgenindeki konumu aplogranitlerin yerleşim basınç değerinin 0.5 kbar'dan az olduğunu göstermektedir.

Saha, petrografi ve jeotermo-barometre sonuçları, ⁴⁰Ar/³⁹Ar ve U-Pb zirkon yaş verileri ile birlikte değerlendirildiğinde Solarya Plütonik Topluluğu'nun farklı üyelerinin kabukta farklı derinliklere farklı mekanizmalar ile yerleştiğini ortaya koymuştur. K-Feldspat megakristalli granodiyorit yerleşimine zorlamalı olarak kabuğun nispeten derin kesimlerinde başlamıştır (or. 1.65 kbar; or. 797°C; 6.1 km derinlik). Zorlamalı yerleşime işaret eden veriler pluton ve temel kayaları arasındaki nispeten dik dokanaklar, plütonun yerleşimi esnasında gelişen yapısal ve bileşimsel değişiklikler olarak sunulabilir. Bu aşamadan sonra mikrogranit-granodiyorit, kazan göçmesi mekanizması ile daha sığ kesimlere pasif olarak yerleşmiştir (or. 0.69 kbar; or. 745°C; 2.4 km derinlik). Bunu izleyen evrede ise levha sokulum kayaları (hipabisal kayalar ve aplogranit) plütonik gövde etrafındaki çembersel kırıklara yaklaşık 1.5 km derinlikte yerleşimini tamamlamıştır. Bu yerleşim sırası elde edilen jeokronoloji verileri ile de desteklenmiştir.

Bütün bu veriler bölge jeolojisi ile birlikte değerlendirildiğinde Solarya Volkano-plütonik Kompleksi ve eş yaşlı diğer volkano-plütonik komplekslerin kıtasal litosfer tabanının sıcak astenosfer tarafından kısmi ergimeye uğratılması veya kıta litosferi tabanının kopup astenosfere gömülmesi mekanizmaları tarafından tetiklenen,

yakınlaşma ile eş zamanlı gelişen genişlemeli rejim (syn-convergent extension)
altında geliştiğine işaret etmektedir.



1. INTRODUCTION

Investigation of post-collisional magmatic terranes has been a popular subject for Earth scientists since many decades. The source characteristics, magma evolution, magma emplacement and possible heat source responsible for the generation of magmatic rocks in a post collisional environment have been controversial topics. To contribute these debates, many researchers studied the extensive Cenozoic magmatism in western Anatolia which is one of the key areas that variety of post-collisional magmatic rocks are observed.

The consumption of a Neo-Tethyan oceanic lithosphere resulted in a continent-continent collision between the Anatolide- Tauride platform and Sakarya continent which is represented by İzmir- Ankara- Erzincan suture zone (IAESZ) (e.g. Şengör and Yılmaz, 1981; Yılmaz, 1989, 1990; Seyitoğlu and Scott, 1996). The timing of this collision is well documented as pre-Eocene by many researchers (e.g. Harris et al., 1994; Okay and Tüysüz, 1999). The extensive magmatic activity postdated this continental collision in western Anatolia and well established in the literature (Altunkaynak, 2007; Altunkaynak and Dilek, 2006; Altunkaynak et al., 2012a, 2012b; Aslan et al., 2017; Boztuğ et al., 2009; Çelebi and Köprübaşı, 2014; Erkül et al., 2005; Ersoy et al., 2017; Genç, 1998; Güraslan and Altunkaynak, 2019; Kamacı et al., 2017; Karacık et al., 2008; Yılmaz, 1989).

The first products of this Cenozoic post-collisional magmatism in western Anatolia are represented by early to late Eocene plutonic and volcanic rocks accompanied by small masses of hypabyssal rocks (Genç and Yılmaz, 1997; Delaloye and Bingöl, 2000; Köprübaşı and Aldanmaz, 2004; Altunkaynak and Dilek, 2006; Altunkaynak, 2007; Altunkaynak et al., 2012b; Güraslan and Altunkaynak, 2019). Plutonic rocks (i.e. Topuk, Gürgenyayla, Tepeldağ, Kapıdağ, Avşa, Fıstıklı) are located linearly through two different E-W trending narrow magmatic belts extending along the IAESZ and south Marmara region. Volcanic rocks are commonly represented by andesitic extrusive rocks whereas hypabyssal rocks are mainly defined as sub-volcanic

counterparts of these plutonic and volcanic rocks. The following magmatic episode is represented by late Oligocene and early Miocene which consists of widespread granitic plutons (i.e. Kozak, Eybek, Çataldağ, Kestanbol, Evciler), volcanic and associated hypabyssal rocks (Yılmaz, 1989; Genç, 1998; Yılmaz et al., 2001; Özgenç and İlbeyli, 2008; Boztuğ et al., 2009; Altunkaynak et al., 2012a).

Many researchers proposed different models to explain the petrogenetic evolution of the magmatic rocks which can be summarized as a) Orogenic collapse related extensional magmatism, b) magmatism caused by compression and crustal thickening, c) syn-convergent extension and magma generation driven by slab-break off, partial delamination or convective removal of the lithosphere. To test these models or develop a viable geochemical and geodynamic model, systematical evaluation of field, petrographical, geochemical and thermochronological properties of magmatic terranes with robust data and their correlation with the geology of the region is essential.

1.1 Scope Of Thesis

Within the scope of the hot debates over the geodynamic history of the western Anatolia, a key area which is represented by approximately 1000 km² area located at the north of the Balıkesir (NW Turkey) city center has been selected. The study area is a critical area in which the plutonic (Ilıca-Şamlı/Solarya Plutonic Association- SPA), hypabyssal and volcanic rocks crop out together and the key field relationships are observable.

This thesis is based on the field and laboratory studies on the different lithologies of the Solarya Volcano-plutonic Complex (SVPC). In field studies the main purposes were i) to reveal the key field relationships of plutonic, hypabyssal and volcanic rocks with country rocks ii) to obtain critical structural data both from the plutonic and country rocks in order to study the emplacement mechanisms of the SPA iii) to determine the eruption centers and the stratigraphy of the volcanic rocks.

Laboratory studies consists of different methods on plutonic, hypabyssal and volcanic rocks which can be summarized as; I) the detailed petrographical studies on both magmatic and basement rocks ii) the whole rock major-trace element and Sr-Nd-Pb-O isotopic analyses of the magmatic rocks iii) Mineral chemistry of the plutonic, hypabyssal and volcanic rocks iv) U-Pb zircon (for only plutonic rocks) and ⁴⁰Ar/³⁹Ar

biotite-feldspar dating of different magmatic rocks. With the collective evaluation of these data, this work contributes to the investigation of following questions:

- The Solarya Plutonic Association (SPA) is one of the important examples of high Ba–Sr granitoids. What is the possible magma evolution and source for this high Ba–Sr magma?
- Many different petrogenetic models are proposed for the generation of the high Ba–Sr granitoids. Which is the most possible petrogenetic model to explain the evolution of SPA?
- Granite emplacement have been a popular matter of debate for the last century. What are the emplacement conditions and mechanisms of the SPA?
- Linking plutonic, hypabyssal and volcanic rocks are essential to examine the evolution of magmatic terranes. What are the key field relationship of these different magmatic rocks? Are they spatially, temporally and genetically related?
- What are the magma chamber processes and mantle-crust interactions developed during the evolution of SVPC on a lithospheric scale?
- Regarding the field, geochemical and geochronological properties of SVPC, what is the most coherent geodynamic model for the post-collisional magmatic evolution of NW Anatolia?

The following chapters will give insights by addressing these different questions.

1.2 Structure of The Thesis

This thesis was structured in the form of introduction (Chapter I) followed by the papers in Chapter II-IV which have been published or accepted during the preparation of this thesis.

Chapter I consists of two sub topics: scope of the thesis and structure of the thesis. The main purpose of the study and the significance of the results are briefly explained in Chapter I.

Chapter II is based on Ünal and Altunkaynak, 2018 reveals the high Ba-Sr characteristics of the SPA and discusses the suggested petrogenetic models for the generation of high Ba-Sr granitoids. In this chapter, detailed field, petrography and

geochemistry of the SPA is presented. With the aid of these data, possible magma source and evolution were investigated. At the end of the chapter, we conclude that the partial melting of EMII which led to the generation of SPA was caused by the upwelling asthenosphere due to the convective removal or partial delamination of the lithosphere beneath western Anadolıa. Therefore, syn-convergent extension related magma generation could be the most viable tectonic process for the development of high Ba- Sr granitoids in western Anatolia, including SPA.

The third chapter is based on Ünal et al., 2019 which is about the emplacement conditions and mechanisms of the SPA for the first time in the literature. In this chapter, the pressure and temperature conditions of the emplacement of the SPA is presented together with the U-Pb zircon and $^{40}\text{Ar}/^{39}\text{Ar}$ biotite- feldspar dating results. Key contact relationships and structural data is also evaluated together in order to provide insights to the different emplacement mechanisms of the SPA. As a result, this chapter reveals that Solarya Pluton began its emplacement forcefully in the relatively deeper levels in the crust. After this stage, it was passively emplaced into the shallow levels via cauldron subsidence

Ünal and Altunkaynak, 2019 provides a basis for chapter IV which presents the detailed volcanic stratigraphy and the petrography of the volcanic rocks located in the study area. This chapter also includes the geochemistry and $^{40}\text{Ar}/^{39}\text{Ar}$ geochronology of the volcanic rocks in order to reveal timing of the magmatism, determine the magma chamber processes and mantle-crust interactions developed during the generation of SVPC. This chapter is a compilation of all of the field, geochemical and geochronological data from plutonic, hypabyssal and volcanic rocks of SVPC. Evaluation of these data collectively suggests that, SVPC was developed under syn-convergent extensional regime.

2. NATURE AND GENESIS OF POTASSIC HIGH Ba/Sr GRANITOIDS ASSOCIATED WITH SYN-CONVERGENT EXTENSION IN NW TURKEY

2.1 Introduction

High Ba–Sr granitoids were primarily defined by Tarney and Jones in 1994 for the Scottish Caledonian granitoids. Many researchers have studied the petrogenesis of high Ba–Sr granitoids worldwide (Tarney and Jones, 1994; Eklund et al., 1998; Fowler et al., 2008; Qin et al., 2009; Choi et al., 2009; Yuan et al., 2010; Yang et al., 2017). High Ba–Sr granitoids are characterized by high Ba (>500 ppm) and Sr (>300 ppm) content. Although petrogenesis of high Ba–Sr granitoids has been studied extensively, there is still a debate on the possible petrogenetic models, including: (1) the partial melting of subducted ocean islands or ocean plateaus which are younger than 25 Ma (Defant and Drummond, 1990, 1993; Tarney and Jones, 1994); (2) partial melting of the mafic lower crust (Choi et al., 2009; Petford and Atherton, 1996; Tarney and Jones, 1994; Ye et al., 2008); (3) the partial melting of veined lithospheric mantle which had been metasomatized by carbonatitic melts (Tarney and Jones, 1994); (4) mixing and/or mingling of mafic (mantle derived mafic melts) and felsic (derived from the partial melting of crust) magmas (Tarney and Jones, 1994).

Western Anatolia, located along the eastern part of the Alpine–Himalayan orogenic system, is widely recognized as one of the best regions to examine the nature of post-collisional magmatism which is represented by variety of magmatic rocks, including high Ba–Sr granitoids. In western Anatolia, extensive magmatic activity occurred during Eocene to Miocene period in an area straddling the continental collision zone between the Sakarya and Anatolide-Tauride continental blocks. This produced several plutons associated with sub-volcanic and volcanic rocks forming volcano-plutonic complexes. Representatives of the plutonic complexes in Western Anatolia are displayed in Figure 2.1.

This chapter is based on the paper; Alp Ünal, Şafak Altunkaynak, “Nature and Genesis of Potassic High Ba/Sr Granitoids Associated with Syn-Convergent Extension in NW Turkey, *Lithos*, (2018), 316-317, 261-277.

There are a number of studies which cover these plutonic associations (Altunkaynak, 2007; Altunkaynak et al., 2012a; Altunkaynak et al., 2012b; Altunkaynak and Yılmaz, 1998; Bingöl et al., 1982; Boztuğ et al., 2009; Çelebi and Köprübaşı, 2014; Delaloye and Bingöl, 2000; Ercan et al., 1995; Genç, 1998; Genç and Yılmaz, 1997; Harris et al., 1994; Kamacı and Altunkaynak, 2011; Karacık et al., 2008; Karacık and Yılmaz, 1998a; Topuz and Okay, 2017; Yılmaz, 1989). The Solarya Plutonic Association (SPA), one of the important examples of a high Ba–Sr granitoid is located in NW Anatolia which is western part of the Aegean extensional province (Figure 2.1, stated as number “10”). Although there are a few studies in the literature which include field characteristics, geochemical and geochronological properties of SPA (Altunkaynak et al., 2012a; Boztuğ et al., 2009; Bürküt, 1966; Çelebi and Köprübaşı, 2014; Karacık et al., 2008; Yılmaz et al., 2014) these studies do not reveal SPA as a high Ba–Sr granitoid and do not provide combined Sr–Nd–Pb–O isotopic

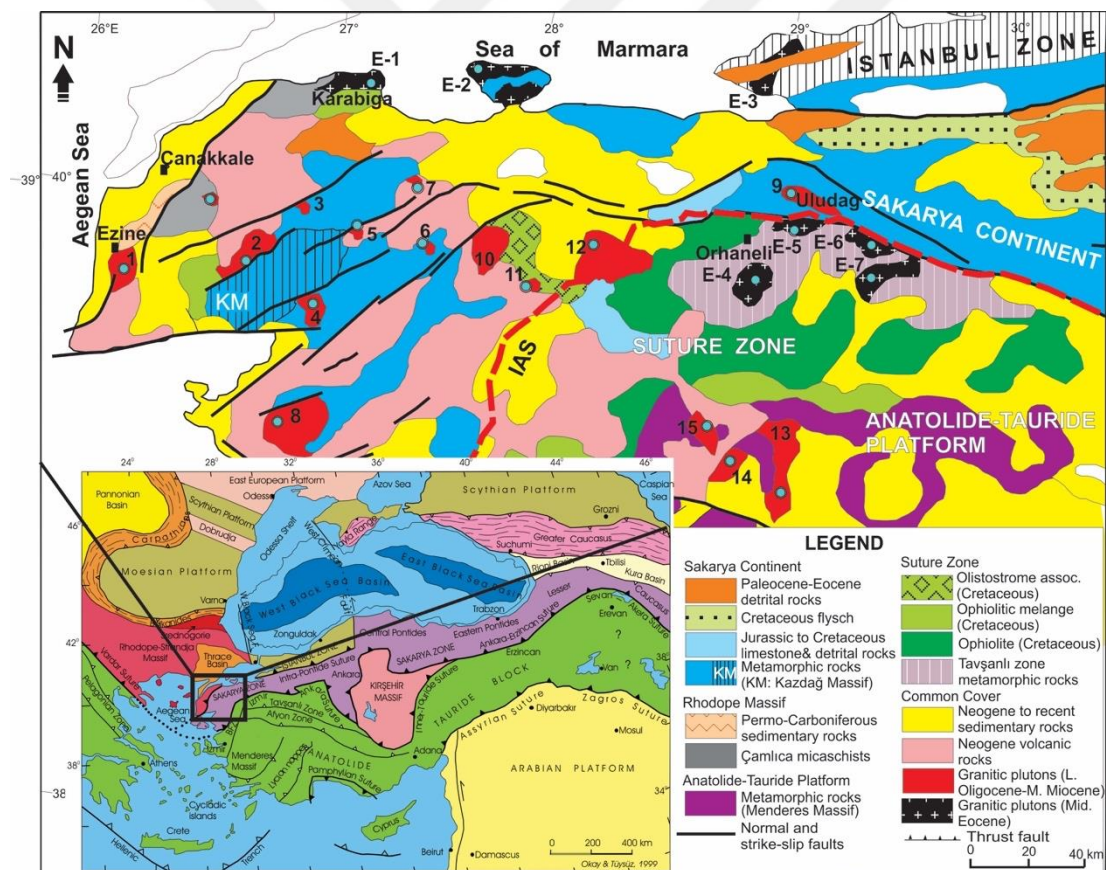


Figure 2.1: Tectonic Units of the East Mediterranean Region (Okay and Tüysüz, 1999) and simplified geological map of northwestern Anatolia showing the distribution of the Eocene (E1 to E7) and Miocene (1 to 15) post-collisional granitoid plutons along with the main rock units (Modified from Okay and Satir, 2006; Yılmaz et al., 2000). IAESZ: Izmir-Ankara-Erzincan Suture Zone.

data to enable discussion of possible magma sources and evolution of this high Ba-Sr magmatic association as well as the geodynamic setting.

In this study, we have investigated the field properties, petrography, geochemistry and petrogenesis of Solarya Plutonic Association. This study provides us an opportunity to evaluate the possible magma sources and the evolution of the magma for high Ba-Sr granitoids. At the end, we discuss the significance of Solarya pluton, and thus the high Ba-Sr granitoids within the geodynamics of western Anatolia. Regarding the geodynamic history of the Western Anatolia and broader Aegean Extensional Province, investigating the possible magma source and evolution of SPA as a high Ba-Sr granitoid in conjunction with the geodynamic implications may contribute to the debate over the relationship between tectonics and high Ba-Sr magmatism.

2.2 Geological Setting

The geological map and the generalized stratigraphical section of the area are given in Figure 2.2 and Figure 2.3, which reveals that there are five different rock types in the area based on their field and petrographical properties: (1) Basement rocks (metamorphic and non-metamorphic), (2) Solarya Plutonic Association (SPA), (3) Hypabyssal Association (HA), (4) Volcanic Association (VA) and (5) Sedimentary Association (SA).

The SPA is divided into three coeval granitic members: (a) K-feldspar megacrystalline granodiorite (KFMG) forming the northern part of the pluton (Figure 2.4a); (b) microgranite-granodiorite (MGG) (Figure 2.4b) forming the southern part of the pluton and (c) haplogranite which crop out between basement rocks and the main plutonic body as a thin outer aureole (Figure 2.4c).

The Solarya pluton is emplaced into the metamorphic basement rocks of Karakaya complex, which consist of metacarbonates, metapelites and metabasites (Bingöl, 1975; Okay et al., 1990). The plutonic association developed contact metamorphism around it to the north, west and east. The contact metamorphic aureole forms hornfels and skarns, which are generally represented by calcsilicate fels. Calcsilicate fels consist of plagioclase + tremolite + calcite + diopside ± garnet ± quartz mineral paragenesis, which indicates that the contact metamorphism reached hornblende-hornfels facies conditions.

The Solarya pluton includes a number of magmatic enclaves. The enclaves have variable sizes between 0.5 cm and 50 cm (Figure 2.4d). Magmatic enclaves are represented by quartz diorite, gabbroic diorite and diorite compositions and they are similar to the “the mafic microgranular enclaves” of Didier and Barbarin (1991). Mafic syn-plutonic dikes, presenting similar mineralogical properties with MMEs are also observable within the main plutonic body.

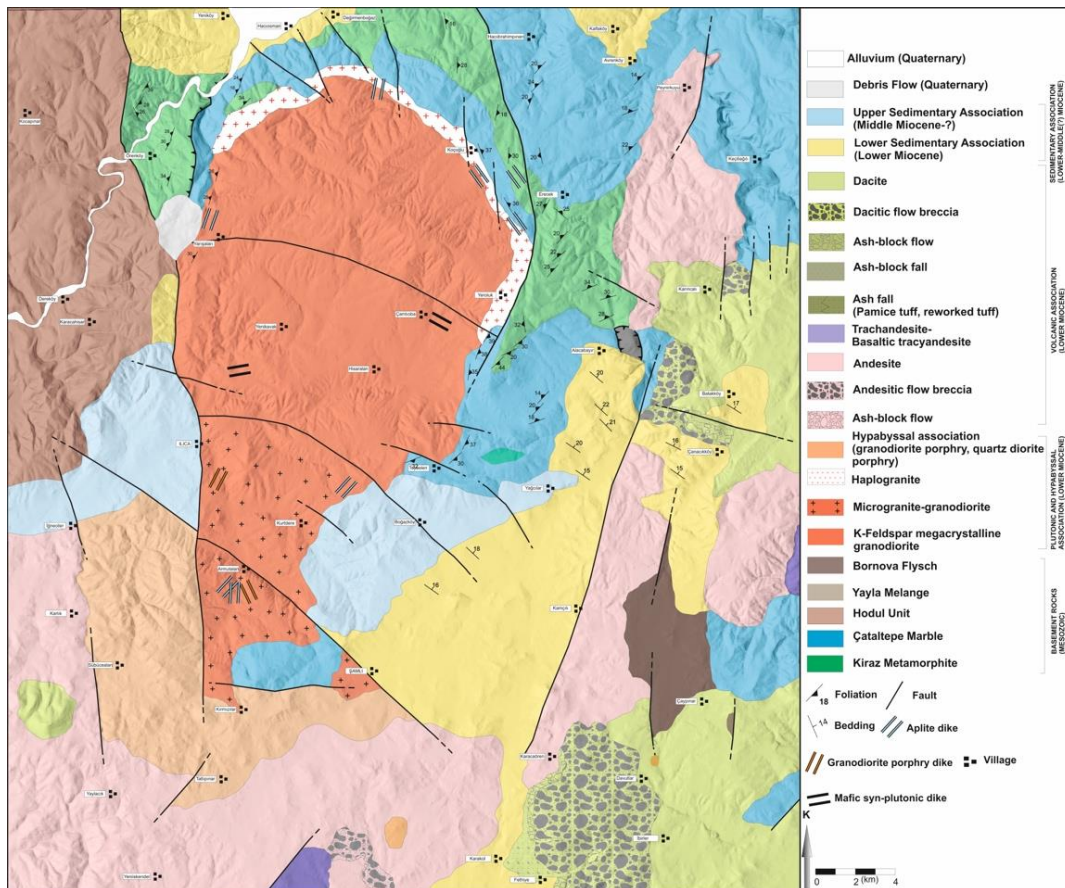


Figure 2.2: Geological map of the study area.

Solarya Plutonic Association (SPA) crops out at the center of the Mount Solarya (Balıkesir) which forms a N-S elongated plutonic body covering approximately 220 km².

The haplogranite crops out along the outer zone between Solarya pluton and basement rocks and forms a thin belt. It is a fine-grained leucocratic-hololeucocratic variety of the main pluton, and it surrounds the main plutonic body along the north, northwest and northeast contacts. The haplogranite is a quartz and feldspar rich rock with no mafic minerals (biotite-amphibole <5%).

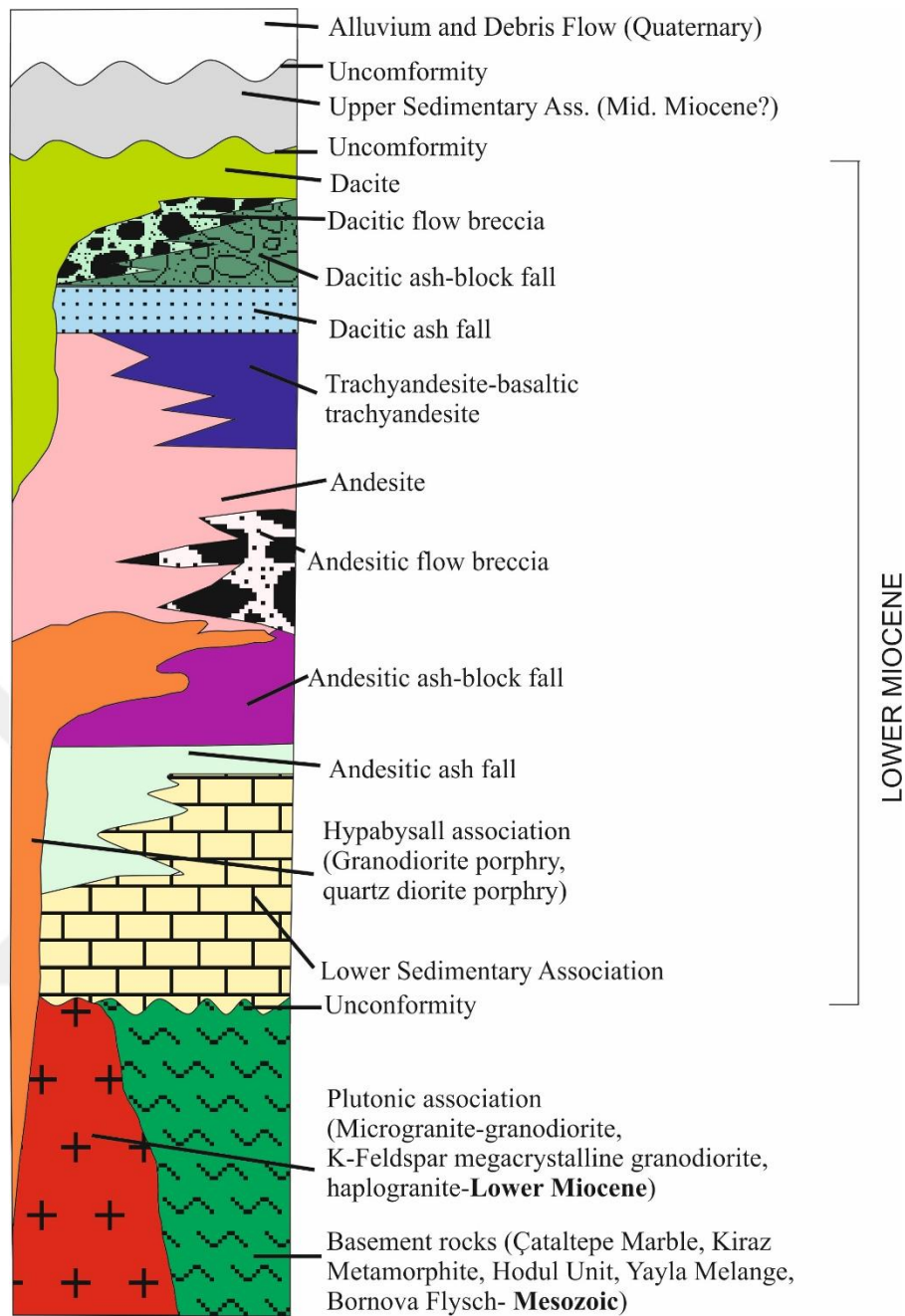


Figure 2.3: Generalized stratigraphic section of the study area (not to scale).

Haplogranites were intruded into the Solarya pluton and basement rocks and in some places; it cuts the Solarya pluton in the form of dikes. The aplite and quartz porphyry dikes cut both the main plutonic body and surrounding basement rocks. They have variable sizes between 1 and 30 cm. Aplitic fine grained texture is common in the aplite dikes.

Hypabyssal association (HA) cut and gradually passes into Solarya pluton at the southern part of the area indicating their *syn*-plutonic emplacement. They are represented by granodiorite/quartz-diorite porphyry sheet intrusive rocks showing

similar mineralogical and petrographical properties with main plutonic body. The hypabyssal rocks were injected into the ring fault system at the southern part of pluton. The hypabyssal rocks also pass laterally into lavas indicating that the magma forming the hypabyssal rocks reached the surface and formed lava flows. Volcanic rocks range between basaltic trachyandesite to dacite, and they are both spatially and temporally associated with SPA and HA.

A sedimentary association crops out at the southeastern and southwestern part of the area and it can be divided into two different groups; (1) Lower Sedimentary Association and (2) Upper Sedimentary association. Lower sedimentary association is formed from conglomerate, sandstone and limestone. It discontinuously overlays the basement rocks and interfingers with volcanic association. Upper Sedimentary Association consists of unlithified coastal sediments, which present coarse sand, and pebble layers were originated from different lithologies. It discontinuously overlays all of the other lithologies in the study area except the alluvial sediments.

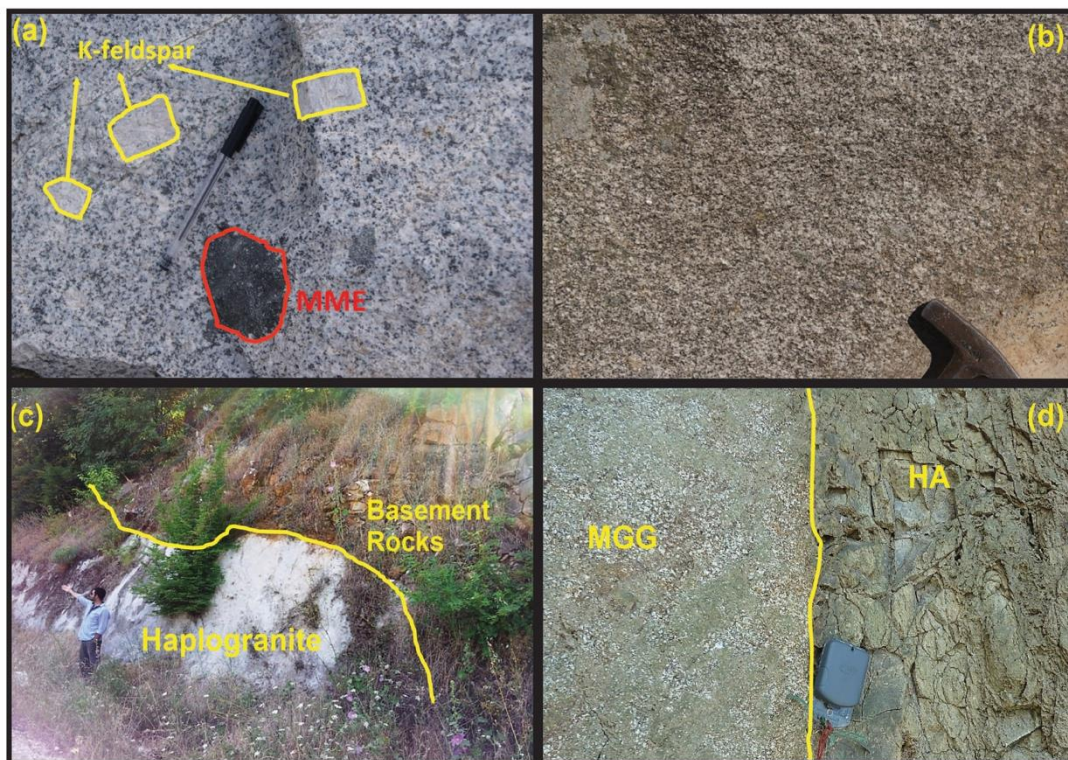


Figure 2.4: Field photographs from the Solarya Plutonic Association a) K-feldspar megacrystalline granodiorite (KFMG) with observable K-feldspar megacrysts and Mafic Microgranular Enclaves (MME) b) Microgranite-granodiorite (MGG) c) Intrusive contact between haplogranite and basement rocks d) Intrusive contact between MGG and hypabyssal association (HA).

2.3 Petrography

The petrography of SPA and HA is summarized in Table 2.1. Mineral composition of K-feldspar megacrystalline granodiorite (KFMG) is represented by 45–55% plagioclase (oligoclase-andesine), 20–25% quartz, 20–25% K-feldspar, 12–20% biotite and hornblende. It can be distinguished by its distinctive holocrystalline porphyritic texture caused by the large K-feldspar megacrystals, which reach to 1-4cm in size (Figure 2.5a). The most abundant mineral in this granodiorite is plagioclase, which is represented by oligoclase-andesine (An_{22–48}), showing albite, albite-Carlsbad, polysynthetic and combined twinnings. Petrographical investigations suggest that, plagioclase minerals are formed in two different stages. At first stage, the plagioclase crystals are represented by idiomorphic- hypidiomorphic megacrysts, which are 1 mm to 4 mm size. The second stage plagioclase minerals are relatively smaller than the first stage plagioclases and found in hypidiomorphic and xenomorphic forms. The distinctive K-feldspar crystals are represented as megacrysts, which show perthitic and poikilitic texture, and occasionally Carlsbad twinning. Quartz crystals are mostly found between the other crystals, formed interstitially at the late stage of crystallization. Biotite is the most abundant mafic mineral in the granodiorite. Biotite crystals are represented by megacrysts as well as they are occasionally found as inclusions in plagioclase and K-feldspar crystals which suggests that the biotite minerals formed relatively early in the crystallization process. In altered samples, it is possible to see opacitization and chloritization around the edges or through the cleavages of the biotite crystals. Hornblende crystals show zircon, sphene and opaque mineral. Also, the textural features of the hornblende crystals indicate that these crystals formed simultaneously with the plagioclase crystals, at the early stages of the crystallization.

Microgranite-granodiorite (MGG) has 42–52% plagioclase (oligoclase-andesine), 25–27% quartz, 23–28% K-feldspar, 10–18% hornblende and biotite, a similar mineralogical composition to KFMG. Thus, the detailed properties of the minerals will not be explained. However, their textures are significantly different from each other. MGG is characterized by a fine-grained, microgranular holocrystalline texture (Figure 2.5b).

Haplogranite of the plutonic association is distinguished from the other members by having sparse mafic minerals (<3% biotite). The mineral composition of the haplogranite is 50–55% K-feldspar (orthoclase/perthite), 40–45% quartz, 5–10% plagioclase (oligoclase), 1–3% biotite. Haplogranites have microgranular holocrystalline texture. They typically show graphic/granophyric texture between quartz and K-feldspar crystals; which indicates that these haplogranites emplaced into, and cooled down in the shallowest part of the crust (Figure 2.5c). Plagioclase crystals in haplogranites are represented by oligoclase composition, and they show albite twinning. Biotite crystals are found sparsely, and they are mostly small, hypidiomorphic crystals. They show chloritization along their cleavages.

Mafic microgranular enclaves of Solarya plutonic association are diorite and quartz-diorite in composition (Figure 2.5d and f). Their mineralogical composition is 40–50% plagioclase, 30–35% hornblende, 15–20% K-feldspar, 5–10% clinopyroxene, 2–5% biotite, >5% quartz. MMEs can be found throughout the plutonic body, distinguishable with their darker color derived by the high mafic mineral content. They present holocrystalline microgranular texture and in thin section, most of the minerals are seen to have poikilitic nature. Their most abundant mineral is plagioclase, which is found in the enclaves in two different types; relatively smaller crystals which are characteristic of the MME itself and megacrysts which have a granitic origin. The plagioclase crystals of mafic origin are labradorite (An_{64–68}) whereas the granitic plagioclases in MME'S are represented by Andesine-Labradorite (An_{38–An56}). Hornblende is the most abundant mafic mineral in MME, and they also present two different types similar to the plagioclases; hornblende crystals originated from host granitic rock, and hornblendes which belong to the MME itself. Hornblendes from the host rock are idiomorphic and acicular, they show green pleochroism and simple twinning. Hornblendes, which are characteristic of the MME, are dominantly basaltic hornblende megacrystals. Biotite crystals are usually found in dioritic enclaves, and they are represented as inclusions along the cleavages of hornblende minerals. Quartz crystals show xenomorphic form, filling the empty spaces at late phases.

Mafic dikes of the plutonic complex are observed scarcely, mostly cutting through the plutonic body. The mafic syn-plutonic dikes are dioritic–quartz dioritic in composition and they present have 60–65% plagioclase, 15–20% hornblende, 5–8% biotite, 5–10% quartz, 1–5% sanidine. Mafic syn-plutonic dikes are highly altered, but the texture can

be observed as microcrystalline, cryptocrystalline porphyritic. Plagioclase minerals are classified as andesine (An_{40–45}) and they are represented by both microlites and large phenocrysts, showing twinning and zoning. Hornblende crystals are altered in most of the samples, they show calcitization and opacitization around the contact zones. Quartz crystals are found as anhedral phenocrysts, they appear to be corroded by the fine-grained matrix, showing embayed structures.

The hypabyssal group can be considered as a transition between the plutonic and volcanic association in the study area, regarding the mineralogical composition and textural characteristics. Their distinctive textural feature is a holocrystalline, microcrystalline-microgranular porphyritic texture (Figure 2.5e). Their mineralogical composition is quartz diorite-granodiorite according to the modal analysis: 50–55% plagioclase (andesine-labradorite), 10–22% quartz, 5–10% K-feldspar, 10–15% hornblende, 5–10% biotite and 2–4% opaque minerals. The most abundant mineral is plagioclase, which can be found as both phenocrysts and microcrysts that form the matrix. Quartz crystals formed interstitially with K-feldspar crystals, and rarely as large phenocrysts. The most abundant mafic mineral of the hypabyssal group is hornblende, which can show glomeroporphyritic texture. Biotite minerals in the hypabyssal group show chloritization, and opacitization around the edges of the mineral.

2.4 Geochemistry

We have performed twenty-eight major and trace element analyses, twenty Sr-Nd-Pb isotopic analyses of plutonic and hypabyssal samples. Eight whole rock and six quartz-feldspar ¹⁸O isotope compositions have also been measured. The analyzed rocks present low LOI (lost on ignition) values between 0.5 and 2.7 wt% which indicate the lack of alteration, consistent with our petrographic observations.

2.4.1 Analytical methods

2.4.1.1 Major, trace elements

The whole rock major and trace element results were obtained at ACME Analytical Laboratories using Perkin Elmer Elan 6100 ICP-MS. See Altunkaynak, 2007 for detailed explanation.

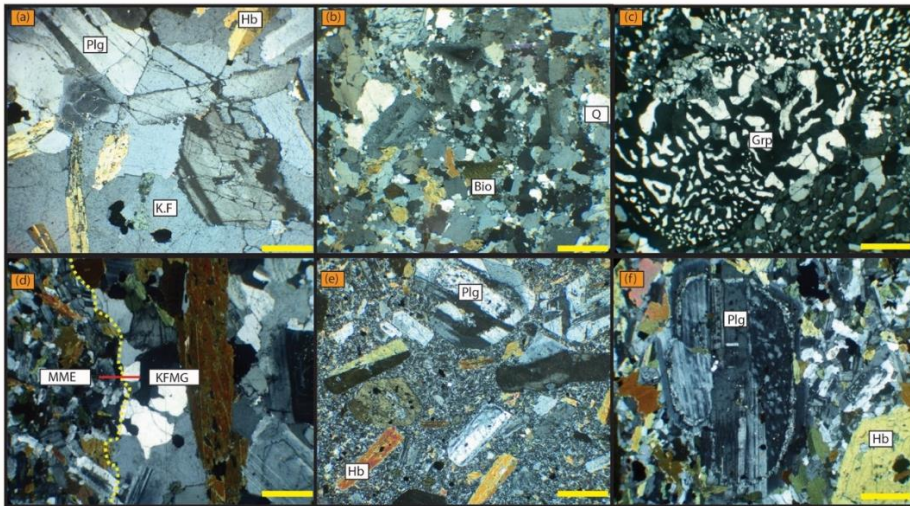


Figure 2.5: Micrographs illustrating the main petrographical features of Solarya Plutonic Association (SPA) and hypabyssal association (HA) a) Holocrystalline porphyritic texture of KFMG b) Fine grained microgranular texture of MGG c) Graphic/granophyric textures from haplogranites d) Contact between MME and KFMG e) Holocrystalline microgranular-porphyritic texture of HA f) Holocrystalline microgranular-porphyritic texture of MME (Bio: Biotite, Plg: Plagioclase, Amp: Amphibole, Q: Quartz, K.F.: K-Feldspar, Grp: Graphic/Granophyric texture).

2.4.1.2 Sr-Nd-Pb-O isotope analyses

All O isotope ratios were measured at the University of Cape Town using a Finnigan Delta XP mass spectrometer in dual-inlet mode on either CO₂ (conventional) or O₂ (laser) gas. All details are given in Harris and Vogeli, 2010.

For Sr-Nd-Pb isotopic analysis, thermal ionization mass spectrometry (TIMS) was used at the Saskatchewan Isotope Laboratory, Dept. Of Geological Sciences at the University of Saskatchewan, Canada. ¹⁴³Nd/¹⁴⁴Nd normalized to a value of 0.7219 for ¹⁴⁶Nd/¹⁴⁴Nd and an internal standard calibrated to a value of 0.511864 for ¹⁴³Nd/¹⁴⁴Nd in BCR-1. All analyses were performed on a Triton mass-spectrometer. ⁸⁷Sr/⁸⁶Sr normalized relative to a value of 0.1194 for ⁸⁴Sr/⁸⁸Sr and to 0.710250 for NIST 987. All analyses performed on a Triton mass spectrometer.

Table 2.1: Petrographical features of SPA and HA.

Rock Group	Composition	Textural Features	Other Features
K-Feldspar Megacrystalline Granodiorite (KFMG)	45-55% plagioclase (oligoclase-andesine), 20-25% quartz, 20- 25% K-feldspar, 12- 20% biotite and hornblende	Holocrystalline, porphyritic	Chloritization in bio and hb, sericitization in plg
Microgranite- granodiorite (MGG)	42-52% plagioclase (oligoclase-andesine), 25-27% quartz, 23-28% K-feldspar, 10-18% hornblende and biotite	Holocrystalline, granular-microgranular	Chloritization in bio and hb, sericitization in plg
Haplogranite	50-55% K-feldspar (orthoclase-perthite), 40-45% quartz, 5-10% plagioclase (oligoclase), % 1-3 biotite	Holocrystalline, granular-microgranular, graphic/granophyric	Chloritization in bio sericitization in plg

Table 2.1: (Continued) Petrographical features of SPA and HA.

Rock Group	Composition	Textural Features	Other Features
MME	40-50% plagioclase, 30-35% hornblende, 15-20% K-feldspar, 5-10% clinopyroxene, 2-5% biotite, >5% quartz	Holocrystalline, microgranular	Chloritization in bio and hb, sericitization in plg
Mafic Dikes	60-65% plagioclase, 15-20% hornblende, 5-8% biotite, 5-10% quartz, 1-5% sanidine	Holocrystalline, microcrystalline, cryptocrystalline porphyritic	Chloritization in bio and hb, sericitization in plg
Hypabyssal Association (HA)	50-55% plagioclase (andesine-labradorite), 10-22% quartz, 5-10% K-feldspar, 10-15% hornblende, 5- 10% biotite , 2-4% opaque minerals	Holocrystalline, microcrystalline- microgranular porphyritic	Chloritization in bio and hb, sericitization in plg

2.4.2 Results

2.4.2.1 Major and trace element geochemistry

The SiO₂ contents of K-feldspar megacrystalline granodiorite (KFMG) and microgranite-granodiorite (MGG) vary between 60.10 and 67.09 wt%, whereas haplogranites range from 73.37–76.97 wt%. The mafic microgranular enclaves (MME) and mafic dikes present SiO₂ values vary between 50.41 and 59.34 wt%. On the TAS diagram (Figure 2.6a; Middlemost, 1985) both KFMG and MGG are represented by granodiorite whereas the haplogranites cluster in the granitefield. The MME's and mafic dikes range from monzogabbro to monzonite. The hypabyssal association is classified as granodiorite. These classifications are also consistent with multicationic P-Q classification diagram of Debon and Le Fort (1983) (Figure 2.6b).

The majority of the samples are sub-alkaline in character and display a calc-alkaline trend (Irvine and Baragar, 1971), except four MME and mafic dike sample (Figure 2.6a and Figure 2.7) which are mid-alkaline. On the K₂O vs. SiO₂ classification diagram (Peccerillo and Taylor, 1976), most of the MME's and mafic dikes are classified as shoshonitic, while KFMG, MGG, haplogranites and hypabyssal association are high-K calc-alkaline in character (Figure 2.8a). In the A/NK (Al₂O₃/Na₂O+K₂O) vs. A/CNK (Al₂O₃/(CaO + Na₂O+K₂O)) diagram, all plutonic and hypabyssal rocks are metaluminous except the haplogranites which present weak peraluminous character. All of the samples show I-type affinity, although one haplogranite sample displays S-type affinity (Figure 8b).

The Harker variation diagrams were prepared to examine the variations of major oxides versus SiO₂ (Figure 2.9). These diagrams show that, the most basic members of the Solarya pluton are MME's and mafic dikes, whereas the most felsic members are represented by haplogranites. The KFMG, MGG and hypabyssal association show trends between these two end members. In these diagrams, MgO (0.05–7.23 wt%), TiO₂ (0.05–1.00 wt%), CaO (0.71–8.67 wt%), Fe₂O₃ (0.23–10.32 wt%) contents and Mg numbers (MME and mafic dikes: 70–48; granodiorites: 48–43; haplogranites: 30–20) decrease with increasing SiO₂. These variations suggest that, all of the plutonic rocks and hypabyssal association (Mg number av.: 45) are originated from a common source.

On PM (primitive mantle) normalized spider diagrams, all groups (KFMG, FGG, haplogranites, MME's, mafic dikes and hypabyssal association) present enrichment in LIL elements (Ra, Ba, U, Th, K) and depletion in Nb, P, Ti and Zr. In the spider diagrams, the average multiple element distribution patterns of representative high Ba–Sr granitoids in the Scottish Caledonians are also presented (Figure 2.10a). It is clear that, Solarya pluton presents similar trace element patterns to those of high Ba–Sr granitoids.

On chondrite normalized spider diagrams, the REE distributions of KFMG, FGG, MME's, mafic dikes and hypabyssal association display significant LREE enrichments with respect to the HREE and MREE (Figure 2.10b). Haplogranites present relatively smaller enrichment in LREE with respect to the other plutonic and hypabyssal samples. As seen from Figure 2.10b, KFMG lack any Eu anomalies, whereas FGG, MME and mafic dikes present weak negative Eu anomalies ($\text{Eu}/\text{Eu}^* = 0.75\text{--}0.85$). These insignificant Eu anomalies are typical characteristics of high Ba–Sr granitoids (Fowler et al., 2008). HREE patterns display enrichment with respect to the MREE's (Figure 2.10b).

2.4.2.2 The Sr-Nd-Pb and ^{18}O isotope geochemistry

The Sr-Nd-Pb and ^{18}O isotopic data for the analyzed plutonic and hypabyssal samples are shown in Table 2.2. The measured $^{87}\text{Sr}/^{86}\text{Sr}_{(m)}$ values vary from 0.707168 to 0.710494 and, $^{143}\text{Nd}/^{144}\text{Nd}_{(m)}$ values range from 0.51243 to 0.51252. The initial Sr-Nd isotopic ratios were calculated for both Solarya pluton and hypabyssal association assuming a mean magma crystallization age of 21 Ma. The $^{87}\text{Sr}/^{86}\text{Sr}_{(i)}$ values vary from 0.707057 to 0.707536 for KFMG, from 0.707207 to 0.707422 for MGG and from 0.707815 to 0.708259 for haplogranites. MME's and mafic dikes present $^{87}\text{Sr}/^{86}\text{Sr}_{(i)}$ values between 0.707102 and 0.707583 whereas hypabyssal association display values from 0.707510 to 0.708046. The $^{143}\text{Nd}/^{144}\text{Nd}_{(i)}$ and ϵNd values for KFMG, $^{143}\text{Nd}/^{144}\text{Nd}_{(i)} = 0.512442\text{--}0.512484$, $\epsilon\text{Nd} = -3.29\text{--} -2.48$; for MGG, $^{143}\text{Nd}/^{144}\text{Nd}_{(i)} = 0.512449\text{--}0.512469$, $\epsilon\text{Nd} = -3.17\text{--} -2.76$; for haplogranites, $^{143}\text{Nd}/^{144}\text{Nd}_{(i)} = 0.512416\text{--}0.512464$, $\epsilon\text{Nd} = -3.33\text{--} -2.86$; for MME's and mafic dikes, $^{143}\text{Nd}/^{144}\text{Nd}_{(i)} = 0.512435\text{--}0.512506$, $\epsilon\text{Nd} = -3.43\text{--} -2.06$. Hypabyssal association present $^{143}\text{Nd}/^{144}\text{Nd}_{(i)} = 0.512355\text{--}0.512420$, $\epsilon\text{Nd} = -5.00\text{--} -3.72$ values.

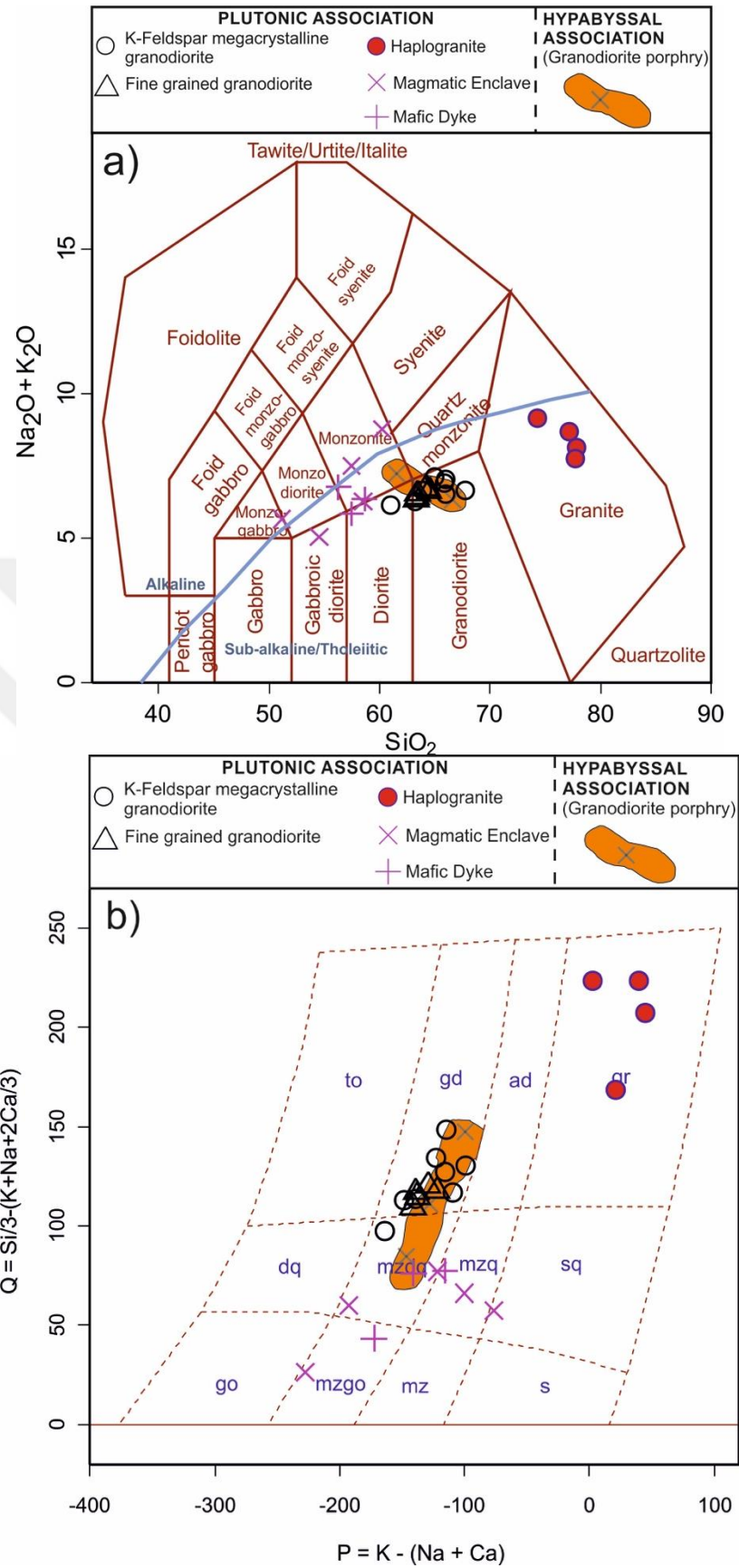


Figure 2.6: a) Total alkali vs. SiO_2 classification diagram (Middlemost, 1985). Alkaline/Sub-alkaline classification of Irvine and Baragar, 1971 is also included to the figure b) Multicationic P-Q classification diagram (Debon and Le Fort, 1983).

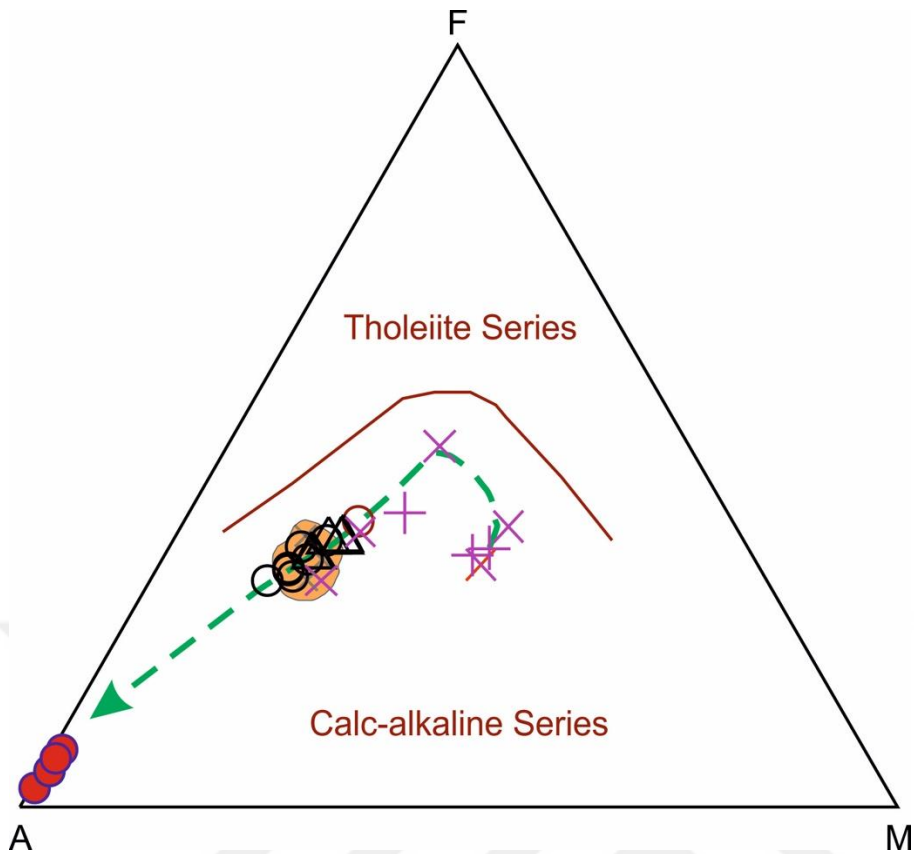


Figure 2.7: AFM diagram of SPA and HA (Irvine and Baragar, 1971).

The Pb isotopic values of Solarya pluton and hypabyssal association present similar values congruently with Sr-Nd isotopic data. $^{206}\text{Pb}/^{204}\text{Pb}$, $^{207}\text{Pb}/^{204}\text{Pb}$, $^{208}\text{Pb}/^{204}\text{Pb}$, $^{208}\text{Pb}/^{206}\text{Pb}$, $^{207}\text{Pb}/^{206}\text{Pb}$ values vary between 18.750 and 18.870, 15.691 and 15.724, 38.955 and 39.069, 2.067 and 2.077, 0.8324 and 0.8367 respectively.

The whole rock $\delta^{18}\text{O}$ isotopic data for Solarya pluton and hypabyssal association range from 8 to 10.4, quartz $\delta^{18}\text{O}$ isotopic data vary from 9.5 to 10.6. The whole rock $\delta^{18}\text{O}$ isotopic data for MME's and mafic dikes present values between 8.2 and 8.8 whereas haplogranites display whole rock $\delta^{18}\text{O}$ isotopic data of 10.4 and quartz $\delta^{18}\text{O}$ isotopic data of 10.6.

2.5 Discussion

2.5.1 Petrological classification

Tarney and Jones (1994) classified granitoids based on their Ba and Sr contents. As a result of this definition, high Ba and Sr granitoids must have Sr values higher than 300 ppm and Ba values higher than 500 ppm. Solarya plutonic association has Ba values between 710 and 1505 ppm and Sr values between 305 and 706 ppm.

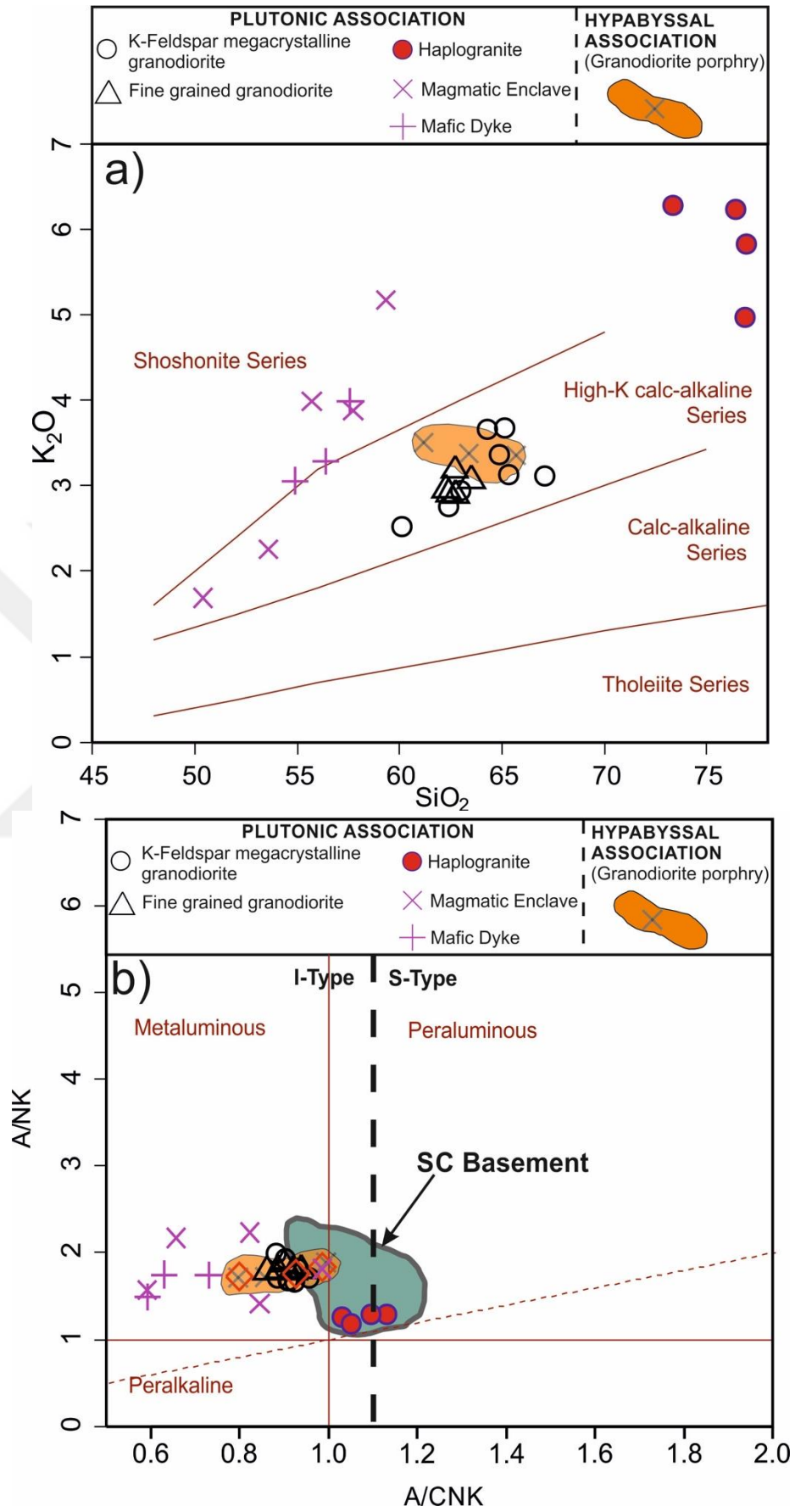


Figure 2.8: AFM diagram of SPA and HA (Irvine and Baragar, 1971).

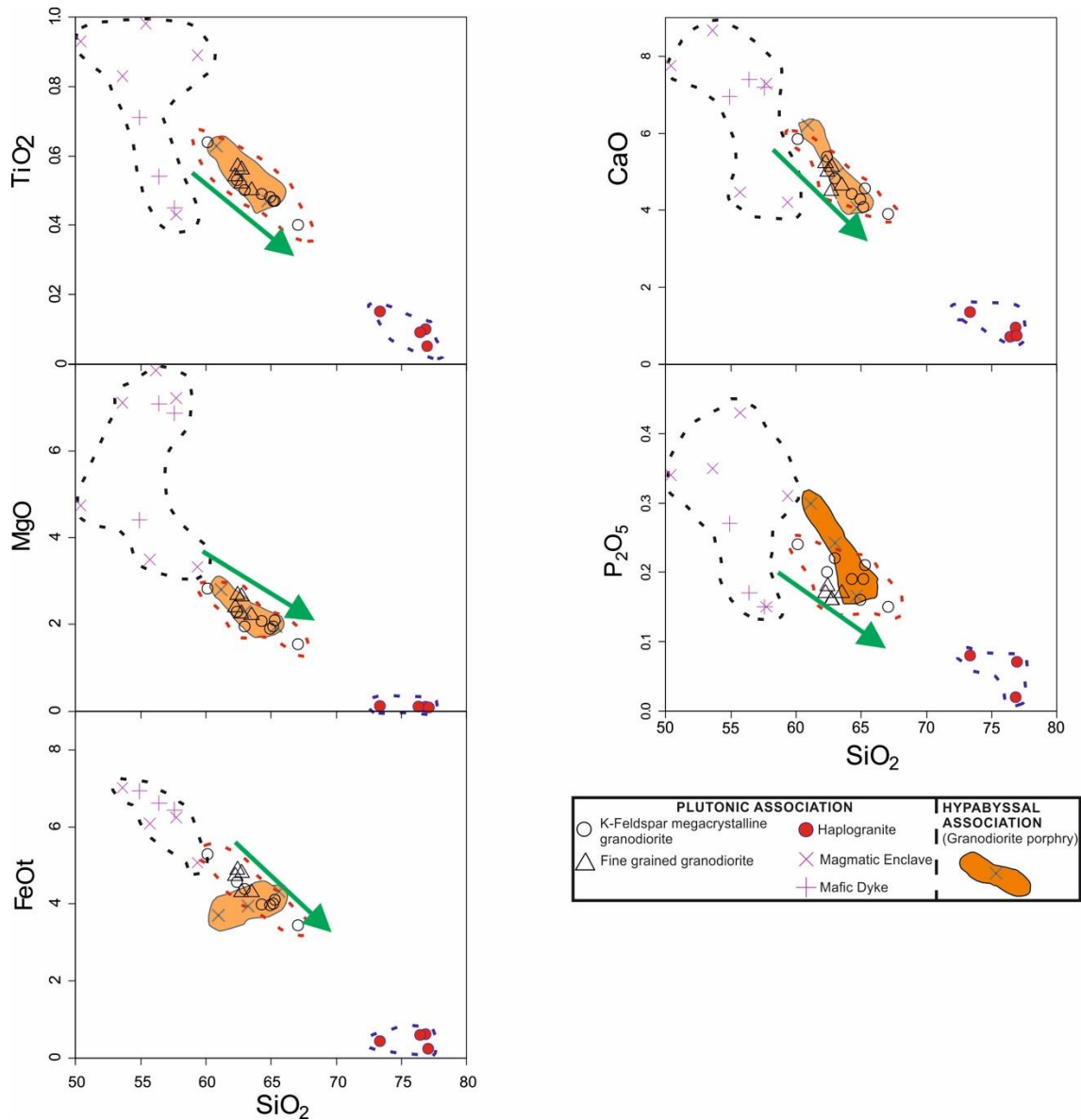


Figure 2.9: Major elements vs. SiO_2 Harker variation diagrams for SPA and HA.

On the Rb-Sr-Ba diagram suggested by Tarney and Jones, 1994, samples from SPA plot into the field of high Ba–Sr granitoids, except for haplogranites (Figure 2.15). Moreover, in addition to the high Ba and Sr values, the fractionated REE patterns of SPA, lack of negative Eu anomaly, depletion in Ta, P, Nb and Ti (Figure 2.10a) and low Y and Yb contents are typical geochemical signatures of high Ba–Sr granitoids defined worldwide (eg. Scottish Caledonian, China, Tibetan Plateau; Tarney and Jones, 1994; Fowler et al., 2008; Qin et al., 2009; Choi et al., 2009; Yuan et al., 2010).

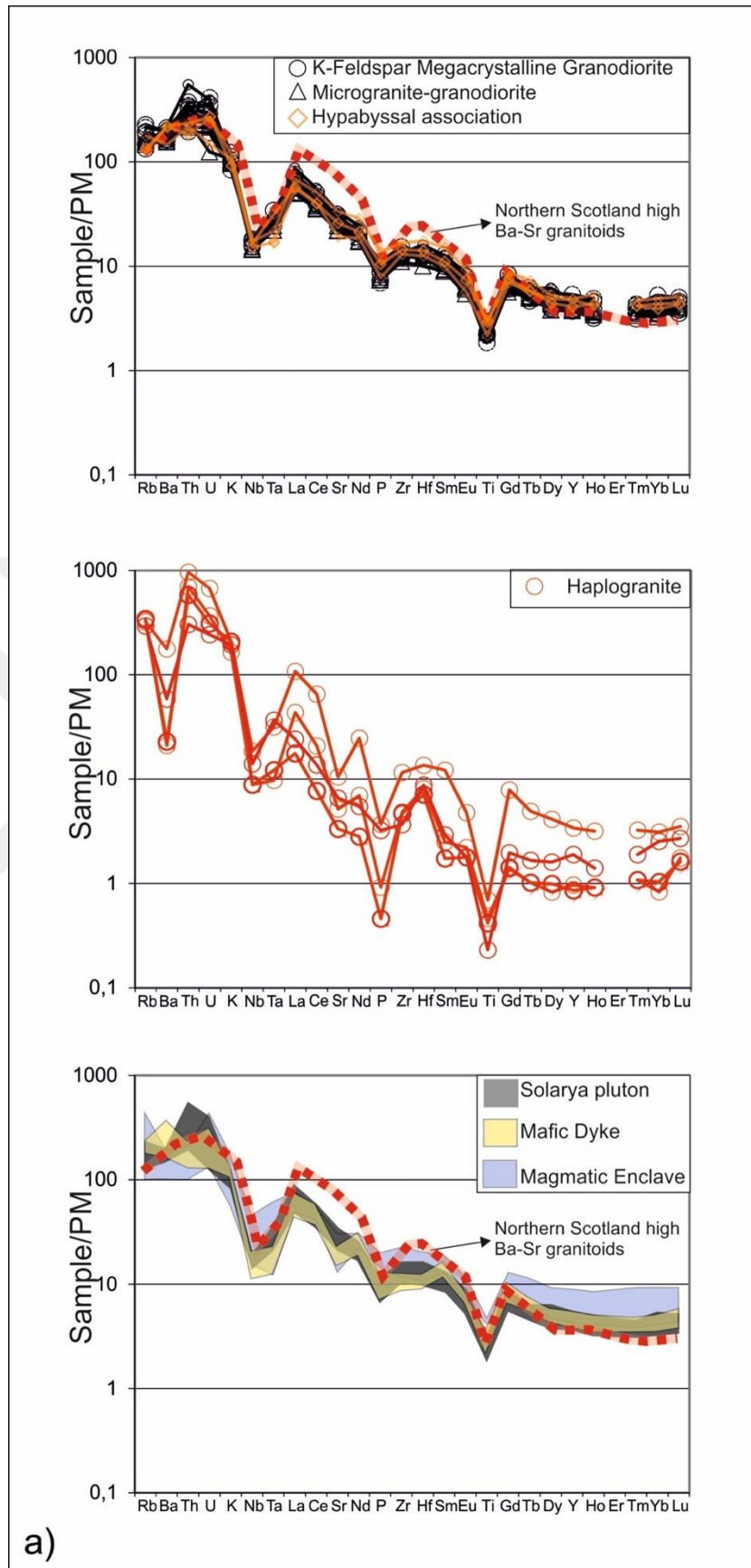


Figure 2.10: a) Primitive-mantle (Sun and McDonough, 1989) normalized multi-element patterns for SPA and HA, b) Chondrite-normalized REE patterns SPA and HA. Chondrite normalizing values are from Boynton (1984).

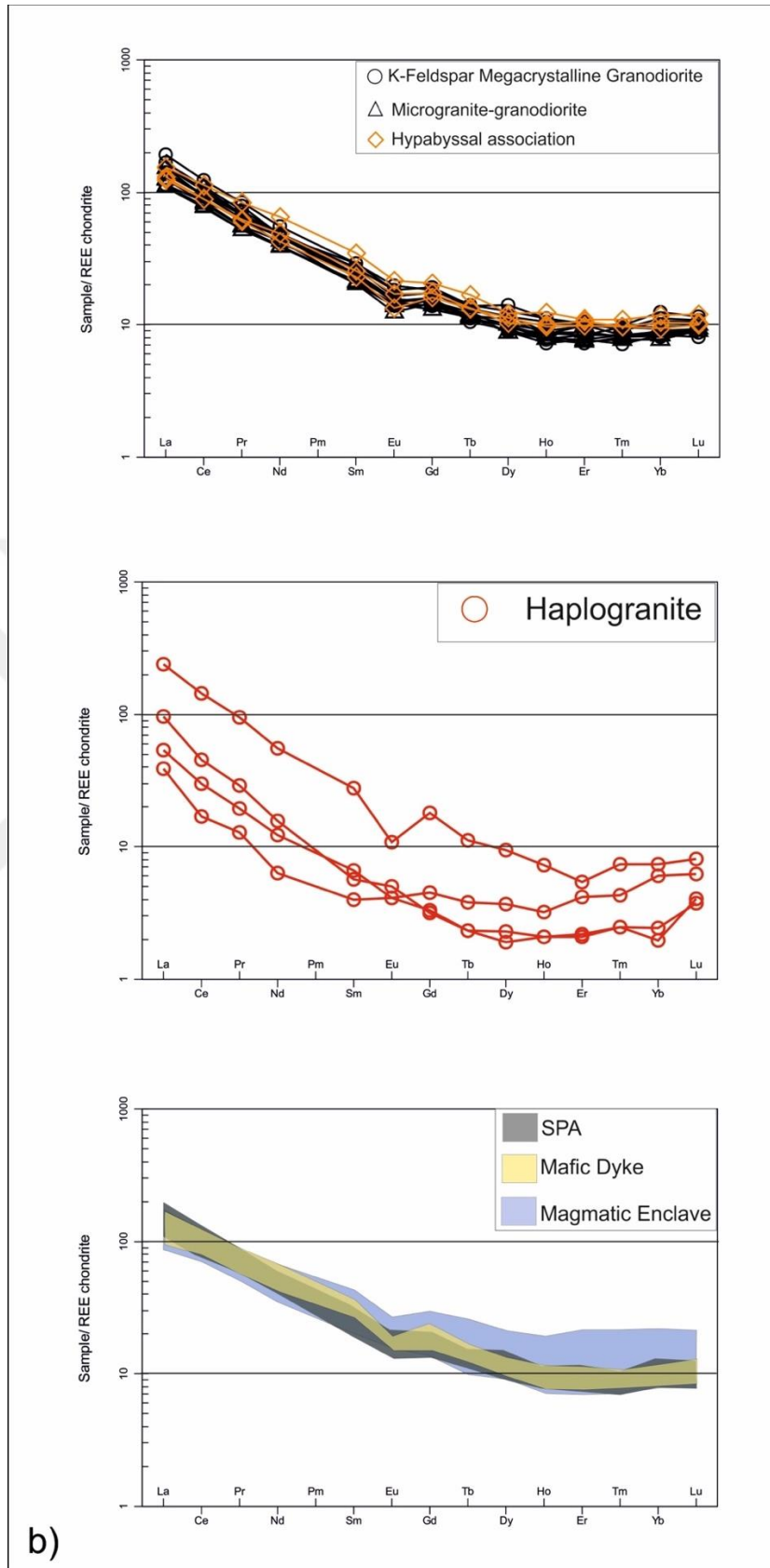


Figure 2.11 (continued): a) Primitive-mantle (Sun and McDonough, 1989) normalized multi-element patterns for SPA and HA, b) Chondrite-normalized REE patterns SPA and HA. Chondrite normalizing values are from Boynton (1984).

Table 2.2: Representative chemical analyses of Solarya Plutonic Association and Hypabyssal Association.

Sample	SiO ₂	Al ₂ O ₃	Fe ₂ O ₃	MgO	CaO	Na ₂ O	K ₂ O	TiO ₂	P ₂ O ₅	MnO	Cr ₂ O ₃	LOI	Total	Cs	Rb	Ba	Sr	Pb	Th	U	Zr
AS-9PG	60.10	16.88	5.87	2.83	5.86	3.50	2.52	0.64	0.24	0.11	<0.002	1.1	99.65	4.5	84.3	1266	651.0	2.1	16.4	4.0	171.5
AS-13	64.26	15.94	4.42	2.08	4.43	3.37	3.67	0.49	0.19	0.08	0.003	0.7	99.65	4.2	143.6	1351	627.1	2.9	31.7	7.5	145.7
AS-16	65.31	15.20	4.56	2.09	4.56	3.33	3.13	0.47	0.21	0.09	<0.002	0.7	99.68	3.4	112.9	1254	611.2	3.7	27.2	8.6	143.3
AS-18	67.09	15.42	3.82	1.54	3.90	3.45	3.11	0.40	0.15	0.10	<0.002	0.7	99.70	4.2	119.7	1131	511.9	6.7	28.6	7.1	135.2
AS-20a	63.00	16.60	4.88	1.95	4.82	3.59	2.94	0.50	0.22	0.10	<0.002	1.1	99.64	2.3	95.4	1475	622.0	5.3	28.4	5.8	152.1
AS-22a	62.40	16.64	5.07	2.30	5.39	3.44	2.75	0.53	0.20	0.10	<0.002	0.8	99.60	3.9	91.0	1505	706.8	4.1	46.5	8.2	150.1
AS 66A	65.17	15.41	4.45	1.96	4.08	3.23	3.68	0.47	0.19	0.08	0.004	0.9	99.66	4.0	135.3	1369	544.4	5.4	29.4	5.9	138.9
AS 77	64.91	15.55	4.40	1.91	4.29	3.42	3.37	0.48	0.16	0.08	0.002	1.1	99.68	3.3	122.3	1146	583.2	5.7	26.8	5.0	140.0
AS 39 G	62.71	16.16	4.78	2.25	4.51	3.38	3.18	0.52	0.16	0.10	<0.002	1.9	99.69	2.9	109.1	1224	463.4	7.8	20.7	2.6	136.9
AS 40	63.51	16.08	4.77	2.21	4.65	3.46	3.07	0.50	0.17	0.09	0.002	1.2	99.68	3.8	109.0	1143	512.5	18.9	21.6	4.8	139.9
AS 113	62.26	15.83	5.25	2.40	5.23	3.44	2.96	0.54	0.17	0.10	0.002	1.5	99.68	3.0	104.2	1104	466.9	12.1	18.3	4.5	143.8
AS 115	62.42	15.84	5.42	2.68	5.01	3.42	2.91	0.57	0.18	0.11	<0.002	1.1	99.69	3.5	98.0	1080	457.7	11.6	23.6	5.2	151.9
AS 120	62.75	16.21	5.33	2.64	5.13	3.37	2.89	0.56	0.16	0.10	<0.002	0.5	99.67	3.1	93.3	1191	462.1	5.0	21.5	5.8	123.8
AS-11 M	76.97	12.78	0.23	0.05	0.77	2.19	5.83	0.05	0.07	<0.01	<0.002	0.9	99.85	4.3	186.1	410	138.3	3.5	25.8	5.1	41.1
AS-10 A	73.37	14.20	0.49	0.11	1.35	2.75	6.29	0.15	0.08	<0.01	<0.002	0.9	99.72	6.6	203.9	1238	221.6	3.7	81.7	14.1	129.2
AS-23	76.87	12.60	0.69	0.10	0.96	2.67	4.97	0.10	0.02	0.02	<0.002	0.9	99.89	7.3	211.3	147	109.0	6.0	59.3	7.7	54.3
AS-24	76.42	12.50	0.65	0.09	0.71	2.34	6.24	0.09	<0.01	0.02	<0.002	0.9	99.91	8.2	217.8	160	70.2	5.4	49.4	6.5	52.5
AS 200P	61.1	16.56	3.98	2.89	6.11	3.47	3.6	0.63	0.3	0.06	0.008	0.9	99.58	0.7	80	1573	708.4	12.2	19.9	5.7	190
AS 202P	65.20	15.01	4.79	2.01	4.21	2.99	3.33	0.49	0.17	0.10		0.96	99.27	4.1	86.2	1516	547.8	20.7	15.7	5.7	162.4
AS 67 P	64.08	16.05	4.57	1.94	4.15	3.20	3.22	0.47	0.17	0.09	<0.002	1.8	99.71	4.0	112.9	1038	406.0	9.8	18.6	3.1	146.9
AS-14a	57.73	12.54	6.94	7.23	7.29	2.30	3.88	0.43	0.15	0.22	0.059	0.8	99.59	4.3	148.2	2222	397.6	5.8	17.2	3.9	98.8
AS-22ab	50.41	18.34	10.32	4.75	7.76	3.88	1.69	0.93	0.34	0.21	0.003	1.0	99.68	4.7	85.3	710	561.1	3.7	8.5	2.8	166.7
AS 66B	55.71	17.55	6.76	3.50	4.47	3.26	3.99	1.00	0.43	0.32	0.003	2.6	99.58	10.8	235.7	1319	492.4	7.6	17.6	9.0	249.3
AS233A	59.34	16.02	5.64	3.33	4.21	3.46	5.18	0.89	0.31	0.19	0.014	2.7	99.69	13.1	273.9	800	273.5	11.9	19.6	8.9	206.5
AS 148	53.59	14.85	7.80	7.12	8.67	2.67	2.26	0.83	0.35	0.16	0.049	1.2	99.58	2.3	63.3	1353	633.6	10.9	17.1	3.5	129.8
AS-14b D	57.60	12.38	7.16	6.88	7.19	2.23	3.99	0.45	0.15	0.25	0.056	1.2	99.56	3.7	143.7	2489	355.8	6.9	19.1	3.8	96.6
AS 81	54.90	15.86	7.70	4.41	6.95	3.52	3.06	0.71	0.27	0.20	0.002	2.1	99.65	3.1	112.6	1089	459.1	5.1	14.9	6.5	136.9
AS 145	56.41	13.25	7.35	7.10	7.40	2.44	3.29	0.54	0.17	0.25	0.051	1.3	99.60	2.4	108.1	1490	305.0	5.8	10.7	2.6	95.4

Table 2.2: (Continued) Representative chemical analyses of Solarya Plutonic Association and Hypabyssal Association.

Sample	Nb	Sc	Cr	Ni	Co	V	Ga	La	Ce	Pr	Nd	Sm	Eu	Gd	Tb	Dy	Ho	Er	Tm	Yb	Lu	As
AS-9PG	12.3	12	n.d	22	13.3	124	17.8	35.3	69.3	7.84	28.2	5.65	1.34	4.98	0.67	4.08	0.80	2.15	0.32	2.59	0.37	1.1
AS-13	12.4	8	<20	n.d	11.1	99	16.1	39.7	71.1	7.49	27.7	4.41	1.11	4.09	0.50	2.93	0.55	1.53	0.26	1.73	0.28	0.7
AS-16	12.5	10	25	n.d	12.0	95	14.7	52.2	89.2	8.87	29.5	5.18	1.20	4.49	0.60	3.77	0.63	1.83	0.26	1.88	0.30	1.0
AS-18	11.3	7	<20	n.d	8.2	71	14.6	47.2	75.8	9.57	28.5	4.61	1.08	3.57	0.53	3.12	0.56	1.75	0.31	1.94	0.33	<0.5
AS-20a	10.9	10	<20	n.d	11.6	93	15.7	44.3	78.0	8.20	29.6	5.23	1.34	4.99	0.63	3.72	0.75	2.21	0.29	2.22	0.34	0.8
AS-22a	12.6	11	n.d	<20	11.9	106	13.7	59.5	99.0	10.22	33.0	5.64	1.46	4.71	0.66	4.52	0.80	2.10	0.30	2.33	0.35	1.0
AS 66A	11.6	10	n.d	<20	46.5	96	14.7	42.6	77.2	7.73	24.7	4.81	1.15	3.87	0.59	3.05	0.62	1.75	0.27	1.70	0.30	2.2
AS 77	12.9	10	n.d	<20	50.2	93	14.5	48.0	83.4	8.11	28.9	4.70	1.10	4.05	0.54	2.84	0.52	1.62	0.23	1.73	0.26	0.8
AS 39 G	10.4	11	n.d	<20	37.9	100	16.8	47.4	86.8	8.45	29.2	4.72	1.08	4.06	0.53	3.20	0.59	1.56	0.25	1.61	0.29	0.7
AS 40	10.9	11	n.d	<20	53.0	100	16.1	34.8	63.7	6.34	23.6	4.16	1.05	3.36	0.54	2.80	0.56	1.62	0.27	1.76	0.30	3.2
AS 113	10.2	12	n.d	<20	54.5	115	13.8	38.8	68.8	6.78	25.8	3.96	1.01	3.95	0.55	3.53	0.61	2.07	0.27	1.86	0.30	2.9
AS 115	10.3	13	n.d	<20	47.3	134	13.7	34.0	62.3	6.36	23.2	4.09	1.01	3.63	0.56	3.21	0.65	2.03	0.31	2.00	0.32	4.7
AS 120	10.3	12	n.d	<20	52.4	115	13.5	39.4	66.5	6.68	23.6	3.95	0.91	3.76	0.56	2.79	0.60	1.85	0.26	1.72	0.29	1.2
AS-11 M	10.0	1	<20	n.d	1.5	<8	11.6	16.6	24.3	2.38	7.4	1.29	0.30	1.17	0.18	1.18	0.23	0.88	0.14	1.25	0.20	0.6
AS-10 A	13.2	3	<20	n.d	1.6	8	13.1	73.8	115.6	11.53	33.4	5.41	0.80	4.69	0.53	3.04	0.52	1.13	0.24	1.53	0.26	<0.5
AS-23	6.3	<1	<20	n.d	1.1	<8	10.5	29.8	36.9	3.52	9.4	1.11	0.37	0.82	0.11	0.61	0.15	0.44	0.08	0.41	0.13	0.8
AS-24	6.3	<1	<20	n.d	1.0	<8	9.4	12.1	13.7	1.57	3.8	0.77	0.30	0.85	0.11	0.73	0.15	0.46	0.08	0.51	0.12	1.7
AS 200P	12.4	12	n.d	8.3	38.6	109	16.1	47.3	90.3	10.16	38.9	6.72	1.57	5.25	0.79	3.9	0.88	2.29	0.35	2.43	0.38	6.6
AS 202P	10.9	17	n.d	15.2	23.2	128	16.1	38.4	71.3	7.53	29.1	4.93	1.24	4.48	0.63	3.28	0.72	2.2	0.31	1.93	0.32	1
AS 67 P	11.9	9	n.d	<20	39.7	84	15.4	40.2	71.5	7.34	25.3	4.45	0.97	4.14	0.62	3.62	0.69	2.04	0.31	2.17	0.33	0.9
AS-14a	7.1	21	n.d	66	27.2	138	13.0	28.6	56.8	6.33	21.0	3.89	1.45	3.60	0.48	2.93	0.52	1.47	0.23	1.62	0.25	<0.5
AS-22ab	11.7	25	n.d	<20	28.6	258	20.0	33.0	72.0	8.88	40.9	7.12	1.54	6.33	0.80	5.05	0.93	2.72	0.40	2.40	0.48	1.4
AS 66B	18.5	13	n.d	22	26.6	138	17.8	51.7	96.1	9.65	33.4	5.40	1.17	4.88	0.68	3.45	0.67	1.80	0.28	2.01	0.32	1.7
AS233A	32.4	13	n.d	28	30.2	88	17.1	36.4	86.5	10.3	39.9	8.31	1.94	7.63	1.21	6.73	1.38	4.57	0.68	4.48	0.68	0.6
AS 148	10.8	26	n.d	24	33.0	195	13.2	36.6	73.0	8.11	30.0	5.72	1.33	4.72	0.65	3.84	0.73	2.16	0.28	1.92	0.31	9.8
AS-14b D	8.9	22	n.d	34	26.4	135	12.7	32.0	66.7	7.91	28.6	5.58	1.41	4.85	0.64	3.89	0.74	1.90	0.33	2.26	0.35	0.7
AS 81	14.2	22	n.d	<20	40.5	181	17.1	49.4	100.5	10.38	40.3	6.98	1.38	6.00	0.78	4.16	0.80	2.36	0.34	2.42	0.41	1.0
AS 145	7.7	26	n.d	53	38.5	166	12.5	29.3	62.7	6.73	24.7	5.10	1.09	3.83	0.57	3.09	0.55	1.60	0.25	1.67	0.27	<0.5

Table 2.2: (Continued) Representative chemical analyses of Solarya Plutonic Association and Hypabyssal Association.

Sample	Mo	Be	Ag	Sn	Sb	Tl	Bi	⁸⁷ Sr/ ⁸⁶ Sr	¹⁴³ Nd/ ¹⁴⁴ Nd	²⁰⁶ Pb/ ²⁰⁴ Pb	²⁰⁷ Pb/ ²⁰⁴ Pb	²⁰⁸ Pb/ ²⁰⁴ Pb	²⁰⁸ Pb/ ²⁰⁶ Pb	²⁰⁷ Pb/ ²⁰⁶ Pb
AS-9PG	0.1	1	<0.1	4	<0.1	0.3	<0.1	0.707648	0.512459	18.836	15.698	38.979	2.069	0.83337
AS-13	0.2	2	<0.1	4	<0.1	0.3	<0.1	0.707230	0.512497	18.784	15.694	39.015	2.077	0.83549
AS-16	0.2	2	<0.1	3	<0.1	0.2	<0.1	0.707224	0.512467	18.771	15.692	38.983	2.077	0.83594
AS-18	0.4	3	<0.1	5	<0.1	0.3	<0.1	0.707363	0.512491	18.804	15.696	38.985	2.073	0.8347
AS-20a	0.3	2	<0.1	2	<0.1	0.1	<0.1	0.707268	0.512476	18.801	15.693	38.994	2.074	0.83467
AS-22a	0.2	3	<0.1	3	<0.1	0.3	<0.1	0.707168	0.512492	18.801	15.693	39.047	2.077	0.83465
AS 66A	0.3	2	<0.1	2	0.1	0.4	n.d							
AS 77	0.3	3	<0.1	2	<0.1	0.3	n.d							
AS 39 G	0.3	3	<0.1	2	<0.1	<0.1	n.d	0.707625	0.512462	18.87	15.714	39.036	2.06868	0.83274
AS 40	1.4	3	<0.1	1	0.2	0.2	n.d	0.707391	0.512478	18.805	15.69	38.959	2.07169	0.83438
AS 113	4.3	2	<0.1	1	<0.1	<0.1	n.d	0.707521	0.512482	18.876	15.735	39.056	2.069	0.83359
AS 115	0.3	2	<0.1	1	<0.1	0.2	n.d	0.707467	0.512471	18.8245	15.6942	38.9651	2.0699	0.8337
AS 120	0.5	2	<0.1	1	<0.1	0.3	n.d							
AS-11 M	<0.1	3	<0.1	2	<0.1	<0.1	<0.1	0.709271	0.512455	18.853	15.705	38.971	2.067	0.83301
AS-10 A	0.3	1	<0.1	3	<0.1	<0.1	<0.1	0.709053	0.512429	18.839	15.701	39.069	2.074	0.83338
AS-23	<0.1	1	<0.1	2	<0.1	<0.1	<0.1							
AS-24	<0.1	1	<0.1	1	0.1	<0.1	0.2	0.710494	0.512481	18.795	15.695	38.955	2.073	0.83505
AS 200P	<0.1	<0.5	<0.1	3	0.3	<0.1	0.4	0.707995	0.512369	18.838	15.7	38.982	2.069	0.833
AS 202P	0.3	<0.5	<0.1	2	<0.1	<0.1	0.1	0.708182	0.512371	18.817	15.702	38.963	2.071	0.834
AS 67 P	0.5	3	<0.1	2	<0.1	0.1	n.d	0.70775	0.512435	18.888	15.724	39.052	2.06748	0.83247
AS-14a	<0.1	3	<0.1	3	<0.1	<0.1	0.1	0.707424	0.512521	18.753	15.691	38.973	2.078	0.8367
AS-22ab	0.1	2	<0.1	5	<0.1	0.5	<0.1	0.707272	0.512485	18.78	15.694	38.969	2.075	0.83565
AS 66B	0.3	4	<0.1	3	<0.1	1.1	n.d							
AS233A	0.4	6	<0.1	11	<0.1	1	0.1							
AS 148	0.2	2	<0.1	3	0.2	0.2	n.d	0.707668	0.512451	18.83	15.697	38.983	2.07021	0.83359
AS-14b D	0.1	2	<0.1	6	<0.1	<0.1	<0.1							
AS 81	0.1	3	<0.1	3	<0.1	0.2	n.d							
AS 145	<0.1	2	<0.1	3	<0.1	<0.1	n.d	0.70752	0.512486	18.75	15.683	38.955	2.07753	0.83643

Therefore, Solarya Plutonic Association can be regarded as high Ba–Sr granitoids. Similar to the SPA, HA also shows high Ba–Sr characteristics. HA is not only overlap with SPA in terms of mineralogy, but also display similar geochemical and isotopic patterns. Thus, HA is also represented by high Ba–Sr magmas only with the difference of the cooling depth.

2.5.2 Petrogenesis of Solarya plutonic association

2.5.2.1 Nature of high Ba–Sr magma

Solarya plutonic association rocks are sub-alkaline in nature, as revealed by their major and trace element characteristics with the exception of few MME and mafic dike samples presenting mid- alkaline character. The main plutonic body (K-feldspar megacrystalline granodiorite and microgranite-granodiorite) and haplogranite display high Kcalc-alkaline character whereas MMEs and mafic dikes show high-K to shoshonitic character (Figure 2.8a). MME and mafic dikes also have higher TiO₂, Fe₂O₃, MgO, CaO, Ni and Cr contents than other plutonic members. These data indicate that MME and mafic dykes represent the most primitive composition compared to the main plutonic body and haplogranites. On the other hand, haplogranites display higher SiO₂ contents (73.37–76.97 wt%) with respect to the granodiorites (60.10–67.09 wt%); this shows that the haplogranite is the most felsic and evolved member of the plutonic association. Granodiorites present a linear and systematic trend between MME's- mafic dikes and haplogranites on Harker variation diagrams. This data and their similar Sr-Nd-Pb and O isotopic characteristics suggest that all of the plutonic members have a common magma source.

Several petrogenetic models have been proposed for the origin of high Ba–Sr granitoids: (1) the partial melting of subducted ocean islands or ocean plateaus which are younger than 25 Ma (Defant and Drummond, 1990, 1993; Tarney and Jones, 1994); (2) partial melting of the mafic lower crust (Choi et al., 2009; Petford and Atherton, 1996; Tarney and Jones, 1994; Ye et al., 2008); (3) the partial melting of veined lithospheric mantle which had been metasomatized by carbonatitic melts (Tarney and Jones, 1994); (4) mixing and/or mingling of mafic (mantle derived mafic melts) and felsic (derived from the partial melting of crust) magmas (Tarney and Jones, 1994). All of these different proposed petrogenetic models are able to produce magmas which could be classified as high Ba–Sr granitoids. However, each individual model requires

a distinct geodynamic environment and different source such as lower crustal, mantle or mixed origin. Therefore, it is essential to test and compare the geochemical features of SPA and geodynamic history of the Aegean region within the framework of these proposed models for high Ba–Sr granitoids.

The crustal structure of NW Anatolia is made up of different amalgamated continental blocks with the collision between Sakarya and TAP starting in late Cretaceous (Dilek et al., 1990; Okay and Tüysüz, 1999; Okay et al., 1996; Şengör and Yılmaz, 1981). Through a north dipping subduction, the northern branches of Neo-Tethyan ocean (IASZ) are proposed to be consumed during the Paleocene-Early Eocene (Harris et al., 1994; Okay and Tüysüz, 1999). Afterwards, the units of the IASZ (Bornova Flysch; Okay, 1997) and Pontide belts were unconformably overlain by the shallow marine sedimentary rocks of the Başlamış formation of middle Eocene age (Akdeniz, 1980; Akyurek and Soysal, 1983; Yılmaz et al., 1997). These stratigraphical data suggest that, the timing of the collision was earlier than the middle Eocene. Thus, it could be suggested that the early Miocene magmatism was post-collisional (e.g., Harris et al., 1994; Genç and Yılmaz, 1997; Köprubaşı and Aldanmaz, 2004; Altunkaynak, 2007, Altunkaynak et al., 2012a and b). Their post-collisional character and large age span between the onset of subduction and generation of high Ba–Sr granitoids rule out their subduction origin. Therefore, the partial melting of the subducted slab and the ocean islands (Defant and Drummond, 1990, 1993; Tarney and Jones, 1994) could not be a possible melt source for the genesis of the high Ba–Sr Solarya pluton.

The metaluminous I-type characteristics of SPA, the ϵ_{Nd} and correlated TDM values and the presence of MME and mafic dykes having similar isotopic compositions to host plutonic rocks points out to an igneous precursor for the magma source. This data indicate that the partial melting of the juvenile mafic lower crustal rocks with continuous fractional crystallization may be one of the possible melt sources for Solarya pluton. Some experimental studies suggest that, the melting of amphibolites and basalts with following magma/crust interaction and fractional crystallization could produce only tonalitic magmas instead of granitic products (Patiño Douce, 1996, 1999; Patiño Douce and McCarthy, 1998; Rapp and Watson, 1995). These studies also show that, melts from amphibolites and basalts are characterized by high Na_2O (>4 wt%) and low K_2O and Mg numbers (lower than 40). SPA have relatively low values of Na_2O (<3.88 wt%), high K_2O and average Mg# 45. Therefore, these geochemical

features of SPA rule out the lower crustal rocks (basalts, amphibolites and metagreywackes) as the possible melt source for SPA. In addition to these lines of evidence, low P₂O₅ content of SPA also eliminate the partial melting of veined lithospheric mantle which had been metasomatized by carbonatitic melts (Tarney and Jones, 1994) as a possible mechanism for the generation of SPA. Several researchers suggested that, for the carbonatitic melt products, the P₂O₅ content should be higher than 4%wt. (Yaxley et al., 1998; Ionov et al., 1993; Rudnick et al., 1993). However, Solarya pluton presents similar characteristics with the low-P₂O₅ granitoids (<4%wt; Li et al., 2007).

To evaluate the mixing and mingling of mafic (mantle derived mafic melts) and felsic (crustal) magmas as a possible mechanism for the generation of SPA, we evaluate the geochemical and isotopic properties of the most primitive samples of the pluton. The isotopic data of the plutonic association and the spatial and temporal relationship between granitic rocks and mafic dikes/MME's suggest that mafic magmas played an active role in the generation of the SPA. The similarities of the isotopic data of mafic rocks and granitic rocks could be explained with two different reasons: 1- The magma source was extremely enriched mantle melts (sub-continental lithospheric mantle) 2- Contamination of the primitive magma with deep crustal rocks. MME's and mafic dikes are high K calc-alkaline to shoshonitic in character (Figure 2.8a) and TiO₂, FeO₃, MgO (Mg#: 65–70), CaO, Ni and Cr contents are higher with respect to the other plutonic and hypabyssal rocks. ϵ Nd values (ϵ Nd₍₂₁₎: -2.04_ -2.72) and $\delta^{18}\text{O}$ (8.8) are relatively low. The ϵ Nd vs. ⁸⁷Sr/⁸⁶Sr diagram (Figure 2.11a) suggests that, MMEs and mafic dikes plot closer to average EMM (average enriched mantle melts; Yang et al., 2004) field. These data show that, MME's and mafic dikes have enriched lithospheric mantle as a possible magma source. In the same figure, KFMG, microgranite-granodiorite and haplogranites show a negative trend in lithospheric mantle array field between MME's/mafic dikes and western Anatolian basement rocks (Altunkaynak et al., 2012a and references there in). This data may suggest that, the KFMG, microgranite-granodiorite and haplogranite have enriched mantle as a mantle source, which are contaminated with western Anatolian crustal rocks. To test the contribution of these different components, a simple bulk mixing model is included into the same figure (Figure 2.11a). The model suggests that, the crustal contribution to the enriched mantle source is about 30–45% (Figure 11a). In the TDM vs. ϵ Nd₍₂₁₎ diagram,

MMEs and mafic dikes plot at the enriched mantle melts (EMM) field, other plutonic and hypabyssal members are located between EMM and basement rocks of the Sakarya continent consistently in the ϵNd vs. $^{87}\text{Sr}/^{86}\text{Sr}$ diagram (Figure 11b). The Pb isotopic results present critical data for the possible magma source of Solarya pluton. To support the Sr-Nd isotopic results, Pb isotopic data are evaluated with $^{207}\text{Pb}/^{204}\text{Pb}$ vs. $^{206}\text{Pb}/^{204}\text{Pb}$ and $^{208}\text{Pb}/^{204}\text{Pb}$ vs. $^{206}\text{Pb}/^{204}\text{Pb}$ diagrams (Figure 2.12a and Figure 2.12b). In both diagrams, the samples from Solarya pluton and hypabyssal association plot at the EMII (enriched mantle II) field, which involves old crustal material. Solarya pluton presents $\delta^{18}\text{O}_{(\text{SMOW})}$ isotopic values between 9.50 and 10.60 for quartz (Table 2.3). Taylor (1978) classification suggests that magmatic rocks with mixed origin have $\delta^{18}\text{O}_{(\text{SMOW})}$ values between 6 and 10. Moreover, at Figure 2.13, $\delta^{18}\text{O}_{(\text{SMOW})}$ data from few plutonic associations worldwide were plotted on a diagram (Boztuğ et al., 2007) which suggests that, Solarya pluton present similar $\delta^{18}\text{O}_{(\text{SMOW})}$ characteristics with mixed origin plutonic associations worldwide (Figure 2.13).

2.5.2.2 Magma evolution

Solarya pluton displays enrichment in LILE and negative Nb, P and Ti anomalies (Figure 2.10a). These characteristics are consistent with the magmas that have been formed at convergent margin settings (Eyüboğlu et al., 2011; McDonough, 1990; Pearce, 1982; Pearce et al., 1990; Pearce and Peate, 1995; Thirlwall et al., 1994) and/or post collisional granitoids (von Blanckenburg and Davies, 1995). Dupuy et al., 1982 suggested that, these features and high Ba–Sr enrichments are observed in post-collisional magmas, which were derived from mantle source and contaminated from crustal components. In order to test quantitatively the petrogenetic evolution of SPA melts, we conducted assimilation and fractional crystallization (AFC) modeling (Figure 2.14b). Variable $^{87}\text{Sr}/^{86}\text{Sr}$ isotope ratios of SPA and the associated microgranular enclaves and mafic dykes are unlikely to be explained by melt generation from a single, chemically homogeneous source. On plots of $^{87}\text{Sr}/^{86}\text{Sr}$ vs. SiO_2 , where SiO_2 is taken as the fractionation index (instead of Th), the samples follow a low angle, linear trend in which $^{87}\text{Sr}/^{86}\text{Sr}$ ratios increase only moderately (from 0.7078 to 0.7083) for a significant increase in SiO_2 (50 to 78%), indicating an influence by mixing of melts from compositionally distinct sources (Figure 2.14).

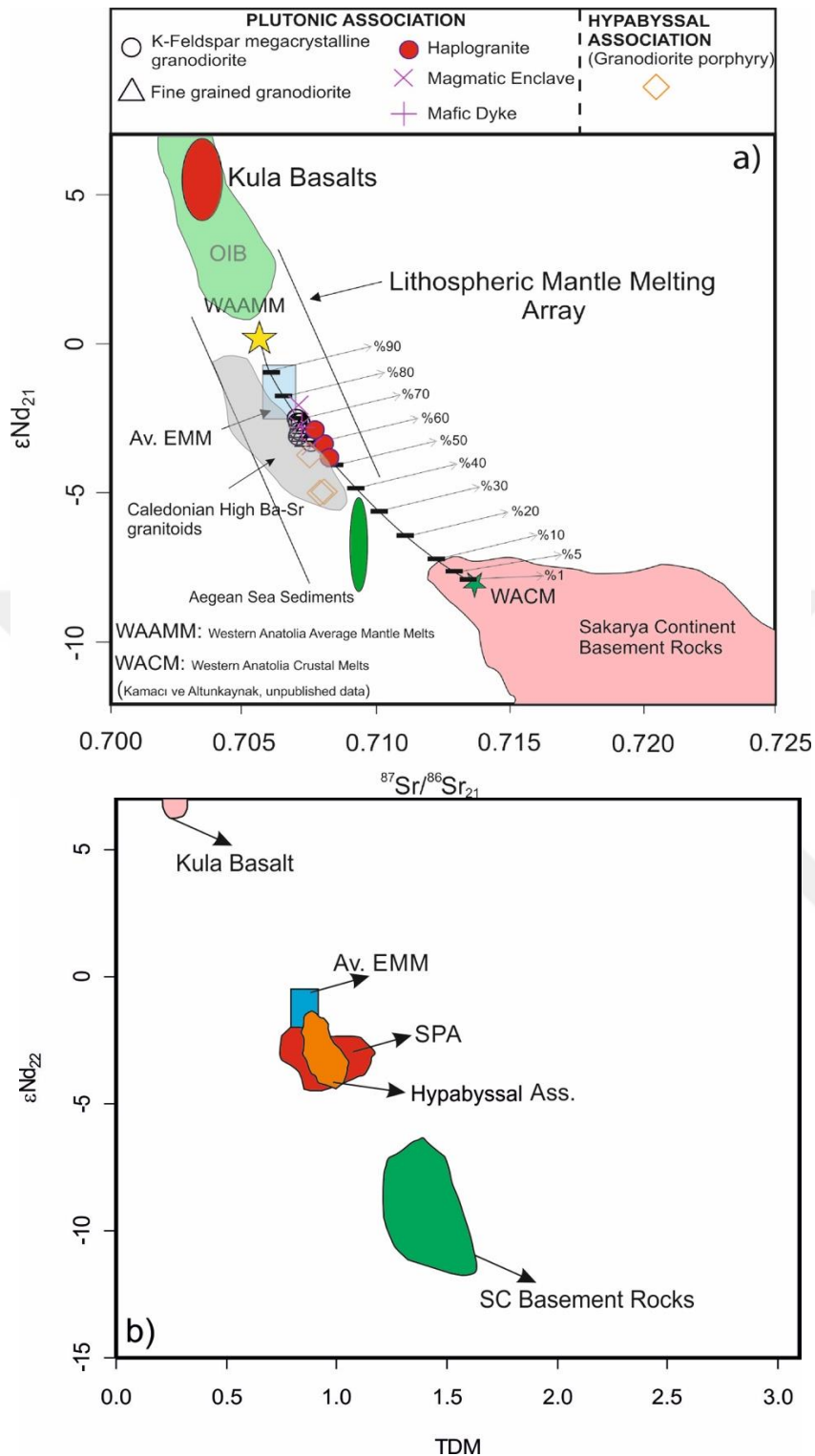


Figure 2.12: a) $\epsilon Nd_{(21)}$ vs. $^{87}Sr/^{86}Sr_{(21)}$ diagram for SPA and HA. Simple bulk-mixing modeling between WAAMM (Kamacı and Altunkaynak, unpublished data) and WACM (Kamacı and Altunkaynak, unpublished data) is also included (Caledonian Granitoid data from Fowler et al., 2008, other data are from Altunkaynak et al., 2012a and references there in). b) $\epsilon Nd_{(21)}$ vs. TDM diagram for SPA and HA. Average EMM (enriched mantle melts: Yang et al. (2004) and Altunkaynak et al. (2010), Kula basalts: Dilek and Altunkaynak (2010), SC Basement Rocks: (Altunkaynak unpublished data; Kamacı and Altunkaynak unpublished data).

In the AFC model (Figure 2.14), calculated using the equations of Depaolo (1981), it is assumed that a primary magma with an isotopic composition similar to a melt derived from an enriched mantle source (EMM) evolved by crystal fractionation and subsequently assimilated by different amounts of crustal material, thus the effects of crustal contamination is increasing. For the crustal end-member, on the other hand, the model uses the average values of various crustal lithologies from western and northwestern Anatolia, including lower crustal amphibolites and upper crustal granitic gneisses sampled from the Menderes and the Kazdağ and Çataldağ massifs (Kamaci and Altunkaynak unpub. data and Altunkaynak et al., 2012a and references there in). The results of model are shown in Figure 2.14 where the data points are compared with the theoretical trends of AFC calculated for a number of (r) values (the ratios of the rate of assimilation to fractional crystallization). On the diagram, SPA rocks plot mostly between the AFC trajectories drawn for $r= 0.1$ and 0.3 , indicating either significantly variable contamination by continental crust or limited isotopic contrast between the mantle and crustal end-members. Higher SiO_2 concentrations seem to have been influenced by FC more significantly. Therefore, crustal assimilation (AFC) did not play a more important role than FC process for evolution of SPA melts from subduction modified enriched mantle source.

Table 2.3: Taylor (1978) classification of magmatic rocks based on their $\delta^{18}\text{O}_{\text{SMOW}}$.

Rock Classification	$\delta^{18}\text{O}_{\text{SMOW}(\text{quartz})}$ value
Altered rocks	between -3 and 0
Mantle origin	between 0 and 6
Hybrid origin	between 6 and 10
Crustal origin	>10

2.5.3 Significance of high Ba-Sr granitoids in western Anatolia Cenozoic geodynamics

This study, the identification of high Ba–Sr Solarya Plutonic Association, supplies further contributions on the overall geodynamics of western Anatolia in Cenozoic time. There is a consensus that, the high Ba–Sr granitoids are essentially developed under extensional or noncompressional regimes such as slab-break off, lithospheric delamination, convective removal of lithospheric mantle or late-to post-orogenic collapse (e.g., Fowler et al., 2008; Peng et al., 2013; Qin et al., 2009; Ye et al., 2008).

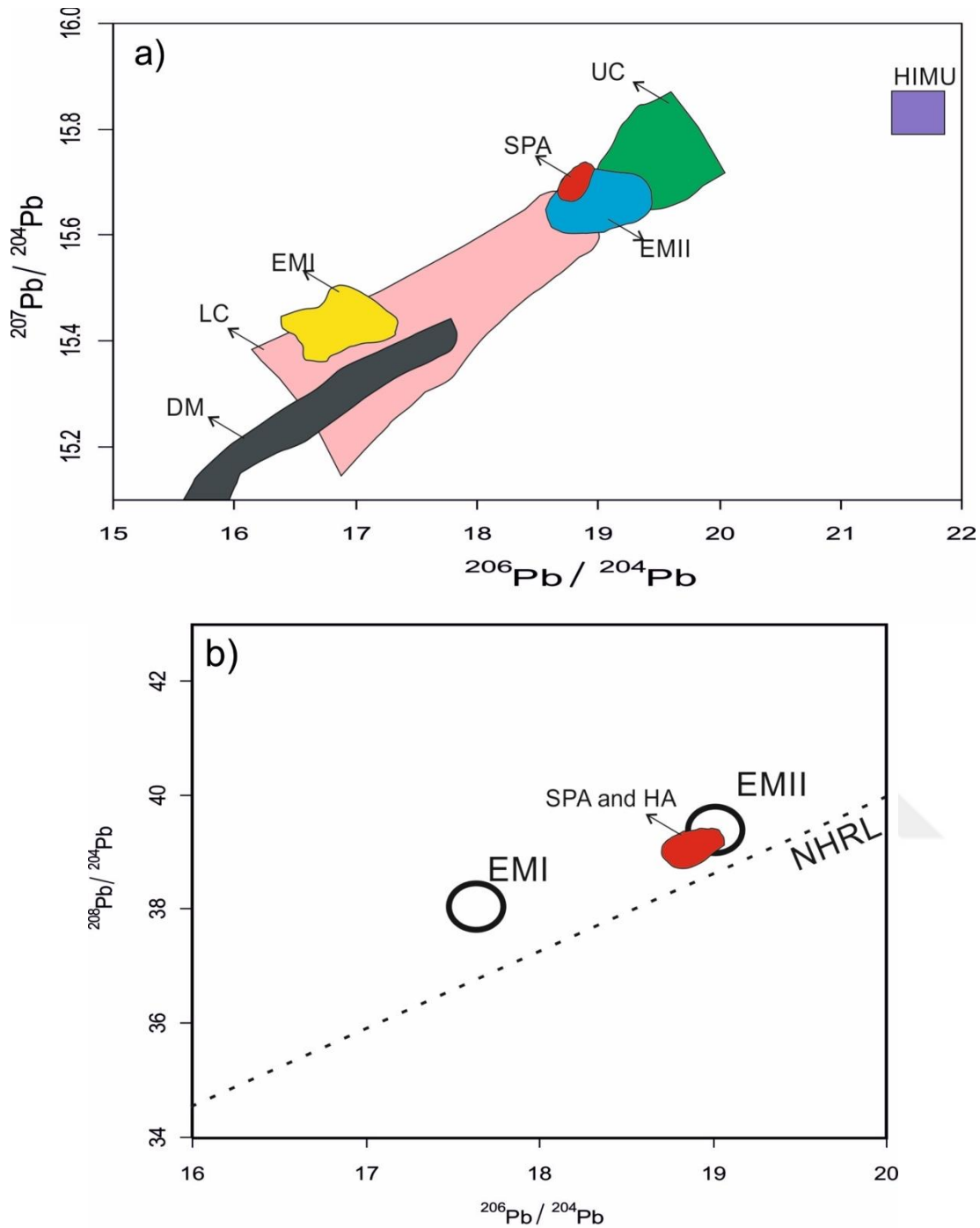


Figure 2.13: a) $\epsilon_{Nd(21)}$ vs. $^{87}Sr/^{86}Sr(21)$ diagram for SPA and HA. Simple bulk-mixing modeling between WAAMM (Kamacı and Altunkaynak, unpublished data) and WACM (Kamacı and Altunkaynak, unpublished data) is also included (Caledonian Granitoid data from Fowler et al., 2008, other data are from Altunkaynak et al., 2012a and references there in). b) $\epsilon_{Nd(21)}$ vs. TDM diagram for SPA and HA. Average EMM (enriched mantle melts: Yang et al. (2004) and Altunkaynak et al. (2010), Kula basalts: Dilek and Altunkaynak (2010), SC Basement Rocks: (Altunkaynak unpublished data; Kamacı and Altunkaynak unpublished data).

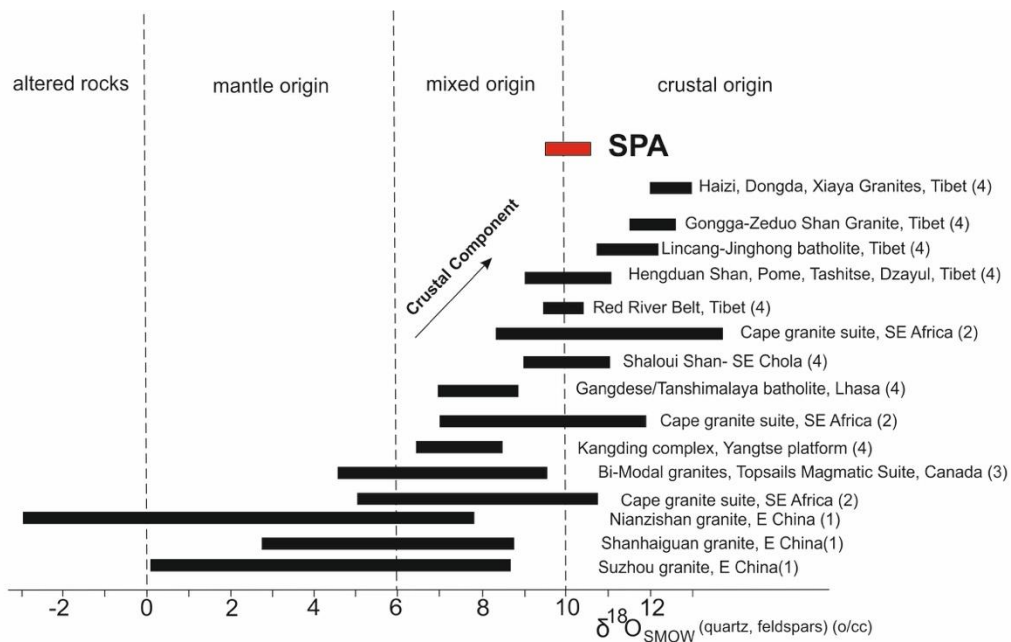


Figure 2.14: $\delta^{18}\text{O}$ (smow) variation of SPA (quartz, feldspar) according to Taylor (1978) classification (1) Wei et al., 2000 (2) Harris et al., 1997 (3) Whalen et al., 1996 (4) Blattner et al., 2002. Figure is modified from Boztuğ et al. (2007).

Indeed, the subduction related arc setting could also be a convenient tectonic environment for the generation of high Ba–Sr granitoids (e.g., Fowler et al., 2008; Tarney and Jones, 1994). Therefore, it is essential to discuss these different possible mechanisms for the generation of high Ba–Sr granitoids within the framework of western Anatolia Cenozoic geodynamics. Cenozoic magmatism in western Anatolia started in Eocene period and continued interruptedly to the present time (Güleç, 1991; Harris et al., 1994; Şengör et al., 1993; Yılmaz, 1989, 1990, 1995). This post collisional magmatism was dominant at Eocene period in NW Anatolia and produced plutonic, hypabyssal and volcanic rocks. Balıklıçeşme volcanites (Ercan et al., 1995), Fıstıklı granitoid and Kızderbent volcanites (Genç and Yılmaz, 1997), Karabiga, Orhaneli, Topuk, Göynükbelen, Gürgenyayla and Kapıdağ granitoids (Altunkaynak, 2007; Altunkaynak et al., 2012b; Bingöl et al., 1982; Delaloye and Bingöl, 2000; Harris et al., 1994; Karacık et al., 2008) are various examples of this severe magmatism. In late Oligocene-early Miocene, this magmatism developed plutonic (Kozak, Evciler, Kestanbol Solarya, Eybek, Çataldağ plutons), hypabyssal and volcanic rocks (Altunkaynak and Yılmaz, 1998; Genç, 1998; Kamacı and Altunkaynak, 2011; Karacık and Yılmaz, 1998b; Yılmaz, 1989).

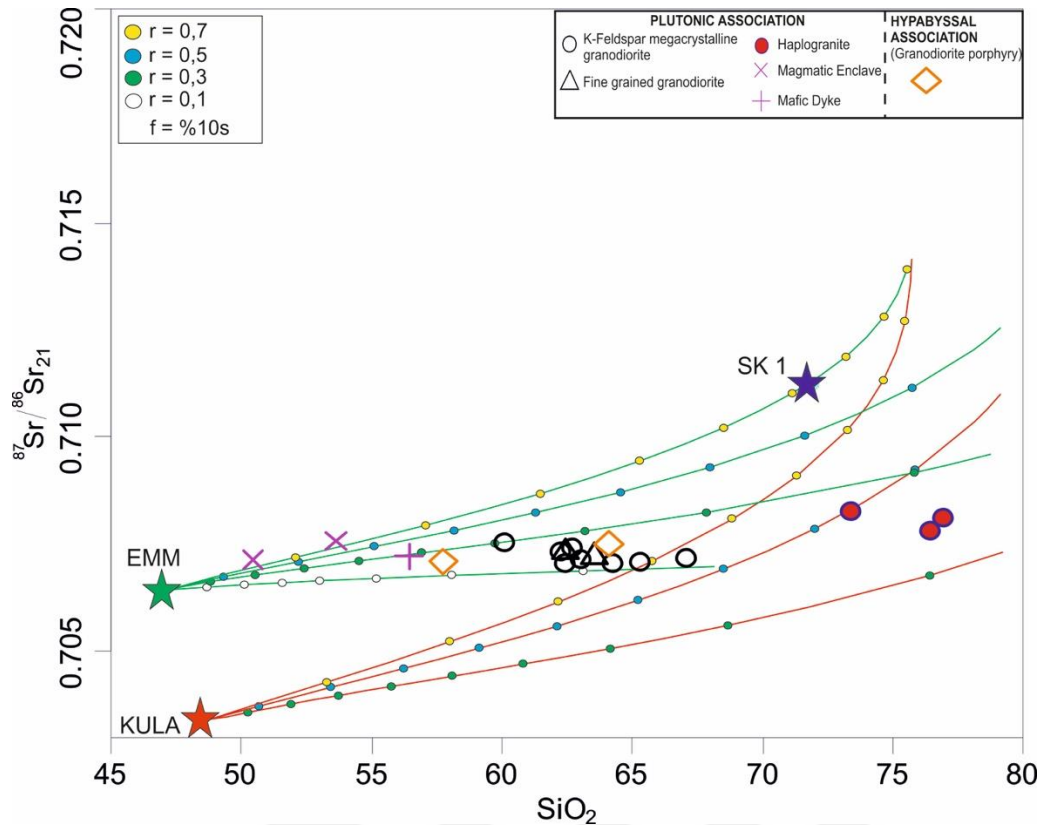


Figure 2.15: Plot of $^{87}\text{Sr}/^{86}\text{Sr}_{(21)}$ versus SiO_2 (wt%), showing the results of AFC modeling for SPA and HA. EMM (Enriched Mantle Melts from Yang et al., 2004), SK1 (Altunkaynak et al., 2012b).

During and after middlelate Miocene, the magmatism proceeded with volcanic rocks, which are enriched in asthenospheric mantle components (Aldanmaz et al., 2000; Aldanmaz et al., 2006; Aldanmaz et al., 2015; Güleç, 1991; Yılmaz, 1989, 1990; Yılmaz and Polat, 1998). There are various studies in the literature which explain and discuss the nature and development of the post-collisional Cenozoic magmatism in western Anatolia (Aldanmaz et al., 2000; Altunkaynak, 2007; Altunkaynak et al., 2012a, 2012b; Altunkaynak and Yılmaz, 1998; Boztuğ et al., 2009; Çelebi and Köprubaşı, 2014; Dilek et al., 2009; Dilek and Altunkaynak, 2007; Ercan et al., 1985; Genç and Yılmaz, 1997; Güleç, 1991; Karacık and Yılmaz, 1998a; Köprubaşı and Aldanmaz, 2004; Savaşçın and Güleç, 1990; Şengör and Yılmaz, 1981; Seyitoğlu, 1997; Seyitoğlu and Scott, 1991; Seyitoğlu and Scott, 1992; Yılmaz, 1989, 1990). To test the possible source for high Ba–Sr magmatism during Cenozoic time in western Anatolia, it is essential to evaluate both of the Eocene and Oligo-Miocene granitoids in terms of high Ba–Sr characteristics.

Eocene plutonism in western Anatolia is well documented in terms of geochemical and geochronological studies (Altunkaynak, 2007; Altunkaynak et al., 2012b; Bingöl

et al., 1982; Delaloye and Bingöl, 2000; Ercan et al., 1995; Genç and Yılmaz, 1997; Harris et al., 1994; Karacık et al., 2008; Topuz and Okay, 2017). These studies reveal both the major-trace element and isotopic (Sr-Nd-Pb) characteristics of Eocene plutons. We have evaluated several Eocene plutons (Fıstıklı, Karabiga, Orhaneli, Topuk, Gürgenyayla, Göynükbelen, Kapıdağ plutons) according to their Sr-Rb-Ba contents from previous studies to test their high Ba–Sr characteristics. Figure 2.15b reveals that, all of the Eocene plutons could be classified as high Ba–Sr granitoids based on Tarney and Jones, 1994 classification.

Similar to Eocene plutonism, there are several fulfilling studies which cover the geochemical and geochronological characteristics of Oligo-Miocene plutonic rocks (Kozak, Evciler, Kestanbol Solarya, Eybek, Çataldağ) in western Anatolia (Altunkaynak et al., 2012a; Altunkaynak and Yılmaz, 1998; Genç, 1998; Kamacı and Altunkaynak, 2011; Karacık and Yılmaz, 1998a; Yılmaz, 1989). Congruently with Eocene plutons, Oligo-Miocene plutonic rocks of western Anatolia are representative examples of high Ba–Sr granitoids (Tarney and Jones, 1994; Figure 15b). The possible models for the generation of high Ba–Sr granitoids could be summarized as; (1) regional extensional related magmatism driven by orogenic collapse, (2) active subduction zone magmatism, (3) magmatism caused by compression-crustal thickening and (4) syn-convergent extension and magma generation driven by slab break-off, convective removal or partial delamination of the lithosphere. The orogenic collapse models propose that, the late Oligocene-Pliocene magmatism in western Anatolia was generated as a result of extensional regime as a consequence of the over thickened crust or lithosphere (Seyitoğlu and Scott, 1991; Seyitoğlu and Scott, 1992; Seyitoğlu et al., 1997). Magmatism in western Anatolia developed uninterruptedly between early Eocene and mid-Miocene period. The products of this period present similar geochemical characteristics (Aldanmaz et al., 2000; Altunkaynak et al., 2012b; Altunkaynak and Dilek, 2013). The orogenic collapse model does not explain these similarities. Moreover, the representative products of orogenic collapse magmatism, such as astenospheric flood basalts, were developed in a limited area (Quaternary Kula Basalts) in western Anatolia (Dilek and Altunkaynak, 2010). Therefore, the orogenic collapse model is not suitable for western Anatolia Cenozoic high Ba-Sr magmatism.

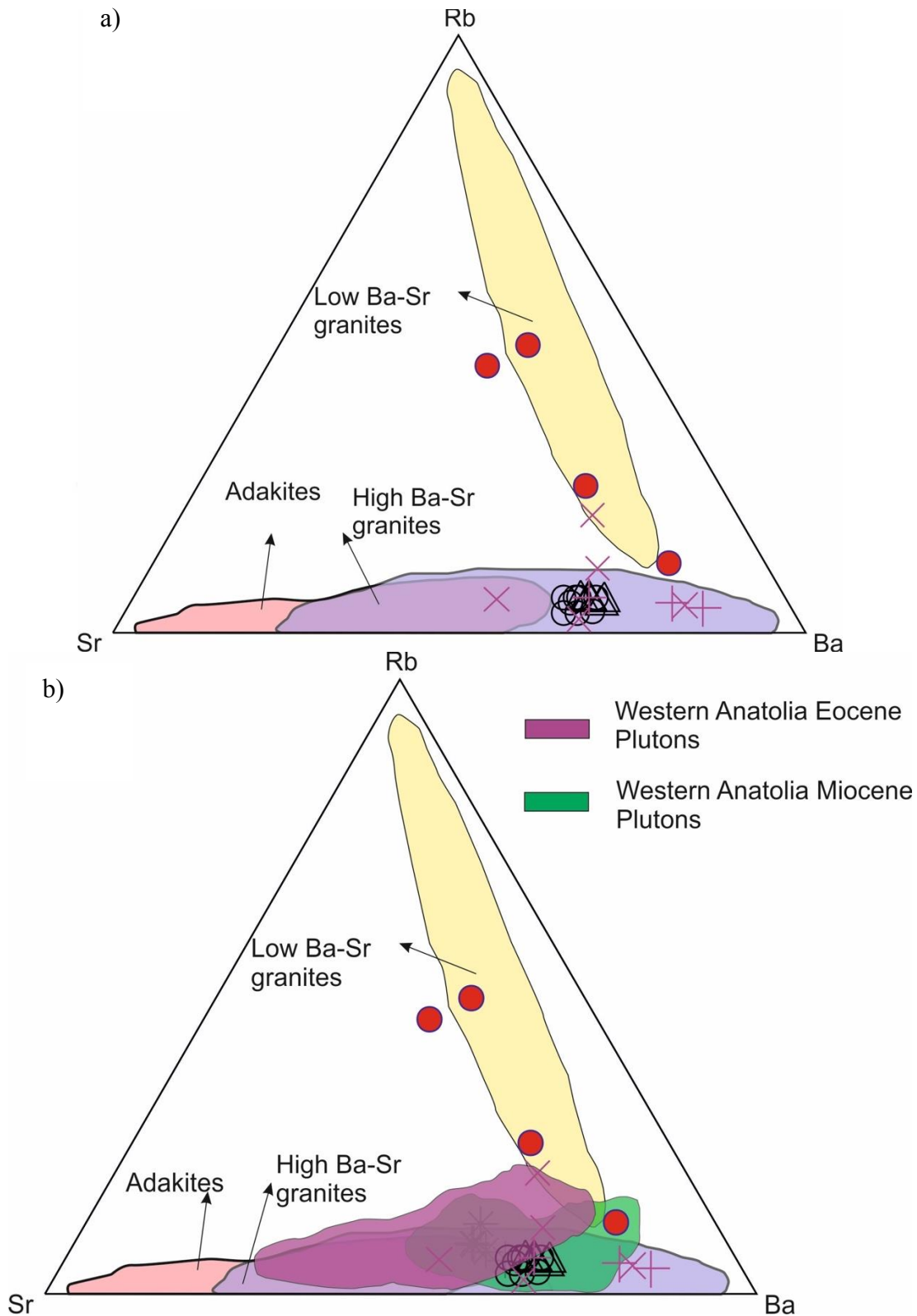


Figure 2.16: Sr–Rb–Ba plot (after Tarney and Jones, 1994) for (a) Solarya Plutonic Association (b) Eocene and Miocene plutons of western Anatolia (See Figure 6 for symbols).

Proposed subduction models for western Anatolia Cenozoic magmatism indicate that, magmatism was either a product of the subduction initiated in the Cretaceous along the IASZ or Miocene subduction along the Hellenic trench through slab retreat (Pe-Piper and Piper, 2006; Spakman, 1990; van Hinsbergen et al., 2005). The units of the IASZ (Bornova Flysch; Okay et al., 1996) and Sakarya Continent were unconformably overlaid by the shallow marine sedimentary rocks of the Gebeler and Başlamış formation of middle Eocene age (Akdeniz, 1980; Akyurek and Soysal, 1983; Yılmaz et al., 1997). This stratigraphical data suggest that, the timing of the collision was earlier than the middle Miocene. Moreover, although the Cenozoic magmatic rocks of western Anatolia present geochemical fingerprints related to a subduction event, there is no geological evidence for active subduction, such as accretionary prism development. For the subduction of African lithosphere beneath Eurasia through the Hellenic trench, Meulenkamp et al., 1988 suggested that this subduction started around 13 Ma. Therefore, it could be suggested that the early Miocene magmatism was developed in a post-collisional setting and the subduction fingerprints in geochemical characteristics of magmatic rocks were associated with late Cretaceous subduction (Altunkaynak et al., 2012a, 2012b; Yılmaz et al., 2000; Yılmaz and Polat, 1998).

The magma generation caused by compression-crustal thickening is a proposed model for Cenozoic magmatism in western Anatolia (Şengör and Yılmaz, 1981; Yılmaz, 1989, 1990; Savaşçın and Güleç, 1990; Güleç, 1991; Altunkaynak and Yılmaz, 1998, Genç and Yılmaz, 1997; Yılmaz and Polat, 1998). This model suggests that, the magmatism in western Anatolia begun under N-S compressional regime and continued with the transition between this compression to N-S extension. Yılmaz, 1989 proposed that, the magmatism driven by the crustal shortening and thickening was developed until late Miocene time. With the aid of the A-type subduction magmatism, H₂O, SiO₂, K₂O, LILE and radiogenic isotopes were released. As a consequence of this, the flux induced partial melting occurred to develop hybrid volcanic rocks with different compositions. Volcanic rocks present deep mantle sources and contaminated by crustal components. With the transition between compression to extension, the alkaline basaltic magmatism developed which represents the final products of the western Anatolia. This model could explain the hybrid (mantle+crust) characteristics of the magmatism. However, experimental studies suggest that, the magmatism related with crustal thickening and continental shear zones would develop a small scale local

magmatism instead of the widespread magmatism in western Anatolia (Petford and Gallagher, 2001; Rushmer, 1993).

Magma generation associated with syn-convergent extension is a widely-proposed model for Cenozoic magmatism in western Anatolia (Aldanmaz et al., 2000; Altunkaynak, 2007; Altunkaynak et al., 2012a, 2012b; Boztuğ et al., 2009; Dilek and Altunkaynak, 2007; Köprubaşı and Aldanmaz, 2004). Different mechanisms such as slab break-off, partial delamination or convective removal of lithosphere have been proposed to explain the Cenozoic magmatism in western Anatolia. The slab break-off model was suggested for both Eocene granitoids (Altunkaynak, 2007; Altunkaynak et al., 2012b; Dilek and Altunkaynak, 2009; Köprubaşı and Aldanmaz, 2004) and Oligo-Miocene granitoids (Boztuğ et al., 2009). Slab break-off mechanism is based on the partial melting of the crust and sub-continental lithospheric mantle which is metasomatized by the previous subduction events by the upwelling hot asthenosphere (Davies and von Blanckenburg, 1995). The linear distribution and narrow time span of the Eocene plutons could be related to the slab break-off related asthenospheric upwelling and associated partial melting (Altunkaynak, 2007; Altunkaynak et al., 2012b; Köprubaşı and Aldanmaz, 2004). Although slab break-off mechanism could explain the nature of the Eocene magmatism, the widespread distribution (from Marmara region at the north to the Bodrum peninsula at the south) of the Oligo-Miocene magmatic rocks of western Anatolia eliminates slab break-off mechanism as a possible model. Partial delamination of the continental lithosphere (Aldanmaz et al., 2000) and convective removal of the lithosphere (Altunkaynak et al., 2010, 2012a) resulting in asthenospheric upwelling and decompressional melting were critical processes for the post collisional Cenozoic magmatism in western Anatolia. I-type granitoids with mantle and crustal components could develop under these different tectonic settings (Aldanmaz et al., 2000; Altunkaynak et al., 2010, 2012a; Bird, 1979; England and Houseman, 1989; Houseman and Molnar, 1997; Keskin, 2003; Molnar et al., 1993; Şengör et al., 2003). The convective removal or partial delamination of the continental lithosphere leads to a broad scale extension and crustal exhumation (Bird, 1979; England and Houseman, 1989; Molnar et al., 1993) which is consistent with the widespread distribution of the Oligo-Miocene magmatism.

Here we conclude that the partial melting of EMII, which led to the generation of Solarya Plutonic Association, was caused by the upwelling asthenosphere due to

convective removal or partial delamination of the continental lithosphere beneath western Anatolia. Therefore, syn-convergent extension related magma generation could be the most suitable tectonic process for the development of high Ba–Sr granitoids in western Anatolia.





3. THE EMPLACEMENT HISTORY OF GRANITIC INTRUSIONS INTO THE UPPER CRUST: FORCEFUL TO PASSIVE EMPLACEMENT OF EARLY MIOCENE SOLARYA PLUTON (NW TURKEY) AS A CASE STUDY

3.1 Introduction

The emplacement of granites is defined as the switch of upward flow to the horizontal flow in the middle to upper crust, which started its ascent through the lower crust (Pitcher, 1979; Marsh, 1982; Brown, 1994; Clemens, 1998; Petford et al., 2000). The emplacement mechanisms of the plutons have been a popular matter of debate for the last century (e.g. Clough et al., 1909; Richey, 1928; 1932; Hutton, 1988b; McCaffrey and Petford, 1997; Altunkaynak and Yılmaz, 1999; Petford et al., 2000, Cole et al., 2005; Stevenson et al., 2007 and 2008; Stevenson, 2009). The main mechanisms that control the granite emplacement can be summarized as forceful emplacement, roof uplift, magmatic stopping and cauldron (floor) subsidence (e.g. Richey, 1928; 1932; Paterson and Fowler, 1993; Cruden, 1998; Petford, et al., 2000; Cole et al., 2005; Stevenson, 2009). From the early stages of the granite emplacement research, the forceful emplacement mechanism has been controversial. The main point of this controversy is the so-called space problem (Pitcher, 1993) in which the forceful emplacement of magma occurs when the amount of magma exceeds the rate of the space therefore magma is required to shoulder aside the country rocks (Stevenson, 2009). Conversely pluton emplacement by floor subsidence through a cauldron subsidence mechanism, involves the sinking of a large block of country rock, controlled by the steep fractures or faults, into the magma

This chapter is based on the paper; Ünal, A., Altunkaynak Ş., Kamacı Ö., Dunkl I., Benowitz J., (2019). The emplacement of shallow intrusions into the upper crust: Implications from the geochronology, geothermobarometry and emplacement mechanisms of Solarya Pluton (NW Anatolia), *Journal of Asian Earth Science*, 315.

chamber in which the space created by subsidence is filled by magma from the same magma chamber (Clough et al., 1909; Anderson, 1936; Hills, 1963; Hall, 1996; Cole et al., 2005; Stevenson et al., 2007; Stevenson, 2009).

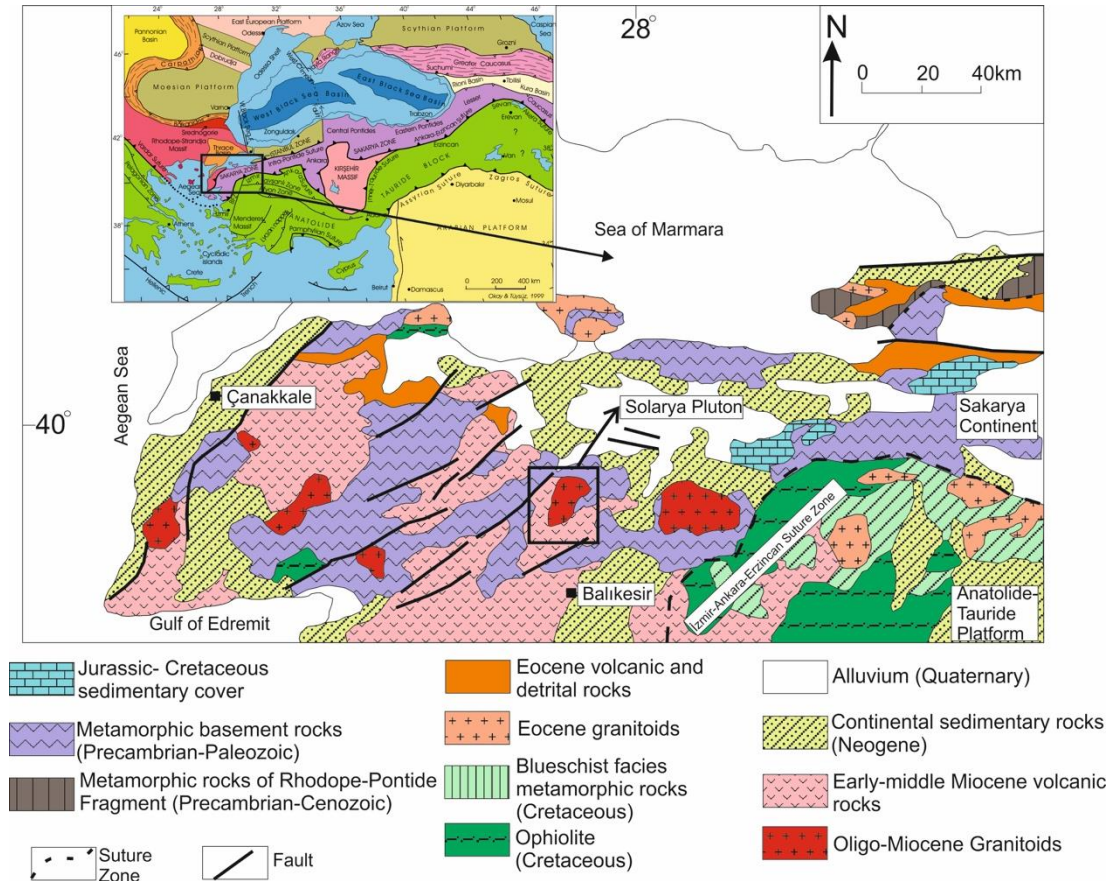


Figure 3.1: Simplified geological map of the NW Anatolia (Modified from Altunkaynak, 2007). Black rectangle shows the Solarya Pluton (SP).

In order to contribute to the debates on granite transport and emplacement space problems, we have undertaken the detailed field, geothermobarometry and geochronology studies in the Solarya pluton (SP), which is located at NW Anatolia within the western Anatolian extensional province (Figure 3.1). The SP is one of the best examples of shallow level intrusions where the wall and roof rock relationships are clear and the indicators of different emplacement mechanisms are traceable. There are few studies in the literature which include geochemical and geochronological properties of the SP (Karacık et al., 2008; Boztuğ et al., 2009, Altunkaynak et al., 2012a; Yilmazer et al., 2014; Çelebi and Köprübaşı, 2014; Ünal and Altunkaynak, 2018). However, the lack of integrated emplacement and cooling ages (U-Pb zircon and $^{40}\text{Ar}/^{39}\text{Ar}$ ages), emplacement conditions and emplacement mechanisms of the SP in the literature stand out in relief.

We present here geochronology (U-Pb zircon, $^{40}\text{Ar}/^{39}\text{Ar}$ biotite and feldspar) and amphibole-feldspar geothermo-barometry results of the different granitic members of the SP to examine the timing and conditions of the emplacement which occurred at different depths with different mechanisms. Contact relationships and structural data indicate that the emplacement of the SP has occurred with successive forceful emplacement and cauldron subsidence mechanisms. Regarding these multiple emplacement stages and emplacement mechanisms of the SP, this study contributes to examination of the journey of granitic magmas in the upper crust as well as the interplay between different emplacement stages and mechanisms.

3.2 Geological Setting

3.2.1 Regional Geology

Crustal structure of western Anatolia and broader Aegean extensional province is made up of different continental blocks that were amalgamated via collision between Anatolide-Tauride platform and Sakarya Continent marked by the İzmir-Ankara-Erzincan Suture Zone (IAESZ) (Şengör and Yılmaz, 1981; Okay, 1984; Okay et al., 1990). In northwestern Anatolia, the basement units are Anatolide-Tauride platform (ATP), İzmir-Ankara-Erzincan Suture Zone (IAESZ), Sakarya Continent (SC), Intra-Pontide Suture Zone (IPSZ) and Rhodope Massif (RM), from south to north (Figure 3.1). During the Late Oligocene-Early Miocene, a number of shallow level intrusions were emplaced into these different basement units following the continental collision. These shallow level intrusions are cogenetic and coeval with associated hypabyssal and volcanic rocks (Yılmaz, 1989; 1990; Altunkaynak and Dilek, 2006; Helvacı et al., 2009; Altunkaynak et al., 2010; 2012a; Ersoy et al., 2012; Ünal et al., 2012; Erkül et al., 2013; Kamacı and Altunkaynak, 2018; Ünal and Altunkaynak, 2018). The SP, one of the representative examples of Early Miocene granitoids in NW Anatolia, was emplaced into the basement rocks of Sakarya Continent. Different rock groups are distinguished in the study area (Figure 3.2). These are; (1) Basement rocks (metamorphic and non-metamorphic), (2) Solarya Pluton (SP), (3) Hypabyssal Association (HA), (4) Volcanic Association (VA) and (5) Sedimentary Association (SA).

3.2.2 Pluton Interior

The SP is represented by N-S elongated plutonic body covering approximately 220 km². It has approximately 20 km length and 10 km width. The long axis of the pluton strikes N05E (N-S) and the short axis strikes N85W (W-E). The SP consists of three nearly coeval granitic members (Figure 3.2): (a) K-feldspar megacrystalline granodiorite (KFMG); (b) microgranite-granodiorite (MGG) and (c) haplogranite.

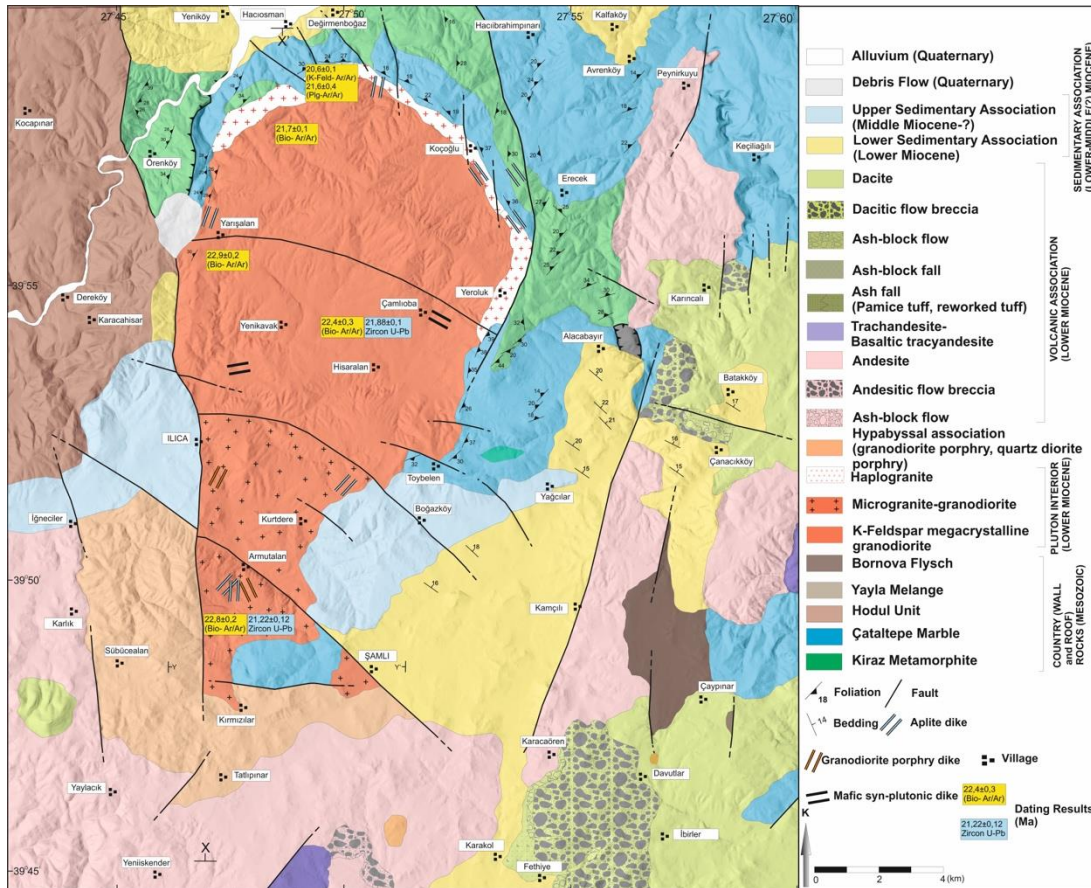


Figure 3.2: Geological map of the study area (Modified after Ünal and Altunkaynak, 2018).

Northern part of the SP is formed from K-feldspar megacrystalline granodiorite (KFMG) whereas southern part is represented by microgranite-granodiorite (MGG). KFMG consists of plagioclase (oligoclase-andesine), quartz, K-feldspar (orthoclase), biotite and magnesio-hornblende. It presents holocrystalline porphyritic texture defined by K-feldspar megacrysts, reaching up to 5cm size (Figure 3.3a and b). Through the southern parts, the boundary between KFMG and MGG is bounded by a normal fault (Ilica Fault) striking 285° (W-E). MGG is characterized by its fine grained-microgranular texture (Figure 3.3c and d). Along the southern contact of the

pluton, MGG interfinger with porphyritic microgranodiorite/ microquartz-diorite (hypabyssal association, HA). Hypabyssal association (HA) is represented by crescent shaped sheet intrusive rocks presenting similar mineralogical properties with main plutonic body (Figure 3.2 and Figure 3.2a). They are typical with their microgranular, porphyritic texture. In some places, they include enclaves of MGG, and both HA and MGG are cut through by aplite dikes.

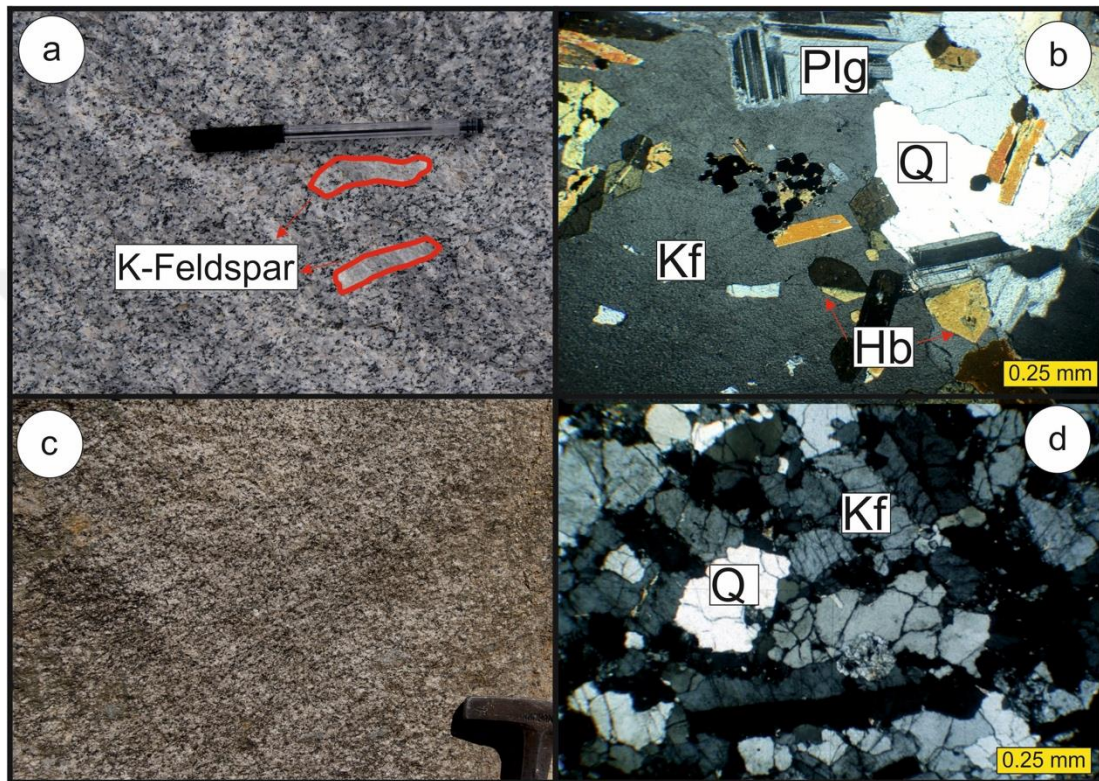


Figure 3.3: a) Field photograph of K-feldspar megacrystalline granodiorite (KFMG). b) Micrograph illustrating the porphyritic texture of KFMG (Kf: K-Feldspar; Plg: Plagioclase; Q: Quartz; Hb: Hornblende). c) Field photograph of microgranite-granodiorite (MGG). d) Micrograph illustrating the microgranular texture of KFMG (Kf: K-Feldspar; Q: Quartz).

Haplogranite is a fine-grained leucocratic-hololeucocratic variety of the main plutonic body and described by feldspar and quartz rich rocks with minor mafic minerals (biotite-amphibole < 5%). Graphic/granophyric textures are common in the haplogranites (for detailed petrographical properties of the SP, please see Ünal and Altunkaynak, 2018).

The SP is generally defined by a non-deformed isotropic granite. Only through the northern contacts of the pluton, a very narrow slight deformation zone was observed within KFMG. The marginal zone of the pluton consists of semi-plastic reorientation

of mica minerals and recrystallization of the quartz minerals. This deformation is mainly characterized by semi-ductile deformation possibly developed due to the emplacement of the pluton (Figure 3.4). The present geomorphology of the pluton is mostly controlled by WNW-ESE directed faults that cut different members of the SP. Ilica Fault, one of the major structural elements in the area, (marked as IF on Figure 3.4) separates the K-Feldspar megacrystalline granodiorite (KFMG) and microgranite-granodiorite (MGG) and follows the primary contact between them. The Armutalan Fault (marked as AF on Figure 3.4) is an active fault (Emre et al., 2018) and cuts the MGG together with basement and cover rocks.

3.2.3 Wall and Roof Rocks

The SP was intruded into the basement rocks of the Sakarya Continent which are represented by metamorphic (Nilüfer Unit) and non-metamorphic (Hodul Unit) rocks of Karakaya Complex (Okay et al., 1990). Nilüfer unit is represented by metabasites, metapelites and marbles (Okay et al., 1990). Metapelites are formed from quartz-mica schists, phyllites and calc-schists whereas metabasites are represented by metavolcanics and metatuffs (Figure 3.5a and b). Marbles are mainly defined by dolomitic marbles (Figure 3.5c and d). The mineral assemblage in the metabasites is actinolite/hornblende+albite+chlorite+epidote whereas the intercalated mica-schists (metapelites) and calc-schists contain quartz+muscovite+biotite+chlorite±garnet and quartz+muscovite+biotite+ calcite, respectively (Figure 3.5b). This mineral paragenesis indicate that, the metamorphism degree of Nilüfer Unit is within the limits of greenschist facies. They present well developed foliation (S-1) and lineation (L-1). The strike and dip directions of the foliation planes suggest that regional metamorphic rocks are represented by an anticline and its main fold axis strike through NE-SW (Figure 3.2). During the emplacement of the SP, a contact metamorphic aureole was developed between the SP and wall rocks mostly forming from dolomitic marbles and calc-schists. Mineralogical and structural changes developed by contact metamorphism can be observed through the northern and eastern contacts of the pluton with the wall rocks. Through the other contacts, the contact metamorphic zone is truncated by faults. The contact metamorphic rocks are represented by different lithologies. Through the contacts of the SP with dolomitic marbles, contact metamorphic rocks are formed from

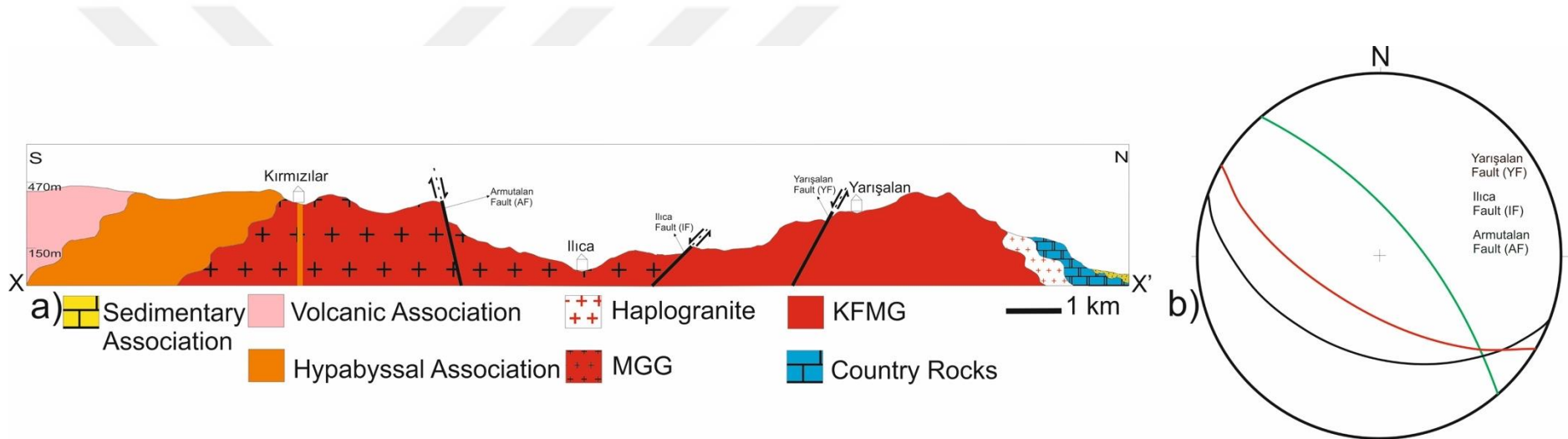


Figure 3.4: a) N-S cross-section of the study area (X-X'). Figure also illustrates the major faults cutting the SP. b) Stereographic projection of three major faults.

hornfels and skarn whereas along the contacts with calc-schists, contact metamorphic rocks are made up of contact schists. Hornfels and skarn display hornfels texture while contact schists display schistose texture defined by the slight elongation of the diopside and wollastonite with sub-grain rotations in quartz through a secondary developed foliation (S-2; Figure 3.6a and b). The shear senses of the contact schists are perpendicular to the strike of the pluton contacts (Figure 3.6a and b) whereas regional metamorphic rocks display complex shear senses. One of the other textural variation that is observed due to the contact metamorphism is the increasing grain size in marbles towards to the pluton boundary (Figure 3.6c and d).

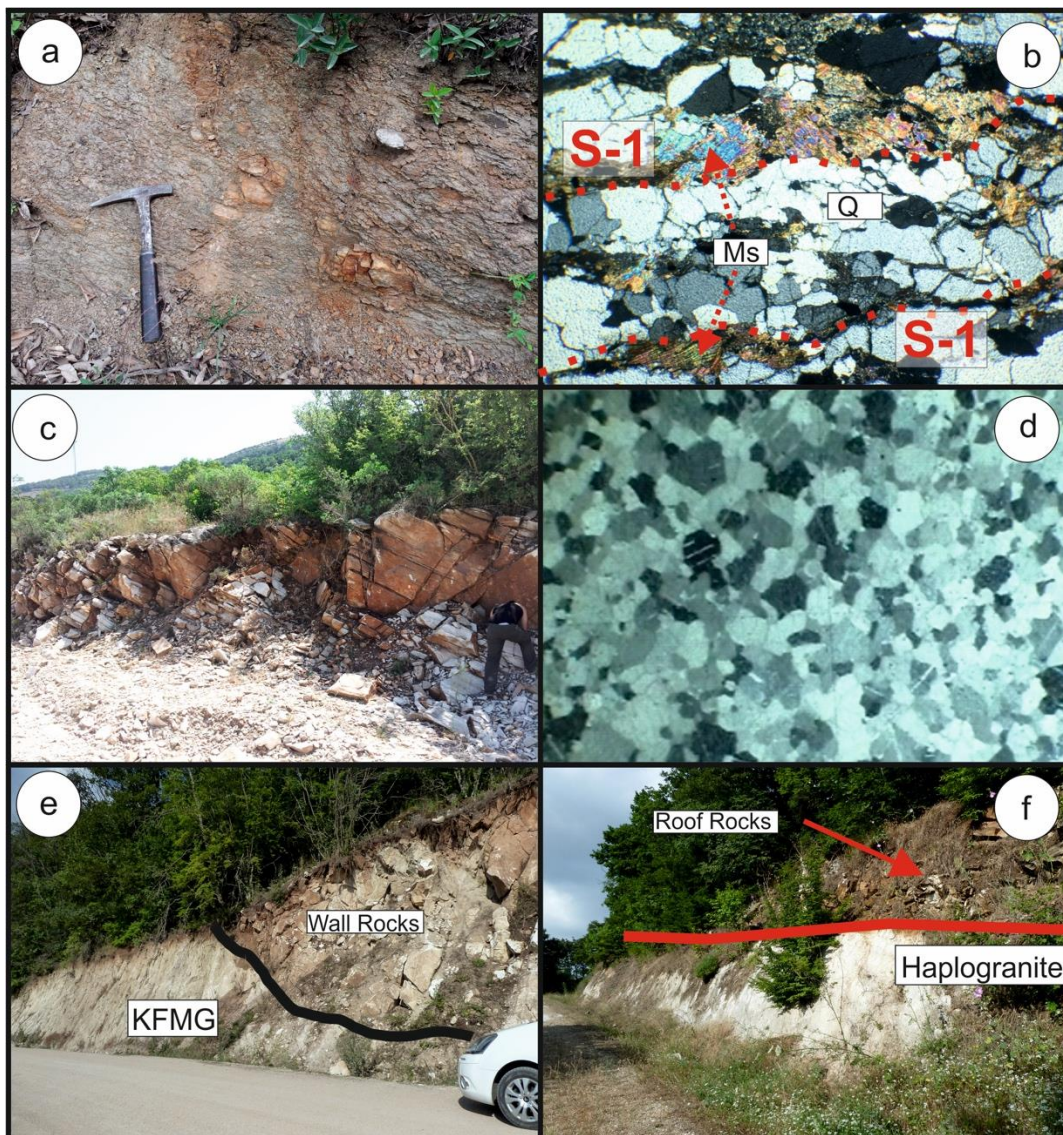


Figure 3.5: a) Field photograph of metapelites b) Micrograph of metapelites. The S-1 foliation plane is shown in the figure. c) Field photograph of marbles. d) Micrograph of marbles. e) The contact intrusive between KFMG and wall rocks. f) The contact between haplogranite and roof rocks.

Contact metamorphic zone can be divided into two different zones (inner and outer) based on mineral paragenesis of contact metamorphic calc-schists. Inner zone is represented by wollastonite + diopside + hypersthene + plagioclase + garnet + quartz (Figure 3.7 a, b and c). Outer zone, on the other hand, is located further from the main plutonic body and represented by calcite + plagioclase + tremolite + diopside + garnet + quartz + epidote (Figure 3.7 d, e and f). These mineral parageneses indicate that the conditions of contact metamorphism were reached to the pyroxene-hornfels facies for the inner zone, and hornblende-hornfels to epidote-hornfels facieses for the outer zone (Yardley et al., 1990).

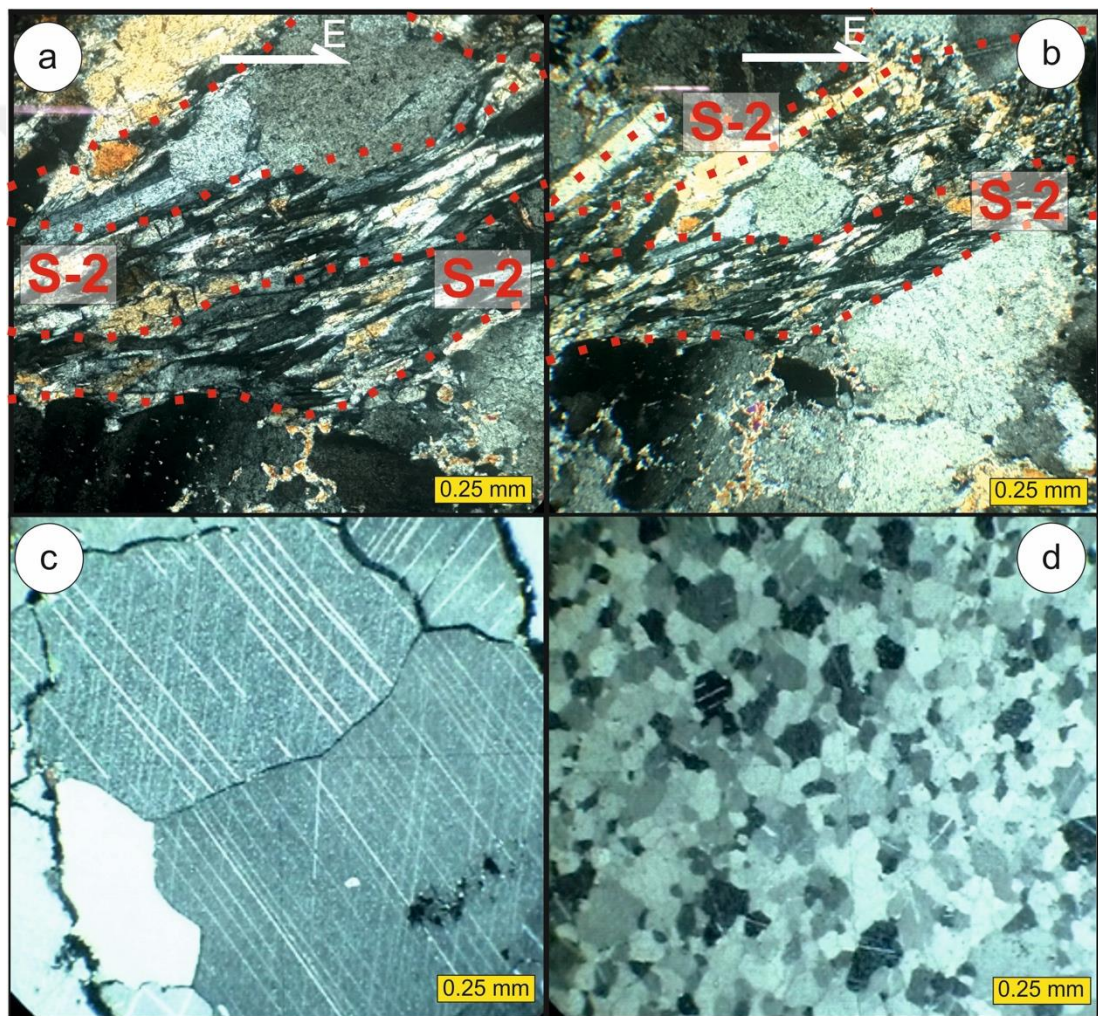


Figure 3.6: a, b) The elongation of wollastonite and diopside in contact schists over a secondary foliation plane (S-2) c, d) Decrease of grain size in marbles outwards the pluton boundary.

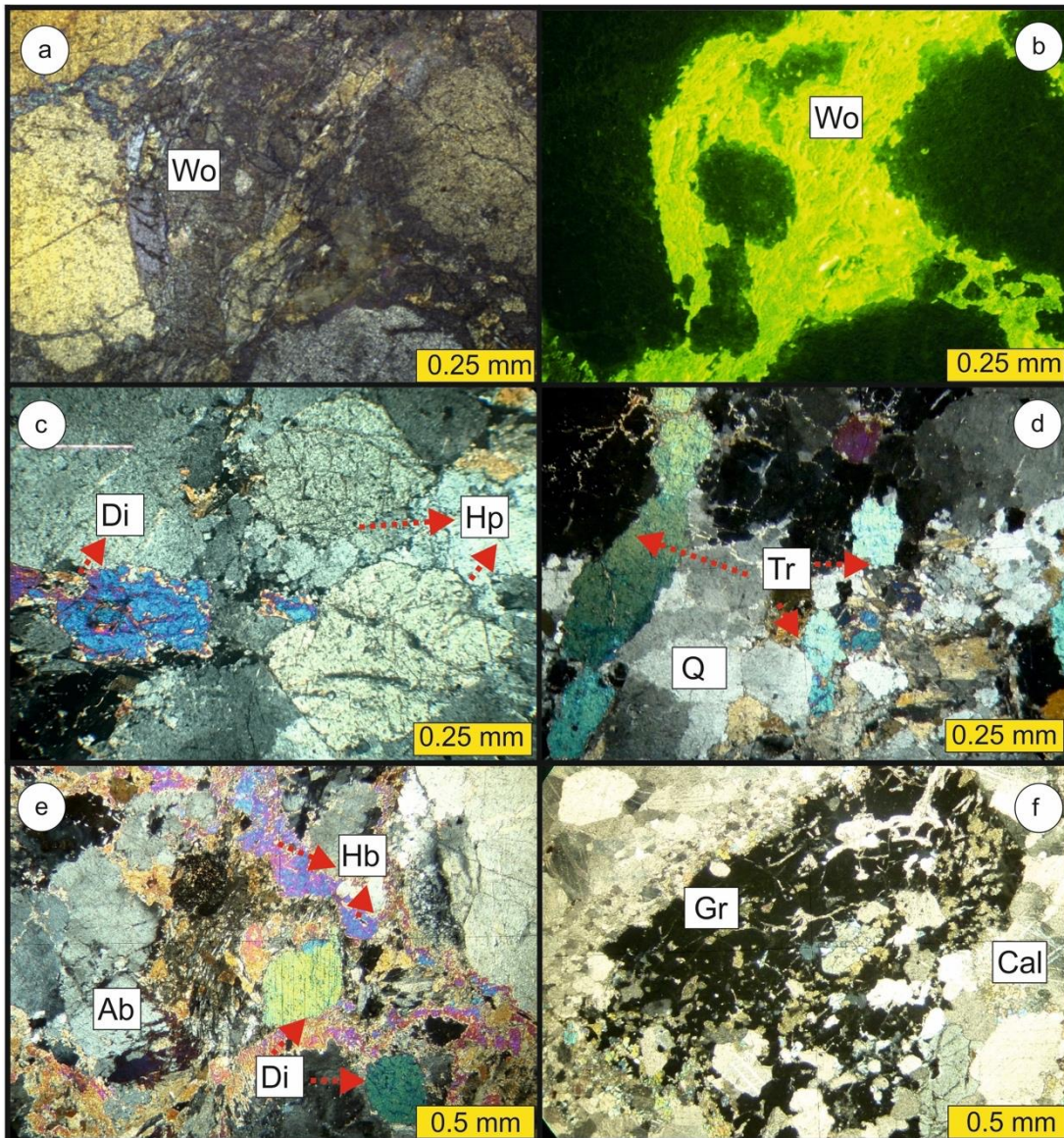


Figure 3.7: a, b) Micrographs illustrating the main petrographical features of the contact metamorphic rocks a) Wollastonite (Wo) porphyroblast in hornfels near the contact. b) Cathodoluminescence image of wollastonite (Wo) within the inner zone. c) Co-existence of diopside (Di) and hyperstene (Hp) in the contact metamorphic rocks of the inner zone. d) Tremolite (Tr) and quartz (Q) development in the contact metamorphic rocks towards the outer zone e) Hornblende (Hb), albite (Ab) and diopside (Di) paragenesis in the outer zone f) Garnet (Gr) with calcite (Cal) in the contact metamorphic rocks of the outer zone.

The structural changes within the wall rocks through the eastern and northern contacts are not only characterized by micro scale variations, but also meso-macro scale structural features. At a distance from the pluton boundary, the trends of the foliation planes of the basement rocks are represented by an anticline and its representative fold axis strike through NE-SW (Figure 3.8a and b). Closer to the contacts of the pluton,

these trends progressively swing towards the contact, finally becoming concordant to the boundary (Figure 3.8a and c).

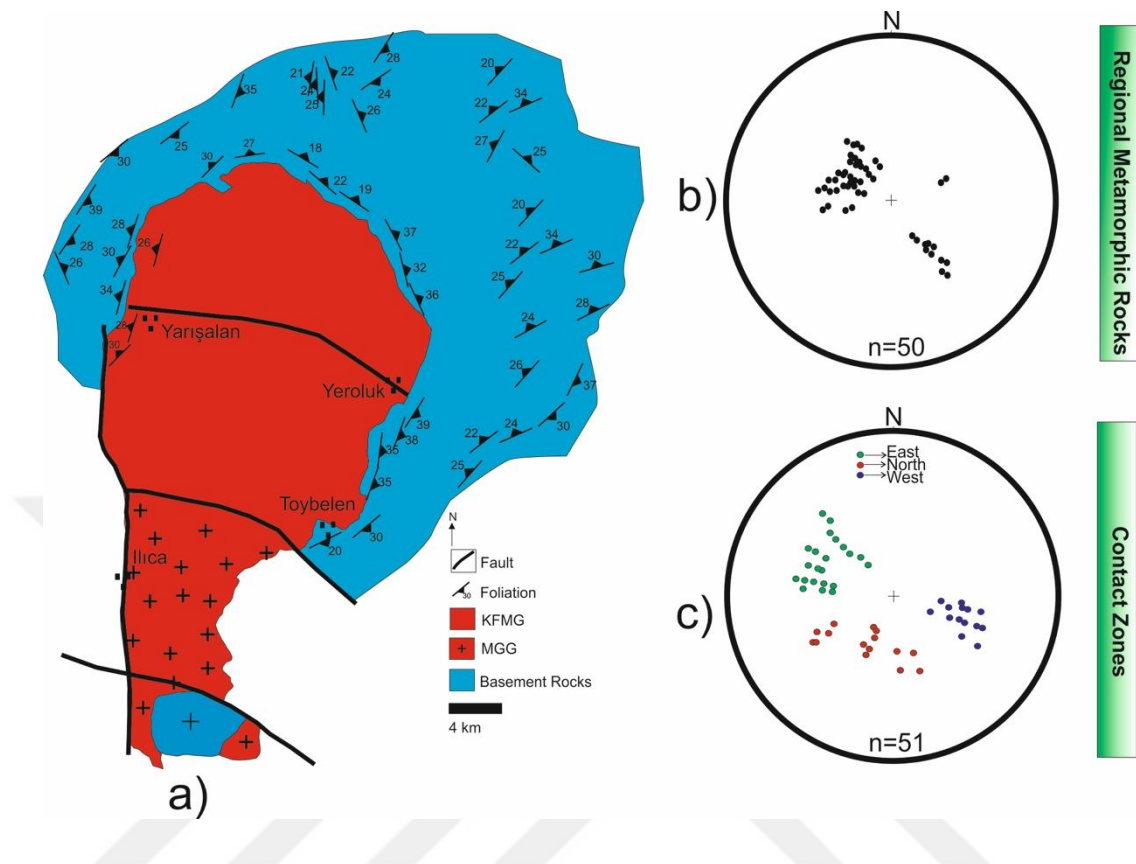


Figure 3.8: a) The structural geology map of the SP and surrounding rocks (wall rocks). b) Stereographic projections of the foliation planes of regional metamorphic rocks c) Stereographic projections of the foliation planes of regional metamorphic rocks along the contact with the SP.

Along the western border, contact metamorphic zone is truncated by a fault zone which separates the SP from the wall rocks (Figure 3.2). The N-S trending normal fault with approximately 25 km length cuts two different main units (KFMG, MGG) of the pluton together with the country rocks. Through the fault zone, the pluton presents cataclastic textures in local places, indicating its brittle deformation. Therefore, this fault should have been active while the pluton is relatively cooled down. Moreover, this N-S trending fault also cuts the upper sedimentary association in several places which overlays the plutonic body and presents younger ages than middle Miocene. These data indicate that, western contact of the pluton with country rocks is bounded by a relatively young, brittle fault. This young fault tucks away the haplogranite and contact metamorphic aureole through the western margin of the pluton.

Roof rocks are observed at the southern margin between the MGG and HA. The contacts between the MGG and roof rocks are smooth and gently dipping which are defined by the contacts with $<10^\circ$ dip angles. In this place, the marbles represent a “roof pendant”, which is defined by the remnants of the roof rocks at the top of the pluton (Figure 3.2).

3.2.4 Cover Rocks

Cover rocks in the study area are represented by volcanic and sedimentary associations. Volcanic Association (VA) covers an area of approximately 240 km² (Figure 3.2) at the southern and eastern parts of the study area. It is formed from three main rock groups; (1) Andesite and associated pyroclastic rocks, (2) Dacite and related pyroclastic rocks (Figure 3.9a), and (3) trachyandesite and dykes. Pyroclastic rocks are represented by flow breccias, pyroclastic fall and flow units (Ünal and Altunkaynak, 2019). Volcanic Association (VA) interfinger with hypabyssal association through southerly parts of the study area.

Sedimentary association can be divided into two different groups based on their structural and lithological properties; (1) Lower Sedimentary Association (LSA) and (2) Upper Sedimentary Association (USA). LSA is formed from sequence of lacustrine sediments. It begins with a coarse-grained basal conglomerate which consists of pebbles of plutonic and basement rocks at the base. The upper parts of the conglomerate are defined by coarse-grained sandstones. A thick sequence of mudstone and shale with thin beddings overlays the sandstones through the northern parts. Shale and mudstones include thin lignite layers (Figure 3.9b). The uppermost parts of LSA are formed from volcanoclastic rocks including reworked tuffs and conglomerate with volcanic pebbles. LSA interfingers with volcanic rocks in many places, however, the stratigraphically upper parts of the sequence penecontamperenously overlays volcanic rocks as well. This relationship between the volcanic and sedimentary rocks suggests that both VA and LSA are coeval. Therefore, LSA presents lower to middle Miocene age.

USA consists of unlithified terrigenous sediments represented by coarse sand and pebble layers which were originated from different lithologies. There is no paleontological data from the upper sedimentary association neither in this study nor in the previous studies. However, since the upper sedimentary association overlays all

units (except Quaternary units) in the area, it must be younger than middle Miocene time. USA consists of granodiorite blocks and pebbles (Figure 3.9c and d) indicating that the SP was uplifted and exhumed before the deposition of the USA.



Figure 3.9: Field photographs of volcanic and sedimentary association a) Dacite b) Sandstone of lower sedimentary association c) and d) upper sedimentary association with granodiorite blocks.

3.3 Analytical Methods

3.3.1 Geochronology

Zircon crystals were fixed on a double-side adhesive tape stuck on a thick glass plate and embedded in a 25 mm diameter epoxy mount. The crystal mounts were lapped by 2500 mesh SiC paper and polished by 9, 3 and 1 micron diamond suspensions.

For all zircon samples and standards used in this study cathodoluminescence (CL) images were obtained using a JEOL JXA 8900 electron microprobe at the Geozentrum Göttingen (Germany) in order to study their internal structure and to select homogeneous parts for the in-situ age determinations. The carbon coating used for CL imaging were later removed with a brief hand polish on a 1 micron diamond cloth. The mounts were cleaned in different steps with diluted HCl, ethanol and deionised water

in an ultrasonic bath to remove surface lead contamination before introduction into the sample cell.

The in-situ U-Pb dating was performed by laser-ablation single-collector sector-field inductively coupled plasma mass spectrometry (LA-SF-ICP-MS). The method employed for analysis is described in details by Frei and Gerdes (2009). A Thermo Finnigan Element 2 mass spectrometer coupled to a Resonetics Excimer laser ablation system was used. All age data presented here were obtained by single spot analyses with a laser beam diameter of 33 μm and a crater depth of approximately 10 μm . The laser was fired at a repetition rate of 5 Hz and at nominal laser energy output of 25%. Two laser pulses were used for pre-ablation. The carrier gas was He and Ar. Analytes of ^{238}U , ^{235}U , ^{232}Th , ^{208}Pb , ^{207}Pb , ^{206}Pb , mass 204 and ^{202}Hg were measured by the ICP-MS. The data reduction is based on the processing of ca. 100 selected time slices (corresponding ca. 10.5 seconds) starting ca. 1 sec. after the beginning of the signal. If the ablation hit zones or inclusions with highly variable actinide concentrations or isotope ratios then the integration interval was slightly resized or the analysis was discarded (~1% of the spots). The individual time slices were tested for possible outliers by an iterative Grubbs test (applied at P=5% level). This test filtered out only the extremely biased time slices, and in this way usually less than 2% of the time slices were rejected. The age calculation and quality control are based on the drift- and fractionation-correction by standard-sample bracketing using GJ-1 zircon reference material (Jackson et al., 2004). For further control the Plešovice zircon (Sláma et al., 2008), the 91500 zircon (Wiedenbeck et al., 1995) and the FC-1 zircon (Paces and Miller, 1993) were analyzed as "secondary standards". The age results of the standards were consistently within 2σ of the published ID-TIMS values. Drift- and fractionation-corrections and data reductions were performed by in-house software (UranOS; Dunkl et al., 2008). The level of Hg-corrected ^{204}Pb signal was very low, thus no common lead correction was required. The number of single-grain measurements per sample ranges between 24 and 29. The concordia plots and age spectra were constructed by the help of Isoplot/Ex 3.0 (Ludwig, 2003) and AgeDisplay (Sircombe, 2004).

For $^{40}\text{Ar}/^{39}\text{Ar}$ analysis, rock samples were submitted to the Geochronology laboratory at University of Alaska Fairbanks where it was crushed, sieved, washed and hand-picked for feldspar and biotite mineral phases. The monitor mineral MMhb-1 (Samson and Alexander, 1987) with an age of 523.5 Ma (Renne et al., 1994) was used to monitor

neutron flux (and to calculate the irradiation parameter, J). The samples and standards were wrapped in aluminum foil and loaded into aluminum cans of 2.5 cm diameter and 6 cm height. The samples were irradiated in position 8b of the uranium enriched research reactor of McMaster University in Hamilton, Ontario, Canada for 150 megawatt-hours.

Upon their return from the reactor, the sample and monitors were loaded into 2 mm diameter holes in a copper tray that was then loaded in an ultra-high vacuum extraction line. The monitors were fused, and samples heated, using a 6-watt argon-ion laser following the technique described in Layer et al. (1987) and Benowitz et al. (2014). Argon purification was achieved using a liquid nitrogen cold trap and a SAES Zr-Al getter at 400 °C. The samples were analyzed in a VG-3600 mass spectrometer at the Geophysical Institute, University of Alaska Fairbanks. The argon isotopes measured were corrected for system blank and mass discrimination, as well as calcium, potassium and chlorine interference reactions following procedures outlined in McDougall and Harrison (1999). Typical full-system 8 min laser blank values (in moles) were generally 2×10^{-16} mol ^{40}Ar , 3×10^{-18} mol ^{39}Ar , 9×10^{-18} mol ^{38}Ar and 2×10^{-18} mol ^{36}Ar , which are 10–50 times smaller than the sample/standard volume fractions. Correction factors for nucleogenic interferences during irradiation were determined from irradiated CaF_2 and K_2SO_4 as follows: $(^{39}\text{Ar}/^{37}\text{Ar}) \text{Ca} = 7.06 \times 10^{-4}$, $(^{36}\text{Ar}/^{37}\text{Ar}) \text{Ca} = 2.79 \times 10^{-4}$ and $(^{40}\text{Ar}/^{39}\text{Ar}) \text{K} = 0.0297$. Mass discrimination was monitored by running calibrated air shots. The mass discrimination during these experiments was 0.8% per mass unit. While doing our experiments, calibration measurements were made on a weekly–monthly basis to check for changes in mass discrimination. No significant variation seen during these intervals.

A summary of $^{40}\text{Ar}/^{39}\text{Ar}$ results is given in Table 1, with all ages quoted to the ± 1 sigma level and calculated using the constants of Renne et al. (2010). The integrated age is the age given by the total gas measured and is equivalent to a potassium-argon (K-Ar) age. The spectrum provides a plateau age if three or more consecutive gas fractions represent at least 50% of the total gas release and are within two standard deviations of each other (Mean Square Weighted Deviation less than 2.5).

Table 3.1: Zircon U-Pb isotopic data for the SP.

Sample	Grain	U	Pb	Th	²⁰⁶ Pb	²⁰⁷ Pb	±1s	²⁰⁷ Pb	±1s	rho	²⁰⁶ Pb	±2s	²⁰⁷ Pb	±2s	²⁰⁷ Pb	±2s	Disc. I.
		[ppm]	[ppm]	U	²³⁸ U	²³⁵ U	[%]	²⁰⁶ Pb	[%]		²³⁸ U	[Ma]	²³⁵ U	[Ma]	²⁰⁶ Pb	[Ma]	[%]
AS-211	6	713	352	0.589	0.0033692	0.022408	8.7	0.04824	8.5	0.21	21.7	0.8	22.5	3.9	110.9	201.5	3.6
	7	832	429	0.617	0.0033699	0.023213	5.7	0.04996	5.5	0.28	21.7	0.7	23.3	2.6	193.2	127.3	6.9
	8	872	539	0.729	0.0034545	0.024506	4.7	0.05145	4.3	0.38	22.2	0.8	24.6	2.3	261.1	99.8	9.6
	9	620	316	0.609	0.0033962	0.025029	6.2	0.05345	6	0.29	21.9	0.8	25.1	3.1	348	135.3	12.9
	10	609	280	0.549	0.0034321	0.024574	5.3	0.05193	5	0.31	22.1	0.7	24.7	2.6	282.4	115.5	10.4
	11	780	375	0.575	0.0033669	0.023581	6.4	0.0508	6.2	0.24	21.7	0.7	23.7	3	231.7	144.2	8.4
	12	1028	543	0.631	0.0033517	0.023255	5.3	0.05032	5	0.3	21.6	0.7	23.3	2.4	209.9	116.4	7.6
	13	791	438	0.663	0.0033044	0.024587	5.4	0.05397	5.1	0.34	21.3	0.8	24.7	2.6	369.7	114.7	13.8
	14	952	583	0.731	0.0034416	0.022855	5.5	0.04816	5.2	0.33	22.1	0.8	22.9	2.5	107.4	123.5	3.5
	20	932	512	0.656	0.0034026	0.02268	5.7	0.04834	5.6	0.21	21.9	0.5	22.8	2.6	116.2	131.4	3.8
	21	842	468	0.663	0.0033059	0.027744	5.5	0.06087	5.3	0.27	21.3	0.6	27.8	3	634.6	115	23.4
	22	863	489	0.677	0.0034247	0.026252	5.4	0.0556	5.2	0.27	22.0	0.6	26.3	2.8	436.3	115.1	16.2
	23	840	409	0.584	0.0038007	0.042144	4.9	0.08042	4.4	0.41	24.5	1	41.9	4	1207.4	87.3	41.7
	24	952	496	0.621	0.0033667	0.021931	4.5	0.04724	4.2	0.37	21.7	0.7	22	2	61.6	100.5	1.6
	25	1044	637	0.729	0.0034486	0.022967	5.1	0.0483	4.9	0.3	22.2	0.7	23.1	2.3	114.1	114.7	3.7
	26	807	468	0.692	0.0033993	0.021581	5.8	0.04604	5.5	0.32	21.9	0.8	21.7	2.5	0.1	47.3	-0.9
	27	1008	504	0.596	0.0034327	0.022662	6.4	0.04788	6.2	0.28	22.1	0.8	22.8	2.9	93.5	146.6	2.9
	28	860	464	0.644	0.0034264	0.022303	5	0.04721	4.6	0.36	22.1	0.8	22.4	2.2	59.9	109.9	1.6
	29	828	449	0.648	0.0033669	0.023586	6.6	0.05081	6.4	0.27	21.7	0.8	23.7	3.1	232.1	146.8	8.5
	35	949	537	0.675	0.0034325	0.022806	5.8	0.04819	5.6	0.3	22.1	0.8	22.9	2.6	108.6	131.4	3.5
36	741	392	0.633	0.0032785	0.024212	6.1	0.05356	5.9	0.28	21.1	0.7	24.3	2.9	352.7	133	13.1	
37	933	525	0.671	0.0033142	0.02328	4.9	0.05095	4.6	0.35	21.3	0.7	23.4	2.3	238.4	107.2	8.7	
38	755	329	0.521	0.0033186	0.022117	5.1	0.04834	4.8	0.34	21.4	0.7	22.2	2.2	115.9	112.3	3.9	
39	699	337	0.577	0.0035824	0.030089	7.1	0.06092	6.8	0.26	23.1	0.9	30.1	4.2	636.3	146.8	23.4	
40	902	544	0.718	0.0032826	0.021228	6.5	0.0469	6.2	0.29	21.1	0.8	21.3	2.8	44.2	149	0.9	

Table 3.1 (continued): Zircon U-Pb isotopic data for the SP.

Sample	Grain	U	Pb	Th	²⁰⁶ Pb	²⁰⁷ Pb	±1s	²⁰⁷ Pb	±1s	rho	²⁰⁶ Pb	±2s	²⁰⁷ Pb	±2s	²⁰⁷ Pb	±2s	Disc. I.
		[ppm]	[ppm]	U	²³⁸ U	²³⁵ U	[%]	²⁰⁶ Pb	[%]		²³⁸ U	[Ma]	²³⁵ U	[Ma]	²⁰⁶ Pb	[Ma]	[%]
AS-211	41	891	581	0.78	0.0034657	0.022448	4.6	0.04698	4.1	0.42	22.3	0.9	22.5	2	48.2	98.9	1.1
	42	842	473	0.671	0.0034682	0.029363	4.8	0.0614	4.5	0.34	22.3	0.7	29.4	2.8	653.5	96.7	24
	43	816	407	0.596	0.0033555	0.021843	6.3	0.04721	6	0.28	21.6	0.8	21.9	2.7	60	143.1	1.6
	44	987	498	0.603	0.0034361	0.022247	5.6	0.04696	5.4	0.27	22.1	0.7	22.3	2.5	47.1	129	1
AS-240	50	983	571	0.694	0.0032379	0.021645	5.5	0.04848	5.3	0.28	20.8	0.7	21.7	2.4	123	124.6	4.2
	51	834	403	0.578	0.0032417	0.0226	5.1	0.05056	4.9	0.32	20.9	0.7	22.7	2.3	221	112.7	8.1
	52	823	470	0.682	0.0033383	0.027722	5.1	0.06023	4.8	0.34	21.5	0.7	27.8	2.8	611.8	102.8	22.6
	53	1059	634	0.713	0.0033629	0.026838	4.6	0.05788	4.3	0.36	21.6	0.7	26.9	2.4	525.3	93.8	19.5
	54	673	338	0.597	0.0032506	0.024983	5.9	0.05574	5.6	0.31	20.9	0.7	25.1	2.9	442.1	124.2	16.5
	55	777	377	0.581	0.0033464	0.022301	6.8	0.04833	6.5	0.26	21.5	0.8	22.4	3	115.7	154.3	3.8
	56	743	390	0.628	0.0033076	0.021417	6.2	0.04696	6	0.28	21.3	0.7	21.5	2.7	47.3	142.9	1.1
	57	1001	558	0.666	0.0033552	0.024165	6.1	0.05223	5.8	0.29	21.6	0.8	24.2	2.9	295.7	132.1	10.9
	58	1254	783	0.746	0.0032998	0.022107	5.5	0.04859	5.1	0.33	21.2	0.8	22.2	2.4	128.1	121.2	4.3
	59	687	349	0.608	0.0042377	0.037398	5.4	0.064	4.9	0.41	27.3	1.2	37.3	3.9	741.8	103.9	26.9
	65	849	476	0.669	0.0034255	0.028448	7.1	0.06023	6.9	0.25	22.0	0.8	28.5	4	612	148.7	22.6
	66	735	324	0.529	0.0033178	0.021575	6.4	0.04716	6.1	0.31	21.4	0.9	21.7	2.8	57.5	145.1	1.5
	67	874	627	0.856	0.0033084	0.025652	4.8	0.05623	4.6	0.32	21.3	0.7	25.7	2.4	461.7	101.2	17.2
	68	975	595	0.73	0.0033683	0.023608	4.9	0.05083	4.7	0.33	21.7	0.7	23.7	2.3	233.3	107.8	8.5
	69	716	380	0.635	0.003326	0.02295	5	0.05004	4.7	0.35	21.4	0.8	23	2.3	197.1	109.3	7.1
	70	805	424	0.63	0.0033558	0.022568	5.6	0.04877	5.3	0.32	21.6	0.8	22.7	2.5	137.1	125.5	4.7
	71	798	457	0.684	0.0034412	0.023712	5.5	0.04998	5.1	0.36	22.1	0.9	23.8	2.6	194	119.5	6.9
	72	3686	7204	2.317	0.003261	0.021495	3.2	0.04781	3	0.34	21.0	0.4	21.6	1.4	89.7	71.4	2.8
	73	1017	350	0.409	0.0032545	0.023972	5.5	0.05342	5.3	0.27	20.9	0.6	24.1	2.6	346.9	120	12.9
	81	819	422	0.61	0.0033245	0.022004	4.6	0.048	4.3	0.35	21.4	0.7	22.1	2	99.5	102.6	3.2
82	856	773	1.065	0.003368	0.03127	4.4	0.06734	4	0.42	21.7	0.8	31.3	2.7	848.3	84	30.7	
83	782	450	0.681	0.0034023	0.023037	3.9	0.04911	3.6	0.42	21.9	0.7	23.1	1.8	153.1	83.5	5.3	
84	1056	709	0.795	0.0033288	0.025121	4.6	0.05473	4.4	0.25	21.4	0.5	25.2	2.3	401.4	99.6	15	

3.3.2 Mineral Chemistry

Samples were analyzed at the University of Georgia Department of Geology with JEOL 8600 electron microprobe using a 15 KV accelerating voltage and 15 nA beam current. Minerals were qualitatively identified using a Bruker 5010 Silicon Drift Detector (SDD) energy dispersive x-ray (EDS) detector controlled by a Bruker Quantax energy dispersive analysis system. Quantitative analyses were performed with wavelength dispersive spectrometers (WDS) automated with Advanced Microbeam, Inc. electronics and Probe for EPMA software, using 10 second counting times, and natural and synthetic mineral standards. Analyses were calculated using Armstrong's (1988) Phi-Rho-Z matrix correction model.

3.4 Results

3.4.1 U-Pb Zircon Chronology

U-Pb zircon dating method has been applied to two different samples from the SP (one sample from K-Feldspar megacrystalline granodiorite (AS 211) and one sample from microgranite-granodiorite (AS 240)). Zircons from the host granite are prismatic and transparent with well-developed oscillatory zoning which indicates a magmatic origin. Their aspect ratio ranges between 1:2 and 1:3.5 (Figure 3.10). Analyzed zircons present Th/U values between 0.52 and 1.06, consistent with a magmatic origin. From AS 211, twenty-nine spots were obtained and it presents a concordia age of 21.8 ± 0.2 Ma. From the other sample, AS 240, twenty-four spot analyses yielded concordia age of 21.2 ± 0.1 Ma (Figure 3.10 and Table 3.2). These two consistent ages are considered to be the emplacement age of the SP.

3.4.2 $^{40}\text{Ar}/^{39}\text{Ar}$ Biotite and Feldspar Chronology

The $^{40}\text{Ar}/^{39}\text{Ar}$ ages of the SP (three samples from KFMG, one from MGG and one from haplogranite) were obtained from biotite, K-feldspar and plagioclase separates. The ages are given in Table 3.2 and the isochron plots are shown in Figure 3.11. All the samples produced generally flat age spectrum reflective of extremely rapid post emplacement cooling.

The five biotite separates display isochron ages between 21.8 ± 0.1 Ma and 23.2 ± 0.2 Ma whereas the K-feldspar and plagioclase separates yield plateau ages of 20.3 ± 0.2

Ma and 21.6 ± 0.4 Ma, respectively. From the K-Feldspar megacrystalline granodiorite (KFMG), biotite separates display isochron ages between 21.8 ± 0.1 Ma and 23.2 ± 0.2 Ma. Microgranite-granodiorite (MGG), on the other hand, presents

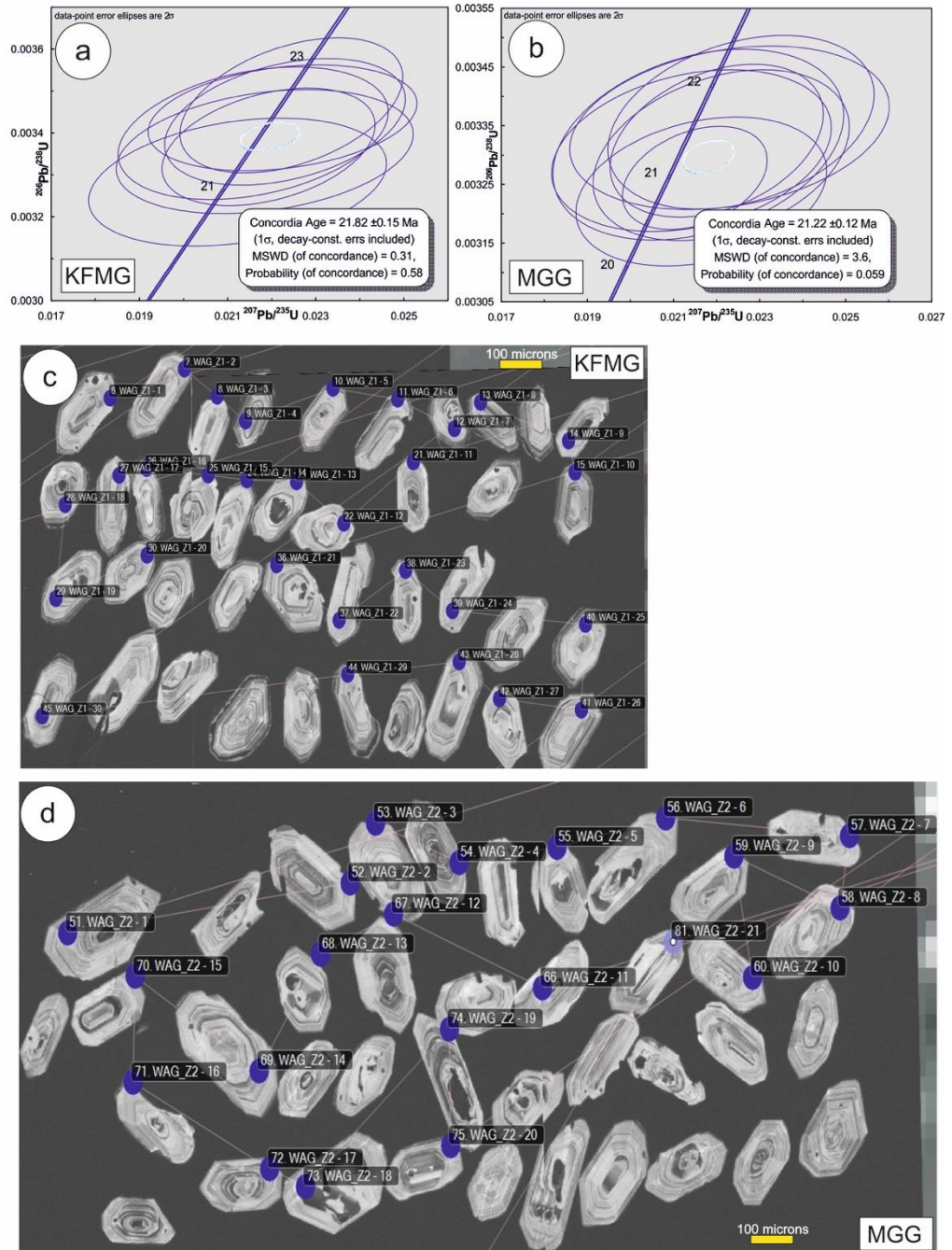


Figure 3.10: a) The $^{206}\text{Pb}/^{238}\text{U}$ vs. $^{207}\text{Pb}/^{235}\text{U}$ concordia diagram for sample AS 211 (KFMG) b) The $^{206}\text{Pb}/^{238}\text{U}$ vs. $^{207}\text{Pb}/^{235}\text{U}$ concordia diagram for sample AS 240 (MGG) c) CL images of dated zircon crystals from AS 211 (KFMG) d) CL images of dated zircon crystals from AS 240 (MGG).

22.6 ± 0.1 Ma, indicating that two main plutonic members are coeval. K-feldspar and plagioclase separates from the haplogranite displays plateau ages of 20.3 ± 0.2 Ma and 21.6 ± 0.4 Ma, respectively. This shows that, haplogranite, consistent with its field properties, is slightly younger than the main plutonic body.

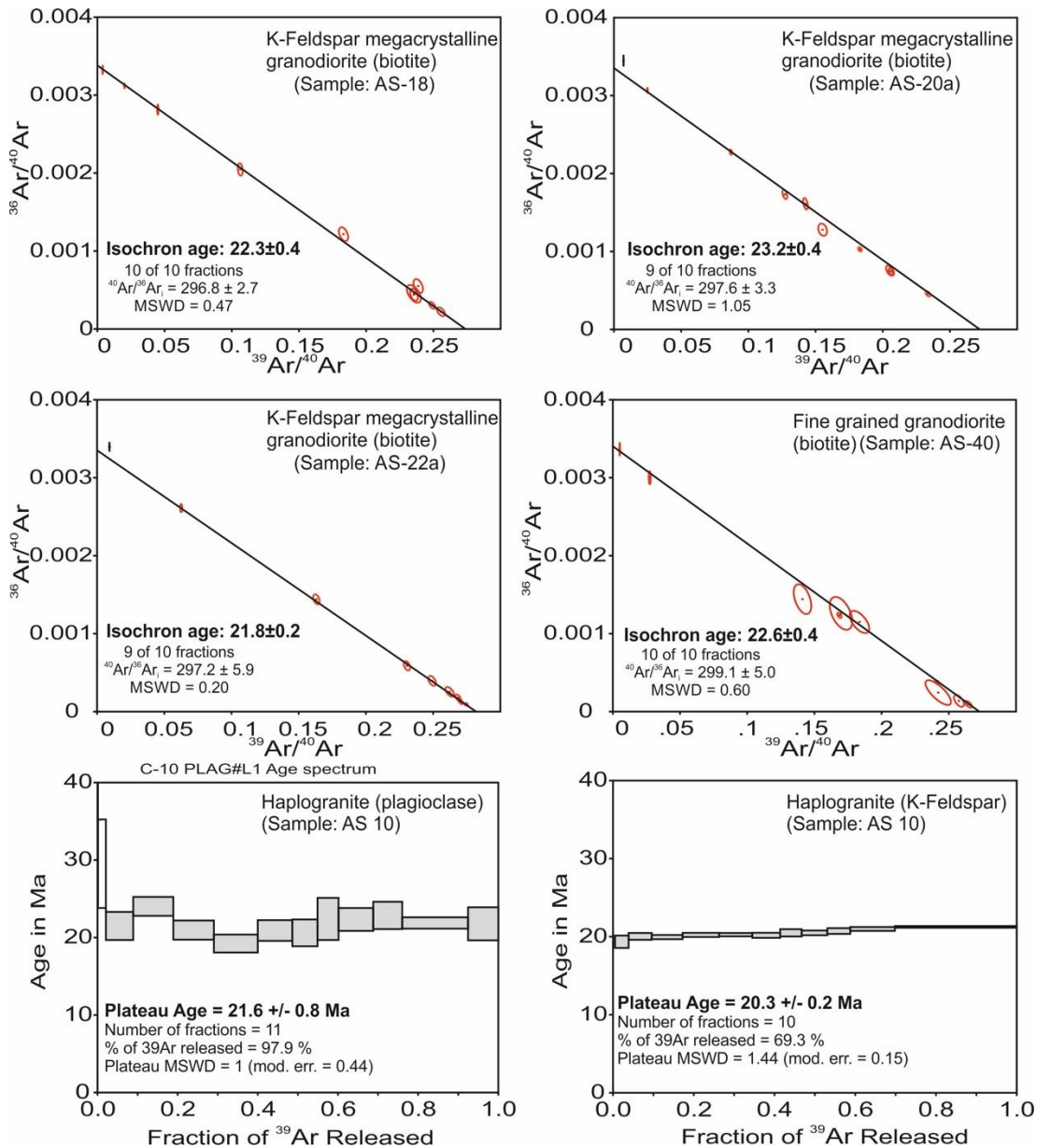


Figure 3.11: a) $^{40}\text{Ar}/^{39}\text{Ar}$ isochron and plateau ages of the SP. The sample name and group are shown on each of the diagrams. Steps in red are used in the isochron age determinations. Steps in grey are used in the plateau age determinations.

3.4.3 Geothermo-barometry Calculations: Al in hornblende geothermo-barometry

Amphibole and plagioclase crystals are widely used by several researchers for pressure and temperature conditions of crystallization (e.g. Blundy and Holland, 1990; Holland and Blundy, 1994 a,b; Anderson and Smith, 1995; Ridolfi et al., 2010; Ridolfi and

Renzulli, 2012). The first empirical thermometer was proposed by Blundy and Holland.

Table 3.2: $^{40}\text{Ar}/^{39}\text{Ar}$ biotite and feldspar data for the SP. Bi: Biotite; KF: K-feldspar; Plg: Plagioclase.

Sample	Rock Type	Mineral	Integrated Age (Ma)	Weighted Average Age (Ma)	Plateau Information	Isochron Age (Ma)	Isochron or other Information
AS 18	K-Feldspar Megacrystalline granodiorite	Bi	22.4 ± 0.3	22.4 ± 0.3	9 of 10 fractions 99.6 % ^{39}Ar release MSWD = 0.49	22.3 ± 0.4	10 of 10 fractions $^{40}\text{Ar}/^{36}\text{Ar}_i = 296.8 \pm 2.7$ MSWD = 0.47
AS 20a	K-Feldspar Megacrystalline granodiorite	Bi	22.9 ± 0.2	23.1 ± 0.2	9 of 10 fractions 99.4% ^{39}Ar release MSWD = 0.99	23.2 ± 0.4	9 of 10 fractions $^{40}\text{Ar}/^{36}\text{Ar}_i = 297.6 \pm 3.3$ MSWD = 1.05
AS 22a	K-Feldspar Megacrystalline granodiorite	Bi	21.7 ± 0.1	21.8 ± 0.1	9 of 10 fractions 99.8% ^{39}Ar release MSWD = 0.19	21.8 ± 0.2	9 of 10 fractions $^{40}\text{Ar}/^{36}\text{Ar}_i = 297.2 \pm 5.9$ MSWD = 0.20
AS 40	Microgranite-granodiorite	Bi	51.6 ± 0.3	22.7 ± 0.2	7 of 10 fractions 96.3% ^{39}Ar release MSWD = 0.67	22.6 ± 0.4	10 of 10 fractions $^{40}\text{Ar}/^{36}\text{Ar}_i = 299.1 \pm 5.0$ MSWD = 0.60
AS 24	Haplogranite	KF	20.6 ± 0.1	20.3 ± 0.4	10 of 13 fractions 69.3% ^{39}Ar release MSWD = 1.44	—	—
AS 24	Haplogranite	Plg	21.9 ± 0.5	21.6 ± 0.8	11 of 13 fractions 97.9% ^{39}Ar release MSWD = 1.00	—	—

(1990) is based on the reaction between edenite-tremolite for a temperature range between 500°C to 1100°C. Afterwards, Holland and Blundy (1994a,b) recalculated the thermometer results based on the edenite-richerite and edenite-tremolite reactions.

Both calculations are suitable for calc-alkaline igneous rocks as a result of their stability over a wide P-T range from 400° to 1150°C and from 1 kbar to 23 kbar (Blundy and Holland, 1990). Several different geobarometry calculations were proposed to determine the emplacement pressure of calc-alkaline felsic plutonic rocks on the basis of Al content in hornblende (Johnson and Rutherford, 1989; Anderson and Smith, 1995; Ridolfi et al., 2010; Ridolfi and Renzulli, 2012). These different pressure and temperature calculations for crystallization conditions are suitable and reliable for SP since it is one of the representatives of the felsic calc-alkaline plutonic bodies of western Anatolia (Ünal and Altunkaynak, 2018). In this study, we analyzed hornblende and plagioclase crystals from nine different samples (six from KFMG and three from MGG) from SP. In total, 89 spots were analyzed from hornblendes and 182 from plagioclases (Supplementary data). Four different calculations were used (Johnson and Rutherford, 1989; Ridolfi et al., 2010; Ridolfi and Renzulli, 2012) to calculate the pressure conditions of the SP. For the temperature conditions, calculations which are proposed by Holland and Blundy (1994a,b); Ridolfi et al. (2010); Ridolfi and Renzulli (2012) were used. The results of these different calculations are given in Table 3.3. The results are given both for KFMG and MGG separately for each sample. Table 3.3 shows that different calculations present different P-T conditions for the emplacement of SP. However, all of the results of different calculations are reliable based on their stability conditions (400° to 1150°C and from 1 kbar to 23 kbar) and chemical properties of the applied rocks (felsic and calc-alkaline plutonic rocks). Therefore, we present the mean results of the P-T calculations of different calculations.

The geothermo-barometry calculations present following results; the mean P and T conditions for different calculations (Johnson and Rutherford, 1989; Holland and Blundy, 1994 (a,b); Anderson and Smith, 1995; Ridolfi et al., 2010; Ridolfi and Renzulli, 2012) of KFMG are 1.65 kbar and 797°C, respectively. For MGG, on the other hand, P and T conditions are 0.69 kbar and 745°C, respectively (Table 3.3).

3.5 Discussion: Emplacement of the Solarya Pluton

The SP is coeval and cogenetic with hypabyssal and volcanic rocks (Ünal and Altunkaynak, 2018; Figure 3.12a). The plutons that are spatially and temporally related with cogenetic volcanic rocks are classified as “sub-volcanic plutons” or as

Table 3.3: Amphibole-plagioclase geothermo-barometry results for the SP.

Reference	Unit	K-Feldspar Megacrystalline Granodiorite (KFMG)						Microgranite-granodiorite (MGG)		
		AS16	AS22a	AS16a	AS81	AS9	AS13	AS120	AS115	AS113
Ridolfi et al., 2010	T (°C)	851.11	837.43	827.79	831.38	830.08	855.27	762.02	796.40	775.40
Ridolfi and Renzulli, 2012	T (°C)	786.96	739.89	792.12	807.86	799.36	803.23	719.88	631.07	685.38
Holand and Blundy, 1994a	T (°C)	819.08	776.30	808.98	818.21	834.84	844.09	758.64	800.07	804.12
Holand and Blundy, 1994b	T (°C)	768.62	716.18	737.29	698.94	772.03	777.16	736.75	723.21	751.25
Average	T (°C)	797.26						745.35		
Ridolfi et al., 2010	P (kbar)	1.37	1.24	1.14	1.15	1.33	1.55	0.70	0.53	0.52
Ridolfi and Renzulli, 2012	P(kbar)	1.28	1.03	1.20	1.29	1.40	1.50	0.68	0.42	0.48
Anderson and Smith, 1995	P(kbar)	1.92	1.80	1.90	1.95	1.86	1.99	1.10	1.68	0.72
Johnson and Rutherford, 1989	P (kbar)	2.30	2.00	1.67	1.77	2.20	2.67	0.78	0.39	0.14
Average	P (kbar)	1.65						0.69		
Ridolfi et al., 2010	Depth (km)	5.06	4.58	4.21	4.25	4.91	5.72	2.58	1.97	1.92
Ridolfi and Renzulli, 2012	Depth (km)	4.74	3.82	4.43	4.76	5.16	5.54	2.53	1.55	1.77
Anderson and Smith, 1995	Depth (km)	7.10	6.88	7.03	7.21	6.88	7.36	4.07	6.22	2.16
Johnson and Rutherford, 1989	Depth (km)	8.52	7.39	6.19	6.56	8.12	9.88	2.87	1.14	0.52
Average	Depth (km)	6.1						2.44		

“caldera type plutons (Pitcher, 1979; Seager and McCurry, 1988). Therefore, the SP could be classified as “sub-volcanic plutons” or “caldera type plutons” which was emplaced into shallow levels in the crust. However, field relations, petrography and geothermo-barometry studies propose that different members of the SP (KFMG, MGG and haplogranite) were emplaced into different levels of crust through different mechanisms.

KFMG developed a contact metamorphic aureole around it. Contact metamorphism conditions reached to pyroxene-hornfels facies which is commonly observed at the deeper levels of epizone conditions (2 kb/600-750°C; Musumeci and Vaselli, 2012). The geothermo-barometry calculations reveal that KFMG (the northern part) represents the deeper parts of the pluton and was emplaced around 6-7 km depth (av. 1.65 kbar, 6.1 km depth).

The southern part of the SP is formed from MGG with a distinct fine grained microgranular texture. The contact of MGG and basement rocks are represented by “roof pendant” structure which are generally defined for shallower level intrusions (Figure 3.12b). In this contact country rocks are flat and the foliation planes are horizontal. Moreover, the interfingering of MGG with the hypabyssal rocks is also a clear indicator for shallow level emplacement (Figure 3.12a). This result is also supported by the geothermo-barometer results. Calculated P-T conditions suggest that, MGG was emplaced into the shallower levels with relatively lower pressure conditions (0.69 kbar; 2.4 km). The haplogranite, which is located between KFMG and basement rocks, display graphic/granophyric texture which suggest a shallow, 1.5 km (0.5 kb), emplacement depths (Figure 3.12c). Therefore, all these evidences indicate that the KFMG, MGG and haplogranite were emplaced into different depths (between 7 to 1.5 km) of the crust through different emplacement mechanisms.

The emplacement stages of the SP can be summarized into two distinct events; 1) emplacement at the deeper levels of the crust with high temperature (Figure 3.13a), 2) emplacement into shallower levels with relatively lower temperatures (Figure 3.13c). The evidences for these stages are summarized as follows;

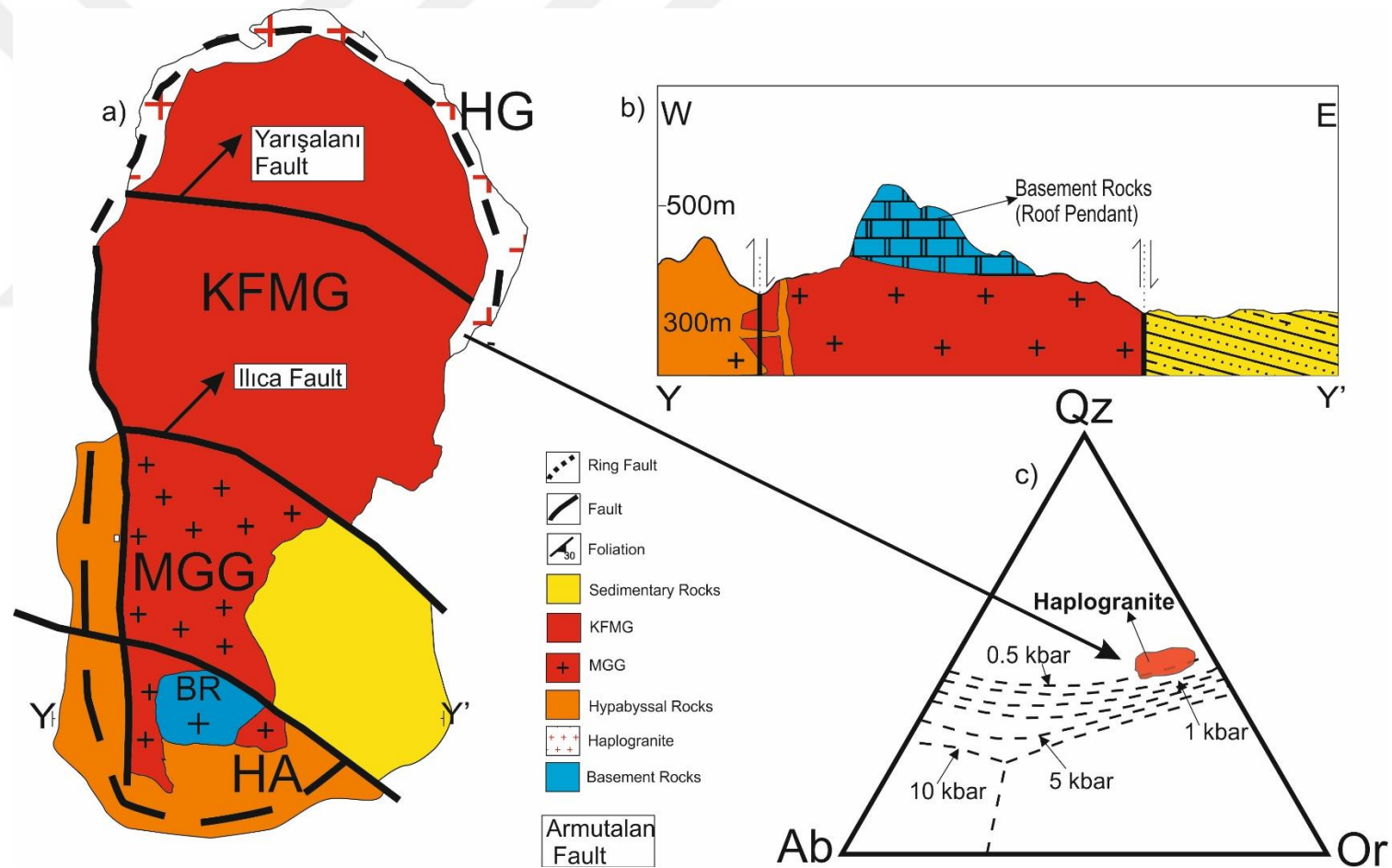


Figure 3.12: a) Ring fractures/faults developed due to the emplacement of the SP. Haplogranite and hypabyssal association were emplaced into the ring faults, which are shown by dashed lines. b) W-E cross section along the southern contact of the SP (horizontally not to scale, the cross-section directions are shown in Figure 12a). c) Qz-Ab-Or triangle illustrating the pressure conditions of haplogranites (Tuttle and Bowen, 1958).

The emplacement of the SP caused several structural and compositional effects on the country rocks through the eastern and northern contacts. Along the contacts between SP and calc-schists, contact metamorphic rocks are made up of contact schists with the elongation of contact metamorphic minerals such as diopside and wollastonite over a secondary foliation plane (S-2) with a shear sense pointing outwards the contacts of the pluton. Development of contact schists with these types of structural properties are commonly attributed to the forceful emplacement of the plutonic bodies (Sardinha et al., 2006; Stevenson, 2009; Festa et al., 2013). Moreover, the foliation planes of the wall rocks progressively swing towards to the pluton boundary. At these boundaries the positions of the wall contacts are steeply dipping outwards the pluton contacts. Stevenson et al. (2007) proposed that, steeply dipping contacts are due to the upward directed forces from a forceful emplacement (Figure 3.13a). After this stage, even if the KFMG was emplaced and consolidated, the pluton is not completely fulfilled its emplacement and there is still magma left (Read, 1957) evidenced by the overlapping emplacement age of MGG with the intrusion of hypabyssal rocks and accumulation of a thick volcanic sequence. This is shown by the radiometric age results of plutonic, hypabyssal and volcanic rocks which are coeval (Ünal and Altunkaynak, 2019). The spatial and temporal connection of plutonic (MGG and KFMG), hypabyssal and volcanic rocks may suggest that the whole magmatic complex has passed through a caldera collapse environment and therefore the static elevation of MGG could be provided by cauldron subsidence mechanism evidenced by as follows.

The forceful emplacement of the SP into the brittle zone of the crust causes to the development of ring and radial fractures in the country rocks around the main plutonic body (Figure 3.13b). Hypabyssal rocks (sheet intrusives) were emplaced into these fractures almost coevally with the pluton. Not only the sheet intrusive rocks, but also the main plutonic body (MGG) was elevated into the shallower levels with the aid of these fractures and faults. The MGG which represents the roof of the plutonic body as a shallower part of the SP is located at the southern part of the main body. Topographically, this southern part is represented by shallower elevations. Under normal circumstances, the shallower parts are expected to be located at the topographically upper parts of the pluton. However, the MGG is well preserved even at the lower elevations which may have been emplaced with the block subsidence along ring fractures/faults. Indeed, the current topography of the region may have been

shaped by erosion and young structural features but these types of topographical patterns are commonly defined as a possible evidence for granite emplacement by cauldron subsidence mechanism similar to Pearly Gates Pluton (Myers et al., 2008), Mount Lister Pluton (Myers et al., 2008) and Kozak Pluton (Altunkaynak and Yılmaz, 1998). The subsidence of blocks resulted in a decompression of the volume which must have been filled with MGG magma. In the latter stages, these faults were re-activated and formed the topographical difference between KFMG and MGG. The subsidence was not only occurred along the ring faults through the central part of the SP but also developed along the contacts of the SP with country rocks. The existence of arch-shaped outcrops of sheet intrusives (cone sheets) which surround and dip outwards the pluton indicate that magma was probably elevated to shallower levels in the crust with the aid of ring fractures. Through these fractures, haplogranites were emplaced (Figure 3.13c). The emplacement of the haplogranite must have occurred at shallower levels as evidenced by graphic/granophyric textures (Tuttle and Bowen, 1955). Therefore, the successive development of cauldron subsidence mechanism after the forceful emplacement could provide the permissive emplacement of the pluton to the sub-volcanic levels in the crust as a result of the sinking of a large country rock block facilitated by fractures or faults into a magma chamber which is replaced by magma from the same chamber (Figure 3.13c). Cauldron subsidence is fundamentally the subterranean or plutonic version of caldera collapse (Clough et al., 1909; Richey, 1932; Anderson, 1936; Hills, 1963; Hall, 1996; Cole et al., 2005). Richey (1928) proposed a model for the emplacement of the remaining magma into the space created by the block subsidence. This model suggests that the emplacement of new magma occurs through repetitive stages. We adapted this model to the SP with combining our field, structural, geothermo-barometry and geochronology data (Figure 3.14). The model proposes that, the upwelling of new magma initiated with the emplacement of microgranite-granodiorite (MGG) which is geochemically and isotopically identical to KFMG (Ünal and Altunkaynak, 2018, 2019). This is followed by the emplacement of the sheet intrusives. The haplogranites were emplaced into the ring faults/fractures at the final stage. The model proposes that these magmas gradually pass into each other which is consistent with our field observations. This sequence of the new magma emplacement is also evidenced by the $^{40}\text{Ar}/^{39}\text{Ar}$ dating of the MGG, hypabyssal rocks and haplogranites.

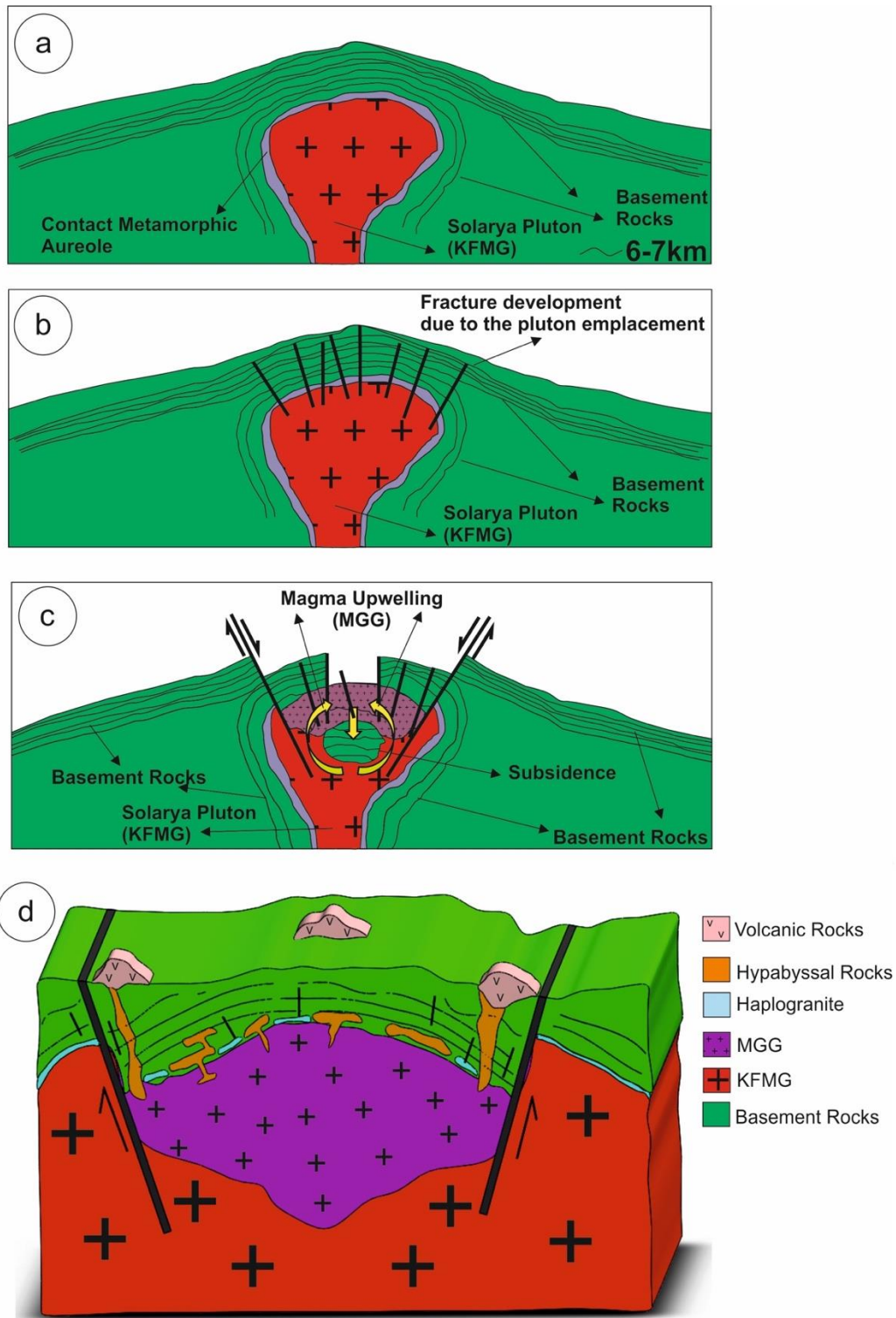


Figure 3.13: Schematic cross-sections illustrating the consecutive emplacement stages of the SP. a) The forceful emplacement of the SP b) Fracture development due to the pluton emplacement c) Passive emplacement (cauldron subsidence) stage of the SP d) Block diagram showing the final position of the SP.

The MGG presents a 22.8 Ma $^{40}\text{Ar}/^{39}\text{Ar}$ age and hypabyssal rocks display $^{40}\text{Ar}/^{39}\text{Ar}$ age of 22.5 Ma (Ünal and Altunkaynak, 2019). Haplogranites, on the other hand, yielded a $^{40}\text{Ar}/^{39}\text{Ar}$ age of 20.6 Ma, representing the youngest member of the SP.

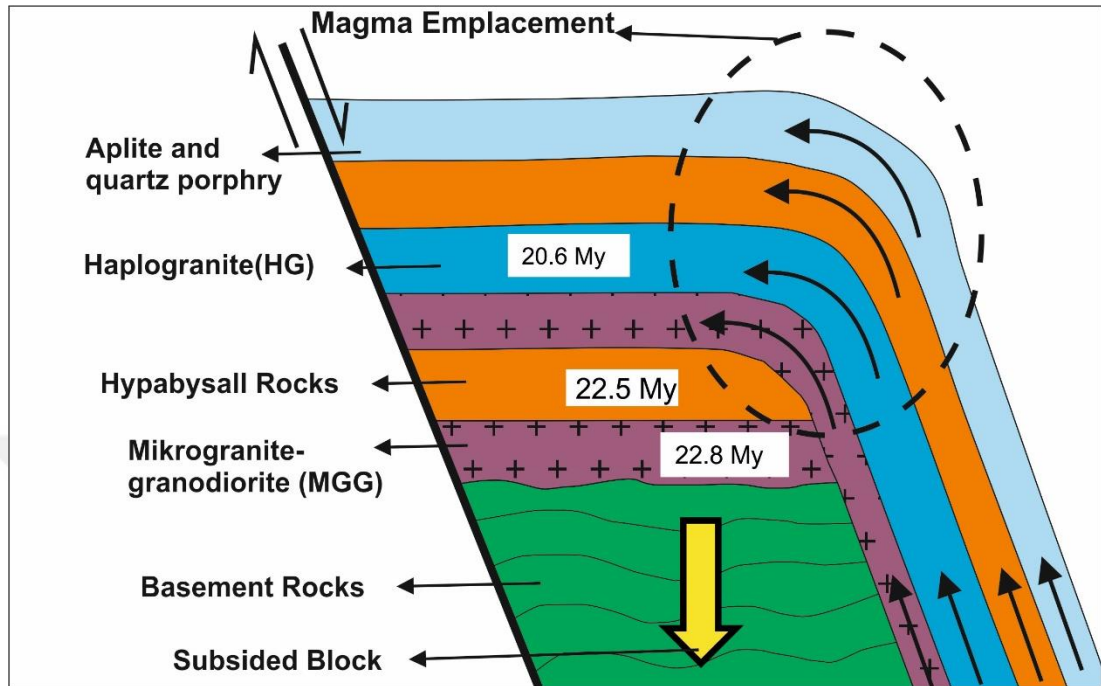


Figure 3.14: Schematic diagram of the upwelling magma in cauldron subsidence (adapted from Richey, 1928).

There is almost a total consensus that the early Miocene magmatic rocks along northwestern Anatolia formed under an extensional tectonic regime (or syn-convergent extension; (Altunkaynak and Dilek, 2006; Boztuğ et al., 2009; Dilek et al., 2009; Erkül, 2009; Öner et al., 2010; Altunkaynak et al., 2012a; Ünal and Altunkaynak, 2018). The geology and petrogenesis of the SP, as presented in detail by Altunkaynak et al. (2012a), Ünal and Altunkaynak (2018) and Ünal and Altunkaynak (2019) indicate clearly that the pluton was emplaced during the period when the region was suffering N-S extension. The subsequent forceful to passive (cauldron subsidence) emplacement and shallow nature of the SP also support this result. Cauldron subsidence mechanism (and passive emplacement) developed extensively under extensional regime exemplified by many plutonic and volcano-plutonic complexes such as Rosses Granitic Complex, Ireland (Stevenson, 2009), Wiborg and Åland Granites, Finland (Karell et al., 2014) and Štiavnica Volcano-plutonic Complex, Western Carpathians (Tomek et al., 2014).

3.6 Conclusions

- The SP consists of three main plutonic members showing different textural properties; a northern part of the plutonic body is represented by K-feldspar megacrystalline granodiorite (KFMG) with distinct porphyritic texture and southern part is made up of microgranite-granodiorite (MGG) displaying microgranular texture whereas haplogranite, which displays graphic/granophyric textures, is represented by a thin aureole between the SP and basement rocks.
- The $^{40}\text{Ar}/^{39}\text{Ar}$ biotite ages for KFMG yield between 21.8 ± 0.1 Ma and 23.2 ± 0.2 Ma. For MGG, $^{40}\text{Ar}/^{39}\text{Ar}$ biotite age is 22.6 ± 0.1 Ma, indicating that two main plutonic members are coeval. K-feldspar and plagioclase separates from the haplogranite display plateau ages of 20.3 ± 0.2 Ma and 21.6 ± 0.4 Ma, respectively.
- The U-Pb zircon ages obtained from KFMG and MGG are 21.8 ± 0.2 and 21.2 ± 0.1 Ma, respectively.
- KFMG have 1.65 kbar pressure and 797°C temperature emplacement conditions. For MGG, on the other hand, P and T conditions are 0.69 kbar and 745°C , respectively.
- The SP were emplaced into different levels of crust with different mechanisms. The SP began its emplacement forcefully in relatively deeper levels in the crust (6.1 km depth). After this stage, MGG was emplaced into the shallow levels (2.4 km depth) via cauldron subsidence and in the late stage the sheet intrusive rocks were emplaced into the ring faults at 1.5 km depth.
- The forceful to passive emplacement of the SP occurred under Aegean extensional tectonics during the Miocene.

4. INTERPLAY BETWEEN VOLCANIC AND PLUTONIC SYSTEMS: A CASE STUDY OF THE EARLY MIOCENE SOLARYA VOLCANO-PLUTONIC COMPLEX IN NW ANATOLIA (TURKEY)

4.1 Introduction

Linking volcanic and plutonic systems and examining them together is critical to evaluate magma chamber processes and mantle-crust interactions on a lithospheric scale. The relationship between volcanic and plutonic rock bodies provides an integrated opportunity to study the evolution of post-collisional magmatic terranes. Plutonic, hypabyssal and volcanic rocks that are related in space and time are defined as volcano-plutonic complexes (Read, 1948). Volcano-plutonic complexes are known to occur within the extensional tectonic systems worldwide (Bickford and Boardman, 1984; Kuepouo et al., 2006; Rioux et al., 2016; Takahashi, 1986; Yan et al., 2018). Western Anatolia, located in the Aegean Extensional System, is one of the best natural laboratories in the world to examine the nature and evolution of post-collisional magmatic rocks and to investigate the link among plutonic, hypabyssal and volcanic environments. Straddling between major core complexes in NW Anatolia, numerous associations of plutonic, hypabyssal and volcanic systems forming volcano-plutonic complexes were developed during Late Oligocene-Early Miocene (Figure 4.1). There are various number of studies on the plutonic and volcanic rocks of NW Anatolia (Altunkaynak, 2007; Altunkaynak and Dilek, 2006; Altunkaynak and Yılmaz, 1998; Altunkaynak et al., 2012a; Altunkaynak et al., 2012b; Aslan et al., 2017; Bingöl et al., 1982; Boztuğ et al., 2009; Çelebi and Köprübaşı, 2014; Delaloye and Ercan et al., 1995; Erkül et al., 2005; Erkül, 2012; Ersoy et al., 2017; Genç, 1998; Genç and Yılmaz, 1997; Harris et al., 1994; Kamacı

This chapter is based on the paper; Alp Ünal, Şafak Altunkaynak, (2019). "Interplay between volcanic and plutonic systems: A case study of the early Miocene Solarya Volcano-plutonic Complex in NW Anatolia (Turkey)." *Journal of Asian Earth Sciences*, 179, 319-336.

et al., 2017; Kamacı and Altunkaynak, 2019; Karacık et al., 2008; Karacık and Yılmaz, 1998; Topuz and Okay, 2017; Yılmaz, 1989; Yücel-Öztürk, 2016) however, studies specifically focusing on the link between volcanic and plutonic systems in order to evaluate their petrochemical evolution on the lithospheric scale are substantially limited (Altunkaynak, 2007; Altunkaynak and Yılmaz, 1998; Erkül, 2012; Genç, 1998; Karacık and Yılmaz, 1998). The Solarya Volcano-plutonic Complex (SVPC) is one of the best examples of the volcano-plutonic complexes located in NW Anatolia. There are a number of detailed accounts on the Solarya (Ilıca-Şamlı) pluton and volcanic rocks (Altunkaynak et al., 2012a; Aslan et al., 2017; Boztuğ et al., 2009; Bürküt, 1966; Çelebi and Köprübaşı, 2014; Karacık et al., 2008; Yılmaz et al., 2014, Ünal and Altunkaynak, 2018). None of the previous studies reveal these magmatic rocks as a volcano-plutonic complex or caldera complex and evaluated plutonic, hypabyssal and volcanic rocks together. Furthermore, there is no study presenting integrated isotope and age results as well as detailed field and petrographic data from volcanic and hypabyssal rocks of SVPC.

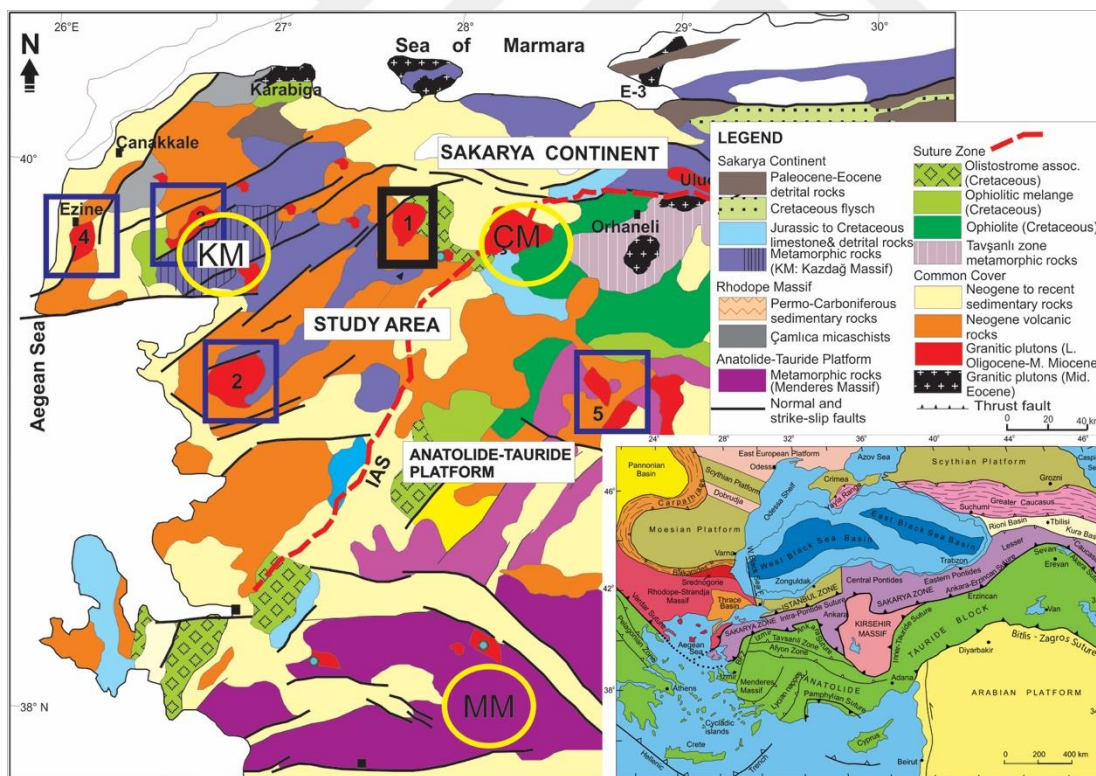


Figure 4.1: Simplified geological map of the NW Anatolia (Modified from Okay and Tüysüz, 1999; Okay and Satır, 2006; Yılmaz et al., 2000). Black rectangle shows Solarya Volcano-plutonic Complex (SVPC) (1), blue rectangles show Kozak (2), Bayramiç (3), Kestanbol (4) and Alaçamdağ (5) volcano-plutonic complexes. Yellow circles exhibit the major core complexes in NW Anatolia (KM: Kazdağ, MM: Menderes, ÇM: Çataldağ).

In order to provide better constrains for the evolution of the SVPC on a lithospheric scale, we have investigated the field and petrographic properties of the SVPC, as well as obtaining new major-trace element, Sr-Nd-Pb-O isotope and $^{40}\text{Ar}/^{39}\text{Ar}$ age results of the volcanic rocks. In our earlier work (Ünal and Altunkaynak, 2018), we have documented the petrogenesis and origin of the high Ba-Sr nature of Solarya Plutonic Association (SPA). In this study, we evaluate our new data together with our previously published data obtained from SPA to document the interplay between volcanic and plutonic systems which leads to a thorough evaluation of magma chamber processes and mantle-crust interactions beneath NW Anatolian crust and broader Aegean Extensional Province.

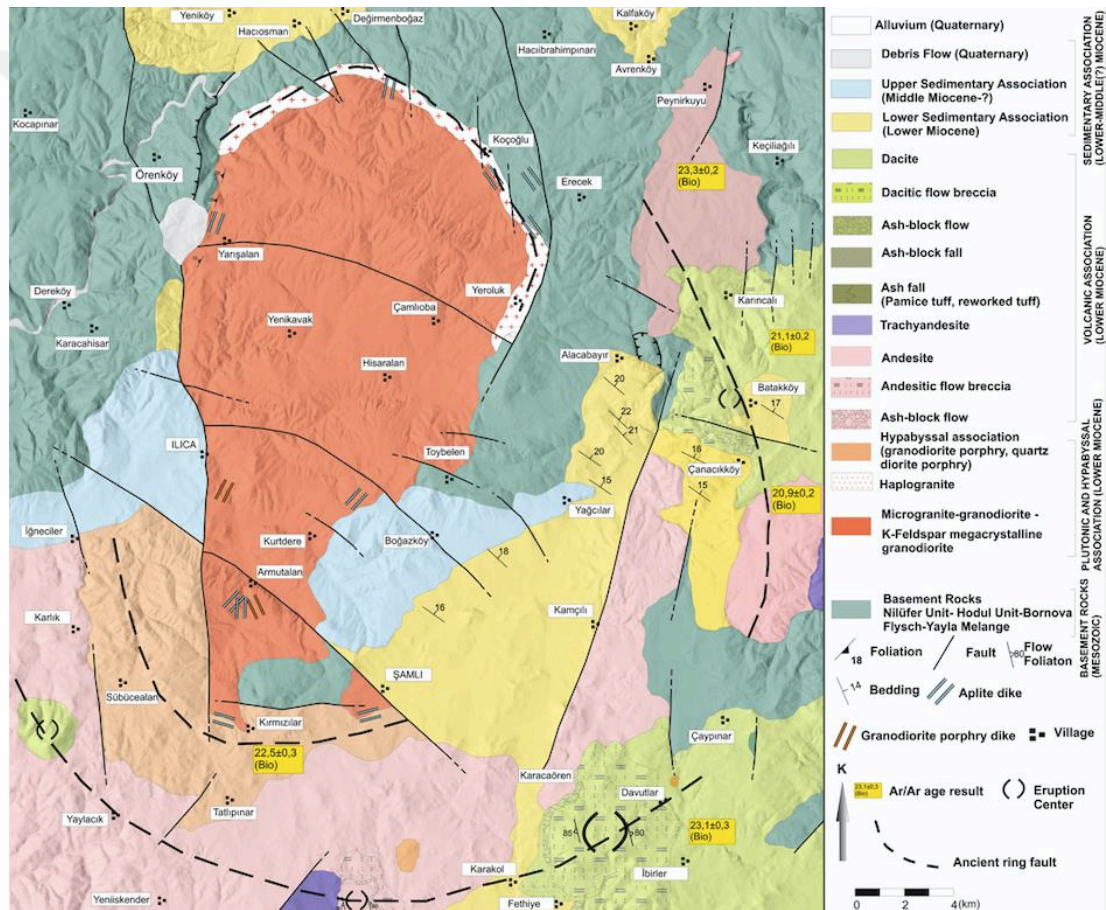


Figure 4.2: Geological Map of the area (modified after Ünal and Altunkaynak, 2018).

4.2 Stratigraphy

The geological map and the generalized stratigraphic section of study area are shown in Figure 4.2 and Figure 4.3. There are five different rock groups in the area: (1) Basement rocks (metamorphic and non-metamorphic), (2) Solarya Plutonic

Association (SPA), (3) Hypabyssal Association (HA), (4) Volcanic Association (VA) and (5) Sedimentary Association (SA).

Basement rocks in the study area are represented by metamorphic (Nilüfer Unit-Karakaya Complex; Okay et al., 1990) and non-metamorphic (Hodul Unit) rocks of Sakarya Continent (Ünal and Altunkaynak, 2018). Nilüfer unit is represented by metabasites, metapelites and marbles (Okay et al., 1990). Metapelites are formed from quartz-mica schists, phyllites and calc-schists whereas metabasites are represented by metalavas and metatuffs.

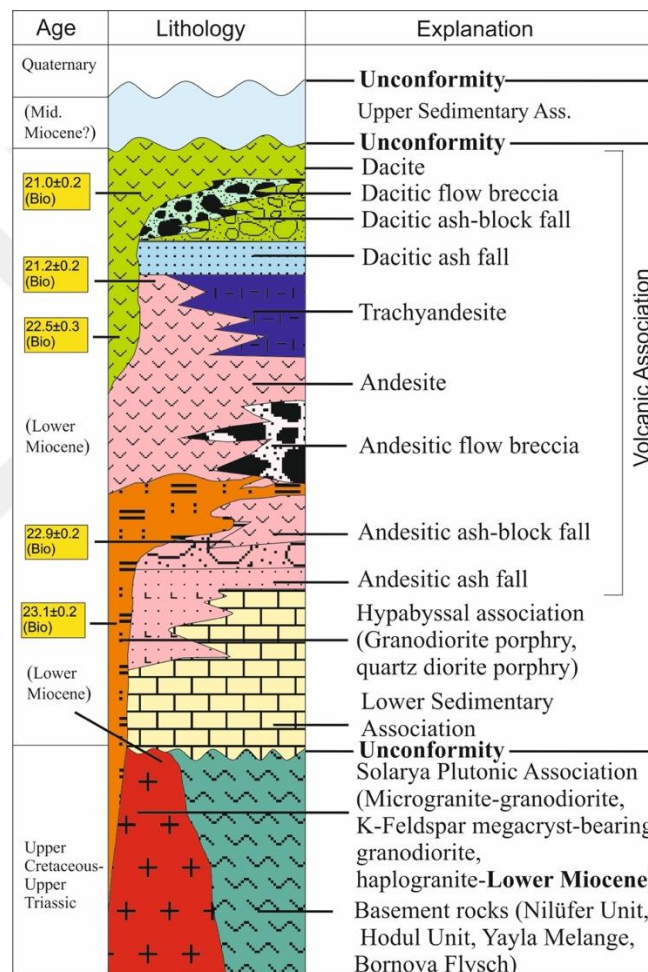


Figure 4.3: Generalized stratigraphical column of the study area (not to scale, modified after Ünal and Altunkaynak, 2018).

SPA is located at the center of the study area and is divided into three coeval granitic members: (a) K-feldspar megacrystalline granodiorite (Figure 4.4a), (b) microgranite-granodiorite (Figure 4.4b), and (c) haplogranite. The Solarya pluton includes a number of magmatic enclaves and mafic dikes within the main plutonic body (For detailed field properties of the plutonic rocks, please see Ünal and Altunkaynak, 2018). The

northern part of the Solarya pluton is composed from porphyritic granodiorite defined by K-feldspar megacrysts whereas the southern portion is defined by microgranodiorite.

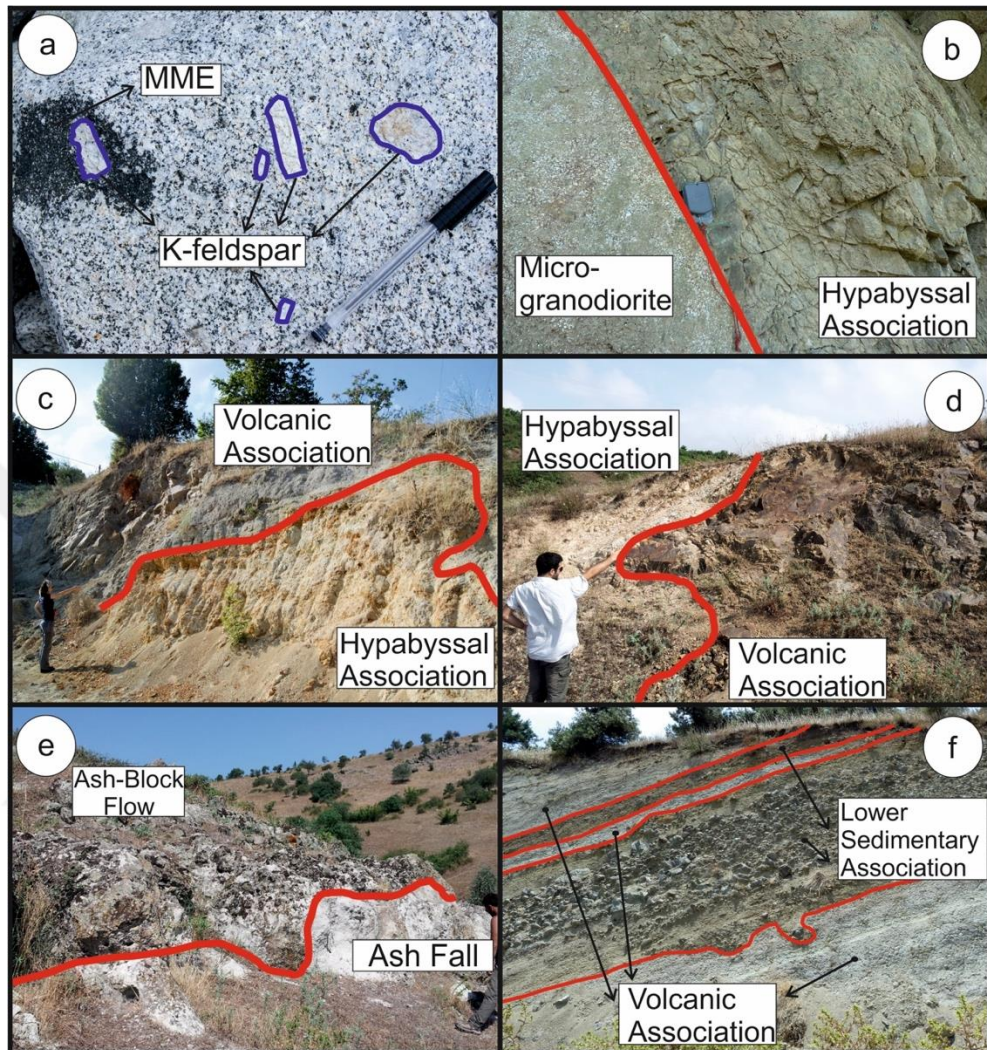


Figure 4.4: Field photographs from the SVPC (a) Porphyritic texture of K-feldspar megacrystalline granodiorite developed with K-feldspar megacrysts. Also, mafic microgranular enclave is shown in the figure. (b) Intrusive contact between Hypabyssal Association (HA) and microgranodiorite. (c) Intrusive contact between HA and volcanic association (VA). (d) Contact between HA and VA showing the interfingering relationship. (e) Contact between ash-block flow and ash fall deposits. (f) The interfingering of VA and Lower Sedimentary Association (LSA). Figure also illustrates the pebbles of LSA from different lithologies.

The southern margin of the Solarya Pluton is bounded by a hypabyssal association. Hypabyssal rocks cut and pass into Solarya pluton, as well as dikes belonging to the plutonic association cut hypabyssal rocks. This contact relationship between hypabyssal and plutonic rocks indicate their synplutonic emplacement (Figure 4.4b).

Hypabyssal rocks are characterized by granodiorite/quartz-diorite porphyry sheet intrusive rocks presenting similar petrographic properties to plutonic rocks in the area. Through the southern margin, granodiorite/quartz-diorite porphyry rocks interfinger with the volcanic rocks. Hypabyssal and volcanic rocks cut one another (Figure 4.4c and 4.d), and fragments of hypabyssal rocks are found in volcanic rocks.

VA outcrops at the southern and eastern part of the Solarya Pluton and covers an area of approximately 240 km². Rock types in VA are distinguished in three main groups; (1) Andesite lavas and associated pyroclastic rocks, (2) Dacite lavas and related pyroclastic rocks, and (3) trachyandesite lavas. Pyroclastic rocks are represented by flow breccias, pyroclastic fall and flow units.

Andesite lavas are purple to pinkish in color and they represent the most abundant volcanic rock type in the study area. They are confined to a main strato-volcano and the main eruption center for andesite lavaş is located at the southern part of the İbirler village which is defined by flow breccias with large andesite blocks along the walls of the eruption center. Moreover, the dip directions of the flow foliations in andesite lavas point outwards from the eruption center with the dip angle of 80–85°. Through the lower parts of the sequence, andesite lavas and andesitic flow breccias give way to the ash-block flow units with andesite blocks/pebbles in an ash matrix and ash fall units with clear beddings represented by the dip angles of 5–10°.

Dacites are represented by both domes and lava flows. Dacite domes are generally formed from circular competent and high hills with glassy and chilled margins. Dacite lava flows, which are mostly located at the eastern part of the study area, interfinger with dacitic flow breccias and overlay the pyroclastic units represented by ash-block flow, ash-block and ash fall units. Dacitic flow breccias are defined by angular dacitic blocks/pebbles with 5–15 cm size in a matrix formed from dacitic lavas. Ash-block flow units, which originated from dacitic lava blocks with sizes up to 2 m, are easily distinguished from flow breccias with their ash matrix. Dacitic pyroclastic fall units display clear beddings with dip angles of 5–10°. They are generally represented by lithic tuffs and reworked tuffs.

Trachyandesite lavas are represented by aphanitic textures with black to dark pinkish colors. Trachyandesite lavas overlay andesitic lavas and pyroclastic units and, they also cut some andesitic units as dikes in some places.

A sedimentary association crops out at the southeastern and southwestern part of the area and it can be divided into two different groups; (1) Lower Sedimentary Association and (2) Upper Sedimentary Association.

The sequence of the Lower Sedimentary Association begins with a coarse-grained base conglomerate with pebbles of plutonic and basement rocks. The upper parts of the conglomerate are represented by coarse-grained sandstones with almost horizontal beddings. A thick sequence of shale and mudstone with thin bedding layers overlays the sandstones through the northern part of the study area. Shale and mudstones are interbedded with thin lignite layers. The uppermost parts of the Lower Sedimentary Association are formed from volcanoclastic rocks including reworked tuffs (tuffaceous sediments) and conglomerate with volcanic pebbles. The Lower Sedimentary Association interfingers with volcanic rocks in many places. This relationship between volcanic and sedimentary rocks suggests that these rocks are coeval. Therefore, Lower Sedimentary Association presents lower Miocene age.

The Upper Sedimentary Association consists of unlithified coastal sediments defined by coarse sand and pebble layers which originated from different lithologies. It discontinuously overlays all of the other lithologies in the study area except the alluvial sediments.

4.3 Petrography

The mineral compositions and textural properties of the SVPC are summarized in Table 4.1. Two different granitic members of Solarya Pluton (K-feldspar megacrystalline granodiorite (Figure 4.5a) and microgranodiorite (Figure 4.5b) display holocrystalline porphyritic and holocrystalline microgranular textures respectively. Both of the rock groups have evidence for disequilibrium textures like sieve and honeycomb textures with oscillatory zoning of plagioclase crystals. Haplogranites, on the other hand, in addition to their compositional difference (see Table 4.1) are easily distinguished with their graphic/granophyric textures. As shown in Table 3.1, HA have similar mineral compositions to granodiorites but they present holocrystalline, microcrystalline-microgranular porphyritic texture (Figure 4.5c; for detailed petrographical features of plutonic and hypabyssal association, see Ünal and Altunkaynak, 2018).

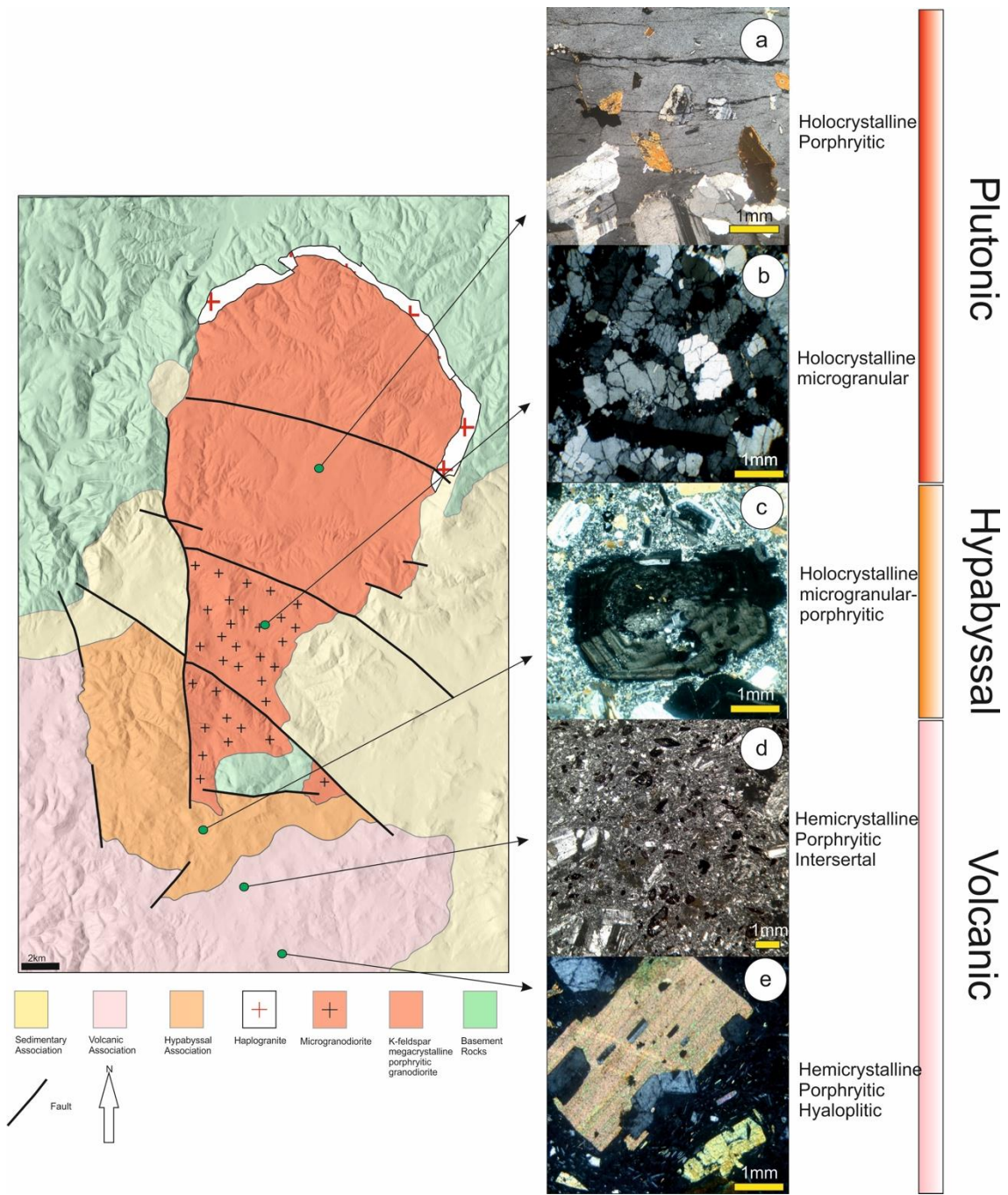


Figure 4.5: The textural properties of the different members of SVPC.

Table 4.1: Petrographical Features of Solarya Volcano-plutonic Complex.

Rock Group	K-Feldspar megacrystalline granodiorite (KFMG)	Microgranite-granodiorite (MGG)	Haplogranite	MME	Mafic Dike (Microgabbroic diorite- diorite porphyry)	Hypabyssal association (HA)	Trachyandesite
Composition	45-55% plagioclase (oligoclase-andesine), 20-25% quartz, 20-25% K-feldspar, 12-20% biotite and hornblende	42-52% plagioclase (oligoclase-andesine), 25-27% quartz, 23-28% K-feldspar, 10-18% hornblende and biotite	50-55% K-feldspar (orthoclase-perthite), 40-45% quartz, 5-10% plagioclase (oligoclase), % 1-3 biotite	40-50% plagioclase, 30-35% hornblende, 15-20% K-feldspar, 5-10% clinopyroxene, 2-5% biotite, >5% quartz	60-65% plagioclase, 15-20% hornblende, 5-8% biotite, 5-10% quartz, 1-5% sanidine	50-55% plagioclase (andesine-labradorite), 10-22% quartz, 5-10% K-feldspar, 10-15% hornblende, 5-10% biotite, 2-4% opaque minerals	50-60% plagioclase, 5-10% hornblende, 10% biotite, 10-15% clinopyroxene (augite), 3-5% sanidine, 1-2% quartz
Textural Features	Holocrystalline, porphyritic	Holocrystalline, granular-microgranular	Holocrystalline, granular-microgranular, graphic/granophyric	Holocrystalline, microgranular	Holocrystalline, microcrystalline, cryptocrystalline porphyritic	Holocrystalline, microcrystalline-microgranular porphyritic	Hemicrystalline, porphyritic

Table 4.1 (Continued): Petrographical Features of Solarya Volcano-plutonic Complex.

Rock Group	Andesite	Dacite	Volcanic enclave
Composition	65-85% plagioclase (andesine), 5-15% biotite, 5-10% hornblende, 3-5% quartz	60-80% plagioclase, 5-10% biotite, 10-15% hornblende, 5-8% sanidine, 10-15% quartz	65-70% plagioclase, 15-20% hornblende, 5-10% biotite, 3-5% sanidine
Textural Features	Hemicrystalline, porphyritic	Hemicrystalline, porphyritic	Holocrystalline, microgranular-porphyritic

The plutonic body itself presents holocrystalline textures with porphyritic and microgranular textures (Figure 4.5a and b). Towards the southern parts of the plutonic body, the grain size decreases. HA display distinct microcrystalline-microgranular porphyritic texture as a typical sub-volcanic texture (Figure 4.5c). HA pass into VA with hemicrystalline porphyritic texture (Figure 4.5d and e).

Andesites and dacites of the SVPC display similar porphyritic and hypocrystalline textures. The major phenocryst phases for trachyandesites are plagioclase (An₃₅₋₅₅) + amphibole + biotite + clinopyroxene ± sanidine ± quartz ± opaque minerals whereas phenocryst phases of andesites consist of plagioclase (An₃₅₋₅₀) + amphibole + biotite ± quartz ± opaque minerals. Dacites contain plagioclase (An₃₅₋₅₅) + quartz + amphibole + biotite + sanidine ± opaque minerals as major phenocryst phases (Figure 4.6a). Few plagioclase phenocrysts contain partially resorbed cores, forming honeycomb or sieve textures (Figure 4.6b). Biotite is the most abundant mafic phenocryst of andesite and dacite samples. They are generally represented by hipidiomorphic crystals up to 3 mm in length. They contain plagioclase and opaque mineral inclusions. Hornblende is the second most abundant mafic mineral in both andesites and dacites. They are generally idiomorphic, and, in a few samples, they display simple twinning. Quartz crystals are represented by xenomorphic crystals which commonly display reaction patterns and embayed textures.

In trachyandesite lavas, particularly hornblende phenocrysts display different textural and compositional characteristics than other samples. They are represented by basaltic hornblende phenocrysts which display red- brown pleochroism. In a few samples, biotite crystals are mantled by hornblendes which present similar basaltic composition to those of the phenocrysts (Figure 4.6c and d). Moreover, few hornblende phenocrysts display transformation to clinopyroxene through the rims of the crystals (Figure 4.6e and f). According to Streck (2008), these reverse reactions could be explained by disequilibrium of hornblende crystals with the magma during its rise. The temperature should have increased in the magma either with the input of hot magma into the chamber or the reaction of the magma with the atmospheric oxygen during its rise (Streck, 2008). Pyroxene phenocrysts in trachyandesites are generally represented by augite crystals according to their extinction angles (42–45°). In a few samples, they form cumulophyric textures with hornblendes.

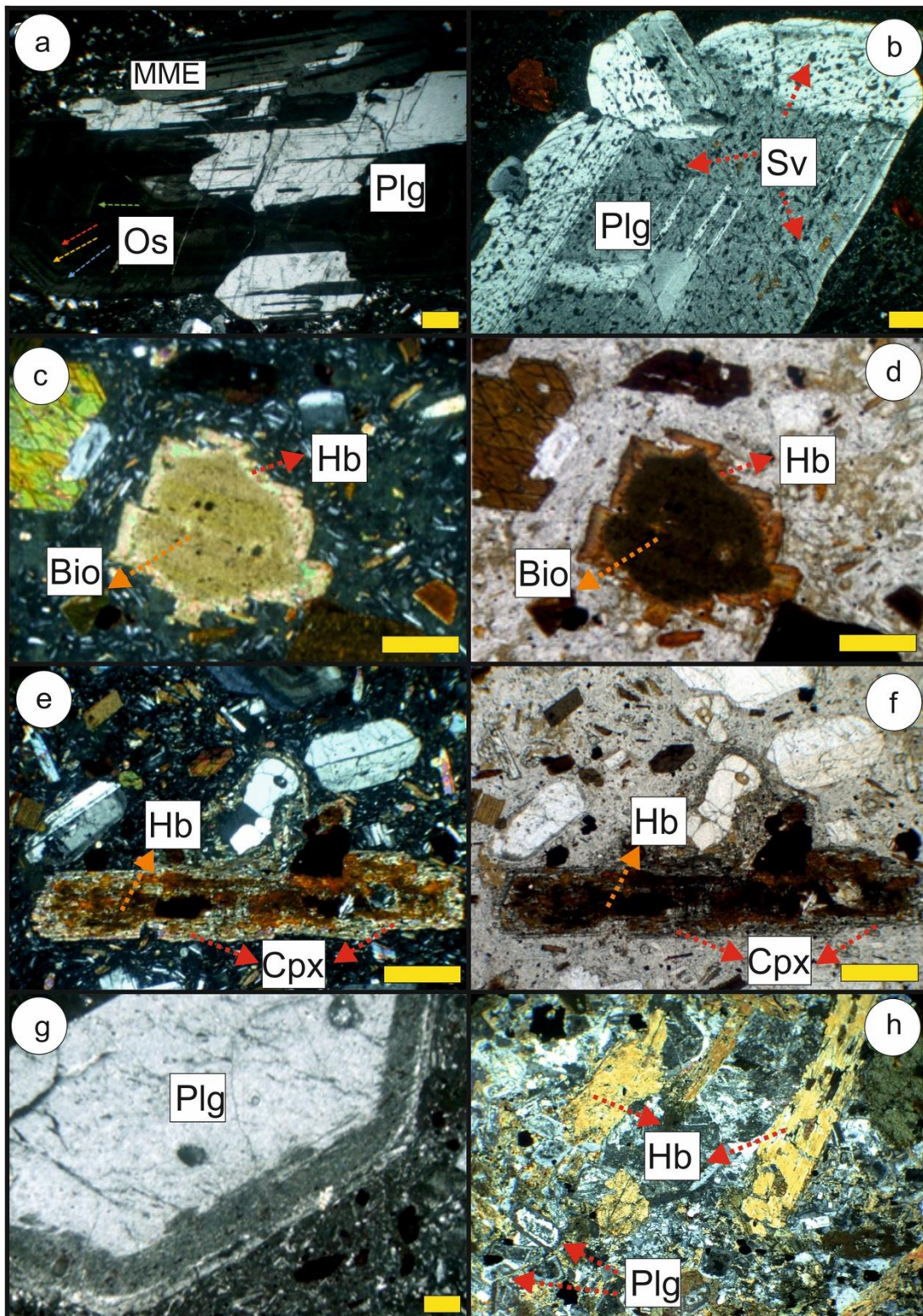


Figure 4.6: Micrographs illustrating the main petrographical features of VA of SVPC (a) Oscillatory zoning (Os) of plagioclase (Plg) in andesite lava, XPL. (b) Sieve texture (Sv) in a single plagioclase crystal (Plg) in dacite lava, XPL. (c, d) Biotite crystal (Bio) in trachyandesite mantled by hornblende (Hb) c: XPL, d: PPL. (e, f) Hornblende crystal (Hb) in trachyandesite mantled by pyroxene (Prx) e: XPL, f: PPL. (g) Corroded plagioclase in dacite lava (XPL) h) Holocrystalline microgranular- porphyritic texture of volcanic enclave (XPL). XPL: Crossed polarised light, PPL: Plane polarised light, scale is 1 mm.

Andesites and dacites show similar characteristics for their mineral properties. Plagioclase constitutes the main phenocryst phase with apparent albite, albite-Carlsbad or complex twinning. They also display normal, patchy or oscillatory zoning (Figure 4.6a, b and g). Samples from the different groups of VA present textural relations, such as corrosion, oscillatory zoning and sieve textures in plagioclase (Figure 4.6a, b and g), existence of hornblende phenocrysts with clinopyroxene reaction rims (Figure 4.6e and f), which suggest that the major population of the phenocrysts are in disequilibrium with their host liquid. These types of textures may be considered as evidence for magma mixing processes (Wyllie, 1962; Hatch and Leventhal, 1992; Hibbard, 1991; Streck, 2008).

In few locations, enclaves are found in the andesite lavas. These volcanic enclaves present microgranular/porphyritic holocrystalline texture and plagioclase (An_{30–55}) + amphibole + biotite ± sanidine mineral assemblage (Figure 4.6h). These textural and compositional characteristics suggest that volcanic enclaves in andesites can be defined as microdiorite porphyry. The mineral characteristics of these enclaves are similar to those of volcanic samples in the area suggesting that these enclaves are represented by the enclaves of the vents feeding the andesite extrusions.

4.4 Analytical Methods

4.4.1 Geochronology

For $^{40}\text{Ar}/^{39}\text{Ar}$ analysis, rock samples were submitted to the Geochronology laboratory at University of Alaska Fairbanks. The monitor mineral MMhb-1 (Samson and Alexander, 1987) with an age of 523.5 Ma (Renne et al., 1994) was used to monitor neutron flux (and calculate the irradiation parameter, J). The samples and standards were wrapped in aluminum foil and loaded into aluminum cans of 2.5 cm diameter and 6 cm height. The samples were irradiated in position 8b of the uranium enriched research reactor of McMaster University in Hamilton, Ontario, Canada for 150 megawatt-hours.

Upon their return from the reactor, the sample and monitors were loaded into 2 mm diameter holes in a copper tray that was then loaded in an ultra-high vacuum extraction line. The monitors were fused, and samples heated, using a 6-W argon-ion laser following the technique described in Layer et al. (1987) and Layer (2000). Argon purification was achieved using a liquid nitrogen cold trap and a SAES Zr-Al getter at

400C. The samples were analyzed in a VG-3600 mass spectrometer at the Geophysical Institute, University of Alaska Fairbanks. The argon isotopes measured were corrected for system blank and mass discrimination, as well as calcium, potassium and chlorine interference reactions following procedures outlined in McDougall and Harrison (1999). Typical full-system 8 min laser blank values (in moles) were generally 2×10^{-16} mol ^{40}Ar , 3×10^{-18} mol ^{39}Ar , 9×10^{-18} mol ^{38}Ar and 2×10^{-18} mol ^{36}Ar , which are 10–50 times smaller than the sample/standard volume fractions. Correction factors for nucleogenic interferences during irradiation were determined from irradiated CaF_2 and K_2SO_4 as follows: $(^{39}\text{Ar}/^{37}\text{Ar}) \text{Ca} = 7.06 \times 10^{-4}$, $(^{36}\text{Ar}/^{37}\text{Ar}) \text{Ca} = 2.79 \times 10^{-4}$ and $(^{40}\text{Ar}/^{39}\text{Ar}) \text{K} = 0.0297$. Mass discrimination was monitored by running calibrated air shots. The mass discrimination during these experiments was 0.8% per mass unit. All ages quoted to the ± 1 sigma level and calculated using the constants of Renne et al. (2010). The integrated age is the age given by the total gas measured and is equivalent to a potassium-argon (K-Ar) age. The spectrum provides a plateau age if three or more consecutive gas fractions represent at least 50% of the total gas release and are within two standard deviations of each other (Mean Square Weighted Deviation less than 2.5).

4.4.2 Geochemistry

The whole-rock powders were split from 1 to 5 kg of crushed rocks. The chemical compositions of samples were determined by using a Spectro Ciros Vision inductively coupled plasma (ICP) emission spectrometer for major oxides, Ba and Sc (0.200-g pulp sample by LiBO_2 fusion) and Cu, Zn, and Ni (0.50-g sample leached with 3 mL 2–2–2 HCl-HNO₃- H₂O at 95 °C for 1 h, diluted to 10 mL), and by using a Perkin Elmer Elan 6100 ICP mass spectrometer for the other elements at the ACME Analytical Laboratories, Vancouver. See Altunkaynak (2007) for detailed explanation.

All O isotope ratios were measured at the University of Cape Town using a Finnigan Delta XP mass spectrometer in dual-inlet mode on either CO₂ (conventional) or O₂ (laser) gas. All data are reported in δ notation where $\delta^{18}\text{O} = (\text{R}_{\text{sample}}/\text{R}_{\text{standard}} - 1) \times 1000$, and R= the measured $^{18}\text{O}/^{16}\text{O}$ ratio. For the whole-rock data, duplicate splits of the quartz standard (NBS28) were run with each batch of eight samples and were used to convert the raw data to the SMOW scale using the $\delta^{18}\text{O}$ value of 9.64‰ for NBS28 recommended by Coplen et al. (1983). The long-term variability of NBS-28 suggests

a 2σ error of 0.16‰. For the laser analyses, two splits of our internal standard MON GT (5.38‰, Harris and Vogeli, 2010) were analyzed with each batch of 10 samples. The long-term average difference in $\delta^{18}\text{O}$ values of duplicates of MON GT is 0.13‰, which corresponds to a 2σ value of 0.16‰ ($n=125$). San Carlos olivine grains were also analyzed during the course of this work and gave an average $\delta^{18}\text{O}$ value of 5.33‰ ($\pm 0.32\%$, $2\sigma, n=9$) which is comparable to the $\delta^{18}\text{O}$ values of 5.35‰ reported by Eiler et al. (2011).

Table 4.2: Interpretive details for $^{40}\text{Ar}/^{39}\text{Ar}$ results of Solarya Volcano-plutonic Complex.

Sample	Lithology	Mineral	Integrated age (Ma)	Weighted average age (Ma)	Isochron age (Ma)
AS-2	Andesite	Biotite	23.2 ± 0.2	23.1 ± 0.2	22.9 ± 0.2
AS-8	Andesite	Biotite	20.9 ± 0.2	21.2 ± 0.2	21.2 ± 0.2
AS-67	Granodiorite porphyry	Biotite	22.5 ± 0.3	22.8 ± 0.3	23.1 ± 0.2
AS-79	Dacite	Biotite	23.1 ± 0.3	22.7 ± 0.3	22.5 ± 0.3
AS-103	Dacite	Biotite	21.1 ± 0.2	21.2 ± 0.2	21.0 ± 0.2

For Sr-Nd-Pb isotopic analysis, thermal ionization mass spectrometry (TIMS) was applied at the Saskatchewan Isotope Laboratory, Dept. of Geological Sciences at the University of Saskatchewan, Canada. Strontium-isotope ratios are quoted relative to a value of 0.710250 for the NIST SRM 987 standard. The 1 σ analytical uncertainty for the sample analyses is 0.005%. For analyses via TIMS, instrument mass fractionation was corrected using NIST SRM 981 (+0.13 AMU-1), yielding average ratios of $^{206}\text{Pb}/^{204}\text{Pb} = 16.891 \pm 0.01$, $^{207}\text{Pb}/^{204}\text{Pb} = 15.430 \pm 0.013$, and $^{208}\text{Pb}/^{204}\text{Pb} =$

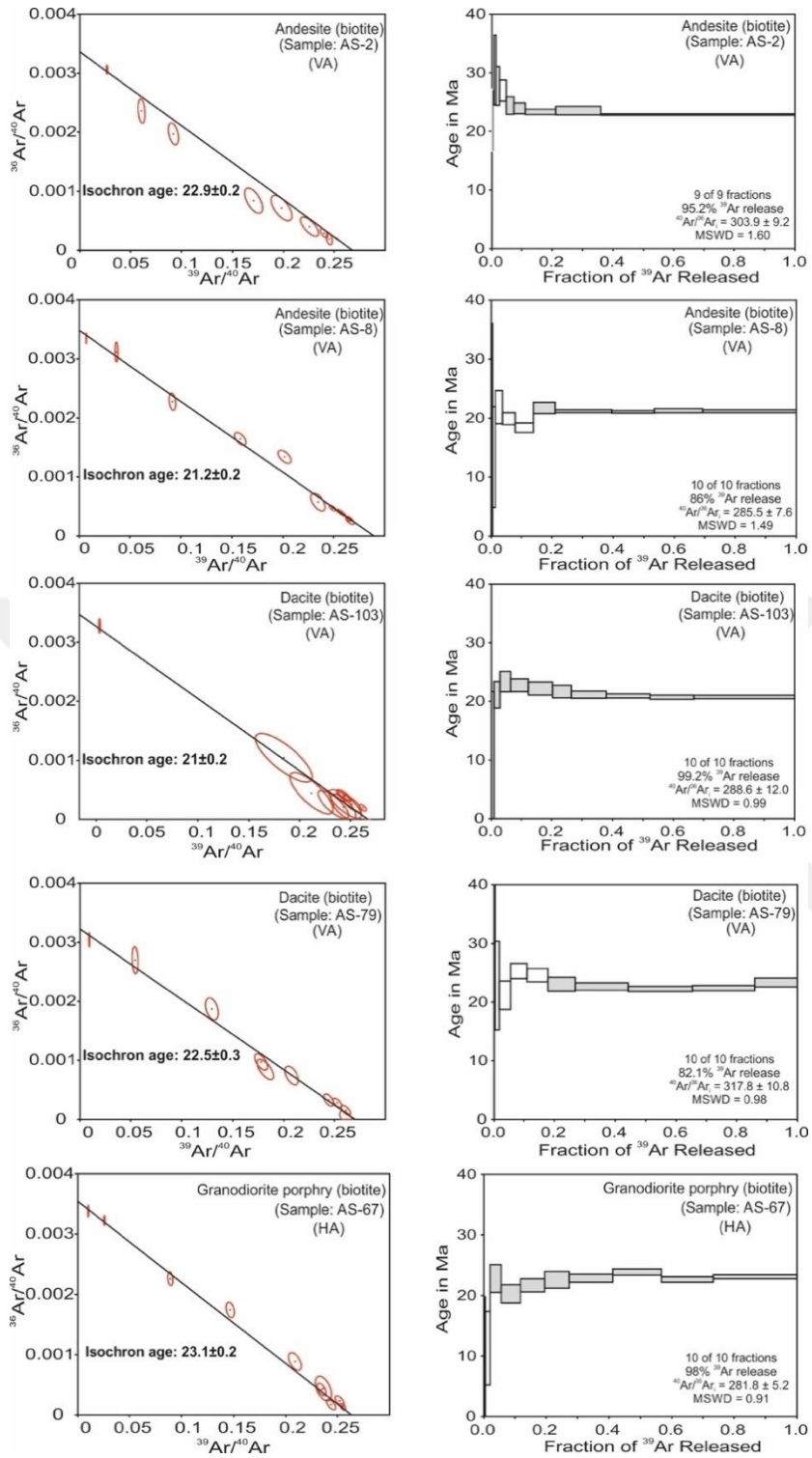


Figure 4.7: $^{36}\text{Ar}/^{40}\text{Ar}$ versus $^{39}\text{Ar}/^{40}\text{Ar}$ ratios and age spectra diagrams for volcanic and hypabyssal associations of SVPC. Figure also shows the isochron ages and the ^{39}Ar release ratio of the samples.

36.505 ± 0.042 (2r). For analyses via MC-ICP-MS, samples were Tl-doped to facilitate corrections for instrumental mass bias based on an exponential dependence on mass law. Corrections were based on values obtained for several aliquots of Tl-doped NIST 982 solution run during the same sample sequence. Analytical uncertainties for repeat analyses of standards are better than 0.01% (2r), but a conservative estimate of 0.05% (2r) has been used for sample analyses based on replicates with varying contents of Pb, and hence differences in beam intensity. Error correlation between ^{207}Pb and ^{206}Pb and between ^{208}Pb and ^{206}Pb were calculated from repeat analyses of NIST 982 and NIST 981.

Whole rock major and trace element data, and Sr-Nd-Pb-O isotopic data are presented in Table 4.3. We used the GCDkit software produced by Janousek et al. (2006) to generate the geochemical diagrams.

4.5 Results

4.5.1 Geochronology

Five biotite separates from five representative samples were submitted to the University of Alaska Fairbanks Geochronology facility for $^{40}\text{Ar}/^{39}\text{Ar}$ dating analysis. Each of the 5 samples produced integrated ages that were within error of both the plateau and isochron age determinations for each individual sample (Figure 4.7). The first few heating steps of each sample's run had large individual errors due to high atmospheric content and hence were not used for plateau age determinations. These steps were generally used for the isochron age determination. We prefer the isochron age determinations for these samples because they included a larger percentage of the gas release and take into account the initial ^{40}Ar component.

The $^{40}\text{Ar}/^{39}\text{Ar}$ ages of volcanic and hypabyssal association obtained from biotite separates are shown in Table 4.2. For volcanic samples, two andesite and two dacite samples were dated. One of the andesite sample (AS-2) yielded 22.9 ± 0.2 Ma isochron age from 5 of 9 fractions with 95.2% ^{39}Ar release. The other andesite sample (AS-8) resulted in 21.2 ± 0.2 Ma isochron age with 86.0% ^{39}Ar release from 5 of 10 fractions. Dacite samples (AS-79 and AS-103), on the other hand, yielded isochron ages of 22.5 ± 0.3 and 21.0 ± 0.2 , respectively. AS-79 displays 82.1% ^{39}Ar release from 5 of 10 fractions. AS-103 presented 99.2% ^{39}Ar release from 9 of 10 fractions. One sample

from hypabyssal association (AS-67) yielded isochron ages of 23.1 ± 0.2 Ma with 98.0% ^{39}Ar release from 8 of 10 fractions. The $^{40}\text{Ar}/^{39}\text{Ar}$ age results of volcanic and hypabyssal rocks indicate that all of the samples have similar age span.

4.5.2 Geochemistry

The major and trace element data and isotopic results for the SPA and HA were presented in Ünal and Altunkaynak (2018). To compare the geochemical properties of the rocks of SVPC which are related to each other in space and time, we will evaluate geochemical and isotopic data all together. In this contribution, we have performed thirteen major and trace elements, ten Sr-Nd-Pb isotopic analysis of the representative samples from VA. Also, four whole rock and two quartzfeldspar ^{18}O isotope compositions have also been measured. The analyzed rocks present low LOI (lost on ignition) values between 1.5 and 2.9 wt%. which indicate the lack of alteration, consistent with our petrographic observations.

4.5.2.1 Major and trace element geochemistry

The SiO_2 contents of VA vary between 54.82 and 73.54 wt% indicating that the volcanic rocks are intermediate-acidic compositions. On the $\text{Na}_2\text{O} + \text{K}_2\text{O}$ versus SiO_2 diagram (Le Bas et al., 1986), VA plots on trachyandesites, andesites and dacites (Figure 4.8a). To test these results, SiO_2 versus Zr/TiO_2 diagram of Winchester and Floyd (1977) has been prepared (Figure 4.8b). In this diagram, similar to Le Bas et al., 1986 (Figure 4.8a), samples cluster on the trachyandesite, andesite and dacite fields.

On the K_2O versus SiO_2 classification diagram (Pecerillo and Taylor, 1976), trachyandesites are classified as shoshonitic, while other volcanic rocks are high-K calc-alkaline in character (Figure 4.9a). VA display calc-alkaline trend from trachyandesite to dacite in AFM diagram (Irvine and Baragar, 1971; Figure 4.9b). These characteristics are consistent with plutonic and hypabyssal rocks as well.

In Harker variation diagrams, all different lithologies of VA present negative correlation between TiO_2 , MgO , CaO , and FeO versus increasing SiO_2 (Figure 4.10). The most mafic member of the volcanic rocks is represented by trachyandesites and volcanic enclaves whereas most evolved members are dacites. Andesites present linear trends between these end members. In Figure 4.10, the trends of plutonic and hypabyssal rocks are presented. All rocks of SVPC display similar patterns in Harker

diagrams indicating their common magma source. They also have similar major element variations with other early Miocene volcanic rocks of northwestern Anatolia (Aldanmaz et al., 2006; Altunkaynak and Genç, 2008).

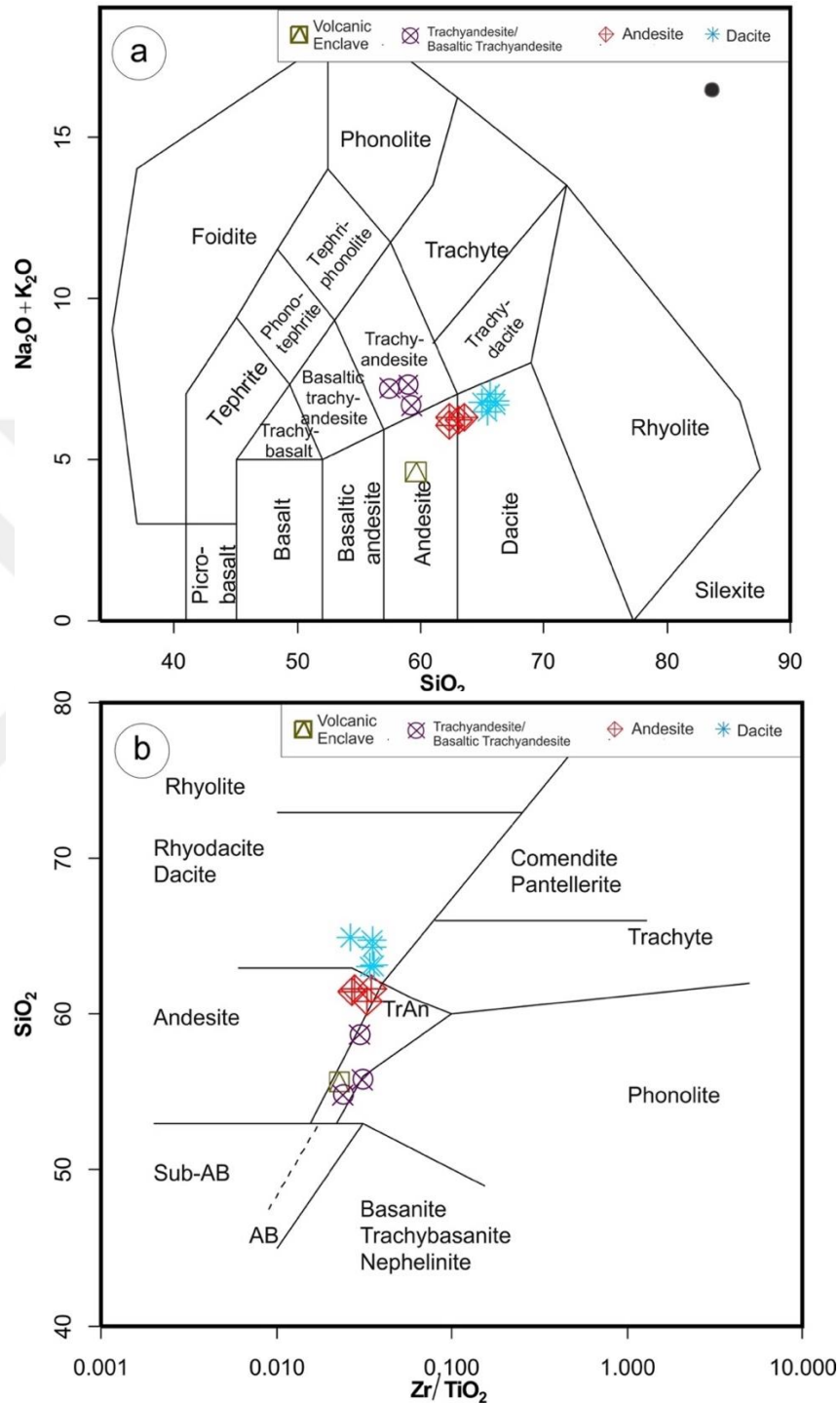


Figure 4.8: a) Total alkali versus SiO₂ classification diagram (Middlemost, 1994).
 (b) SiO₂ versus Zr/TiO₂ classification diagram (Winchester and Floyd, 1977).

Table 4.3: Major-trace and isotopic compositions of the volcanic association of Solarya Volcano-plutonic Complex

Sample no.	AS-2	AS-5	AS-8	AS 79	AS 90	AS 103	AS 153	AS 155	AS 222	AS 223	AS 226	AS 227	AS229
SiO₂	60.82	64.36	61.63	64.74	64.92	63.13	55.81	63.06	61.48	55.69	58.68	54.82	61.62
Al₂O₃	16.32	15.36	16.27	16.56	15.99	15.77	14.60	16.22	16.79	15.33	15.99	15.12	16.49
Fe₂O₃	5.48	4.46	5.33	4.12	4.89	4.80	7.67	4.88	5.58	7.83	6.22	5.84	5.25
MgO	2.65	2.23	2.47	1.42	1.15	2.36	4.15	1.50	2.54	4.69	3.76	3.37	2.09
CaO	5.40	3.87	5.10	3.84	3.73	3.75	5.95	3.71	5.14	4.66	6.41	6.33	4.67
Na₂O	3.08	3.40	3.24	3.63	2.99	2.95	2.74	3.10	3.41	2.46	3.04	2.89	3.19
K₂O	2.83	3.46	2.84	2.93	3.71	3.62	4.25	3.12	2.79	1.83	4.23	3.27	2.92
TiO₂	0.60	0.56	0.53	0.44	0.56	0.47	1.09	0.48	0.58	0.62	0.81	0.57	0.56
P₂O₅	0.30	0.25	0.20	0.17	0.22	0.19	0.62	0.19	0.20	0.19	0.29	0.17	0.17
MnO	0.10	0.09	0.08	0.09	0.05	0.09	0.21	0.10	0.10	0.14	0.10	0.14	0.07
Cr₂O₃	0.01	0.01	0.01	<0.002	0.00	0.00	0.04	<0.002	0.00	0.01	0.01	0.01	0.00
LOI	2.50	1.60	2.10	1.80	1.50	2.60	2.40	2.90	2.70	2.10	2.70	2.30	2.90
Total	99.60	99.70	99.70	99.80	99.70	99.70	99.50	99.80	99.67	99.65	99.65	99.65	99.90
Cs	7.70	3.70	5.00	2.30	2.20	4.90	4.70	3.40	2.70	9.00	5.60	16.70	2.80
Rb	123.10	131.30	77.70	102.60	101.50	134.00	166.70	101.30	101.10	61.20	78.50	98.80	95.10
Ba	1459.00	1211.00	1377.00	1025.00	1053.00	1213.00	1915.00	1085.00	1347.00	1111.00	1155.00	811.00	1251.00
Sr	596.70	563.10	628.50	382.70	462.90	549.70	835.50	412.10	524.90	447.60	585.30	419.50	515.60
Pb	4.40	6.20	25.80	4.60	8.40	8.40	13.20	3.60	101.10	61.20	78.50	98.80	95.10
Th	25.60	30.10	34.10	15.70	15.90	28.10	29.30	17.90	16.60	15.60	17.40	16.70	19.30
U	6.50	5.90	5.50	4.90	5.40	6.80	7.00	4.00	5.40	4.90	6.80	4.40	5.00
Zr	198.20	197.80	185.30	154.30	147.20	168.90	335.70	164.00	155.30	141.00	241.40	136.40	155.60

Table 4.3 (Continued): Major-trace and isotopic compositions of the volcanic association of Solarya Volcano-plutonic Complex

Sample no.	AS-2	AS-5	AS-8	AS 79	AS 90	AS 103	AS 153	AS 155	AS 222	AS 223	AS 226	AS 227	AS229
Hf	5.20	5.30	5.00	4.10	4.00	4.50	8.40	4.10	3.70	3.70	3.60	3.60	4.20
Ta	1.10	1.20	1.30	0.80	1.30	1.10	1.00	1.30	0.90	0.70	0.70	0.60	0.70
Y	21.70	20.80	19.80	18.20	18.00	12.50	25.00	14.60	20.00	25.50	20.30	20.00	15.30
Nb	16.60	16.30	16.60	10.50	10.80	12.60	16.80	11.80	12.20	8.80	9.80	9.30	10.30
Sc	11.00	10.00	9.00	8.00	13.00	9.00	20.00	9.00	12.00	16.00	15.00	14.00	12.00
Ni	33.00	26.00	24.00	<20	<20	<20	87.00	<20	<20	24.00	28.00	26.00	<20
Co	13.50	12.70	12.80	23.50	38.80	14.10	35.20	18.30	25.70	27.80	22.90	18.40	15.10
V	109.00	91.00	95.00	68.00	121.00	84.00	158.00	79.00	103.00	132.00	132.00	97.00	78.00
W	2.60	3.30	1.50	150.20	185.50	29.60	72.90	55.90	121.30	47.50	63.30	41.70	37.40
Ga	18.20	18.70	18.10	14.80	14.60	13.90	14.40	14.10	17.00	15.40	15.00	14.40	15.30
Zn	30.00	38.00	23.00	51.00	27.00	34.00	47.00	53.00	48.00	70.00	56.00	40.00	40.00
Cu	9.40	16.40	9.60	4.20	9.40	12.10	21.70	9.20	7.10	8.60	10.80	3.60	9.40
La	50.00	49.90	53.70	32.40	37.80	40.10	52.60	39.70	40.10	36.90	38.30	37.30	37.60
Ce	85.60	88.70	98.20	60.80	65.60	67.30	113.20	66.40	73.50	70.20	68.50	67.10	65.60
Pr	9.97	9.48	10.39	6.28	7.35	7.06	13.72	7.57	7.69	7.29	7.08	6.96	6.68
Nd	36.70	33.80	35.20	22.30	28.00	24.60	58.70	28.60	27.50	27.60	26.90	25.20	23.00
Sm	6.96	6.14	6.11	3.81	4.60	4.18	10.00	4.32	4.72	5.26	4.64	4.84	3.91
Eu	1.46	1.24	1.40	1.00	1.11	0.90	2.08	1.14	1.15	1.22	1.18	1.27	0.95
Gd	5.32	5.23	4.83	3.46	3.89	3.26	7.04	3.87	4.24	4.67	4.21	4.30	3.53
Tb	0.67	0.64	0.62	0.52	0.59	0.42	0.93	0.54	0.64	0.69	0.64	0.63	0.50
Dy	4.38	4.26	4.02	2.64	2.84	2.21	4.56	2.99	3.35	4.34	3.63	3.75	2.79
Ho	0.74	0.75	0.60	0.57	0.51	0.43	0.84	0.55	0.76	0.90	0.78	0.79	0.55

Table 4.3 (Continued): Major-trace and isotopic compositions of the volcanic association of Solarya Volcano-plutonic Complex

Sample no.	AS-2	AS-5	AS-8	AS 79	AS 90	AS 103	AS 153	AS 155	AS 222	AS 223	AS 226	AS 227	AS229
Er	1.78	2.07	1.96	1.83	1.79	1.28	2.11	1.49	2.05	2.57	2.20	2.37	1.80
Tm	0.32	0.30	0.29	0.25	0.26	0.17	0.28	0.23	0.33	0.43	0.33	0.34	0.25
Yb	1.82	1.99	1.96	1.81	1.63	1.14	2.15	1.65	2.16	2.69	2.22	2.17	1.80
Lu	0.31	0.31	0.32	0.31	0.26	0.20	0.30	0.25	0.35	0.46	0.36	0.39	0.28
As	1.10	2.30	2.50	<0.5	11.70	17.90	15.10	0.90	3.70	2.70	3.40	2.40	1.70
Mo	0.30	0.60	0.20	0.40	0.40	0.30	0.50	0.60	0.30	0.50	0.60	0.20	<0.1
Be	6.00	4.00	5.00	2.00	3.00	3.00	4.00	2.00	<1	2.00	<1	<1	<1
Ag	<0.1	<0.1	<0.1	<0.1	<0.1	<0.1	<0.1	<0.1	<0.1	<0.1	<0.1	<0.1	<0.1
Sn	3.00	5.00	4.00	2.00	2.00	2.00	2.00	1.00	524.90	447.60	585.30	419.50	515.60
Sb	1.40	0.20	0.90	<0.1	0.30	1.70	0.20	0.30	<0.1	0.70	0.50	0.40	0.10
Tl	0.20	<0.1	0.60	0.10	<0.1	0.10	<0.1	<0.1	<0.1	0.10	<0.1	<0.1	<0.1
Bi	<0.1	0.10	2.60	n.d.	n.d.	n.d.	n.d.	n.d.	<0.1	<0.1	<0.1	<0.1	<0.1
⁸⁷ Sr/ ⁸⁶ Sr	0.7079	0.70732	0.7073	0.7077	0.7076	n.d.	0.7088	n.d.	0.7077	0.70779	0.7074	0.7074	n.d.
¹⁴³ Nd/ ¹⁴⁴ Nd	0.5124	0.51247	0.5125	0.5125	0.5125	n.d.	0.5123	n.d.	0.5125	0.51244	0.5125	0.5125	n.d.
²⁰⁶ Pb/ ²⁰⁴ Pb	18.802	18.76	18.735	18.824	18.85	n.d.	18.703	n.d.	18.849	18.835	18.828	18.831	n.d.
²⁰⁷ Pb/ ²⁰⁴ Pb	15.699	15.693	15.681	15.692	15.698	n.d.	15.698	n.d.	15.696	15.697	15.695	15.695	n.d.
²⁰⁸ Pb/ ²⁰⁴ Pb	38.986	38.991	38.952	38.945	38.964	n.d.	39.082	n.d.	38.968	38.96	38.953	38.953	n.d.

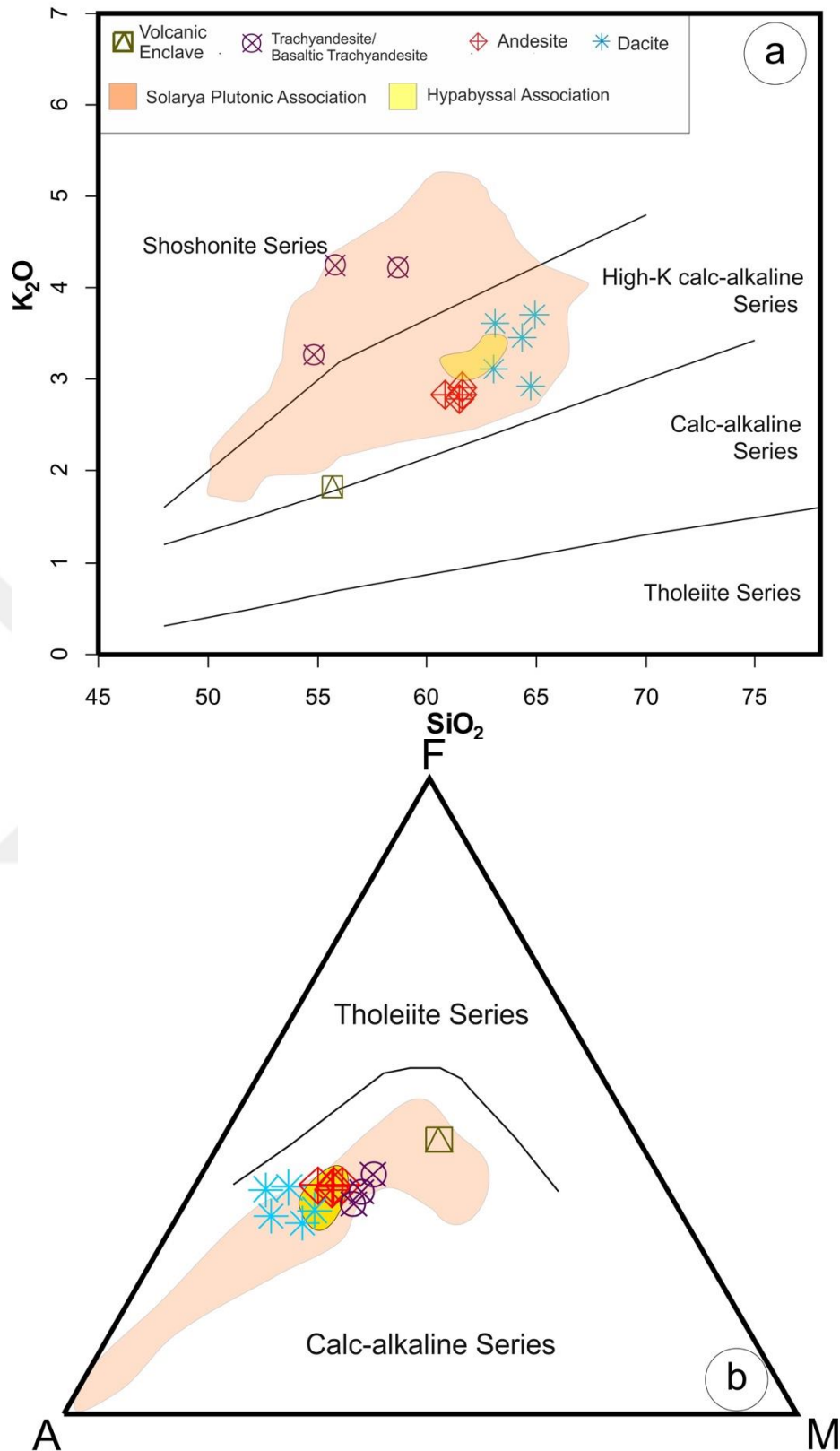


Figure 4. 9: (a) K₂O versus SiO₂ diagram of VA using the classification of Peccerillo and Taylor (1976), results of Solarya Plutonic Association (SPA) and HA are also included (Ünal and Altunkaynak, 2018).

In the PM normalized spider diagrams, all different lithologies of VA present similar multi-element patterns (Figure 4.11a). These patterns suggest that volcanic rocks display enrichment in LIL elements such as K, Rb, Ba, Th and depletions in P, Nb and Ti (Figure 4.11a). These variations point out to a subduction related magmatism for VA. In previous studies, it is reported that enrichment in LILE and depletions in P, Nb and Ti is a result of the migration of slab related fluids towards the mantle wedge (McCulloch and Gamble, 1991; McDonough, 1990; Pearce, 1982; Pearce and Peate, 1995; Thirlwall et al., 1994). On chondrite normalized spider diagrams, the REE distributions of all the samples from VA display significant LREE enrichments relative to the HREE and MREE (Figure 4.11b).

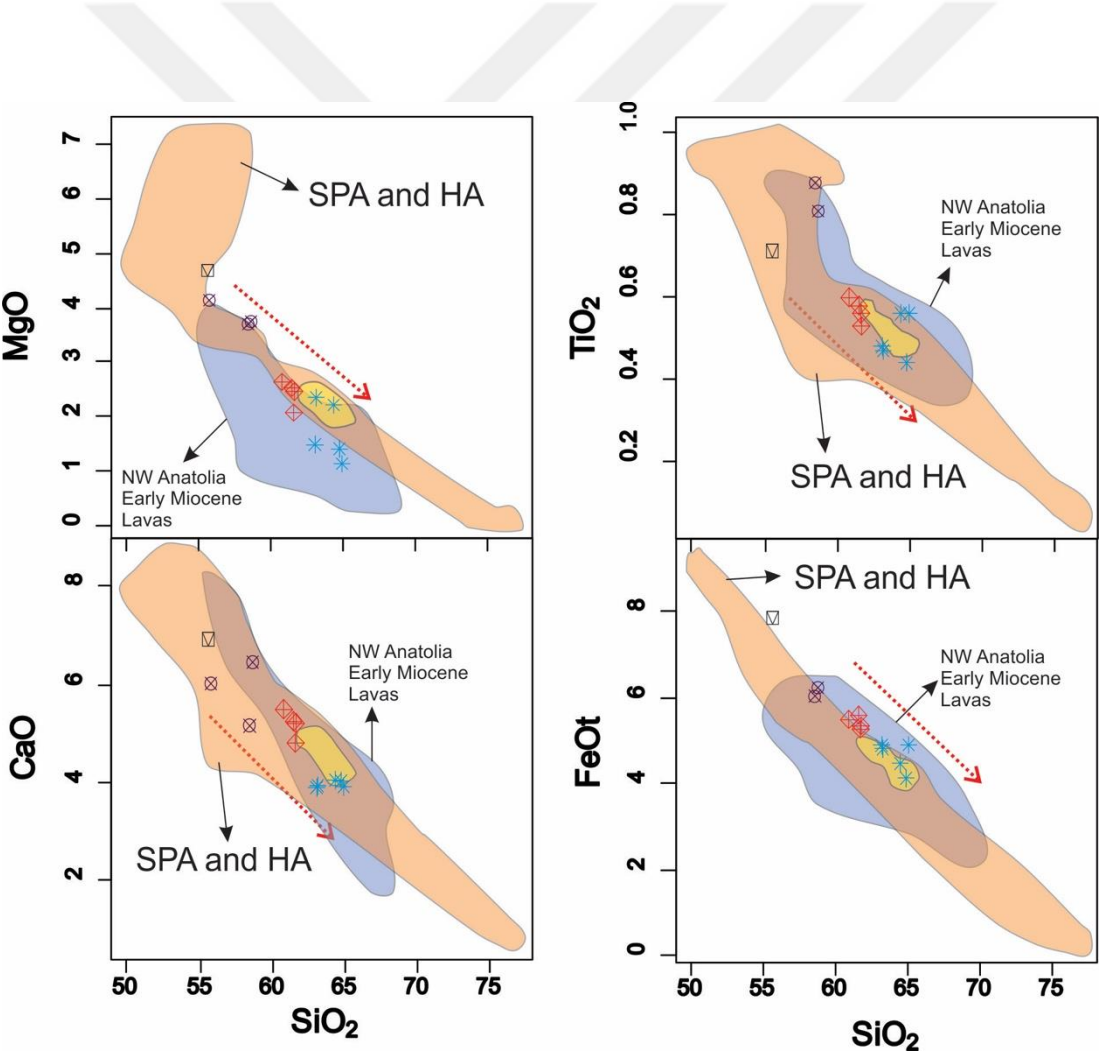


Figure 4. 10: Harker variation diagrams VA, presented together with results of SPA and HA. For legend please see Figure 2.9.

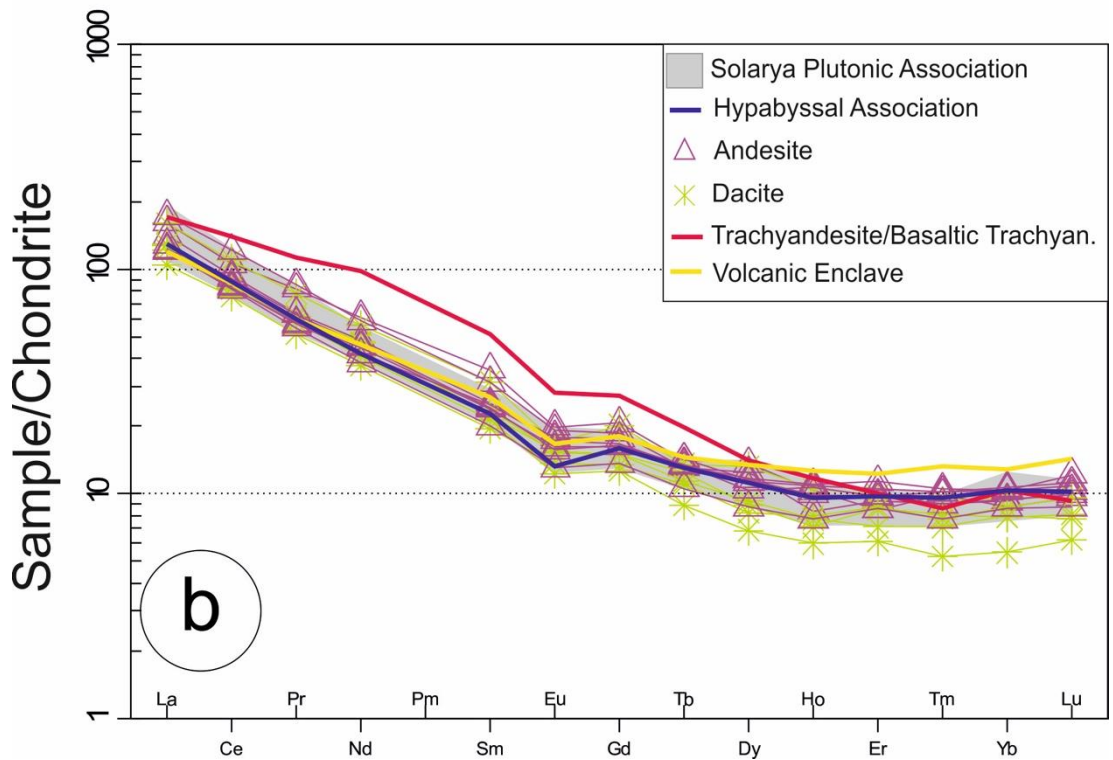
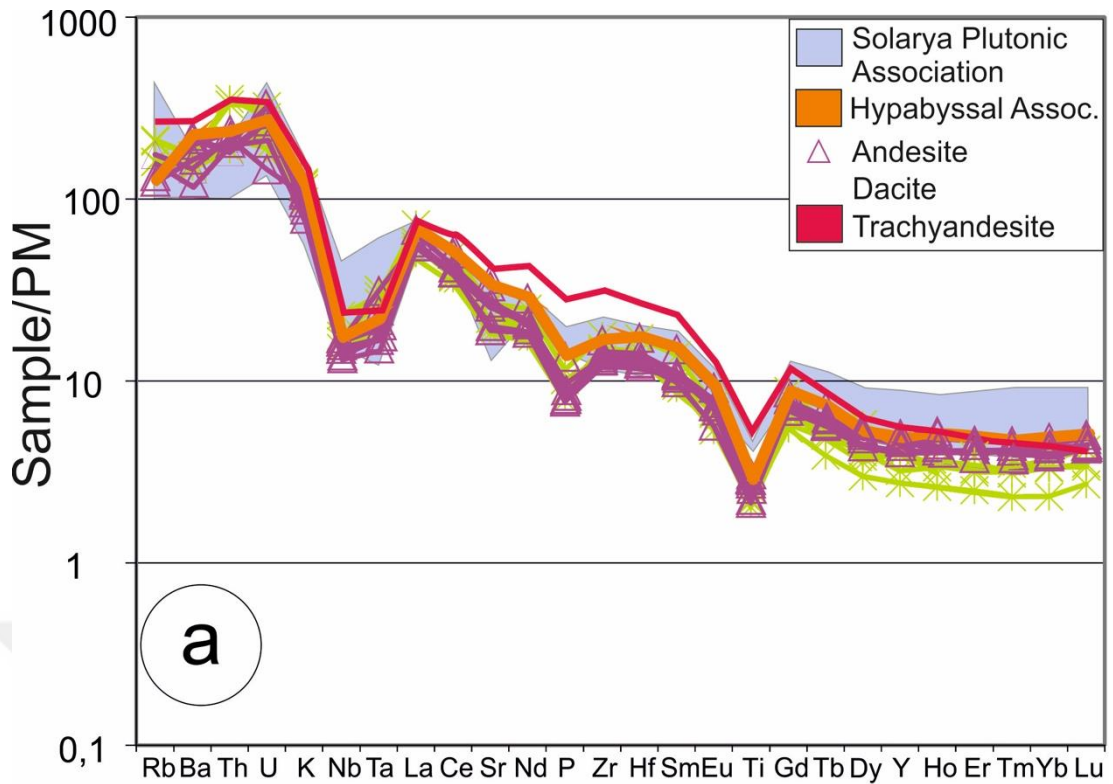


Figure 4. 11: Primitive-mantle (Sun and McDonough, 1989) normalized multi-element patterns for SVPC. (b) Chondrite-normalized REE patterns of SVPC (Boynton, 1984).

4.5.2.2 Sr-Nd-Pb-O isotopes

We have conducted ten Sr-Nd-Pb isotope analyses from VA. Measured $^{87}\text{Sr}/^{86}\text{Sr}_{(m)}$ values differ from 0.70725 to 0.70880, $^{143}\text{Nd}/^{144}\text{Nd}_{(m)}$ values change between 0.51233 and 0.51249. Initial isotopic compositions were calculated with the age of 22 Ma. Initial isotopic compositions are $^{87}\text{Sr}/^{86}\text{Sr}_{(22)}$ values range between 0.70710 and 0.70862, $^{143}\text{Nd}/^{144}\text{Nd}_{(22)}$ range from 0.51232 to 0.51247. $\epsilon\text{Nd}_{(i)}$ values range from -5.61 to -2.63.

The Pb isotopic values of VA present similar values congruently with Sr-Nd isotopic data. $^{207}\text{Pb}/^{204}\text{Pb}$, $^{206}\text{Pb}/^{204}\text{Pb}$, $^{208}\text{Pb}/^{204}\text{Pb}$, $^{207}\text{Pb}/^{206}\text{Pb}$, $^{208}\text{Pb}/^{206}\text{Pb}$ values vary between 15.681 and 15.699, 18.703 and 18.850, 38.945 and 39.082, 0.8327 and 0.8392, 2.067 and 2.089, respectively. The whole rock $\delta^{18}\text{O}$ values vary between 8.3 and 11.9 and the quartz $\delta^{18}\text{O}$ values change between 8.3 and 9.

These initial values are consistent with the data from other northwestern Anatolian lavas of lower Miocene age. Values also overlap with the isotopic data of the SPA (Ünal and Altunkaynak, 2018), which are spatially and temporally related.

4.6 Discussion

4.6.1 Magma source

Major and trace element, and Sr-Nd-Pb-O isotopic characteristics of plutonic, hypabyssal and volcanic samples from SVPC have similar characteristics. We hereby discuss the possible magma source of the SVPC together.

All lithologies of SVPC are sub-alkaline in nature. Granodiorites of SPA, HA, andesites, dacites and volcanic enclaves display high K-calcalkaline character whereas mafic microgranular enclaves (MME) and trachyandesite show shoshonitic character (Figure 4.9a). With their lower SiO_2 and higher FeO, TiO_2 , CaO, MgO than other rocks, MMEs, trachyandesites and volcanic enclaves represent the least evolved members of the SVPC. Haplogranites on the other hand, with their higher SiO_2 contents represent the most evolved member of the SVPC. Granodiorites, hypabyssal rocks, dacites and andesites display a linear trend between these two end members on Harker diagrams (Figure 4.10). This data and their isotopic characteristics suggest that all units forming SVPC have a common magma source.

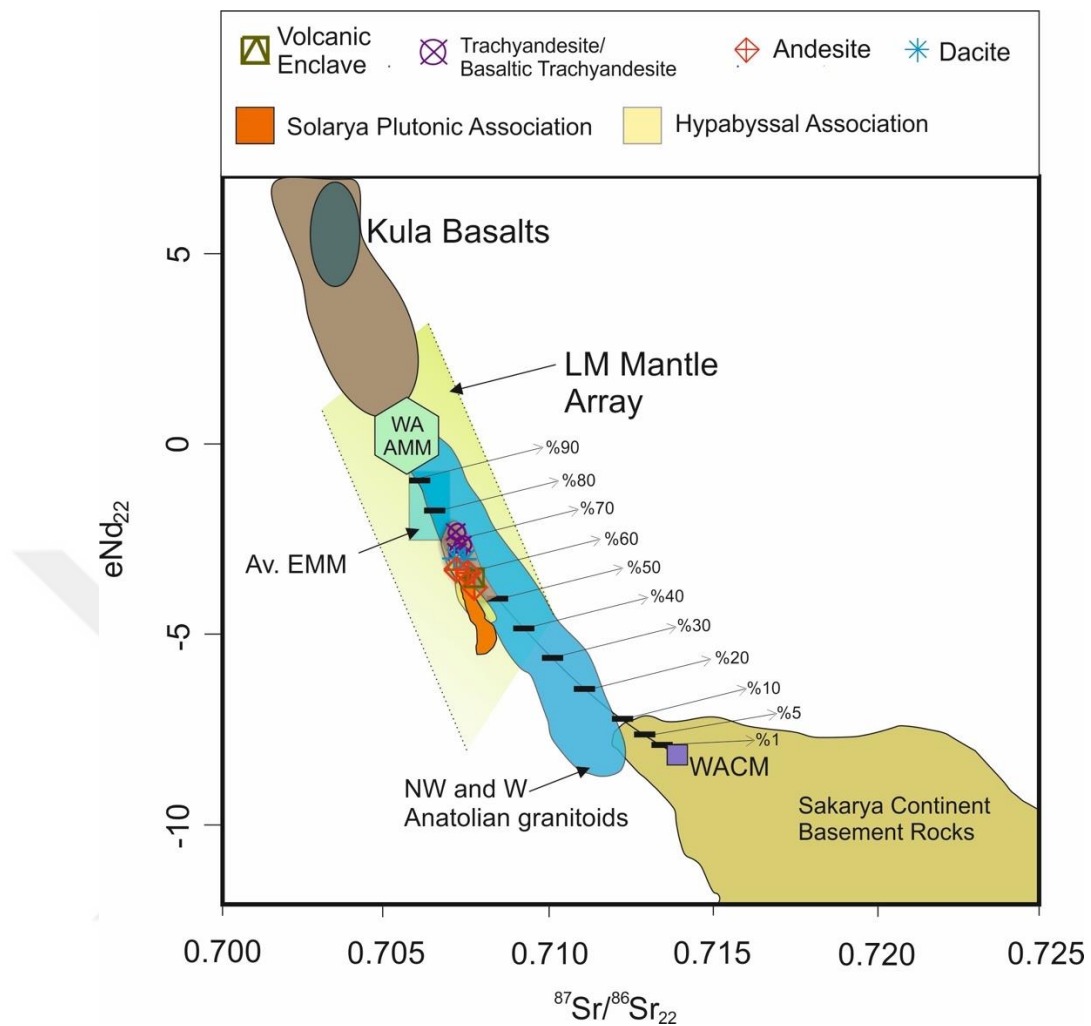


Figure 4. 12: $\epsilon\text{Nd}_{(22)}$ versus $^{87}\text{Sr}/^{86}\text{Sr}_{(22)}$ diagram for SVPC. Simple bulk-mixing modelling is also included to the figure. (Kula Basalts: Dilek and Altunkaynak, 2010; average enriched mantle melts (EMM): Yang et al., 2004 and Altunkaynak et al., 2010; lithospheric mantle (LM) array: Davies and von Blanckenburg, 1995; NW and W Anatolian granitoids: Altunkaynak et al., 2012a; WAAMM- Western Anatolian Average Mantle Melts and WACM-Western Anatolian Crustal Melts are from Kamacı and Altunkaynak, unpublished data).

MMEs, trachyandesites and volcanic enclaves of SVPC display similar Sr-Nd-Pb-O isotope characteristics with other rock types. These similar evolved isotopic data of relatively basic and felsic members of SVPC may be explained by either the contamination of the primitive magma with deep crustal rocks or a significantly enriched mantle as the magma source. Low ϵNd values (-5.61 to -2.63) and relatively high $^{87}\text{Sr}/^{86}\text{Sr}_{(22)}$ values (0.70710 – 0.70862) of SVPC and high abundances of many incompatible elements (Table 4.3) suggest an enriched mantle as a possible magma source. Moreover, the inferred enriched nature of the mantle source is also evidenced

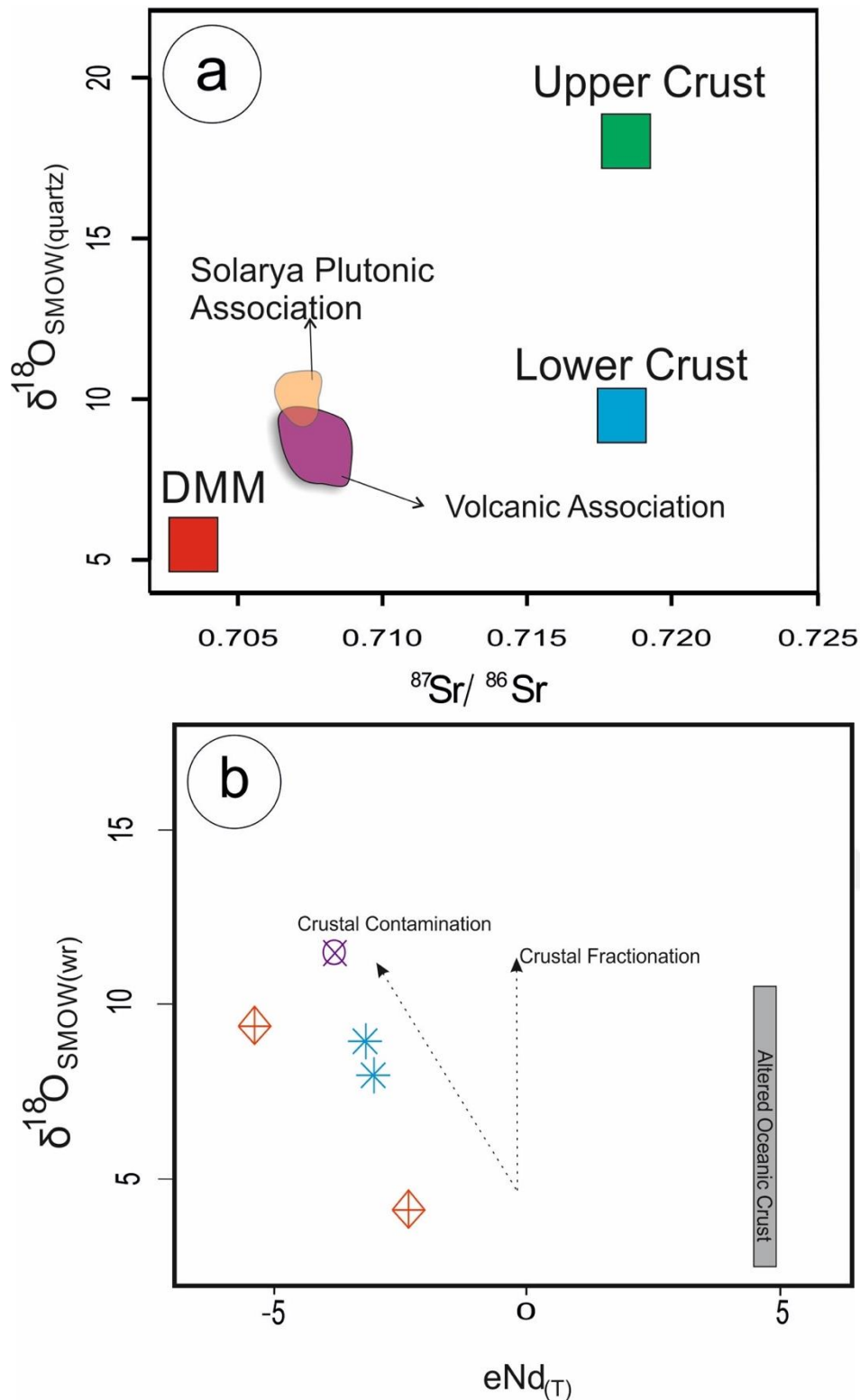


Figure 4. 13: (a) $\delta^{18}\text{O}_{(\text{SMOW})}$ quartz versus $^{87}\text{Sr}/^{86}\text{Sr}$ diagram for SVPC. DMM (Depleted Mantle Melts, Downes, 1990), Lower Crust (Kempton and Harmon, 1992), Upper Crust (Mason et al., 1996). (b) $\delta^{18}\text{O}_{(\text{SMOW})}$ whole rock versus $\epsilon\text{Nd}(t)$ diagram for SVPC (Yücel-Öztürk, 2016).

by trace element characteristics such as enrichment in LILE and depletions in Nb, Ta, Ti and P displayed by all different lithologies of SVPC.

4.6.1.1 Mantle-continental crust interactions

The ϵ_{Nd} versus $^{87}Sr/^{86}Sr$ diagram illustrates that, MMEs, trachyandesites and volcanic enclave plot closer to average EMM (average enriched mantle melts; Yang et al., 2004) field. This data show that, even the most primitive members of the SVPC have a magma source of enriched mantle. SVPC samples, including the most primitive and evolved member, show negative trend between EMM and the basement rocks of western Anatolia (Altunkaynak et al., 2012a and references there in). This trend is a clear indicator of the interaction of enriched mantle source with crustal rocks. A simple bulk mixing model (Ünal and Altunkaynak, 2018) is included to this ϵ_{Nd} versus $^{87}Sr/^{86}Sr$ diagram to test the contribution of the crustal components to enriched mantle melts (Figure 4.12). The model shows that, the contribution of the crust to the enriched mantle source is about 25–45% for volcanic rocks of SVPC. This result is consistent with the bulk mixing model of SPA and HA (Ünal and Altunkaynak, 2018). In addition, in the same figure, the ϵ_{Nd} versus $^{87}Sr/^{86}Sr$ results of other early Miocene volcanic associations of western Anatolia present similar trends with SVPC samples in the bulk mixing model. This consistency suggests that all samples have a similar magma source and bulk mixing processes in early Miocene.

In Figure 4.13a, the $\delta^{18}O_{(SMOW)}$ quartz versus $^{87}Sr/^{86}Sr$ results of volcanic rocks are shown. Samples plot between DMM (Depleted Mantle Melts) and crustal rocks. The $\delta^{18}O_{(SMOW)}$ whole rock versus $\epsilon_{Nd(T)}$ diagram (Figure 4.13b) displays that, the volcanic rocks show similar trends with crustal contamination trajectory. This data suggests the contribution of crustal material to mantle melts. To support the results obtained from Sr-Nd and O isotopic characteristics, Pb isotopic data are evaluated with $^{207}Pb/^{204}Pb$ versus $^{206}Pb/^{204}Pb$ and $^{208}Pb/^{204}Pb$ versus $^{206}Pb/^{204}Pb$ diagrams (Figure 4.14a and b). Both of the figures show that, all of the volcanic samples plot on the EMII (enriched mantle II) field, once again consistent with plutonic and hypabyssal association (Ünal and Altunkaynak, 2018).

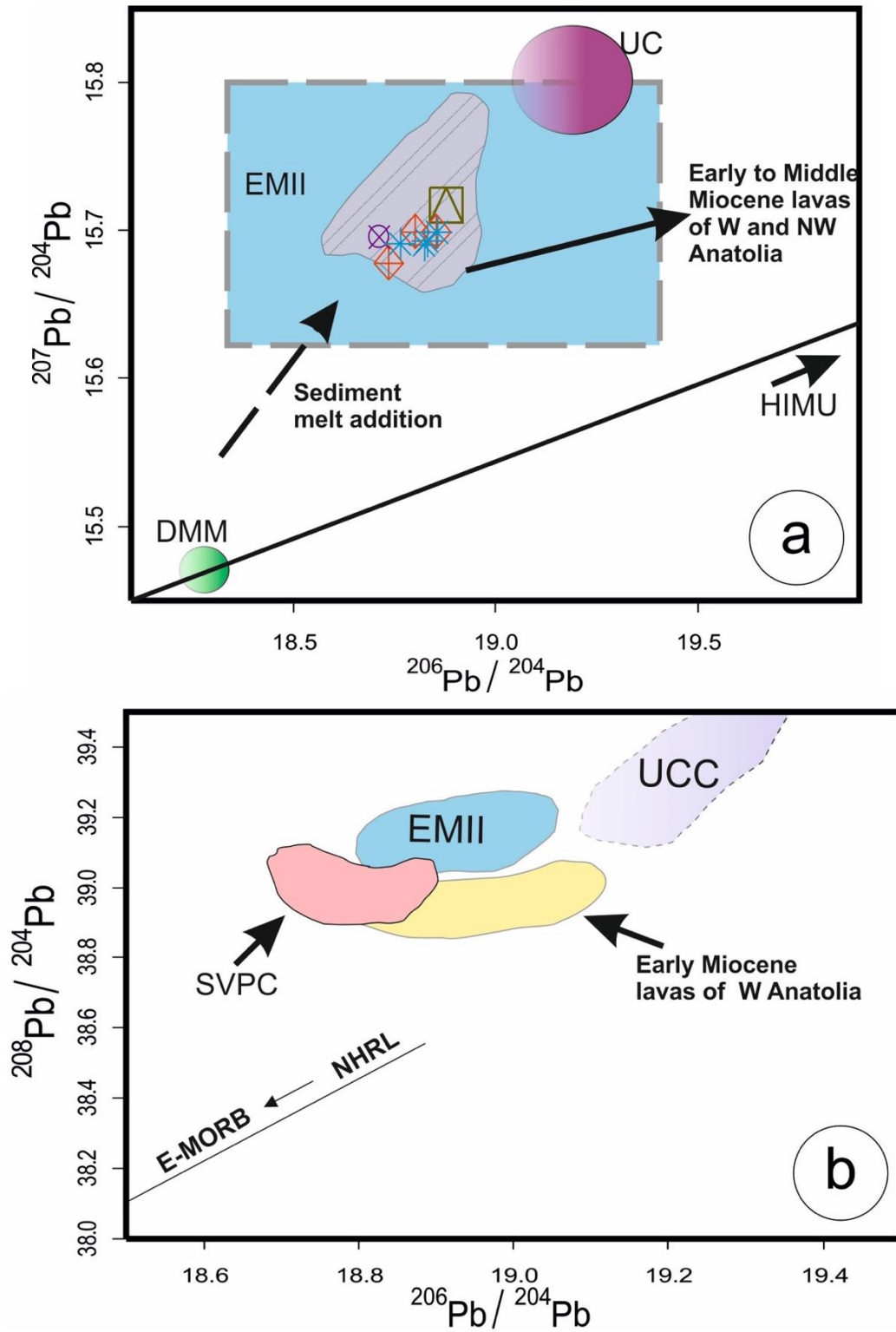


Figure 4. 14: (a) $^{207}\text{Pb}/^{204}\text{Pb}$ versus $^{206}\text{Pb}/^{204}\text{Pb}$ diagram for SVPC. EMI: Enriched Mantle I, EMII: Enriched mantle II, DM: Depleted Mantle, HIMU: high U/Pb mantle, (Zindler and Hart, 1986; Rollinson, 1993; Aldanmaz et al., in press and references there in). (b) The position SVPC samples on $^{208}\text{Pb}/^{204}\text{Pb}$ versus $^{206}\text{Pb}/^{204}\text{Pb}$ diagram. Source Data is from Erkül et al., 2013 and references there in).

4.6.2 Evolution of magma

PM-normalized trace element patterns and chondrite-normalized REE patterns indicate that all plutonic, hypabyssal and volcanic rocks have similar characteristics among each other. They are all enriched in the HFSE, LREE, LILE and have high LILE–HFSE ratios consistent with derivation of their magmas from at convergent margin settings (McDonough, 1990; Pearce, 1982; Pearce et al., 1990; Pearce and Peate, 1995; Thirlwall et al., 1994). However, there is almost a total consensus on the Eocene and Miocene magmatic rocks of northwestern Anatolia are classified as “post-collisional” (Dupuy, 1982; Seyitoğlu et al., 1997; Aldanmaz et al., 2000; Yılmaz et al., 2000; Altunkaynak et al., 2012a; Altunkaynak and Dilek, 2006; Altunkaynak, 2007; Dilek and Altunkaynak, 2007; Ersoy et al., 2012; Erkül, 2009; Erkül, 2012; Ersoy et al., 2017). Therefore, the subduction imprints of SVPC are possibly related to the previous subduction events (Aldanmaz et al., 2000; Altunkaynak and Dilek, 2006; Altunkaynak, 2007; Altunkaynak et al., 2012a; Dilek and Altunkaynak, 2007; Dupuy, 1982; Seyitoğlu et al., 1997; Ünal and Altunkaynak, 2018; Yılmaz et al., 2000).

Textural properties of plutonic, hypabyssal and volcanic rocks present crucial data for magma chamber processes. Petrographic investigations of SVPC present clear disequilibrium textures such as oscillatory zoning, sieve and honeycomb textures of plagioclase crystals. Moreover, in trachyandesites, the biotite crystals mantled by hornblende and hornblende crystals mantled by pyroxene are also clear indicators for disequilibrium conditions. Therefore, it could be suggested that during the evolution of SVPC, open system processes played an active role. These open system processes are also evidenced by the positive trend with Th/Yb versus Ta/Yb ratio in Figure 4.15. The samples show trend between enriched mantle melts (EMM) and western Anatolia continental crust. The linear trend of the samples suggests that, after the subduction zone enrichment, the melts from enriched mantle source are contaminated by crustal components via mixing/mingling or AFC processes.

In order to test the role of AFC in the magma evolution, we conducted an AFC model for volcanic rocks using the equations of DePaolo (1981). In Figure 4.16a, volcanic rocks plot mostly between the AFC trajectories drawn for $r = 0.1$ and 0.3 consistent with plutonic and hypabyssal rocks of SVPC.

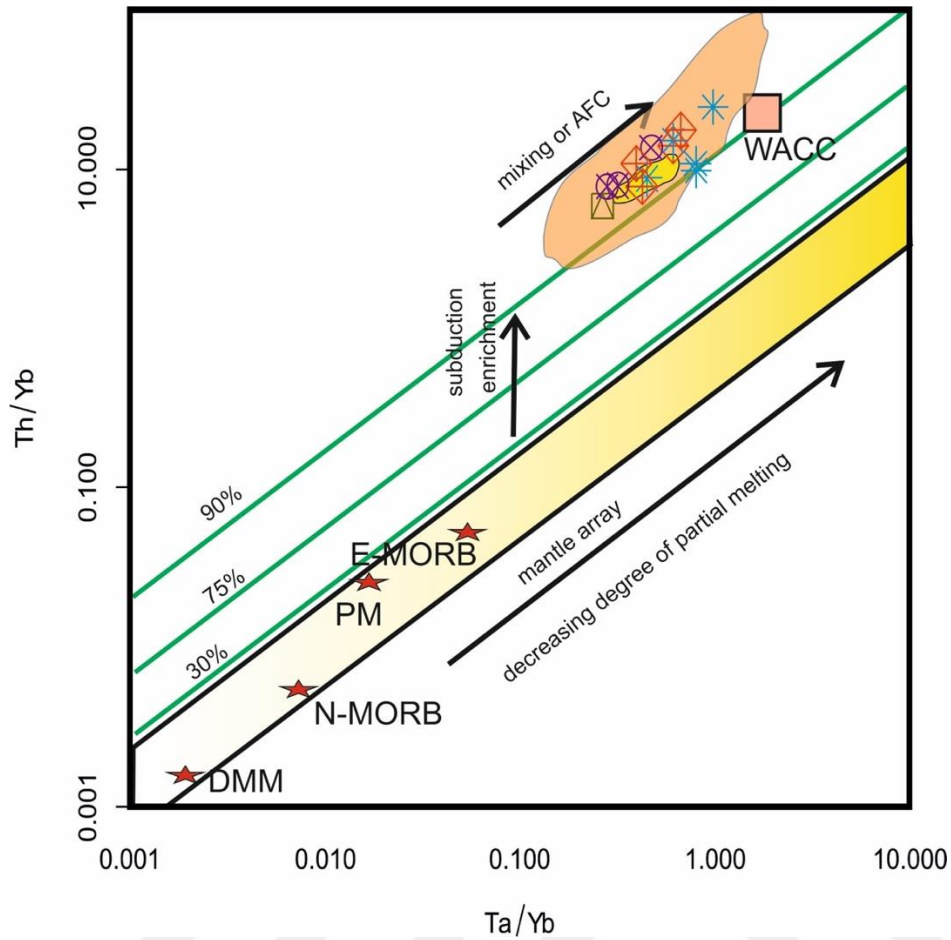


Figure 4. 15: Th/Yb versus Ta/Yb log–log diagram for SVPC. Subduction-enriched mantle (EM) and mantle array are also included (Pearce et al., 2005).

In $^{87}\text{Sr}/^{86}\text{Sr}$ versus $1/\text{Sr}$ diagram, the samples from volcanic rocks plot linearly through the FC trajectory. Both of the diagrams indicate that the contribution of crustal assimilation accompanying the ongoing fractional crystallization played a minor role for evolution of SVPC.

4.6.3 Connections between regional extension and Volcano-Plutonic Complexes

During the Late Cretaceous, subduction of the Tethyan seafloor was terminated by the collision of Sakarya and Anatolide-Tauride continents giving way to the emplacement of ophiolites along the İzmir-Ankara suture zone (Şengör and Yılmaz, 1981; Okay, 1984; Okay et al., 1990). Time constraints on the obduction of these ophiolites suggest that, timing of the collision was most probably pre-early Eocene. Moreover, shallow marine sedimentary rocks of the Gebeler (Akyürek and Soysal, 1983) and Başlamış (Akdeniz, 1980) Formations unconformably overlay the suture zone units. This crucial

stratigraphic data suggests that, the collision between Sakarya and Anatolide-Tauride continents took place earlier than the middle Eocene. Therefore, the Eocene and Miocene magmatic rocks of western Anatolia are “postcollisional” with respect to the collision between Sakarya and Anatolide-Tauride continent (Aldanmaz et al., 2000; Altunkaynak, 2007; Altunkaynak and Dilek, 2006; Altunkaynak et al., 2012a; Dilek and Altunkaynak, 2007; Dupuy, 1982; Erkül, 2012; Ersoy et al., 2010; Ersoy et al., 2012; 2017; Seyitoğlu et al., 1997; Ünal and Altunkaynak, 2018; Yılmaz et al., 2000).

Subsequent to the collision of Sakarya and Anatolide-Tauride platforms, intensive magmatism in western Anatolia started in the Eocene period and continued to the present time (Güleç, 1991; Harris et al., 1994; Şengör et al., 1993; Yılmaz, 1989, 1990, 1995). This post-collisional magmatism produced plutonic, hypabyssal and volcanic rocks both in Eocene and Miocene. There are numerous volcano-plutonic complexes in the region as a product of this extensive Cenozoic magmatism. Kestanbol (Karacık and Yılmaz, 1998), Kozak (Altunkaynak and Yılmaz, 1998), Bayramiç (Genç, 1998) and Alaçamdağ (Erkül, 2012) volcano-plutonic complexes are analogous examples to those of the Miocene plutonic and coeval hypabyssal and volcanic rocks. Plutons that are spatially and temporally related with volcanic rocks are classified as “sub-volcanic plutons” or as “caldera type plutons” and they are together defined as “caldera complex” (John, 1995; Pitcher, 1979; Seager and McCurry, 1988). Similar to these volcano-plutonic complexes, SVPC is a caldera complex with coeval and co-genetic plutonic, volcanic and hypabyssal rocks.

The radiometric ages obtained from the plutonic, hypabyssal and volcanic rocks are overlapping. Solarya pluton has $^{40}\text{Ar}/^{39}\text{Ar}$ radiometric ages (hornblende and biotite) varying from 22.3 ± 0.1 to 21.9 ± 0.1 Ma (Altunkaynak et al., 2012a). Our $^{40}\text{Ar}/^{39}\text{Ar}$ radiometric ages from biotite mineral for hypabyssal and volcanic association range between 23.1 ± 0.2 and 21.0 ± 0.2 Ma. This data clearly suggests that, plutonic, hypabyssal and volcanic rocks are coeval.

Not only the radiometric age data of plutonic, hypabyssal and volcanic rocks, field properties of SVPC also indicate that these rocks were formed coevally. These data are summarized as;

a) Granitic and hypabyssal rocks cut one another

b) Hypabyssal and volcanic rocks cut one another, and fragments of hypabyssal rocks are found in volcanic rocks.

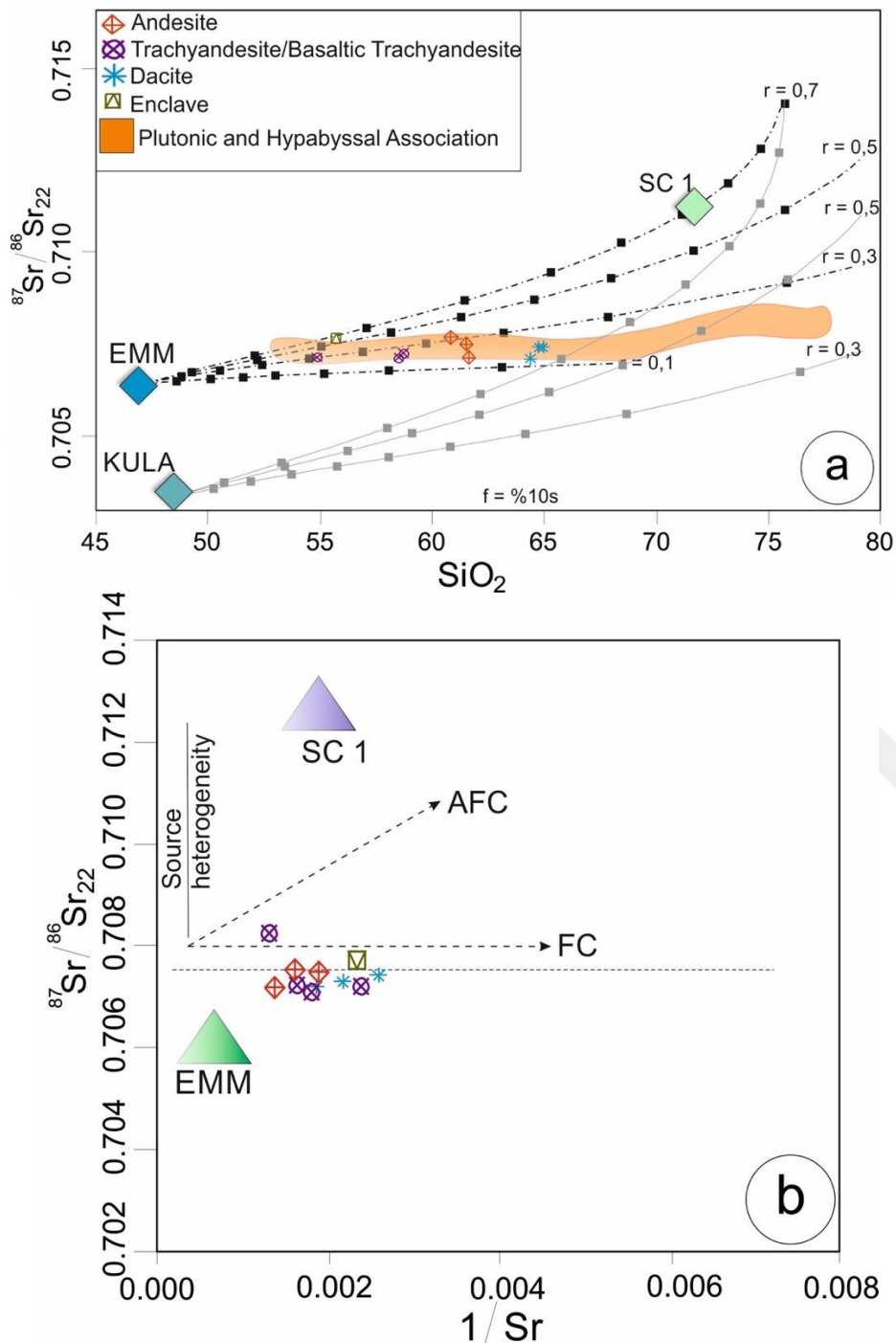


Figure 4. 16: (a) Diagram of $^{87}\text{Sr}/^{86}\text{Sr}_{(22)}$ versus SiO_2 (wt.%), presenting the results of AFC modeling for SVPC (proportions from Ünal and Altunkaynak, 2018). (b) $^{87}\text{Sr}/^{86}\text{Sr}_{(22)}$ versus $1/\text{Sr}$ diagram displaying the AFC and FC trajectories. EMM (Enriched Mantle Melts from Yang et al., 2004), SK1 (Altunkaynak et al., 2012b).

The stratigraphic data together with radiometric age results reveal that, plutonic, hypabyssal and volcanic members of SVPC are temporally and spatially related. Their

spatial association is shown in Figure 4.2 in which, Solarya Pluton is located at the center of the study area. The Solarya pluton is represented by a shallow level epizonal intrusion which was emplaced at sub-volcanic levels in the crust. Towards the southern margin of the pluton, the grain size of the plutonic rocks decreases, and they pass into hypabyssal rocks. Hypabyssal rocks are initially injected into the ring and radial faults, as evidenced by their crescent shape along the southern contact of the pluton, coevally with the emplacement of the pluton (Figure 4.2). Hypabyssal rocks are represented by sheet intrusions and similar to their contact relationship with plutonic rocks, they pass into volcanic rocks. All these characteristics of coeval and cogenetic plutonic, hypabyssal and volcanic rocks suggest that, SVPC is represented by a “caldera complex”.

Different models have been proposed for the generation of post-collisional magmatism in Aegean region. These models could be summarized as; (1) magmatism related to an active subduction event (Borsiet al., 1972; Fytikas et al., 1984; Pe-Piper and Piper, 1989; Gülen, 1990; Delaloye and Bingöl, 2000; Okay and Satır, 2000; 2006), (2) regional extension related magmatism driven by orogenic collapse (Seyitoğlu and Scott, 1991, 1992; Seyitoğlu et al., 1997), (3) magmatism caused by compression-crustal thickening (Şengör and Yılmaz, 1981; Ercanet al., 1984, 1995; Yılmaz, 1989, 1990; Savaşçın and Güleç, 1990; Güleç, 1991, Altunkaynak and Yılmaz, 1998; Genç and Yılmaz, 1997; Karacık and Yılmaz, 1998) and (4) syn-convergent extension and magma generation driven by partial delamination, convective removal of the lithosphere or slab break-off (Aldanmaz et al., 2000; Altunkaynak, 2007; Altunkaynak and Dilek, 2006; Altunkaynak and Genç, 2008; Boztuğ et al., 2009; Altunkaynak et al., 2012a,b; Dilek and Altunkaynak, 2007; Ersoy et al., 2017; Köprübaşı and Aldanmaz, 2004; Ünal and Altunkaynak, 2018). The production of magma forming SPA and HA was caused by upwelling asthenosphere due to convective removal or partial delamination of the continental lithosphere beneath western Anatolia (for detailed discussion, please see Ünal and Altunkaynak, 2018). Thus, the generation of the magma forming plutonic and hypabyssal rocks of SVPC is related to the syn-convergent extension in western Anatolia during early Miocene time. Since the volcanic members of the SVPC are coeval and cogenetic with plutonic and hypabyssal rocks, they should have developed under the same extensional regime.

The structural features of the SVPC also displays extension related characteristics. E-W trending major normal fault systems cut plutonic, hypabyssal and volcanic rocks as illustrated in Figure 4.2. These faults are responsible for the emplacement of the pluton as well as hypabyssal rocks. The linear alignment of the volcanic centers also suggests that, these faults are known to have formed during the development of the volcanic rocks of SVPC.

Evaluation of stratigraphic, geochronological, structural and petrological characteristics of SVPC in lithospheric scale collectively suggests that, it was developed under N-S extensional regime during the early Miocene period. This data is close agreement with the development of the other volcano-plutonic and core complexes (eg. Kozak, Menderes, Kazdağ, Çataldağ) both in Aegean region and worldwide.

4.7 Conclusions

SVPC is formed from plutonic, hypabyssal and volcanic rocks. Plutonic rocks are represented by K-feldspar megacrystalline granodiorite, microgranodiorite and haplogranite. HA is defined by granodiorite/quartz-diorite porphyry sheet intrusive rocks. VA includes andesite and dacite lavas with associated pyroclastic rocks and trachyandesite- basaltic trachyandesite lavas. The $^{40}\text{Ar}/^{39}\text{Ar}$ radiometric ages and geochemical data (collectively with Sr-Nd-Pb-O) obtained from this study indicate that they are cogenetic and coeval. Radiometric ages of SVPC ranges between 23.1 ± 0.2 and 21.0 ± 0.2 . SVPC is comprised of hybrid magmas, consisting of mantle and crustal components. The contribution of the crustal components to enriched mantle source is 25–45%. The prepared AFC model indicates that the contribution of crustal assimilation accompanying the ongoing fractional crystallization played a minor role for evolution of SVPC. The field properties, geochronological, and petrological characteristics of SVPC combined with the geology of the region collectively indicate that, SVPC was developed under N-S extensional regime during the early Miocene period concurrently with the development of the other volcano-plutonic and core complexes (eg. Kozak, Menderes, Kazdağ, Çataldağ) both in Aegean region and worldwide.

5. CONCLUSIONS

In order to contribute to the understanding on the nature, genesis and tectonothermal evolution of the western Anatolian post-collisional magmatic rocks, which are some of the major problems of western Anatolia and broader Aegean region, the main questions at the beginning of this thesis were; i) What are the key field relationship of the different magmatic rocks of SVPC? Are they spatially, temporally and genetically related? ii) What are the magma chamber processes and possible magma source responsible for the evolution of high Ba-Sr Solarya Plutonic association, volcanic and hypabyssal rocks? iii) What are the emplacement conditions and mechanisms of the SPA? iv) Regarding the field, geochemical and geochronological properties of SVPC, what is the most coherent geodynamic model for the post-collisional magmatic evolution of NW Anatolia?

The detailed answers to these questions were given in the subtopics within the chapters. Nevertheless, a brief summary of the conclusions is given below:

SVPC consists of coeval and cogenetic plutonic (SPA), hypabyssal and volcanic rocks. Plutonic rocks are represented by K-feldspar megacrystalline granodiorite (KFMG), microgranite-granodiorite (MGG) and haplogranite. Plutonic rocks interfinger with hypabyssal rocks consisting of microgranodiorite/ microquartz-diorite porphyry sheet intrusive rocks. Hypabyssal rocks are represented as feeder dykes for the extrusion of volcanic rocks. Volcanic sequence consists of andesite and dacite lavas with associated pyroclastic rocks and trachyandesite- basaltic trachyandesite lavas. Volcanic rocks interfinger with the sedimentary rocks at the bottom of the sequence. The U-Pb zircon dating results of SPA range between 21.8 ± 0.2 Ma to 21.2 ± 0.1 Ma. The $^{40}\text{Ar}/^{39}\text{Ar}$ biotite isochron ages differ from 23.2 ± 0.2 to 21.8 ± 0.1 Ma whereas the K-feldspar and plagioclase separate yield plateau ages of 20.3 ± 0.2 Ma and 21.6 ± 0.4 Ma, respectively. The $^{40}\text{Ar}/^{39}\text{Ar}$ radiometric ages of volcanic and hypabyssal associations display that, they have $^{40}\text{Ar}/^{39}\text{Ar}$ biotite ages changing from 23.1 ± 0.2 to 21.0 ± 0.2 indicating that they, are coeval with SPA. Geochemically, plutonic, hypabyssal and volcanic rocks of SVPC present similar characteristics. SVPC is

comprised of hybrid magmas consisting of mantle and crustal components. The contribution of the crustal material to the enriched mantle source is about 25–45%. During the evolution of SVPC, AFC (assimilation fractional crystallization) played a minor role. The emplacement of the Solarya Pluton into the crust was occurred at different levels of crust with different mechanisms. The SP began its emplacement forcefully in relatively deeper levels in the crust (6.1 km depth). Following this stage, MGG was emplaced into the shallow levels (2.4 km depth) via cauldron subsidence and in the late stage the sheet intrusive rocks were emplaced into the ring faults at 1.5 km depth. Evaluation of all these data together with the geology of the region collectively suggests that Solarya Volcano-plutonic Complex and other coeval volcano-plutonic complexes was developed under syn-convergent extensional regime driven by the convective removal or partial delamination of the continental lithosphere beneath western Anaoia.

REFERENCES

- Abrahart, R. J., and See, L.** (1998). Neural Network vs. ARMA Modelling: Constructing Benchmark Case Studies of River Flow Prediction. In GeoComputation '98. *Proceedings of the Third International Conference on GeoComputation*, University of Bristol, United Kingdom, 17–19 September (CD-ROM).
- Akdeniz, N.** (1980). Başlamış Formasyonu. *Jeoloji Mühendisliği Dergisi*. 10, 39–47 (in Turkish).
- Akyurek, B., and Soysal, Y.** (1983). Biga yarımadası güneyinin (Savastepe–Kırkagac–Bergama–Ayvalık) temel jeoloji özellikleri. *Bulletin of Mineral Research and Exploration Institute, Turkey*, 95, 1–12.
- Aldanmaz, E., Pearce, J.A., Thirlwall, M.F., and Mitchell, J.G.** (2000). Petrogenetic evolution of the late Cenozoic, post-collision volcanism in western Anatolia, Turkey. *Journal of Volcanology and Geothermal Research*, 102, 67–95.
- Aldanmaz, E., Köprübaşı, N., Gürer, Ö.F., Kaymakçı, N., and Gourgaud, A.** (2006). Geochemical constraints on the Cenozoic, OIB-type alkaline volcanic rocks of NW Turkey: implications for mantle sources and melting processes. *Lithos*, 86 (1), 50–76.
- Aldanmaz, E., Pickard, M., Meisel, T., Altunkaynak, Ş., Sayit, K., Şen, P., ... Furman, T.** (2015). Source components and magmatic processes in the genesis of Miocene to quaternary lavas in western Turkey: constraints from HSE distribution and Hf-PbOs isotopes. *Contributions to Mineralogy and Petrology*. 170:23–42.
- Aldanmaz, E., Altunkaynak, Ş., and Güçtekin, A.** (2019). Some remarks on the nature of mantle metasomatism beneath western Anatolian-Aegean region: Contrasting isotopic signatures recorded in the Miocene lavas from the Söke Basin. *Geological Journal* (in press).
- Altunkaynak, Ş.** (2007). Collision-driven slab breakoff magmatism in Northwestern Anatolia, Turkey. *Journal of Geology*, 115, 63–82.

- Altunkaynak, Ş., and Dilek, Y.** (2006). Timing and nature of postcollisional volcanism in western Anatolia and geodynamic implications. *Geological Society of America Special Papers*, 409.
- Altunkaynak, Ş., and Yılmaz, Y.** (1998). The Kozak magmatic complex, Western Anatolia. *Journal of Volcanology Geothermal Research*, 85, 211–231.
- Altunkaynak, Ş., and Yılmaz, Y.** (1999). The Kozak Pluton and its emplacement. *Geological Journal*, 34(3), 257-274.
- Altunkaynak, Ş., and Genç, Ş.C.** (2008). Petrogenesis and time-progressive evolution of the Cenozoic continental volcanism in the Biga Peninsula, NW Anatolia (Turkey). *Lithos*, 102 (1), 316–340.
- Altunkaynak, Ş., Rogers, N.W., and Kelley, S.P.** (2010). Causes and effects of geochemical variations in late Cenozoic volcanism of the Foça volcanic centre, NW Anatolia, Turkey. *International Geology Review*, 52 (4–6), 579–607.
- Altunkaynak, Ş., Dilek, Y., Genç, Ş.C., Sunal, G., Gertisser, R., Furnes, H., ... Yang, Y.** (2012a). Spatial, temporal and geochemical evolution of oligo–Miocene granitoid magmatism in western Anatolia, Turkey. *Gondwana Research*, 21, 961–986.
- Altunkaynak, Ş., Sunal, G., Aldanmaz, E., Genç, C.Ş., Dilek, Y., Furnes, H., ... Yıldız, M.** (2012b). Eocene granitic magmatism in NW Anatolia (Turkey) revisited: new implications from comparative zircon SHRIMP U-Pb and ^{40}Ar – ^{39}Ar geochronology and isotope geochemistry on magma genesis and emplacement. *Lithos*, 155, 289–309.
- Altunkaynak, Ş., and Dilek, Y.** (2013). Eocene mafic volcanism in northern Anatolia: its causes and mantle sources in the absence of active subduction. *International Geology Review*, 55, 1641–1659.
- Anderson, R. V. V.** (1936). *Geology in the coastal Atlas of western Algeria* (No. 4). Geological Society of America.
- Anderson, J. L., and Smith, D. R.** (1995). The effects of temperature and $f\text{O}_2$ on the Al-in-hornblende barometer. *American Mineralogist*, 80(5-6), 549-559.

- Aslan, Z., Erdem, D., Temizel, İ., and Arslan, M.** (2017). SHRIMP U-Pb zircon ages and wholerock geochemistry for the Şapçı volcanic rocks, Biga Peninsula, Northwest Turkey: implications for pre-eruption crystallization conditions and source characteristics. *International Geology Review*, 59 (14), 1764–1785.
- Bickford, M.E., and Boardman, S.J.** (1984). A Proterozoic volcano-plutonic terrane, Gunnison and Salida areas, Colorado. *Journal of Geology*, 92 (6), 657–666.
- Bingöl, E.** (1975). *Batı Anadolunun jeotektonik evrimi*, M.T.A. Dergisi 86, 14–34.
- Bingöl, E., Delaloye, M., and Ataman, G.** (1982). Granitic intrusions in Western Anatolia: a contribution to the geodynamic study of this area. *Eclogae Geologicae Helvetiae*, 75, 437–446.
- Bird, P.** (1979). Continental delamination and the Colorado plateau. *Journal of Geophysical Research*, Solid Earth 84 (B13), 7561–7571.
- Blanckenburg, F., and Davies, J.H.** (1995). Slab breakoff: a model for syncollisional magmatism and tectonics in the alps. *Tectonics*, 14 (1), 120–131.
- Blattner, P., Abart, R., Adams, C.J., Faure, K., and Hui, L.** (2002). Oxygen isotope trends and anomalies in granitoids of the Tibetan plateau. *Journal of Asian Earth Sciences*, 21 (3), 241–250.
- Blundy, J. D., & Holland, T. J.** (1990). Calcic amphibole equilibria and a new amphibole-plagioclase geothermometer. *Contributions to Mineralogy and Petrology*, 104(2), 208-224.
- Borsi, S., Ferrara, G., Innocenti, F., and Mazzuoli, R.** (1972). Geochronology and petrology of recent volcanics in the Eastern Aegean Sea (West Anatolia and Lesvos Island). *Bulletin of Volcanology*, 36 (3), 473.
- Boynton, W.V.** (1984). Geochemistry of the rare earth elements: meteorite studies. In: Henderson, P. (Ed.), *Rare Earth Element Geochemistry*. Elsevier, Amsterdam, Netherlands, pp. 63–114.
- Boztuğ, D., Harlavan, Y., Arehart, G.B., Satır, M., and Avcı, N.** (2007). K–Ar age, whole-rock and isotope geochemistry of A-type granitoids in the Divriği–Sivas region, eastern-Central Anatolia, Turkey. *Lithos*, 97 (1), 193–218.

- Boztuğ, D., Harlavan, Y., Jonckheere, R.C., Can, I., and Sarı, R.** (2009). Geochemistry and K-Ar cooling ages of the Ilıca, Çataldağ (Balıkesir) and Kozak (İzmir) granitoids, west Anatolia, Turkey. *Geological Journal*, 44, 79–103.
- Brown, M.** (1994). The generation, segregation, ascent and emplacement of granite magma: the migmatite-to-crustally-derived granite connection in thickened orogens. *Earth-Science Reviews*, 36 (1–2), 83–130.
- Burkut, Y.** (1966). *Kuzeybatı Anadolu'da yer alan plutonların mukayeseli jenetik etüdü*. (Doctoral Thesis). ITU Faculty of Mines, p. 272.
- Choi, S.G., Rajesh, V.J., Seo, J., Park, J.W., Oh, C.W., Pak, S.J., and Kim, S.W.** (2009). Petrology, geochronology and tectonic implications of Mesozoic high Ba–Sr granites in the Haemi area, Hongseong Belt, South Korea. *Island Arc*, 18, 266–281.
- Clemens, J. D.** (1998). Observations on the origins and ascent mechanisms of granitic magmas. *Journal of the Geological Society*, 155(5), 843-851.
- Clough, C. T., Maufe, H. B., and Bailey, E. B.** (1909). The cauldron-subsidence of Glen Coe, and the associated igneous phenomena. *Quarterly Journal of the Geological Society*, 65(1-4), 611-678.
- Cole, J.W., Milner, D.M., and Spinks, K.D.** (2005). Calderas and caldera structures: a review. *Earth-Science Reviews*, 69 (1–2), 1–26.
- Coplen, T.B., Kendall, C., and Hoppo, J.** (1983). Comparison of stable isotope reference samples. *Nature*, 302, 236–238.
- Cruden, A. R.** (1998). On the emplacement of tabular granites. *Journal of the Geological Society-London*, 155(5), 853-862.
- Çelebi, D., and Köprübaşı, N.** (2014). The geochemical and Sr–Nd isotopic characteristics of Eocene to Miocene NW Anatolian granitoids: Implications for magma evolution in a post-collisional setting. *Journal of Asian Earth Science*, 93, 275–287.
- Davies, J.H., and von Blanckenburg, F.** (1995). Slab breakoff: a model of lithosphere detachment and its test in the magmatism and deformation of collisional orogens. *Earth and Planetary Science Letters*, 129 (1–4), 85–102.

- Debon, F., and Le Fort, P.** (1983). Achemical–mineralogical classification of common plutonic rocks and associations. *Earth and Environmental Science Transactions of the Royal Society of Edinburgh*, 73 (3), 135–149.
- Defant, M.J., and Drummond, M.S.** (1990). Derivation of some modern arc magmas by melting of young subducted lithosphere. *Nature*, 347, 662–665.
- Defant, M.J., and Drummond, M.S.** (1993). Mount St. Helens: potential example of the partial melting of the subducted lithosphere in a volcanic arc. *Geology*, 21 (6), 547–550.
- Delaloye, M., and Bingöl, E.** (2000). Granitoids from Western and Northwestern Anatolia: geochemistry and modeling of geodynamic evolution. *International Geology Review*, 42 (3), 241–268.
- Depaolo, D.J.** (1981). Neodymium isotopes in the Colorado front range and crust–mantle evolution in the Proterozoic. *Nature*, 291 (5812), 193–196.
- Didier, J., and Barbarin, B.** (1991). Enclaves and granite petrology. *Developments in Petrology*. vol. 13. Elsevier, Amsterdam (625 p).
- Dilek, Y., Thy, P., Moores, E.M., and Ramsden, T.W.** (1990). Tectonic evolution of the Troodos ophiolite within the Tethyan framework. *Tectonics*, 9 (4), 811–823.
- Dilek, Y., and Altunkaynak, Ş.** (2007). Cenozoic crustal evolution and mantle dynamics of postcollisional magmatism in western Anatolia. *International Geology Review*, 49 (5), 431–453.
- Dilek, Y., and Altunkaynak, Ş.** (2009). Geochemical and temporal evolution of Cenozoic magmatism in western Turkey: mantle response to collision, slab break-off, and lithospheric tearing in an orogenic belt. *Geological Society of London Special Publications*, 311 (1), 213–233.
- Dilek, Y., Altunkaynak, Ş., and Öner, Z.** (2009). Syn-extensional granitoids in the Menderes core complex and the late Cenozoic extensional tectonics of the Aegean province. In: Ring, U., Wemické, B.B. (Eds.), *Continental Extensional Tectonics*. vol. 321. *Geological Society of London Special Publications*, pp. 197–223.
- Dilek, Y., and Altunkaynak, Ş.** (2010). Geochemistry of Neogene-Quaternary alkaline volcanism in western Anatolia, Turkey, and implications for the Aegean mantle. *International Geology Review*, 52 (4–6), 631–655.

- Downes, H.** (1990). Shear zones in the upper mantle—relation between geochemical enrichment and deformation in mantle peridotites. *Geology*, 18 (4), 374–377.
- Dunkl, I., Mikes, T., Simon, K., and von Eynatten, H.** (2008). *Brief introduction to the Windows program Pepita: data visualization, and reduction, outlier rejection, calculation of trace element ratios and concentrations from LA-ICP-MS data*. In: Sylvester, P. (Ed.), *Laser Ablation ICP-MS in the Earth Sciences: Current Practices and Outstanding Issues*. Mineralogical Association of Canada, Short Course, pp. 334–340.
- Dupuy, C., Dostal, J., Marcelot, G., Bougault, H., Joron, J.L., and Treuil, M.** (1982). Geochemistry of basalts from central and southern New Hebrides arc: implication for their source rock composition. *Earth and Planetary Science Letters*, 60 (2), 207–225.
- Eiler, J.M.** (2011). Paleoclimate reconstruction using carbonate clumped isotope thermometry. *Quaternary Science Reviews*, 30 (25–26), 3575–3588.
- Eklund, O., Konopelko, D., Rutanen, H., Fröjdö, S., and Shebanov, A.D.** (1998). 1.8 Ga Svecofennian post-collisional shoshonitic magmatism in the Fennoscandian shield. *Lithos*, 45, 87–108.
- Emre, Ö., Duman, T.Y., Özalp, S., Şaroğlu, F., Olgun, Ş., Elmacı, H., and Çan, T.** (2018). Active fault database of Turkey. *Bulletin of Earthquake Engineering*, 16 (8), 3229–3275
- England, P., Houseman, G.** (1989). Extension during continental convergence, with application to the Tibetan plateau. *Journal of Geophysical Research*, Solid Earth 94 (B12), 17561–17579.
- Ercan, T., Türkögen, A., Akyürek, B., Günay, E., Çam, A., Ateş, M., Can, B., Erkan, M., Özkirişçi, C.** (1984). Dikili-Bergama-Çandarlı (Batı Anadolu) Yöresinin Jeolojisi ve Magmatik Kayaçlarının Petrolojisi. *Jeoloji Mühendisliği Dergisi*, 8 (2), 47–60.
- Ercan, T., Satır, M., Kreuzer, H., Türkecan, A., Günay, E., Çevikbaş, A., ... Can, B.** (1985). Batı Anadolu Senozoyik volkanitlerine ait yeni kimyasal, izotopik ve radyometrik verilerin yorumu. *Türkiye Jeoloji Kurumu Bülteni*, 28, 121–136.

- Ercan, T., Satır, M., Steinitz, G., Dora, A., Sarifakioglu, E., Adis, C., ...Yildirim, T.** (1995). Biga yarımadası ile Gökçeada, Bozcaada ve Tavşan adalarındaki (KB Anadolu) Tersiyer volkanizmasının özellikleri. *Maden Tetkik Arama Dergisi*, 117, 55–86 (in Turkish).
- Erkül, F.** (2009). Tectonic significance of synextensional ductile shear zones within the Early Miocene Alaçamdağ granites, northwestern Turkey. *Geological Magazine*, 147 (4), 611–637.
- Erkül, F., Helvacı, C., and Sözbilir, H.** (2005). Evidence for two episodes of volcanism in the Bigadic borate basin and tectonic implications for western Turkey. *Geological Journal*, 40 (5), 545–570.
- Erkül, S.T.** (2012). Petrogenetic evolution of the Early Miocene Alaçamdağ volcano-plutonic complex, northwestern Turkey: implications for the geodynamic framework of the Aegean region. *International Journal of Earth Sciences*, 101 (1), 197–219.
- Erkül, F., Erkül, S.T., Ersoy, Y., Uysal, İ., and Klötzli, U.** (2013). Petrology, mineral chemistry and Sr–Nd–Pb isotopic compositions of granitoids in the central Menderes metamorphic core complex: constraints on the evolution of Aegean lithosphere slab. *Lithos*, 180, 74–91.
- Ersoy, E.Y., Helvacı, C., and Palmer, M.R.** (2010). Mantle source characteristics and melting models for the early-middle Miocene mafic volcanism in Western Anatolia: implications for enrichment processes of mantle lithosphere and origin of K-rich volcanism in post-collisional settings. *Journal of Volcanology Geothermal Research*, 198 (1), 112–128.
- Ersoy, Y.E., Helvacı, C., Uysal, İ., Karaoğlu, Ö., Palmer, M.R., and Dindi, F.** (2012). Petrogenesis of the Miocene volcanism along the İzmir-Balıkesir Transfer Zone in western Anatolia, Turkey: Implications for origin and evolution of potassic volcanism in post collisional areas. *Journal of Volcanology and Geothermal Research*, 241, 21–38.
- Ersoy, E.Y., Akal, C., Genç, Ş.C., Candan, O., Palmer, M.R., Prelević, D., ... MertzKraus, R.** (2017). U-Pb zircon geochronology of the Paleogene-Neogene volcanism in the NW Anatolia: Its implications for the Late Mesozoic-Cenozoic geodynamic evolution of the Aegean. *Tectonophysics* 717, 284–301.

- Eyübođlu, Y., Chung, S.L., Santosh, M., Dudas, F.O., and Akaryalı, E.** (2011). Transition from shoshonitic to adakitic magmatism in the eastern Pontides, NE Turkey: implications for slab window melting. *Gondwana Research*, 19 (2), 413–429.
- Festa, V., Caggianelli, A., Langone, A., and Prosser, G.** (2013). Time–space relationships among structural and metamorphic aureoles related to granite emplacement: a case study from the Serre Massif (southern Italy). *Geological Magazine*, 150 (3), 441–454.
- Fowler, M.B., Kocks, H., Darbyshire, D.P.F., and Greenwood, P.B.** (2008). Petrogenesis of high Ba–Sr plutons from the northern highlands terrane of the British Caledonian Province. *Lithos* 105, 129–148.
- Fytikas, M., Innocenti, F., Manetti, P., Peccerillo, A., Mazzuoli, R., and Villari, L.** (1984). Tertiary to Quaternary evolution of volcanism in the Aegean region. *Geological Society of London Special Publications*, 17 (1), 687–699.
- Genç, Ş.C., and Yılmaz, Y.** (1997). An example of post-collisional magmatism in Northwestern Anatolia: the Kızderbent volcanics (Armutlu peninsula, Turkey). *Turkish Journal of Earth Sciences*, 6, 33–42.
- Genç, Ş.C.** (1998). Evolution of the Bayramiç magmatic complex. *J. Volcanol. Geoth. Res.* 85 (1–4), 233–249.
- Güleç, N.** (1991). Crust–mantle interaction in western Turkey: implications from Sr and Nd isotope geochemistry of Tertiary and Quaternary volcanics. *Geological Magazine*, 23, 417–435.
- Gülen, L.** (1990). Isotopic characterization of Aegean magmatism and geodynamic evolution of Aegean subduction. In: Savascin, M.Y., Eronat, A.H. (Eds.), *International Earth Science Colloquium on the Aegean Region (IESCA), İzmir, Turkey, Proceedings II*, pp. 143–166.
- Güraslan, I. N., and Altunkaynak, Ş.** (2019). Role of mantle and lower continental crust in the genesis of Eocene post-collisional granitoids: Insights from the Topuk pluton (NW Turkey). *Journal of Asian Earth Sciences*, 179, 365-384.
- Hall, A., Pereira, M.D., and Bea, F.** (1996). The abundance of ammonium in the granites of central Spain, and the behaviour of the ammonium ion during anatexis and fractional crystallization. *Mineralogy and Petrology*, 56 (1–2), 105–123.

- Harris, C., and Vogeli, J.** (2010). Oxygen isotope composition of garnet in the Peninsula Granite, Cape Granite Suite, South Africa: constraints on melting and emplacement mechanisms. *South African Journal of Geology*, 113 (4), 401–412.
- Harris, N.B.W., Kelley, S., and Okay, A.I.** (1994). Post- collisional magmatism and tectonics in northwest Anatolia. *Contributions to Mineralogy and Petrology*, 117, 241–252.
- Harris, C., Faure, K., Diamond, R.E., and Scheepers, R.** (1997). Oxygen and hydrogen isotope geochemistry of S-and I-type granitoids: the cape granite suite, South Africa. *Chemical Geology*, 143 (1–2), 95–114.
- Hart, S.R.** (1984). He diffusion in olivine. *Earth and Planetary Science Letters*, 70 (2), 297–302.
- Hart, S.R., Gerlach, D.C., and White, W.M.** (1986). A possible new Sr-Nd-Pb mantle array and consequences for mantle mixing. *Geochimica et Cosmochimica Acta*, 50 (7), 1551–1557.
- Hart S.R.** (1988). Heterogeneous mantle domains: signatures, genesis and mixing chronologies. *Earth and Planetary Science Letters*, 90 (3), 273–296.
- Hatch, J.R., and Leventhal, J.S.** (1992.) Relationship between inferred redox potential of the depositional environment and geochemistry of the Upper Pennsylvanian (Missourian) Stark Shale Member of the Dennis Limestone, Wabaunsee County, Kansas, USA. *Chemical Geology*, 99 (1–3), 65–82.
- Hibbard, M.J.** (1991). Textural anatomy of twelve magma-mixed granitoid systems. In: Didier, J., Barbarin, B. (Eds.), *Enclaves and Granite Petrology, Developments in Petrology*, vol. 13. Elsevier, Amsterdam, pp. 431–444.
- Hills, S.E.** (1963). *Elements of Structural Geology*. Wiley, New York.
- van Hinsbergen, D.J.J., Hafkenscheid, E., Spakman, W., Meulenkamp, J.E., and Wortel, R.** (2005). Nappe stacking resulting from subduction of oceanic and continental lithosphere below Greece. *Geology*, 33 (4), 325–328.
- Holland, T., and Blundy, J.** (1994). Non-ideal interactions in calcic amphiboles and their bearing on amphibole-plagioclase thermometry. *Contributions to Mineralogy and Petrology*, 116(4), 433-447.

- Houseman, G.A., and Molnar, P.** (1997). Gravitational (Rayleigh–Taylor) instability of a layer with non-linear viscosity and convective thinning of continental lithosphere. *Geophysical Journal International*, 128 (1), 125–150.
- Hutton, D.H.** (1988). Granite emplacement mechanisms and tectonic controls: inferences from deformation studies. *Earth and Environmental Science Transactions of the Royal Society of Edinburgh*, 79 (2–3), 245–255.
- Ionov, D.A., Dupuy, C., O'Reilly, S.Y., Kopylova, M.G., and Genshaft, Y.S.** (1993). Carbonated peridotite xenoliths from Spitsbergen: implications for trace element signature of mantle carbonate metasomatism. *Earth and Planetary Science Letters*, 119 (3), 283–297.
- Irvine, T.N.J., and Baragar, W.R.A.F.** (1971). A guide to the chemical classification of the common volcanic rocks. *Canadian Journal of Earth Science*, 8 (5), 523–548.
- Janoušek, V., Farrow, C.M., and Erban, V.** (2006). Interpretation of whole-rock geochemical data in igneous geochemistry: introducing Geochemical Data Toolkit (GCDkit). *Journal of Petrology*, 47 (6), 1255–1259.
- John, D.A.** (1995). Tilted middle Tertiary ash-flow calderas and subjacent granitic plutons, southern Stillwater Range, Nevada: cross sections of an Oligocene igneous center. *Geological Society of America Bulletin*, 107 (2), 180–200.
- Johnson, M. C., and Rutherford, M. J.** (1989). Experimental calibration of the aluminum-in-hornblende geobarometer with application to Long Valley caldera (California) volcanic rocks. *Geology*, 17(9), 837-841.
- Kamacı, O., and Altunkaynak, S.** (2011). Petrogenetic implications of two contrasting granite types in the çataldag plutonic complex, NW Turkey. *Mineralogical Magazine*, 1138.
- Kamacı, Ö., Ünal, A., Altunkaynak, S., Georgiev, S., and Billor, Z.M.** (2017). The Çataldag Plutonic Complex in Western Anatolia: roles of different granites on the crustal buildup in connection with the core complex development. *Active Global Seismology*, 225, 189.
- Kamacı, Ö., and Altunkaynak, Ş.** (2019). Cooling and deformation history of the Çataldağ Metamorphic Core Complex (NW Turkey). *Journal of Asian Earth Sciences*, 172, 279–291.

- Karacık, Z., and Yılmaz, Y.** (1998a). Geology of the ignimbrites and the associated volcano–plutonic complex of the Ezine area, northwestern Anatolia. *Journal of Volcanology and Geothermal Research*, 85 (1), 251–264.
- Karacık, Z., and Yılmaz, Y.** (1998b). The ignimbrite eruptions and the associated magmatic rocks of the Ezine area, northern Anatolia. *Journal of Volcanology and Geothermal Research*, 85, 252–264.
- Karacık, Z., Yılmaz, Y., Pearce, J., and Ece, I.** (2008). Petrochemistry of the South Marmara granitoids, northwestern Anatolia. *International Journal of Earth Sciences*, 97, 1181–1200.
- Kempton, P.D., and Harmon, R.S.** (1992). Oxygen isotope evidence for large-scale hybridization of the lower crust during magmatic underplating. *Geochimica et Cosmochimica Acta*, 56 (3), 971–986.
- Keskin, M.** (2003). Magma generation by slab steepening and breakoff beneath a subduction-accretion complex: an alternative model for collision-related volcanism in eastern Anatolia, Turkey. *Geophysical Research Letters*, 30 (24).
- Koprubasi, N., and Aldanmaz, E.** (2004). Geochemical constraints on the petrogenesis of Cenozoic I-type granitoids in Northwest Anatolia, Turkey: evidence for magma generation by lithospheric delamination in a post-collisional setting. *International Geology Review*, 46 (8), 705–729.
- Kuepouo, G., Tchouankoue, J.P., Nagao, T., and Sato, H.** (2006). Transitional tholeiitic basalts in the Tertiary Bana volcano–plutonic complex, Cameroon Line. *Journal of African Earth Sciences*, 45 (3), 318–332.
- Layer, P.W.** (2000). Argon-40/argon-39 age of the El'gygytgyn impact event, Chukotka, Russia. *Meteorit. Meteoritics & Planetary Science*, 35 (3), 591–599.
- Layer, P.W., Hall, C.M., and York, D.** (1987). The derivation of $^{40}\text{Ar}/^{39}\text{Ar}$ age spectra of single grains of hornblende and biotite by laser step-heating. *Geophysical Research Letters*, 14 (7), 757–760.
- Le Bas, M.J., Le Maitre, R.W., Streckeisen, A., and Zanettin, B.** (1986). A chemical classification of volcanic rocks based on the total alkali-silica diagram. *Journal of Petrology*, 27 (3), 745–750.

- Li, X.H., Li, Z.X., Li, W.X., Liu, Y., Yuan, C., Wei, G., and Qi, C.** (2007). U–Pb zircon, geochemical and Sr–Nd–Hf isotopic constraints on age and origin of Jurassic I-and A-type granites from Central Guangdong, SE China: a major igneous event in response to foundering of a subducted flat-slab? *Lithos*, 96 (1), 186–204.
- Ludwig, K.** (2003). Isoplot/Ex 3.0. A Geochronological Toolkit for Microsoft Excel. *Berkeley Geochronology Center Special Publication*, 4.
- Marsh, B. D.** (1982). On the mechanics of igneous diapirism, stoping, and zone melting. *American Journal of Science*, 282(6), 808-855.
- Mason, P.R., Downes, H., Thirlwall, M.F., Seghedi, I., Szakács, A., Lowry, D., and Matthey, D.** (1996). Crustal assimilation as a major petrogenetic process in the East Carpathian Neogene and Quaternary continental margin arc, Romania. *Journal of Petrology*, 37 (4), 927–959.
- McCaffrey, K. J. W., and Petford, N.** (1997). Are granitic intrusions scale invariant?. *Journal of the Geological Society*, 154(1), 1-4.
- McCulloch, M.T., and Gamble, J.A.** (1991). Geochemical and geodynamical constraints on subduction zone magmatism. *Earth and Planetary Science Letters*, 102 (3–4), 358–374.
- McDonough, W.F.** (1990). Constraints on the composition of the continental lithospheric mantle. *Earth and Planetary Science Letters*, 101 (1), 1–18.
- McDougall, I., and Harrison, T.M.** (1999). Geochronology and Thermochronology by the $^{40}\text{Ar}/^{39}\text{Ar}$ Method. *Oxford University Press on Demand*.
- Meulenkamp, J.E., Wortel, M.J.R., Van Wamel, W.A., Spakman, W., and Strating, E.H.** (1988). On the Hellenic subduction zone and the geodynamic evolution of Crete since the late middle Miocene. *Tectonophysics*, 146 (1–4), 203–215.
- Middlemost, E.A.K.** (1985). *Magmas and Magmatic Rocks: An Introduction to Igneous Petrology*. Longman, London.
- Middlemost, E.A.** (1994). Naming materials in the magma/igneous rock system. *Earth-Science Reviews*, 37 (3–4), 215–224.
- Molnar, P., England, P., and Martinod, J.** (1993). Mantle dynamics, uplift of the Tibetan plateau, and the Indian monsoon. *Reviews of Geophysics*, 31 (4), 357–396.

- Musumeci, G., and Vaselli, L.** (2012). Neogene deformation and granite emplacement in the metamorphic units of northern Apennines (Italy): Insights from mylonitic marbles in the Porto Azzurro pluton contact aureole (Elba Island). *Geosphere*, 8(2), 470-490.
- Myers, J.S., Voordouw, R.J., and Tettelaar, T.A.** (2008). Proterozoic anorthosite–granite Nain batholith: structure and intrusion processes in an active lithosphere-scale fault zone, northern Labrador. *Canadian Journal of Earth Sciences*, 45 (8), 909–934.
- Okay, A.İ.** (1984). Distribution and characteristics of the north-west Turkish blueschists. *Geological Society of London Special Publications*, 17 (1), 455–466.
- Okay, A.I., Siyako, M., and Bürkan, K.A.** (1990). Geology and tectonic evolution of the Biga Peninsula (in Turkish). *Bulletin of the Turkish Association of Petroleum Geologists*, 2, 83–121.
- Okay, A.I., Satir, M., Maluski, H., Siyako, M., Monie, P., Metzger, R., and Akyüz, S.** (1996). Paleo and neo-Tethyan events in Northwest Turkey: geological and geochronological constraints. *Tectonics of Asia*. Cambridge University Press, 420–441.
- Okay, A.I.** (1997). Jadeite-K-feldspar rocks and jadeitites from Northwest Turkey. *Mineralogical Magazine*, 61, 835–843.
- Okay, A.I., and Tüysüz, O.** (1999). Tethyan sutures of northern Turkey. *Geological Society of London Special Publications*, 156 (1), 475–515.
- Okay, A.I., and Satir, M.** (2000). Coeval plutonism and metamorphism in a latest Oligocene metamorphic core complex in northwest Turkey. *Geological Magazine*, 137 (5), 495–516.
- Okay, A., and Satir, M.** (2006). Geochronology of Eocene plutonism and metamorphism in northwest. *Geodinamica Acta*, 19 (5), 251–266.
- Oner, Z., Dilek, Y., and Kadioglu, Y. K.** (2010). Geology and geochemistry of the synextensional Salihli granitoid in the Menderes core complex, western Anatolia, Turkey. *International Geology Review*, 52(2-3), 336-368.
- Ozgenç, I., and Ilbeyli, N.** (2008). Petrogenesis of the Late Cenozoic Egrigöz pluton in western Anatolia, Turkey: implications for magma genesis and crustal processes. *International Geology Review*, 50(4), 375-391.

- Paces, J. B., and Miller Jr, J. D.** (1993). Precise U-Pb ages of Duluth complex and related mafic intrusions, northeastern Minnesota: Geochronological insights to physical, petrogenetic, paleomagnetic, and tectonomagmatic processes associated with the 1.1 Ga midcontinent rift system. *Journal of Geophysical Research: Solid Earth*, 98(B8), 13997-14013.
- Patiño Douce, A.E.** (1996). Effects of pressure and H₂O content on the compositions of primary crustal melts. *Earth and Environmental Science Transactions of the Royal Society of Edinburgh*, 87 (1–2), 11–21.
- Patiño Douce, A.E., and McCarthy, T.C.** (1998). Melting of crustal rocks during continental collision and subduction. *When Continents Collide: Geodynamics and Geochemistry of Ultrahigh-Pressure Rocks*. Springer, Netherlands, pp. 27–55.
- Patiño Douce, A.E.** (1999). What do experiments tell us about the relative contributions of crust and mantle to the origin of granitic magmas? *Geological Society of London Special Publications*, 168 (1), 55–75.
- Paterson, S. R., and Fowler Jr, T. K.** (1993). Re-examining pluton emplacement processes. *Journal of Structural Geology*, 15(2), 191-206.
- Pearce, J.A.** (1982). Trace element characteristics of lavas from destructive plate boundaries. *Andesites*, 8, 525–548.
- Pearce, J.A., Bender, J.F., De Long, S.E., Kidd, W.S.F., Low, P.J., Güner, Y., ... Mitchell, J.G.** (1990). Genesis of collision volcanism in Eastern Anatolia, Turkey. *Journal of Volcanology and Geothermal Research*, 44 (1–2), 189–229.
- Pearce, J.A., and Peate, D.W.** (1995). Tectonic implications of the composition of volcanic arc magmas. *Annual Review of Earth and Planetary Sciences*, 23 (1), 251–285.
- Pearce, J.A., Stern, R.J., Bloomer, S.H., and Fryer, P.** (2005). Geochemical mapping of the Mariana arc-basin system: Implications for the nature and distribution of subduction components. *Geochemistry, Geophysics, Geosystems*, 6 (7).
- Peccerillo, A., and Taylor, S.R.** (1976). Geochemistry of Eocene calcalkaline volcanic rocks from the Kastamonu area, northern Turkey. *Contributions to Mineralogy and Petrology*, 58, 63–81.

- Peng, R., Zhai, Y., Li, C., and Ripley, E.M.** (2013). The Erbutu Ni-cu deposit in the central Asian Orogenic Belt: a Permian magmatic sulfide deposit related to boninitic magmatism in an arc setting. *Economic Geology*, 108 (8), 1879–1888.
- Pe-piper, G., and Piper, D.J.** (1989). Spatial and temporal variation in late Cenozoic back-arc volcanic rocks, Aegean Sea region. *Tectonophysics* 169 (1–3), 113–134.
- Petford, N., and Atherton, M.** (1996). Na-rich partial melts from newly underplated basaltic crust: the cordillera Blanca batholith, Peru. *Journal of Petrology*, 37 (6), 1491–1521.
- Petford, N., Cruden, A. R., McCaffrey, K. J. W., and Vigneresse, J. L.** (2000). Granite magma formation, transport and emplacement in the Earth's crust. *Nature*, 408(6813), 669.
- Petford, N., and Gallagher, K.** (2001). Partial melting of mafic (amphibolitic) lower crust by periodic influx of basaltic magma. *Earth and Planetary Science Letters*, 193 (3), 483–499.
- Pitcher, W.S.** (1979). The nature, ascent and emplacement of granitic magmas. *Journal of Geological Society*, 136 (6), 627–662.
- Pitcher W.S.** (1993). *The Nature and Origin of Granite*. Chapman & Hall, Glasgow
- Qin, J.F., Lai, S.C., Grapes, R., Diwu, C., Ju, Y.J., and Li, Y.F.** (2009). Geochemical evidence for origin of magma mixing for the Triassic monzonitic granite and its enclaves at Mishuling in the Qinling orogen (Central China). *Lithos*, 112, 259–276.
- Rapp, R.P., and Watson, E.B.** (1995). Dehydration melting of metabasalt at 8–32 kbar: implications for continental growth and crust-mantle recycling. *Journal of Petrology*, 36 (4), 891–931.
- Read, H.H.** (1948). A commentary on place in plutonism. *Quarterly Journal of the Geological Society of London*, 104 (1–4), 155–205.
- Read, H. H.** (1957). *The granite controversy: geological addresses illustrating the evolution of a disputant*. London, Murby.
- Renne, P.R., Deino, A.L., Walter, R.C., Turrin, B.D., Swisher III, C.C., Becker, T.A., ... Jaouni, A.R.** (1994). Intercalibration of astronomical and radioisotopic time. *Geology*, 22 (9), 783–786.

- Renne, P.R., Mundil, R., Balco, G., Min, K., and Ludwig, K.R.** (2010). Joint determination of ^{40}K decay constants and $^{40}\text{Ar}^*/^{40}\text{K}$ for the Fish Canyon sanidine standard, and improved accuracy for $^{40}\text{Ar}/^{39}\text{Ar}$ geochronology. *Geochimica et Cosmochimica Acta*, 74, 5349–5367.
- Richey, J.E.** (1928). The structural relations of the Mourne granites, Northern Ireland. *Quarterly Journal of the Geological Society of London*, 83 (1–5), 653–NP.
- Richey, J.E.** (1932). The tertiary ring complex of Slieve Gullion (Ireland), with petrological notes by Herbert Henry Thomas. *Quarterly Journal of the Geological Society of London*. 88 (1–4), 776–849.
- Ridolfi, F., Renzulli, A., and Puerini, M.** (2010). Stability and chemical equilibrium of amphibole in calc-alkaline magmas: an overview, new thermobarometric formulations and application to subduction-related volcanoes. *Contributions to Mineralogy and Petrology*, 160(1), 45–66.
- Ridolfi, F., and Renzulli, A.** (2012). Calcic amphiboles in calc-alkaline and alkaline magmas: thermobarometric and chemometric empirical equations valid up to 1,130° C and 2.2 GPa. *Contributions to Mineralogy and Petrology*, 163(5), 877–895.
- Rioux, M., Farmer, G.L., Bowring, S.A., Wooton, K.M., Amato, J.M., Coleman, D.S., and Verplanck, P.L.** (2016). The link between volcanism and plutonism in epizonal magma systems; high-precision U-Pb zircon geochronology from the Organ Mountains caldera and batholith, New Mexico. *Contributions to Mineralogy and Petrology*, 171 (2), 13.
- Rollinson, H.R.** (1993). A terrane interpretation of the Archaean Limpopo Belt. *Geological Magazine*, 130 (6), 755–765.
- Rudnick, R.L., McDonough, W.F., and Chappell, B.W.** (1993). Carbonatite metasomatism in the northern Tanzanian mantle: petrographic and geochemical characteristics. *Earth and Planetary Science Letters*, 114 (4), 463–475.
- Rushmer, T.** (1993). Experimental high-pressure granulites: some applications to natural mafic xenolith suites and Archean granulite terranes. *Geology* 21 (5), 411–414.
- Samson, S.D., and Alexander Jr., E.C.** (1987). Calibration of the interlaboratory $^{40}\text{Ar}/^{39}\text{Ar}$ dating standard, MMhb-1. *Chemical Geology: Isotope Geoscience Section*, 66 (1–2), 27–34.

- Sardinha, A. S., de Mesquita Barros, C. E., and Krymsky, R.** (2006). Geology, geochemistry, and U–Pb geochronology of the Archean (2.74 Ga) Serra do Rabo granite stocks, Carajás Metallogenic Province, northern Brazil. *Journal of South American Earth Sciences*, 20(4), 327–339.
- Savaşçın, M.Y., and Güleç, N.** (1990). Relationship between magmatic and tectonic activities in western Turkey. In: *Proceedings of the International Earth Science Colloquium on the Aegean Region (IESCA)*, pp. 300–313.
- Seager, W.R., and McCurry, M.** (1988). The cogenetic organ cauldron and batholith, south central New Mexico: Evolution of a large-volume ash flow cauldron and its source magma chamber. *Journal of Geophysical Research*, Solid Earth 93 (B5), 4421–4433.
- Seyitoğlu, G., and Scott, B.** (1991). Late Cenozoic crustal extension and basin formation in West Turkey. *Geological Magazine*, 128 (2), 155–166.
- Seyitoğlu, G., and Scott, B.** (1992). Late Cenozoic volcanic evolution of the northeastern Aegean region. *Journal of Volcanology and Geothermal Research*, 54, 157–176.
- Seyitoğlu, G., and Scott, B.C.** (1992). The age of the Büyük Menderes graben (west Turkey) and its tectonic implications. *Geological Magazine*, 129 (2), 239–242.
- Seyitoğlu, G., and Scott, B. C.** (1996). Age of the Alaşehir graben (west Turkey) and its tectonic implications. *Geological Journal*, 31(1), 1–11.
- Seyitoğlu, G.** (1997). Late Cenozoic tectono–sedimentary development of the Selendi and Usak–Güre basins: a contribution to the discussion on the development of E–W and north trending basins in western Turkey. *Geological Magazine*, 134, 163–175.
- Seyitoğlu, G., Anderson, D., Nowell, G., and Scott, B.** (1997). The evolution from Miocene potassic to Quaternary sodic magmatism in western Turkey: implications for enrichment processes in the lithospheric mantle. *Journal of Volcanology and Geothermal Research*, 76, 127–147.
- Shand, S.J.** (1949). Rocks of the mid-Atlantic ridge. *Journal of Geology*, 57 (1), 89–92.
- Sircombe, K. N.** (2004). AgeDisplay: an EXCEL workbook to evaluate and display univariate geochronological data using binned frequency histograms and probability density distributions. *Computers & Geosciences*, 30(1), 21–31.

- Sláma, J., Košler, J., Condon, D. J., Crowley, J. L., Gerdes, A., Hanchar, J. M., ... Schaltegger, U.** (2008). Plešovice zircon—a new natural reference material for U–Pb and Hf isotopic microanalysis. *Chemical Geology*, 249(1-2), 1-35.
- Spakman, W.** (1990). Tomographic images of the upper mantle below Central Europe and the Mediterranean. *Terra Nova* 2 (6), 542–553.
- Streck, M.J.** (2008). Mineral textures and zoning as evidence for open system processes. *Reviews in Mineralogy and Geochemistry*, 69 (1), 595–622.
- Sun, S.S., and McDonough, W.S.** (1989). Chemical and isotopic systematics of oceanic basalts: implications for mantle composition and processes. *Geological Society of London Special Publications*, 42 (1), 313–345.
- Stevenson, C.** (2009). The relationship between forceful and passive emplacement: The interplay between tectonic strain and magma supply in the Rosses Granitic Complex, NW Ireland. *Journal of Structural Geology*, 31 (3), 270–287.
- Stevenson, C.T., Owens, W.H., and Hutton, D.H.** (2007). Flow lobes in granite: The determination of magma flow direction in the Trawenagh Bay Granite, northwestern Ireland, using anisotropy of magnetic susceptibility. *Geological Society of America Bulletin*, 119 (11–12), 1368–1386.
- Stevenson, C., Hutton, D., and Price, A.** (2008). The Trawenagh Bay Granite and a new model for the emplacement of the Donegal Batholith. *Earth and Environmental Science Transactions of the Royal Society of Edinburgh*. 97 (4), 455–477.
- Şengör, A.M.C., and Yilmaz, Y.** (1981). Tethyan evolution of Turkey: a plate tectonic approach. *Tectonophysics* 75 (3–4), 181193203–190199241.
- Şengör, A.M.C., Natalin, B.A., and Burtman, V.S.** (1993). Evolution of the Altiid tectonic collage and Palaeozoic crustal growth in Eurasia. *Nature*, 364 (6435), 299–307.
- Şengör, A.M.C., Özeren, S., Genç, T., and Zor, E.** (2003). East Anatolian high plateau as a mantle-supported, north-south shortened domal structure. *Geophysical Research Letters*. 30 (24).
- Takahashi, M.** (1986). Anatomy of a middle Miocene Valles-type caldera cluster: Geology of the Okueyama volcano-plutonic complex, southwest Japan. *Journal of Volcanology and Geothermal Research*, 29 (1–4), 33–70.

- Tarney, J., and Jones, C.E.** (1994). Trace element geochemistry of orogenic igneous rocks and crustal growth models. *Journal of Geological Society*, 151 (5), 855–868.
- Taylor, E.M.** (1978). *Field Geology of SW Broken Top Quadrangle, Oregon (No. 2)*. State of Oregon, Dept. of Geology and Mineral Industries.
- Thirlwall, M.F., Smith, T.E., Graham, A.M., Theodorou, N., Hollings, P., Davidson, J.P., and Arculus, R.J.** (1994). High field strength element anomalies in arc lavas: source or process? *Journal of Petrology*, 35 (3), 819–838.
- Tomek, F., Žák, J., Holub, F.V., Chlupáčová, M., and Verner, K.** (2014). Growth of intra-caldera lava domes controlled by various modes of caldera collapse, the Štiavnica volcano-plutonic complex, Western Carpathians. *Journal of Volcanology and Geothermal Research*, 311, 183–197.
- Topuz, G., and Okay, A.I.** (2017). Late Eocene-Early Oligocene two-mica granites in NW Turkey (the Uludağ Massif): Water-fluxed melting products of a mafic metagreywacke. *Lithos*, 268, 334–350.
- Tuttle, O.F., and Bowen, N.L.** (1958). Origin of granite in the light of experimental studies in the system NaAlSiO₈-KAlSi₃O₈-SiO₂-H₂O. *Geological Society of America*.
- Ünal, A., and Altunkaynak, Ş.** (2018). Nature and genesis of potassic high Ba-Sr granitoids associated with syn-convergent extension in NW Turkey. *Lithos*, 316–317, 261–277.
- Ünal, A., and Altunkaynak, Ş.** (2019). Interplay between volcanic and plutonic systems: A case study of the early Miocene Solarya Volcano-plutonic Complex in NW Anatolia (Turkey). *Journal of Asian Earth Sciences*, 179, 319-336.
- Ünal, A., Altunkaynak Ş., Kamacı Ö., Dunkl I., and Benowitz J.** (2019). The emplacement of shallow intrusions into the upper crust: Implications from the geochronology, geothermo-barometry and emplacement mechanisms of Solarya Pluton (NW Anatolia). *Journal of Asian Earth Sciences*, 183.
- Wei, C.S., Zheng, Y.F., and Zhao, Z.F.** (2000). Hydrogen and oxygen isotope geochemistry of A-type granites in the continental margins of eastern China. *Tectonophysics* 328 (1), 205–227.

- Whalen, J.B., Jenner, G.A., Longstaffe, F.J., Robert, F., and Gariépy, C.** (1996). Geochemical and isotopic (O, Nd, Pb and Sr) constraints on A-type granite petrogenesis based on the topsails igneous suite, Newfoundland Appalachians. *Journal of Petrology*, 37 (6), 1463–1489.
- Wiedenbeck, M. A. P. C., Alle, P., Corfu, F., Griffin, W. L., Meier, M., Oberli, F. V., ... Spiegel, W.** (1995). Three natural zircon standards for U-Th-Pb, Lu-Hf, trace element and REE analyses. *Geostandards newsletter*, 19(1), 1-23.
- Winchester, J.A., and Floyd, P.A.** (1977). Geochemical discrimination of different magma series and their differentiation products using immobile elements. *Chemical Geology*, 20, 325–343.
- Wyllie, P.J., Cox, K.G., and Biggar, G.M.** (1962). The habit of apatite in synthetic systems and igneous rocks. *Journal of Petrology*, 3 (2), 238–243.
- Yan, L.L., He, Z.Y., Beier, C., and Klemd, R.** (2018). Zircon trace element constrains on the link between volcanism and plutonism in SE China. *Lithos*, 320–321, 28–34.
- Yang, L., Dilek, Y., Wang, Z., Weinberg, R., and Liu, Y.** (2017). Late Jurassic high Ba-Sr Linglong granites in the Jiaodong Peninsula, East China: Lower crustal melting products in the eastern North China Craton. *Geological Magazine*, 155(5), 1040-1062.
- Yang, J.H., Wu, F.Y., Chung, S.L., Wilde, S.A., and Chu, M.F.** (2004). Multiple sources for the origin of granites: geochemical and Nd/Sr isotopic evidence from the Gudaoling granite and its mafic enclaves, northeast China. *Geochimica et Cosmochimica Acta*, 68 (21), 4469–4483.
- Yaxley, G.M., Green, D.H., and Kamenetsky, V.** (1998). Carbonatite metasomatism in the southeastern Australian lithosphere. *Journal of Petrology*, 39 (11-12), 1917–1930.
- Ye, H.M., Li, X.H., Li, Z.X., and Zhang, C.L.** (2008). Age and origin of high Ba–Sr appinite–granites at the northwestern margin of the Tibet plateau: implications for early Paleozoic tectonic evolution of the western Kunlun orogenic belt. *Gondwana Research*, 13, 126–138.
- Yilmaz, Y.** (1989). An approach to the origin of young volcanic rocks of western Turkey. In *Tectonic evolution of the Tethyan region*, (pp. 159-189). Springer, Dordrecht.

- Yılmaz, Y.** (1990). Comparison of young volcanic associations of western and eastern Anatolia under compressional regime; a review *Journal of Volcanology and Geothermal Research*, 44, 69–87.
- Yılmaz, Y.** (1995). Ege bölgesinde genç magmatizmanın oluşumu ile litosferin evrimi arasındaki ilişki üzerine düşünceler. *Jeofizik*, 9 (10), 107–110.
- Yılmaz, Y., Polat, A.** (1998). Geology and evolution of the Thrace volcanism, Turkey. *Acta Vulcanologica*, 10 (2), 293–303.
- Yılmaz, Y., Tüysüz, O., Yiğitbaş, E., Genç, Ş.C., and Şengör, A.M.C.** (1997). Geology and tectonic evolution of the Pontides. In: Robinson, A.G. (Ed.), *Regional and Petroleum Geology of the Black Sea and Surrounding Region*. vol. 68. American Association of Petroleum Geologists, Memoir, pp. 183–226.
- Yılmaz, Y., Genç, Ş.C., Gürer, F., Bozcu, M., Yılmaz, K., Karacık, Z., Elmas, A., and Elmas, A.** (2000). When did the western Anatolian grabens begin to develop? *Geological Society of London Special Publications*, 173 (1), 353–384.
- Yılmaz, Y., Genç, Ş. C., Karacık, Z., and Altunkaynak, Ş.** (2001). Two contrasting magmatic associations of NW Anatolia and their tectonic significance. *Journal of Geodynamics*, 31(3), 243-271.
- Yılmaz, E., Güleç, N., Kuşcu, İ., and Lentz, D.R.** (2014). Geology, geochemistry, and geochronology of Fe-oxide Cu (± Au) mineralization associated with Şamlı pluton, western Turkey. *Ore Geology Reviews*, 57, 191–215.
- Yuan, C., Zhou, M.F., Sun, M., Zhao, Y.J., Wilde, S.A., Long, X.P., and Yan, D.P.** (2010). Triassic granitoids in the eastern Songpan Ganzi Fold Belt, SW China: magmatic response to geodynamics of the deep lithosphere. *Earth and Planetary Science Letters*, 290, 481–492.
- Yücel-Öztürk, Y.** (2016). O, Sr and Nd isotopic constraints on Cenozoic granitoids of Northwestern Anatolia, Turkey: Enrichment by subduction zone fluids. *Journal of African Earth Sciences*, 117, 12–28.
- Zindler, A., and Hart, S.** (1986). Chemical geodynamics. *Annual Review of Earth and Planetary Sciences*, 14 (1), 493–571.



CURRICULUM VITAE



Name Surname : Alp ÜNAL
Place and Date of Birth : Çankaya/ 21.07.1989
-Mail : alp.unal@itu.edu.tr

EDUCATION :

- **B.Sc.** : 2011, Istanbul Technical University, Faculty of Mines, Geological Engineering Department
- **M.Sc.** : 2013, Istanbul Technical University, Faculty of Mines, Geological Engineering Department

PROFESSIONAL EXPERIENCE AND REWARDS:

- 2013-2019 Istanbul Technical University Faculty of Mines Research Assistant.
- 2018 TUBITAK 2214a Scholarship

PUBLICATIONS, PRESENTATIONS AND PATENTS ON THE THESIS:

- **Ünal, A.,** and Altunkaynak Ş., (2018). Nature and genesis of potassic, high Ba-Sr granitoids associated with syn-convergent extension in NW Turkey, *Lithos*, 316-317: 261-277.
- **Ünal, A.,** and Altunkaynak, Ş. (2019). Interplay between volcanic and plutonic systems: A case study of the early Miocene Solarya Volcano-plutonic Complex in NW Anatolia (Turkey). *Journal of Asian Earth Sciences*, 179, 319-33.
- **Ünal, A.,** Altunkaynak Ş., Kamacı Ö., Dunkl I., and Benowitz J., (2019). The emplacement of shallow intrusions into the upper crust: Implications from the geochronology, geothermo-barometry and emplacement mechanisms of Solarya Pluton (NW Anatolia), *Journal of Asian Earth Sciences*, 183.

- **Ünal A.**, Kamacı Ö., and Altunkaynak Ş. (2014). “Solarya Pluton (Balıkesir): An example to the epizonal plutons of NW Anatolia”, *67. Geological Congress of Turkey*, p. 498-499.
- **Ünal A.**, Kamacı Ö., and Altunkaynak Ş. (2014). “The Solarya Volcano-Plutonic Complex (NW Turkey): Petrography, Petrogenesis and Tectonic Implications”, *EGU General Assembly Conference Abstracts*, Vol. 16, p. 9096.
- **Ünal A.**, Kamacı Ö., and Altunkaynak Ş. (2015). “Petrogenesis of Post-collisional high Ba-Sr granitoids: the Solarya Pluton, NW Turkey.” *Geophysical Research Abstracts*, Vol. 17, p. 7014.
- **Ünal A.**, and Altunkaynak Ş. (2016). “The Petrology and Tectono-magmatic evolution of Solarya Volcano-Plutonic Complex (Balıkesir, NW Anatolia), *69. Geological Congress of Turkey*.
- **Ünal A.**, Altunkaynak Ş., and Benowitz, J. A. (2016). Petrogenesis of the post-collisional Oligo-Miocene Volcanism in NW Anatolia (Turkey): Balıkesir Volcanites. *EGU General Assembly Conference Abstracts*, Vol. 18, p. 4533.
- **Ünal A.**, and Altunkaynak Ş. (2016). “Geochemistry And Sr-Nd-Pb Isotopic Characteristics Of Solarya Pluton (Balıkesir): An Example Of High Ba-Sr Granites Of Western Anatolia”, *7th Geochemistry Symposium, Antalya*, p. 232-233.
- **Ünal A.**, and Altunkaynak Ş. (2017). “Emplacement of the Solarya Pluton (NW Turkey)”, *EGU General Assembly Conference Abstracts*, Vol. 19, p. 8170.
- **Ünal A.**, and Altunkaynak Ş. (2017). “Mineral Chemistry, Geothermobarometer Calculations and Emplacement Mechanisms of Solarya Pluton (NW Anatolia)”, *40th Geology Symposium*, p. 156-157.
- **Ünal A.**, and Altunkaynak Ş. (2018). “Role of the Mantle-Continental Crust Interactions in the Generation of NW Anatolian Oligo-Miocene Volcanism: Geochemical and Isotopic Evidences from Balıkesir Volcanites “, *8th Geochemistry Symposium, Antalya*, p. 90-91.

OTHER PUBLICATIONS, PRESENTATIONS AND PATENTS:

- Altunkaynak Ş., **Ünal A.**, Howarth, G. H., Aldanmaz, E., and Nývlt, D. (2019). The origin of low-ca olivine from ultramafic xenoliths and host basaltic lavas in a back-arc setting, James Ross Island, Antarctic Peninsula. *Lithos*, 342-343, 276-287.
- Altunkaynak Ş., Aldanmaz E., Güraslan I.N., Çalışkanoğlu A.Z, **Ünal A.**, and Nývlt D., (2018). Lithostratigraphy and petrology of Lachman Crags and Cape Lachman lava-fed deltas, Ulu Peninsula, James Ross Island, north-eastern Antarctic Peninsula: Preliminary results, *Czech Polar Reports*, 8 (1): 60-83,
- Kamacı, Ö., **Ünal A.**, Altunkaynak Ş., Georgiev, S., and Billor, Z. M., (2017), The Çataldağ Plutonic Complex in Western Anatolia: Roles of Different Granites on the Crustal Buildup in Connection With the Core Complex Development In: Çemen, İ. & Yılmaz, Y. (eds) *Active Global Seismology: Neotectonics and Earthquake Potential of the Eastern Mediterranean Region*, 189-222.
- Papadopoulos, A., Altunkaynak Ş., Koroneos, A., **Ünal A.**, and Kamacı, Ö. (2017). Geochemistry of uranium and thorium and natural radioactivity levels of the western Anatolian plutons, Turkey. *Mineralogy and Petrology*, 111: 677-691.

- Papadopoulos, A., Altunkaynak, Ş., Koroneos, A., **Ünal, A.**, and Kamacı, Ö. (2016). Distribution of natural radioactivity and assessment of radioactive dose of Western Anatolian plutons, Turkey. *Turkish Journal of Earth Sciences*, 25: 434-455.
- Papadopoulos, A., Altunkaynak, S., Koroneos, A., **Ünal, A.**, and Kamaci, O. (2016). “Natural Radioactivity Of Western Anatolian Plutons, Turkey”. *Bulletin of the Geological Society of Greece*, 50(4), 2332-2341.
- **Ünal A.**, Kamacı Ö., Yildiz M., Atabek G., Yarar S., and Altunkaynak Ş., (2012). “Volcanic Stratigraphy and Petrology of Susurluk Volcanites (NW Turkey), *12th Multidisciplinary Scientific GeoConference*, pp 391-398,
- **Ünal A.**, Kamacı Ö., Altunkaynak Ş., Sunal G., and Billor M.Z. (2013). “Origin Of The Ductile and Overlaying Brittle Deformation in Çataldağ Plutonic Complex (Nw Anatolia)”, *66. Geological Congress of Turkey*, p. 104.
- Kamacı Ö., **Ünal A.**, Altunkaynak Ş., Billor M.Z, Georgiev S., and Marchev P. (2013). “Emplacement, Deformation and Exhumation of the Çataldag Plutonic Complex: Implications for Neotectonic Evolution of NW Anatolia (Turkey)”, *American Geophysical Union Abstracts, Fall Meeting*, 2013.
- Güraslan, I.N., **Ünal, A.**, and Altunkaynak, Ş. (2016). “Contact relations and petrography of the Solarya intrusive complex (NW Turkey)”, *EGU General Assembly Conference Abstracts*, Vol. 18, p. 8965.
- Çalışkanoğlu, A.Z., **Ünal, A.**, Karadağ, E., Altunkaynak, Ş., and Görür, N. (2016). “Volcano-stratigraphy and Petrography of the Hasandag Volcanites (Central Anatolia)”, *EGU General Assembly Conference Abstracts*, Vol. 18, p. 4420.
- Çalışkanoğlu A.Z, **Ünal A.**, Karadağ E., Altunkaynak Ş., and Görür N. (2016). "The Geology and Petrography of Hasandağ Volcanites", *69. Geological Congress of Turkey*.
- Çalışkanoğlu, A.Z., **Ünal, A.**, Kamaci, Ö., and Altunkaynak, Ş. (2017). “The Origin and Petrogenesis of Mount Hasan (Small Mt. Hasan) and Keçiboyduran Stratovolcanoes”. *EGU General Assembly Conference Abstracts*, Vol. 19, p. 849.
- Güraslan, I.N, **Ünal, A.**, and Altunkaynak, Ş. (2017). “Geochemistry and Sr-Nd-Pb isotopic characteristics of mantle xenoliths of Hacikoy and Karatepe alkaline lavas in Thrace Region (NW Turkey)”, *EGU General Assembly Conference Abstracts*, Vol. 19, p. 10685.

